CHARACTERIZATION AND MODELING OF TWO DIMENSIONAL CRACK GROWTH IN GAS TURBINE MATERIALS

A Dissertation
Presented to
The Academic Faculty
By

Morris Mandel Satin

In Partial Fulfillment
Of the Requirements for the Degree
Doctor of Philosophy in Materials Science and Engineering

Georgia Institute of Technology

May 2020

CHARACTERIZATION AND MODELING OF TWO DIMENSIONAL CRACK GROWTH IN GAS TURBINE MATERIALS

Approved by:

Dr. W. Steven Johnson, Co-Advisor
George W. Woodruff School of Mechanical Engineering
School of Materials Science and Engineering
Georgia Institute of Technology

Dr. Richard W. Neu, Co-Advisor
George W. Woodruff School of Mechanical Engineering
School of Materials Science and Engineering
Georgia Institute of Technology

Dr. Arun Gokhale
School of Materials Science and Engineering
Georgia Institute of Technology

Dr. Olivier Pierron
George W. Woodruff School of Mechanical Engineering
Georgia Institute of Technology

Dr. Christopher Muhlstein
School of Materials Science and Engineering
Georgia Institute of Technology

Date Approved: November 21, 2019

DEDICATION

This work is dedicated to my mother Irene Carol Margolin Satin who gave me life and whom I miss every day

ACKNOWLEDGEMENTS

This project, and all of the work leading up to and around it would not have been possible without a team of people serving as my mentors, supporters, and advisors. I'd like to thank my advisors, Dr. Steven Johnson and Dr. Richard Neu who provided me with thoughtful discussion, background knowledge, and professional support throughout the project. I'd like to also thank the dedicated staff in the Georgia Tech machine shop for their expertise and hard work, Tim Waters and Braddock Metallurgical for being a mentor, a source of knowledge, and for providing heat treatment services for the project, and Dr. Brett Ziegler for being a tireless ally. Thank you to Pratt & Whitney for graciously funding this research. I'd like give a special thank you to James Huggins, Kyle Brindley, and especially James Collins without whom there would be no experiments. I'd like to show my appreciation for my lab partner Bryan Vitale who taught me how to be a grad student and to all my friends and colleagues: Ernesto Estrada, Chuchu Zhang, Anirudh Bhat, Zachary Towner, Sanam Gorgan Nejad, and Jonathan Fok Wai who have been incredible sources of ideas and help. Finally I'd like to thank my family. My father Allan Satin who has supported me through many long phone calls, my sister Elana Richter who has shared my life through good and bad, my dog Carly who was always happy to see me when I got home. Finally I'd like to thank my wife Rachel Berman who is a constant source of strength and support, and my daughter Sonya Satin who I love more than anything in the world and will write an even better thesis then this someday.

TABLE OF CONTENTS

LIST OF TABLES

LIST OF FIGURES

LIST OF SYMBOLS

a, Crack length in the depth direction of a surface flaw; Crack length of a one-dimensional through crack

a', Fictitious crack length in the depth direction of a surface flaw exceeding the plate-thickness, used to define the elliptical crack contour in the SGT and SGT(λ) methods

$\mathbf{a_{through}}$, Crack length of a through crack that results from a fully transitioned surface crack (labeled *c* before transition)

c, Crack length in the width direction along the front face of a quarter-elliptical corner crack or half the crack length in the width direction along the front face of a semi-elliptical surface flaw

C, Modified Forman Equation crack growth law constant

c', Crack length in the width direction along the back face of a quarter-elliptical corner crack or half the crack length in the width direction along the back face of a semi-elliptical surface flaw

CGIN718, Coarse grained Inconel 718

d, Mean grain diameter

da/dN, Instantaneous crack growth increment for a single cycle

EDM, Electrical Discharge Machining

EPD, Electrical Potential Drop

f, Frequency

F, Fast band in the high temperature isothermal test either at f = 5 Hz or f = 2 Hz

FGIN718, Fine grained Inconel 718

h, Full gage height of clamped specimens (distance between clamping grips)

IN718, Inconel 718

K, Stress intensity factor

$\mathbf{K_{IC}}$, Mode I critical stress intensity factor

M, Marker band designation in TMF test

n, Modified Forman Equation crack growth law constant

$\mathbf{N_f}$, Number of consecutive cycles in a single fatigue band

N_m, Number of consecutive cycles in a single marker band

Q, Activation energy

r, Hole radius for center through hole surface flaw configurations

R, Fatigue stress ratio (S_{min}/S_{max})

R, Ideal gas constant (8.31446 mol/J*K)

R_{bl}, Fatigue stress ratio in the "baseline load" or fatigue band waveform

R_{ml}, Fatigue stress ratio in the "marker load" or marker band waveform

RUT, Remote Uniform Tension boundary condition

S, Far field/Global applied stress

S, Slow band or f = 0.1 Hz band in the high temperature isothermal test

SEM, Scanning Electron Microscope

SENT, Fixed end Single Edge Notched Tension sample configuration

SGT, Simple Geometric Transition method

SGT(λ), Modified Simple Geometric Transition method with the λ scaling factor

t, Plate thickness

T, TMF band in the TMF test

TAF, TAZ Acceleration Factor

TAZ, Temperature Affected Zone

TMF, Thermomechanical Fatigue

w, Full plate width for SENT and quarter elliptical corner cracks, half plate width for semi-elliptical surface flaws

$\bar{x}$, Average x-coordinate along an elliptical curve section

$x_{centroid}$, Centroid x-coordinate of a quarter ellipse

Y, Stress intensity factor geometric parameter

ΔK, Stress intensity range (K_{max}-K_{min})

ΔK_a', Stress intensity range in the depth direction after the breakthrough of a surface flaw

ΔK_{th}, Threshold stress intensity range

ΔK_{theff}, Effective threshold stress intensity range

λ, Scaling factor augmenting the back face crack growth in the SGT(λ) method

$\boldsymbol{\varphi}$, Parametric angle defined as the angle from a crack origin to the perimeter of a circle whose radius is the smaller of the dimensions *a* and *c*

$\boldsymbol{\psi}$, Elliptical angle defined as the angle from a crack origin to the perimeter of an ellipse

SUMMARY

Cracks starting at surfaces will grow under fatigue loading conditions both along the surface and in the thickness direction of the component geometry. These can be caused by many common problems such as marks from machining, foreign object damage, manufacturing defects, or corrosion. For this reason, the fatigue crack growth of surface flaws has been a subject of study for decades and are of particular interest in critical hardware such as aircraft components. In those cases where the crack grows through the thickness, the fatigue crack may transition to a corresponding through crack geometry. While the fatigue crack growth behavior of both the surface flaws and complete through cracks are well understood, the method for modeling the process by which they transition from one to the other is not. This project seeks to bring greater clarity and understanding to the transition process by implementing a transition method, and developing the associated codes and equations to do so based on careful consideration of boundary conditions, experimental data and finite element simulations.

Jet engine components experience additional complications due to the fact that they not only experience mechanical cyclic loading but also thermal cyclic loading. The effect of this Thermomechanical Fatigue (TMF) has also been a subject of a great amount of research due to the complex interactions between the two types of cyclic loading. The second portion of this project will take the model of surface flaws and study how TMF influences the growth and shape of the crack. This portion builds on the previous research by Andrew Radzicki[1] who quantified and modeled the effects of TMF on Inconel 718 in

through cracks. This project seeks to look further into the mechanisms by which the material is damaged at high temperatures and see how they are influenced by surface flaws.

By describing the growth of surface flaws more accurately, better life predictions can be made with more confidence. This increase in precision can result in cost savings and improved safety for engine manufacturers are aircraft operators. Hardware with surface flaws could be flown for longer before retirement or inspection intervals could be increased, decreasing costs and downtime.

A realistic description of the transition can allow for other effects in fatigue crack growth to be accounted for in a way that is not possible with the traditional instant transition method. For example, if there is some material inhomogeneity in the transition region that would accelerate crack growth, it would be ignored when the crack is instantly transformed to a through crack. This could have important ramifications for how TMF damage develops in this region of the part's life.

Knowing how surface flaws interact with TMF is vital to understanding how to appropriately predict failure in jet engine components with these types of cracks. Due to the differences in the behavior of the Temperature Affected Zone (TAZ) in plane strain and plane stress conditions, it is not currently known how this may affect the growth of these flaws. The plane strain nature of the internal part of the crack could cause it to grow TAZ at an enhanced rate, changing the normal aspect ratio evolution of the crack and causing it to breakthrough and transition more quickly. This project updates the MPYZ-TMF code with the goal of accurately predicting surface flaw crack growth under TMF.

Radzicki [1] found that the TAZ had a very negative impact on the life of Inconel 718 under TMF. It's possible that if the composition and morphology of the TAZ was better understood, there could be a way to manage or retard its growth. For this reason, part of this project will be devoted to characterizing the way TAZ develops and how damage is accumulated in Inconel 718 at high temperatures over time.

The views expressed in this work are those of the author and do not reflect the views of any company mentioned herein.

CHAPTER I

ROOM TEMPERATURE TRANSITION OF SURFACE FLAWS TO THROUGH CRACKS

1.1. Background on the Fatigue of Surface Flaws

Fatigue crack growth modeling of surface flaws can be challenging and is inherently more difficult than modeling through cracks. Through cracks are most often collapsed to a single dimension so that their crack growth can be described by a single stress intensity factor that is dependent on the length of the crack, *a*. Surface flaws on the other hand, are two dimensional by nature having both a width direction, *c*, and a depth direction, *a* (see Figure 1). This means that surface flaws, not only must be grown in two directions at once, with two separate stress intensity factors, but those stress intensity factors must have an inherent relationship based on the relative sizes of *a* and *c*.

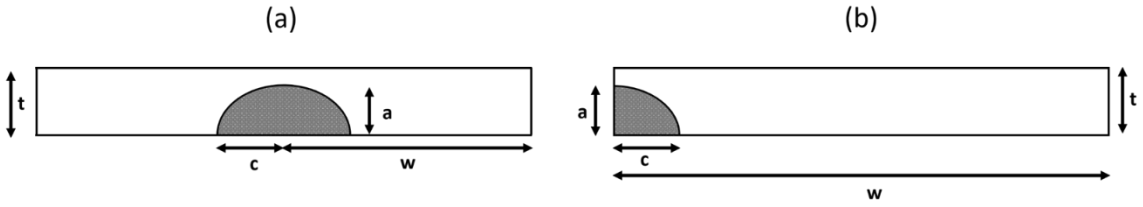

Figure 1: Geometric definitions of: (a) Semi-elliptical surface flaw (b) Quarter-elliptical corner crack

Over the years different stress intensity factors have been proposed to quantify the relationship between the crack lengths *a* and *c*, as well as geometric factors like plate width *w*, plate thickness *t*, and hole radius (when applicable) *r*. The basis for most modern crack

modeling programs comes from solutions developed by I.S. Raju and J.C. Newman in the 1970's and 1980's. These stress intensity factors were developed using finite element models on semi-elliptical surface flaws and were first available only as coefficients in a look-up table [2]. To make the factors easier to use, equations were fit that could be more easily implemented in computer codes for crack modeling [3]. Eventually equations were produced for five of the most common surface flaw geometries, semi-elliptical surface cracks and quarter-elliptical corner cracks at plate surfaces and at through holes, as well as embedded elliptical cracks [4] (see Figure 2). These stress intensity solutions are used for surface flaws in many of the most popular fatigue crack growth modeling programs today, and are the basis for the treatment of surface flaws in this current work.

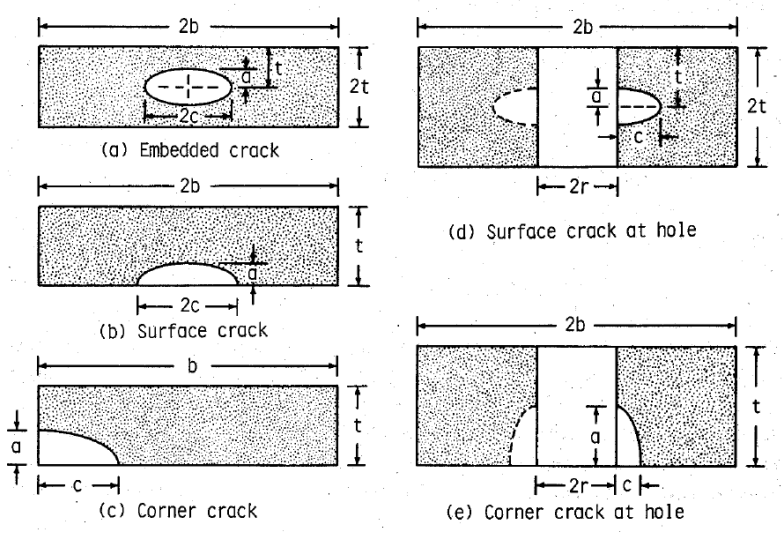

Figure 2: Surface flaw configurations covered by the Raju-Newman equations [4]

Commercial fatigue crack growth software packages such as AFGROW use the Raju-Newman equations to grow cracks as surface flaws until a particular transition criterion is met [5]. In AFGROW this can either be defined as 95% thickness penetration, or an equivalent fracture toughness criterion. Other programs will transition when the

crack depth has reached 100% thickness penetration [6]. Once this criterion is reached, the crack is instantly converted to a through crack, whose crack length is equivalent to the previous crack contour's front-face crack length. For the purposes of this document, these transition methods will be described as "instant transition" methods.

Other transition methods have been suggested before. One focused on back face yielding [7]. Another used the finite-element alternating method to analyze the transition for a specific scenario [8]. W. S. Johnson [6] put forward a method that continues to use the stress intensity solutions for surface flaws through the transition by extending the elliptical crack contours into a fictitious space beyond the back face of the material. Once the depth direction of the contour (a) becomes greater than the plate thickness (t), the back face crack length (c') can be computed using the following ellipse equation:

$$\frac{c'^2}{c^2} + \frac{t^2}{a'^2} = 1 \qquad (1)$$

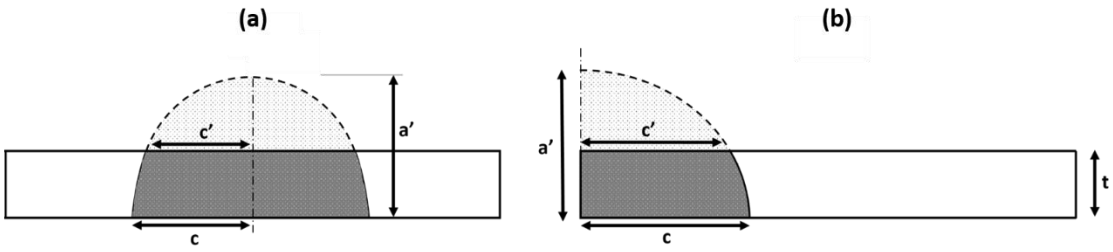

Figure 3: Extended geometries for Johnson's method in (a) Semi-elliptical surface flaws, (b) Quarter-elliptical corner cracks

In his method, Johnson only transitioned the flaw to a fully through-the-thickness crack when the ratio c'/c reached a specific threshold, for example, 0.9 (Figure 4). The Johnson method originally used older stress intensity solutions empirically fit to experimental data [9]. This method will be referred to as the Simple Geometric Transition (SGT) method.

This work will combine the SGT method with the Raju-Newman solutions and then make modifications based on experimental observations.

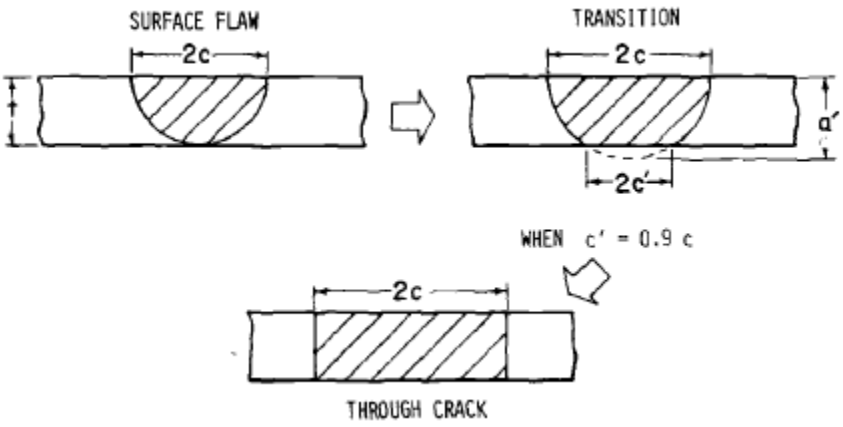

Figure 4: Johnson transition method showing fictitious ellipse extension with backface crack length c' [6]

This method has many distinct advantages when compared to the instant type transition methods. Figure 5 shows a comparison of different stages of crack growth with the two methods. Both methods start using a similar method (part *a* and part *e*). However, the instant type transition transforms, completely ignoring the effects of crack growth in the light grey region in part *c*. This area of ignored growth is much smaller in the SGT method and can be seen as the medium grey segment in part *h*. In addition, the crack growth occurring in part *d* misses all the shape information that is present in the crack growth seen in part *f*.

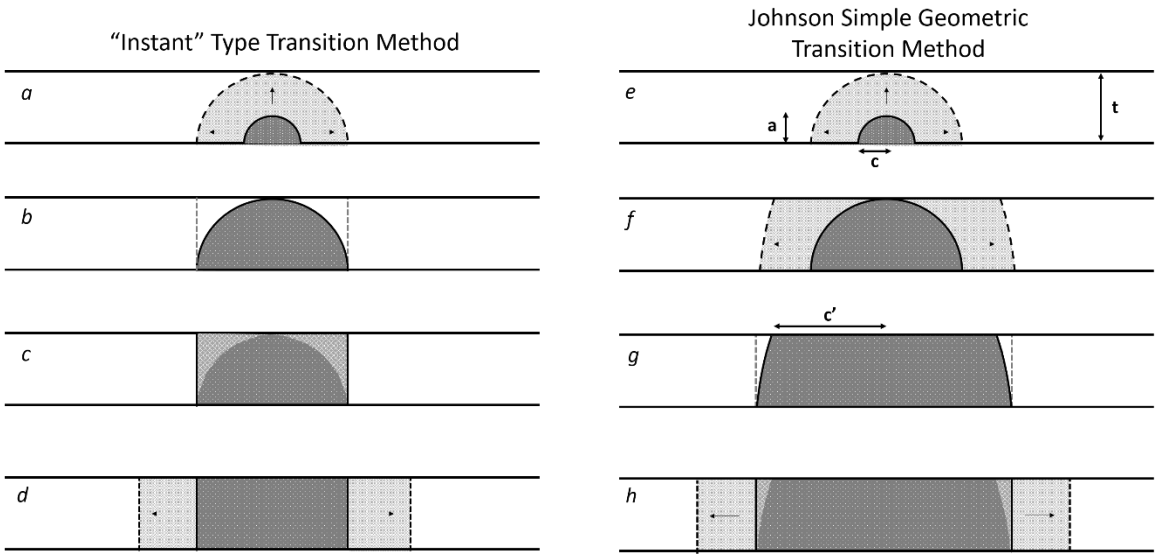

Figure 5: (Left) Instant Type Transition Methods, (Right) Simple Geometric Transition (SGT) Method at the same scale

One of the inherent challenges to performing fatigue crack growth experiments on surface flaws is that one of the crack dimensions is often hidden in the interior of the material. One experiment observing the behavior of quarter-elliptical corner cracks and semi-elliptical surface flaws at a hole was done on transparent polymethyl-methacrylate in order to observe the crack growth in-situ [10]. The potential drop method has also been used to monitor surface crack growth in-situ, but can be complicated since multiple crack lengths must be derived from single potential drop values [11]. By far the most common method involves the use of marker bands [12]–[14]. In this method the applied stress is periodically changed in such a way that the appearance of the fracture surface is altered for a specific number of cycles. After the experiment is complete, the marks on the fracture surface can be measured. This will tell the observer both the shape and location of the crack front at the start and end of the marker region.

Modeling for this project involves the use of the Multi-Parameter Yield Zone model with Thermomechanical Fatigue (MPYZ-TMF). The original MPYZ model was developed by Johnson [15] to model isothermal load interaction effects on crack growth. The model was modified by Barker et al. to account for changes in fracture properties at different temperatures [16], [17]. Barker's modifications also allowed for a Temperature Affected Zone (TAZ) to form ahead of the crack tip at high temperatures. This TAZ accelerated crack growth through the region, even at lower temperatures. The most recent additions to the MPYZ-TMF program have been made by Radzicki [1] who quantified the TMF effects on Inconel 718 and made modifications to the way the TAZ develops in the model.

1.2.Experimental and Analytical Methods

1.2.1. Experimental Methods

1.2.1.1. Materials and Testing Techniques

Baseline experiments at room temperature and constant amplitude were conducted on Inconel 718 and 17-4 H1025 precipitation hardened stainless steel to investigate the transition of corner cracks, surface flaws, and corner cracks at a hole to through cracks. These experiments made use of a servo-hydraulic fatigue testing frame using hydraulic wedge grips to hold the material. Hydraulic fatigue frames have the advantage of being relatively flexible in the range of loads that can be applied, and are easily programmable through a computer interface. In addition they can be used at a relatively high frequency (up to 15 Hz for this experiment), making them ideal for use in this project with experiments lasting many hundreds of thousands of cycles.

A baseline stress ratio of R=0.1 ($\sigma_{min}/\sigma_{max} = 0.1$) was selected for the "fatigue band" portions of the experiment. This keeps the experiment in a state of constant tension. This is generally better for stability of the test stand as well as negating buckling concerns. A series of experiments were conducted on 4130 low alloy steel and Inconel 718 compact tension specimens to find the optimal marker band ratio to get good contrast in the marker band regions. In order to get the necessary contrast in the marker bands, the crack growth rate must be significantly different from the fatigue band. One way to achieve this involves applying a smaller stress amplitude while keeping the maximum stress constant (Figure 6). This ensures that there are no overload effects on the subsequent crack growth. A marker ratio of R=0.7 was found to have a good balance of enhanced contrast from its relatively large loading difference, but still had a large enough stress amplitude to result in measurable crack growth. This combination matched the recommendation made by Dong et al. [14] which found the optimal marker ratio to be:

$$R_{ml} = 0.65 + 0.5R_{bl} \qquad (2)$$

Where ml stands for "marker load" and bl stands for "baseline load".

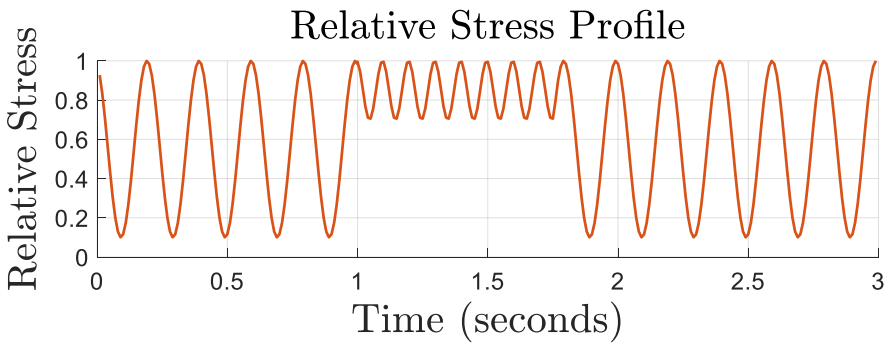

Figure 6: Representative load spectrum showing the "marker spectrum" in the center with the same maximum stress but a higher R ratio

1.2.1.2. Specimen Design

Inconel 718 plates of dimensions 101.6 mm x 38.1 mm x 6.35 mm (8 in x 1.5 in x ¼ in) were supplied by Pratt & Whitney for testing but its properties do not present any Pratt & Whitney hardware or intellectual property. These plates were found to be made of a fine-grained (4 μm mean diameter) microstructure where the δ precipitates had been given a spheroid morphology (see section 2.2). The width and thickness of the plates were selected to be near the maximum allowable for our wedge grips. This thickness allows for the best resolution in the pre-breakthrough and transition regions of crack growth. The height was selected to ensure that sufficient material was available for clamping with a gauge height tall enough to minimize clamping effects for the centered specimen configurations. Due to a material shortage, some of these plates were cut and reused with shorter gauge heights for the room temperature corner crack testing which was later accounted for in the data analysis.

For room temperature testing, experiments were also conducted on 17-4 H1025 precipitation hardened stainless steel obtained from Valbruna Stainless Inc. through McMaster-Carr. 17-4 H1025 was selected as an appropriate substitute for Inconel 718 due to its very similar mechanical properties at room temperature (Table 1). Plate sizes for 17-4 samples were similar to the Inconel 718 plates for the corner crack configurations, however the plate dimensions for the semi-elliptical surface flaws and corner cracks at holes were 101.6 mm x 76.2 mm x 6.35 mm (8 in x 3 in x ¼ in), which was twice as wide. For specimens requiring a center through hole, the hole was drilled with a drill press, and then reamed to the final dimensions before final heat treatment to result in a smooth finish and minimize residual stresses. The material was obtained in the as-solutioned condition

(condition A). Heat treatment was performed by the Braddock Metallurgical company by heating the material to 552 ºC (1025 ºF) for 4 hours.

Table 1: Room temperature mechanical and fracture properties of Inconel 718 and 17-4 H1025 [18]

	Inconel 718	**17-4 H1025**
Yield	1030 MPa	1000 MPa
UTS	1240 MPa	1070 MPa
E	203 GPa	197 GPa
KIC	131 MPa√m	129 MPa√m

Metallic samples had starter notches of various sizes and aspect ratios cut with electrical discharge machining (EDM). EDM electrodes were cut from either 0.05 mm (0.002 in) copper or 0.2 mm (0.008 in) brass sheet stock in the shape of quarter and semi ellipses with wire EDM. These electrodes were then used to burn thin notches (on the order of 300 μm thick) into the appropriate location on the IN718 or 17-4 plate material. Early samples had the EDM electrodes inserted multiple times to ensure notch shape accuracy. This was found to widen the notch considerably, while also causing material degradation in the future crack path. Later samples were instead machined using the "single plunge" method where a single electrode was inserted to the desired depth on a single pass. The resulting notch had a less regular shape, but it was found that the crack front very quickly became elliptical during its growth. The resulting decrease in material degradation allowed for data to be taken closer to the initial notch, and the thinner starting notch resulted in faster crack initiation times.

Samples were then polished on the surface (c-direction) around the starting notch to allow for in-situ observation of the cracks at the surface. The 17-4 material had a rough finish from rolling and heat treatment and therefore required sanding with progressively fine sand paper before polishing. This was accomplished with a combination of Dremel tool sanding disks, and hand sanding with sandpaper strips to a grit size of 320. Both the 17-4 and the IN718 were then polished in the region surrounding the starting notch with a small felt wheel attached to a Dremel tool. Each sample was polished with progressively finer diamond slurry (9, 3, and 1 μm) for 3 minutes per step. Between steps the surfaces were cleaned first with acetone and then with water and immediately dried with compressed air. In some cases, residue from the felt wheels interacting with notch got stuck to the surface. This could be removed by applying a clean felt wheel with water. All polishing was done in the direction perpendicular to the future crack growth. This way, any polishing marks that were still present at the time of the experiment would not be confused for the crack and wouldn't interfere with crack measurements.

Samples with semi-elliptical surface flaws and corner cracks at a hole were then dried in an environmental chamber set to 0 RH and 80 ºC for at least 4 hours. This ensured that liquid from the EDM process and polishing that may have remained trapped in the starting notch was removed prior to testing. The now polished samples were scribed with calibration marks using a carbide tipped depth measurement tool, while orientation was maintained with a vice on a level surface. These calibration marks were scribed at 1 mm intervals perpendicular to the crack growth direction and were used both for calibration of the Questar traveling microscope, used to monitor crack growth, and as reference points to overcome difficulties with the limited field of view of the instrument.

1.2.1.3. Experimental Setup

Specimens were placed in the hydraulic wedge grips with 50.8 mm (2 in) inserted into the serrated wedge inserts. This ensured that no slipping occurred during testing and the specimen remained in alignment until failure. For the sub-size IN718 experiments, test specimens were only inserted to 19.05 mm (3/4 in) to maximize the available gauge section height. Since these specimens were all the 38.1 mm wide specimens, the test system was still able to remain stable with the smaller grip area. These samples carefully had their exact gauge heights measured before insertion since they were cut to different sizes depending on remaining material.

For room temperature testing the following stresses were selected to ensure a large enough ΔK for initiation, but slow enough crack growth to ensure data could be taken in the transition region:

Table 2: Room temperature applied stresses for surface crack experiments

	σ_{max}	σ_{min}	σ_{amp}
R=0.1 Fatigue Bands	181.9 MPa	18.2 MPa	81.9 MPa
R=0.7 Marker Bands	181.9 MPa	127.3 MPa	27.3 MPa

Crack initiation was accomplished by running the R=0.1 fatigue cycle at 15 Hz for 38.1 mm wide specimens and 10 Hz for 76.2 mm wide samples for blocks of 100,000 or 50,000 cycles. At the end of each block, the sample was inspected with the Questar traveling microscope to find evidence of crack initiation. Once initiation was detected the experiment proceeded with alternating block fatigue bands (at 5 Hz), and marker blocks (at 10 Hz). The surface dimension of the cracks were observed with the Questar

microscope at the end of a pre-set number of blocks. The number of cycles in each fatigue and marker band in the next block were determined by looking at the crack length and a combination of past experiments and modeling to get visible marker bands that were spaced appropriately for data collection.

1.2.1.4. Data Collection

After fracture, micrographs were taken of the fracture surfaces for analysis. The observation of marker bands are highly dependent on lighting conditions. It was found that for Inconel 718, optimum lighting could be achieved using the built-in ring lighting on the Keyence VHX-600 digital optical microscope. For 17-4, marker bands were more visible using an LED ring light attachment covered by a plastic diffusor available on the Leica M125 and the Leica DVM6 microscopes. The field of view in the Leica microscopes are not sufficient for observation of the entire fracture surface, and therefore smaller micrographs were taken and then stitched together using the Adobe Photoshop photo-editing software. Like before, calibration marks were scribed on the surfaces at 1 mm intervals in order to aid with calibration of the image measurement software, and to serve as reference points for image stitching.

Measurements were taken using ImageJ (a free open source Java based image manipulation tool). The rotational misalignment of each micrograph was measured using the software. The images were then rotated so that the coordinate system of the image coincided with the crack growth axes *a* and *c*. The ImageJ measurement system was calibrated with the 1 mm spaced scribe marks and/or the thickness of the plate material. The image was then cropped for corner cracks so that the origin of the crack matched the

origin of the micrograph. For surface flaws the image was cropped in the thickness direction and the width direction coordinates were adjusted in later analysis.

Points were selected in ImageJ corresponding to the furthest extent of crack growth for each contour using a set of predefined rules. For the *c* direction of growth (front face) the crack length was defined by the point of farthest horizontal growth of the crack front. For the depth direction *a* the crack length was defined by the point of farthest vertical growth of the crack front. For *c'* measurements (back face) in the transition region, the horizontal measurements were made at the point where the crack front intersected the back face of the material. For crack contours where this intersection point could not be resolved, the crack contour was extrapolated to the back surface and the measurement was taken there. For semi-elliptical surface flaws, the image origin couldn't be made coincident to the crack origin. Instead for horizontal measurements, the distance from the rightmost and leftmost points along a crack contour was found and then averaged to get the *c* measurement. In the transition region the "center" coordinate for system was found by finding the top-most point in the last crack contour before breakthrough and the *c* and *c'* measurements were made on one side of the image with reference to this point.

1.2.2. Analytical Methods

The main modeling tools used for this project are the MPYZ-TMF computer program and finite element simulation. MPYZ-TMF is used both as a predictive tool, and also as the main system to be optimized in the project. 2D FE simulations are done using the ANSYS Parametric Design Language (APDL), and 3D FE simulations use a combination of ANSYS and FRANC3D which is a commercially available fatigue and fracture package offered by the Process Optimization Corporation.

Inputs for MPYZ-TMF include information about the plate and crack geometry (*h, w, t, a, c, r*), information about the loading (applied stress/load and temperature spectrum), information about the material (E, σ_y, K_{IC}, K_{th}, fatigue crack growth constants for Paris, Forman, and modified Forman equations, information about the applied marker bands (when appropriate), and transition options/parameters which will be discussed later.

1.2.2.1. Fatigue Crack Growth Law

The modeling for the room temperature portion of this project uses the Modified Forman Equation [19] which has been added to MPYZ-TMF as one of the crack growth law options:

$$\frac{da}{dN} = \frac{C(\Delta K - \Delta K_{th_{eff}})^n}{((1-R) * K_{Ic} - \Delta K)} \qquad (3)$$

Where:

$$\Delta K_{th_{effective}} = \Delta K_{th} * (1 - R_{effective}) \qquad (4)$$

While the Modified Forman Equation does account for R ratio effects, it does not seem to be very accurate for very high R ratios (like R=0.7) when it has originally been fit to lower R values. Because of this MPYZ-TMF was modified to accept two separate sets of Modified Forman parameters, the second of which to be applied specifically in the marker band region.

For Inconel 718, fatigue crack growth data was found in the literature for both R=0.1 and R=0.7 which included near-threshold values [20]. The Modified Forman equation was fit to the data using a non-linear regression technique in which the log(da/dN)

and log(ΔK) data was used to ensure a good fit in all regions of the curve. The fitted constants were:

Table 3: Modified Forman constants for IN718 at room temperature where da/dN is in mm/cycle and stress intensity is in MPa√m

	R=0.1	**R=0.7**
C	7.62E-08	3.54E-06
n	3.5755	2.0537
K_{IC}	131	131
K_{theff}	3.94	3.4952

For 17-4 H1025, fatigue crack growth data was fit to experiment 174-S-003 (semi-elliptical surface flaw) on the Valbruna Stainless material used for this experiment. A similar fitting method was used to find the fatigue crack growth constants for R=0.1 as was used in IN718. The fitted constants for 17-4 H1025 were:

Table 4: Modified Forman constants for 17-4 H1025 at room temperature where da/dN is in mm/cycle and stress intensity is in MPa√m

	R=0.1	**R=0.7**
C	7.50E-06	1.53E-05
n	2.2157	1.2505
K_{IC}	129	129
K_{theff}	3.5	2.5

1.2.2.2. Changes to MPYZ-TMF

The MPYZ-TMF program has been substantially modified to allow for the use of surface crack geometries. A simultaneous crack growth system has been added so that the crack lengths *c* and *a* can be grown together cycle by cycle. Since the stress intensity factor

in each growth direction is dependent on both crack lengths, these parameters cannot be run independently. This means that all parameters that track with crack length must be tracked in parallel such as plastic zone size, extent of TAZ, and load interaction effects. Once the crack breaks through, it enters the transition region where the crack depth *a* continues to grow to values greater then *t*, however, the Raju-Newman equations are partially dependent on a depth ratio parameter *a/t*. Since the equations were not meant to be used with values of $a/t > 1$, the ratio is fixed in this region at $a/t = 0.95$. Once the crack has met the transition criteria (usually $c' = 0.9 * c$), the program retains the information stored for the *c* direction of crack growth and continues to grow the crack as the appropriate through thickness geometry using the *c* direction information for the new crack length $a_{through}$.

Additional changes have been made to the program to include a graphical user interface (GUI) that runs in a Microsoft Excel VBA shell program. This program allows the user to control all the input properties in a graphically pleasing and straightforward manner. The GUI also automatically imports the output of MPYZ-TMF and plots useful information such as the crack length vs. number of cycles, and a plot of either iso-life crack contours or marker band locations on every simulation run. The GUI has several built in functions to automate tasks such as saving and loading crack and material information, building marker banding tables, and running parametric studies.

1.2.2.3. Finite Element Simulations

Finite element simulations were conducted by constructing a model in with APDL in ANSYS and then using FRANC3D to analyze the fracture properties. A rectangular prism is constructed and then meshed using Solid186 20 node quadratic elements. The

meshing is set up to provide a relatively fine mesh in the center portion of the model, with a coarser mesh at the top and bottom surfaces. This allows for a stable interaction with FRANC3D crack mesh later, but decreases computation time for the model when compared to a uniformly fine mesh. The model material is selected as a linear elastic isotropic material with a Young's modulus of 204 GPa and a Poisson's ratio of 0.333. Since this project is based on Linear Elastic Fracture Mechanics (LEFM) this simplified material model is allowable for calculation of K values.

Boundary conditions are also added with APDL. For the Remote Uniform Tension (RUT) boundary condition, the nominal stress is applied to top and bottom surfaces of the model, the origin node is fixed in width and thickness directions, and the bottom surface is fixed in the vertical direction. This prevents ridged body motion, but still allows the upper and lower surfaces to rotate from bending due to the crack. In the clamped boundary condition, nodes on the upper and lower surfaces are given a co-displacement condition that ensures all displacement in the vertical direction is uniform at those surfaces and the material at the clamped boundary is prevented from displacing in the width direction. The origin node is fixed in the thickness direction, and the bottom surface is fixed in the vertical direction to prevent rigid body motion.

The model is then imported into the FRANC3D software [21]. The center portion of the model is removed leaving a finely meshed interface with the original model. FRANC3D allows for insertion of different shaped crack fronts in the material which it then meshes to match the interface that was left behind. The ANSYS model can then be run with the crack front inserted and using the displacement information FRANC3D can calculate the stress intensity factor at different nodes along the crack front. FRANC3D

uses the stress intensity information to extend the crack using a median extension and a user defined fatigue crack growth law. For this project the Modified Forman information was loaded into FRANC3D as a look-up table. FRANC3D is then able to fit a new crack front to the extended nodes and remeshes the model for finite element simulation. The FE simulation tool is used to explore the differences in stress intensity due to differing boundary conditions, as well as providing a way to test crack geometries that cannot be done with physical experiments.

To facilitate the use of FE models to explore stress intensity factors, the relationship between the "parametric angle" defined by Newman and Raju [4] and what will be referred to as the "elliptical angle" needed to be established. The parametric angle used in the Newman-Raju solutions (φ) is defined as the angle from the crack origin to the perimeter of a circle whose radius is the smaller of the dimensions *a* and *c* (see Figure 7). The "elliptical angle" (ψ) is simply the angle from the crack origin to the point on the ellipse of interest.

1.2.2.4. Parametric Angles

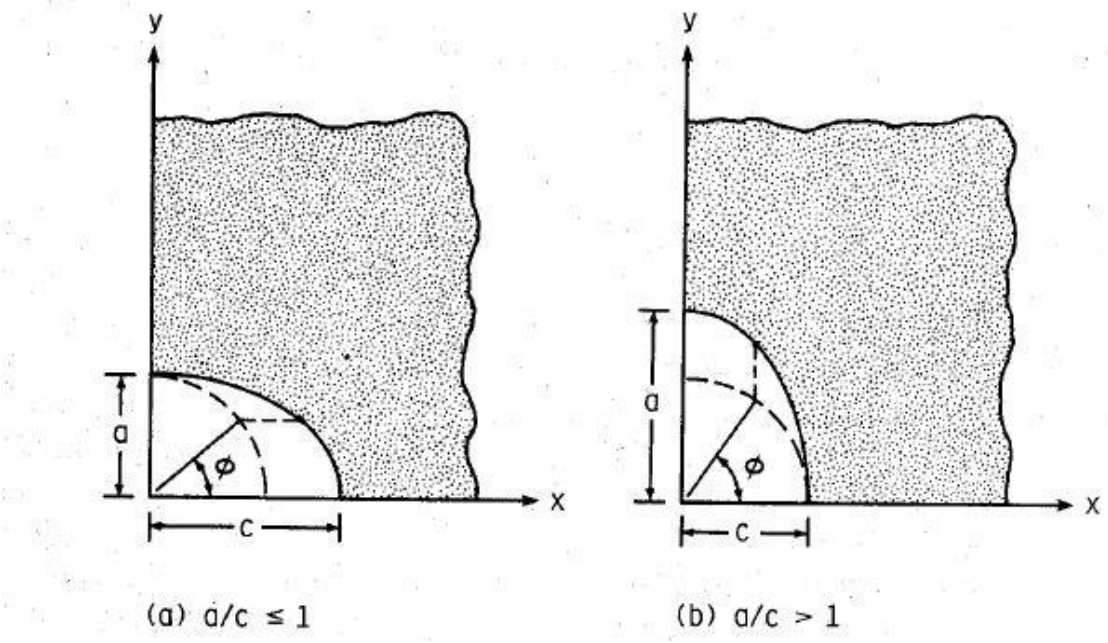

Figure 7: Parametric angle as defined by Newman and Raju [4]

Equations were carefully derived to convert from ψ to φ, and from φ to ψ for both $a/c \leq 1$ and for $a/c > 1$.

For $a/c \leq 1$ to find φ:

$$\phi = \tan^{-1}\frac{\sqrt{\lambda}}{\sqrt{a^2-\lambda}} \qquad (5)$$

Where:

$$\lambda = \left(\frac{1}{tan^2\,\psi\,c^2} + \frac{1}{a^2}\right)^{-1} \qquad (6)$$

For $a/c \leq 1$ to find ψ:

$$\psi = \tan^{-1}\frac{a\mu}{\sqrt{c^2(a^2-\mu^2)}} \qquad (7)$$

Where:

$$\mu = \frac{a \tan \phi}{\sqrt{\tan^2 \phi + 1}} \qquad (8)$$

For $a/c > 1$ to find φ:

$$\phi = \text{cotan}^{-1} \frac{\sqrt{\lambda}}{\sqrt{c^2 - \lambda}} \qquad (9)$$

Where:

$$\lambda = \left(\frac{1}{cotan^2 \psi \, a^2} + \frac{1}{c^2}\right)^{-1} \qquad (10)$$

For $a/c > 1$ to find ψ:

$$\psi = \tan^{-1} \frac{a\sqrt{c^2 - \mu^2}}{c\mu} \qquad (11)$$

Where:

$$\mu = \frac{c \, \text{cotan} \, \phi}{\sqrt{\text{cotan}^2 \phi + 1}} \qquad (12)$$

These equations were verified by creating figures of various aspect ratios and dimensions and carefully measuring the angles to ensure the equations held for all situations. The equations were then used for calculating and plotting coordinates along crack fronts in finite element simulations to see how stress intensity varied across crack fronts.

1.3.Room Temperature Transition Results

1.3.1. Surface Flaw Transition – Boundary Conditions

The Raju-Newman solutions, and subsequently many fatigue crack growth simulation tools pre-suppose a Remote Uniform Tension (RUT) boundary condition in which the upper and lower surfaces of the model geometry are allowed to rotate freely in

response to the bending moment introduced by the crack. Because of the hydraulic wedge grips used in the physical experiments in this work, the "clamped" boundary condition plays an important role in determining the stress intensity factors of these surface flaws. In the clamped condition, the material at the clamped boundary is not allowed to rotate, and instead must displace in the vertical direction evenly (uniform displacement). The effect of this clamping is especially significant in non-center symmetric crack configurations like the quarter-elliptical corner crack and the Single Edge Notch Tension (SENT) geometries and must be understood and accounted for to get accurate predictions.

In SENT crack configurations, the clamped boundary condition decreases the stress intensity factor when compared to the RUT condition. An equation for a clamped SENT specimen with a gauge height to width ratio of 2.67 was found in previous work using the boundary element method and was pre-programmed into MPYZ-TMF [22] based on Newman's FADD2D computer code [23]. This solution had the disadvantage of only being defined for a single height and could no longer be used for the shorter IN718 samples.

A series of FE simulations were conducted using FRANC3D on 38.1 mm wide x 6.35 mm thick plates at a variety of crack lengths and gauge heights using the clamped boundary condition (Figure 8). The deviation of the clamped solution from the RUT solution increases with increasing crack length, and decreases with increasing gauge height. Gauge heights greater than 52 times the width resulted in solutions very close to the RUT condition. Polynomial surface functions were fit to the data to create a set of equations to describe the SIF of a clamped SENT specimen of arbitrary height and width.

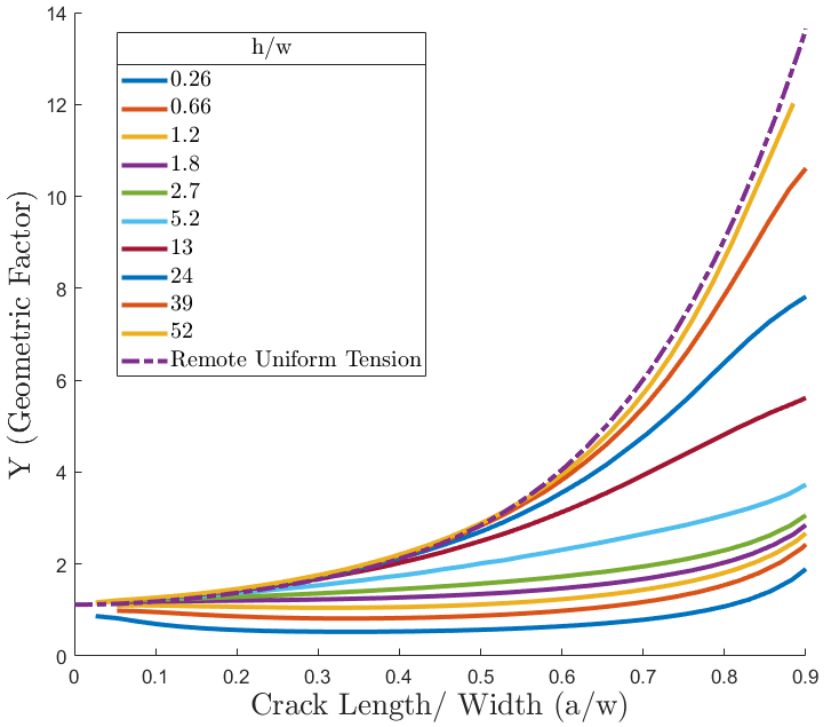

Figure 8: Selected geometric factor contours for Clamped Single Edge Notch Tension specimens by normalized crack length and gauge height

For fitting, the data was broken into two regimes, $h/w \leq 4$ and $h/w > 4$. This allowed for a fit that captured the behavior well at very small heights while still having an option for taller samples. Data was fit to the polynomial (see Figure 9):

$$\begin{aligned} \mathbf{Y} = \sqrt{\mathbf{1000}}\big(&\boldsymbol{p_{00}} + \boldsymbol{p_{10}x} + \boldsymbol{p_{01}y} + \boldsymbol{p_{20}x^2} + \boldsymbol{p_{11}xy} + \boldsymbol{p_{02}y^2} \\ &+ \boldsymbol{p_{30}x^3} + \boldsymbol{p_{21}x^2y} + \boldsymbol{p_{12}xy^2} + \boldsymbol{p_{03}y^3} + \boldsymbol{p_{40}x^4} \\ &+ \boldsymbol{p_{31}x^3y} + \boldsymbol{p_{22}x^2y^2} + \boldsymbol{p_{13}xy^3} + \boldsymbol{p_{04}y^4} + \boldsymbol{p_{50}x^5} \\ &+ \boldsymbol{p_{41}x^4y} + \boldsymbol{p_{32}x^3y^2} + \boldsymbol{p_{23}x^2y^3} + \boldsymbol{p_{14}xy^4}\big) \end{aligned} \qquad (13)$$

Where x is the normalized crack width (a/w) and y is the normalized gauge height (h/w). The stress intensity factor is found with the equation:

$$K = SY\sqrt{\pi a} \qquad (14)$$

With K in MPa√m, stress in MPa, and crack length in meters. Values for the polynomial coefficients can be found in Table 14. The polynomials were added to MPYZ-TMF to be used for clamped SENT configurations.

Table 5: Polynomial coefficients for equation (13)

	y<4	**y≥4**
p00	0.02119	0.03505
p10	-0.01428	-0.0451
p01	0.02012	0.001105
p20	-0.4066	0.7352
p11	0.07777	-0.00818
p02	-0.01035	-3.83E-05
p30	1.663	-2.471
p21	-0.1395	0.0436
p12	-0.02306	-4.22E-05
p03	0.00186	1.01E-06
p40	-2.43	3.105
p31	0.1911	-0.02619
p22	0.00032	-0.00082
p13	0.008755	4.96E-06
p04	-9.04E-05	-1.37E-08
p50	1.272	-1.274
p41	-0.0789	0.000207
p32	-0.01473	0.000784
p23	0.003613	-3.24E-06
p14	-0.0014	-5.49E-09

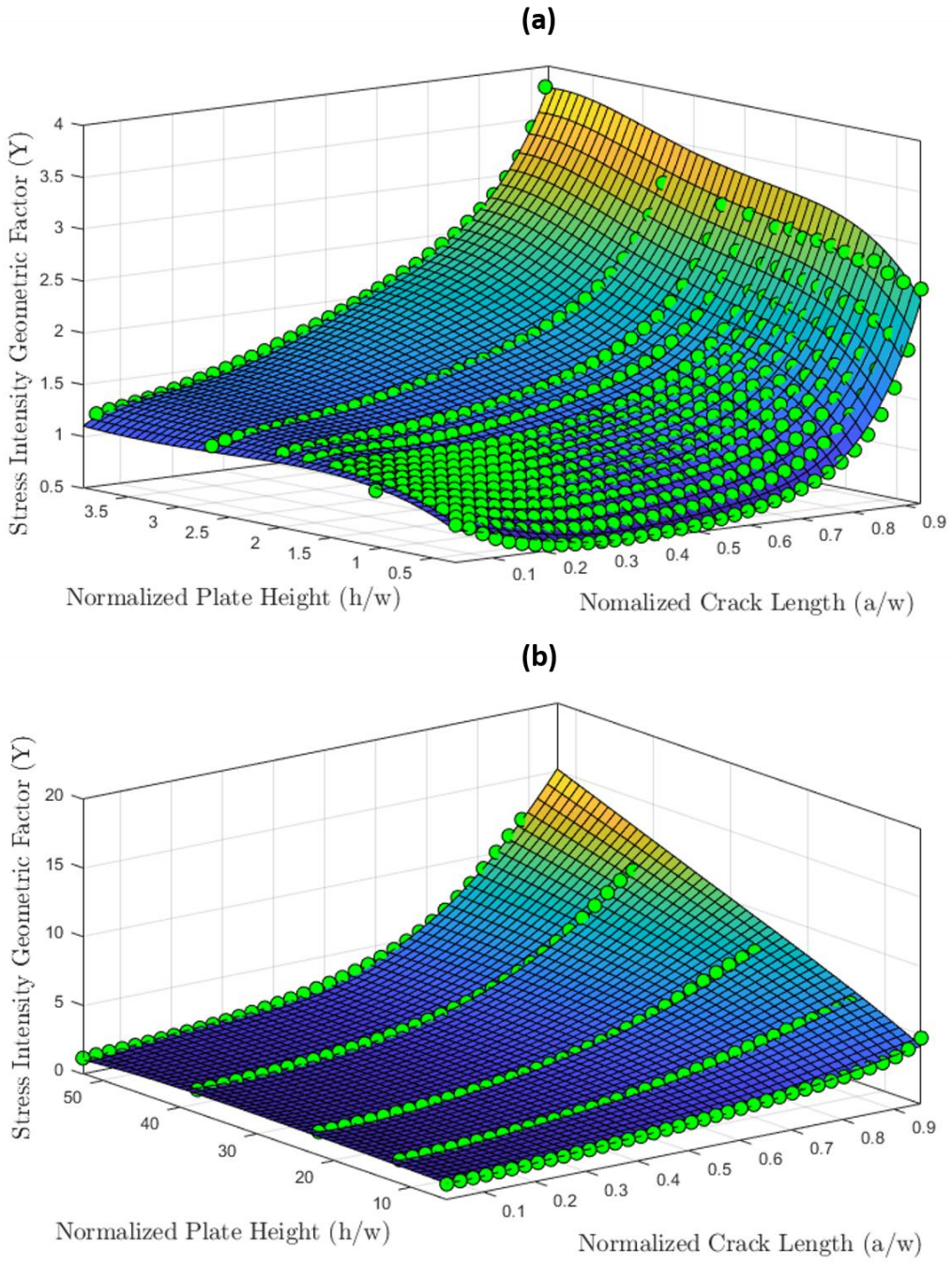

Figure 9: Polynomial surface functions fit to FEA data for the stress intensity geometric factor broken into (a): $h/w \leq 4$ and (b): $h/w > 4$

A system was developed to apply the clamped stress intensity factors to a corner crack. For each cycle in the MPYZ-TMF simulation an equivalent SENT crack length is

determined for each quarter-elliptical crack contour. Before breakthrough the equivalent SENT length is given by the *x*-coordinate of the quarter-ellipse's centroid:

$$\boldsymbol{x_{centroid} = \frac{4c}{3\pi}} \qquad (15)$$

After breakthrough, in the transition region, the equivalent SENT length is given by the average x coordinate along the elliptical curve when restricted to the inside of the specimen cross-section ($c' \leq x \leq c$):

$$\boldsymbol{\overline{x} = \frac{1}{t}\left[\frac{c}{2}\left\{t\sqrt{1-\frac{t^2}{a'^2}} + a'\sin^{-1}\frac{t}{a'}\right\}\right]} \qquad (16)$$

Where t is the specimen thickness, a' is the projected depth direction dimension of the ellipse, and c is the front face width of the ellipse.

Once an equivalent SENT crack length is found, the quotient of the RUT stress intensity factor and the clamped stress intensity factor is calculated. This quotient is applied as a penalty to each direction of crack growth (a and c) of the corner crack, resulting in a stress intensity factor somewhat less than the Raju-Newman solution. The influence of this clamping is limited for shorter crack lengths, since the deviation between the RUT and clamped conditions is minimal. However, in the transition region the retardation due to clamping can be significant and will result in an extended crack life when compared to RUT alone.

A similar study was conducted on center crack specimens. A series of center cracks were inserted into a FE model with FRANC3D to evaluate the effect of clamping on the stress intensity factor (Figure 10). With the exception of very short gauge heights, it was

found that for this symmetric configuration, clamping had a negligible effect and could be ignored for the purposes of simulation.

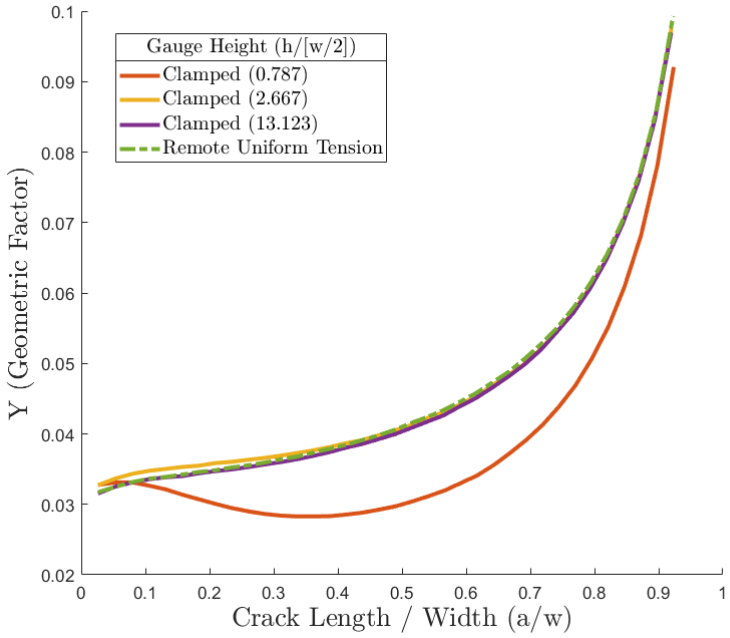

Figure 10: Stress intensity geometric factors for simulated clamped center through cracks

1.3.2. Surface Flaw Transition Method

When the Raju-Newman solution (corrected for boundary conditions) was combined with Johnson's simple geometric transition (SGT) method, simulations showed good agreement up to breakthrough. However, once the crack entered the transition region, the SGT method predicted a longer transition with a lower aspect ratio (*a'/c*) elliptical contours then what was seen in the experimental data (Figure *11*).

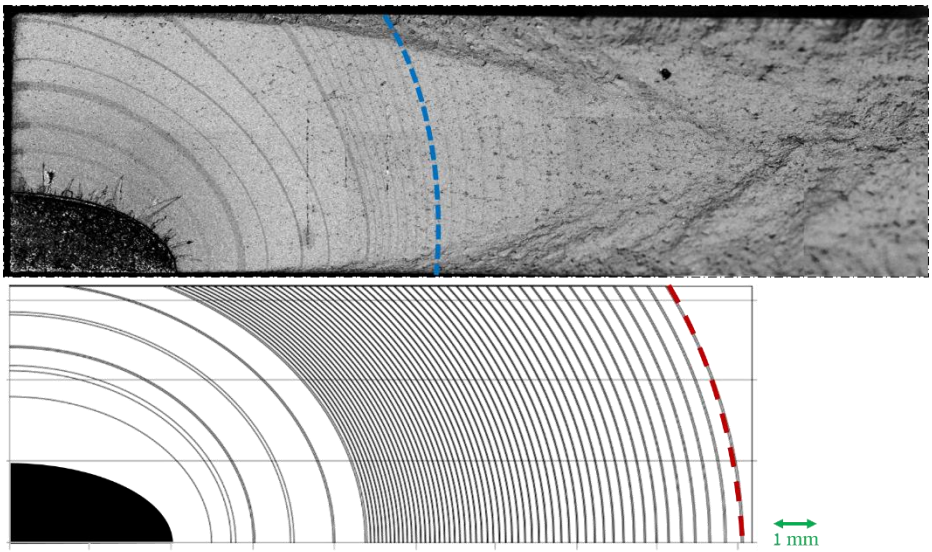

Figure 11*: Experimental result from a quarter-elliptical corner crack with starting aspect ratio (a/c<1) compared to the MPYZ-TMF simulated marker band placement using the SGT method. Simulated marker bands have a decreased aspect ratio, resulting in an extended transition zone.*

FE simulations were conducted on a quarter-elliptical corner crack grown through a plate of the same geometry as the experimental specimens (w = 38.1 mm, t = 6.35 mm, h = 30 mm) using the clamped boundary conditions to explore the stress intensity field associated with the crack at different stages of its growth (Figure 12). In the pre-breakthrough region, the stress intensity factor is relatively even across the crack contours. Once the crack breaks through, the stress intensity factor very quickly increases on the back face, causing the crack to grow very quickly in the *c'* (and by extension *a'*) direction. The stress intensity on the back face increases until the crack reaches a transition ratio (*c'/c*) of approximately 0.5. Afterwards, the stress intensity drops to meet the stress intensity on the front face, and the crack continues as a SENT crack.

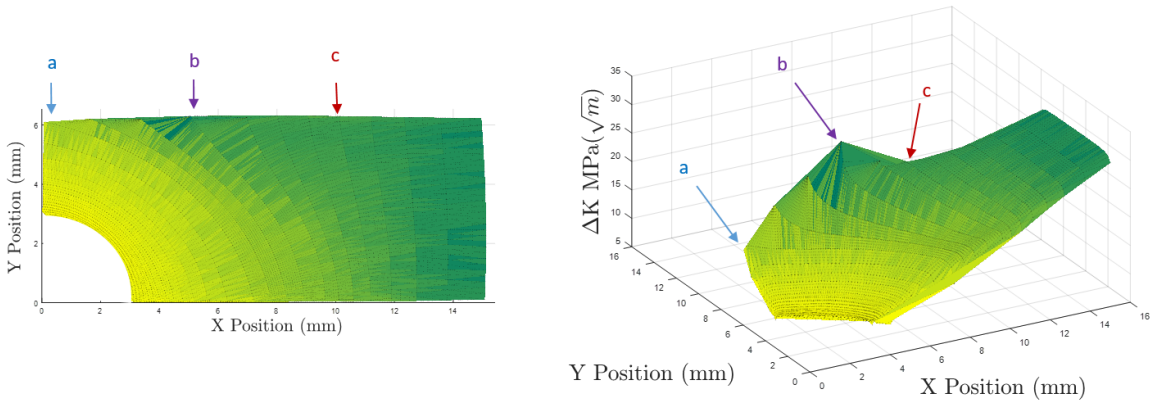

Figure 12: Stress intensity field at points on corner crack contours with; (a) break through point, (b) peak back face stress intensity, (c) transition to through crack

To facilitate this more rapid growth in the *c'* direction a scaling factor is multiplied by the stress intensity factor for the *a'* direction. This has been implemented in the MPYZ-TMF code as the SGT(λ) method, with a changeable parameter λ that can be specified through the user interface. The SGT(λ) rule can be summarized as follows:

$$\textbf{For a'/t>1: } \Delta K\ (a'\textbf{direction}) = \lambda \Delta K_{a'} \qquad (17)$$

The values of λ were found by comparing the transition ratio (*c'*/*c*) to the location of the contour along the front face, *c*. The resulting curves can be seen in Figure 15, Figure 18, Figure 21, and Figure 24. An example of how the value of λ effects the transition shape can be seen in Figure 13:

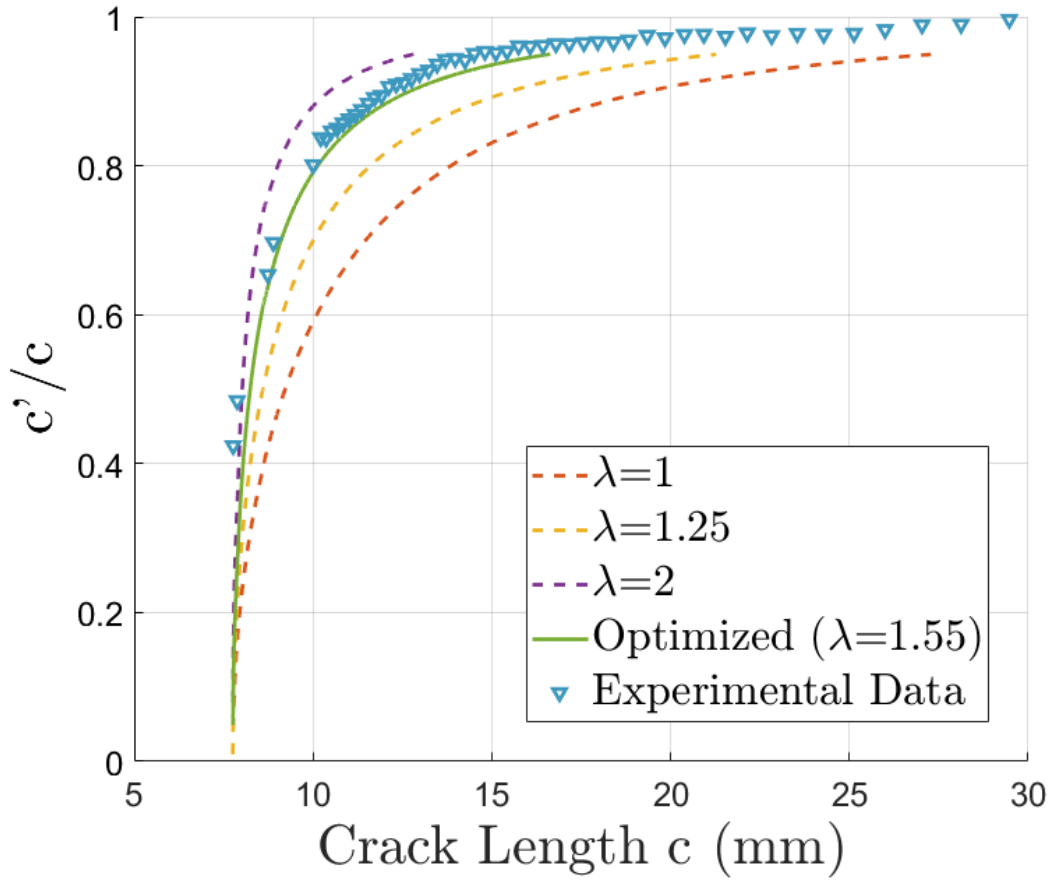

Figure 13: Effect of λ on the transitions shape in the a/c<1 semi-elliptical surface flaw in 17-4 H1025

Each of the quarter-elliptical corner crack and semi-elliptical surface flaw experiments were compared to the simulated transition ratio (*c'/c*) values for given front face crack lengths (*c*). The mean absolute error was calculated by comparing values whose *c'/c* ratios were between 0.5 and 0.9. The lower thresholding was necessary because many of the experiments broke through the back face of their geometries slightly before the simulation and as such they would not have values for a given *c*. The upper thresholding was implemented because the simulations end their transition regions once *c'/c* = 0.9.

In order for a transition ratio to be available for each value of front face crack length from the simulated data set, a curve was interpolated between the discrete outputs of the MPYZ-TMF software. This was accomplished by using the linear interpolant method in Mathwork's Matlab software. The mean absolute percent error was calculated using the following formula:

$$MAPE = \frac{100 * \sum \frac{|y_i - \hat{y}_i|}{y_i}}{n} \qquad (18)$$

Where y_i is the experimental value of c'/c and $\hat{y}_i$ is the corresponding value of c'/c from the interpolated MPYZ-TMF curve.

Each λ parameter selected for a given geometry was selected to yield a MAPE < 5% for any given starting condition within that geometry. The values of the MAPE for the quarter-elliptical corner cracks and the semi-elliptical surface flaws are listed in Table 6:

Table 6: Mean absolute percent errors for transition shapes in quarter elliptical corner cracks and semi-elliptical surface flaws

Experiment	**MAPE**
Quarter Ellipse $a/c < 1$	4.98%
Quarter Ellipse $a/c > 1$	2.19%
Semi Ellipse $a/c \approx 1$	1.91%
Semi Ellipse $a/c < 1$	2.27%

This is a great improvement over the instant transition methods which can be thought of as having a c'/c ratio of 1 for every data point, and even for the original SGT method which

is equivalent to a λ value of 1. For example for the semi-elliptical surface flaw with starting aspect ratio (a/c) < 1, the MAPE for the original SGT method is 24.70 %.

1.3.3. Experiment and Model Comparisons – Quarter Elliptical Corner Cracks

The primary verification method in this work for the MYPZ-TMF output is to compare the simulated results to what has been observed via physical experiments. For quarter-elliptical corner cracks, a variety of configurations were tested. Two of those tests are exemplary of the process and have good combination of readable marker bands that are spaced in such a way to make meaningful observations. One configuration had a starting aspect ratio (a/c) < 1 (sample GA-03-02) and the other had a starting aspect ratio > 1 (sample GA-04-01). These samples had a nominal starting dimensions of a = 2 mm, c = 4 mm and a = 4 mm, c = 2 mm respectively.

All experiments included some material degradation near the initial EDM notch that could be seen as radial cracks emanating from the notch into the bulk. In order to avoid the effects of these and other notch related defects, the initial flaw size for the simulations are started at a chosen marker band away from the notch. All cycle counts and crack lives are in reference to this offset starting point.

The a/c < 1 (GA-03-02) corner crack was simulated using the inputs discussed in the experimental methods section for Inconel 718 as well as the following geometric and marker banding information:

Table 7: Quarter-elliptical corner crack simulation information for a/c < 1 (GA-03-02) sample

Geometry		Number of Blocks	Fatigue	Marker
$a_{initial}$	3.62 mm	First	50,000	100,000
$c_{initial}$	4.99 mm	Next Two	20,000	20,000
Gauge Height	45 mm	Next Two	10,000	10,000
		Marker Bands to Failure	1,000	3,000

The simulation can be compared qualitatively by overlaying the marker band output from MPYZ-TMF (using the SGT(λ) method) onto the micrograph of the fracture surface. A good simulation will put the marker bands in the correct locations with the correct shape, and width (Figure 14). The resulting data is compared based on three criterion, how well the shape matches (aspect ratio evolution), how well the transition aligns (transition evolution) (Figure 15), and crack life (Figure 16).

As the crack grows longer and the stress state at the crack tip becomes less constrained, a larger area of slant growth or "shear lips" becomes dominant. Note that the life predictions track very closely with the experiment until the shear lips dominate the crack profile. The simulation is not designed to model this type of crack growth and because of this a deviation occurs in this region with the actual crack growing faster then what is predicted in the simulation.

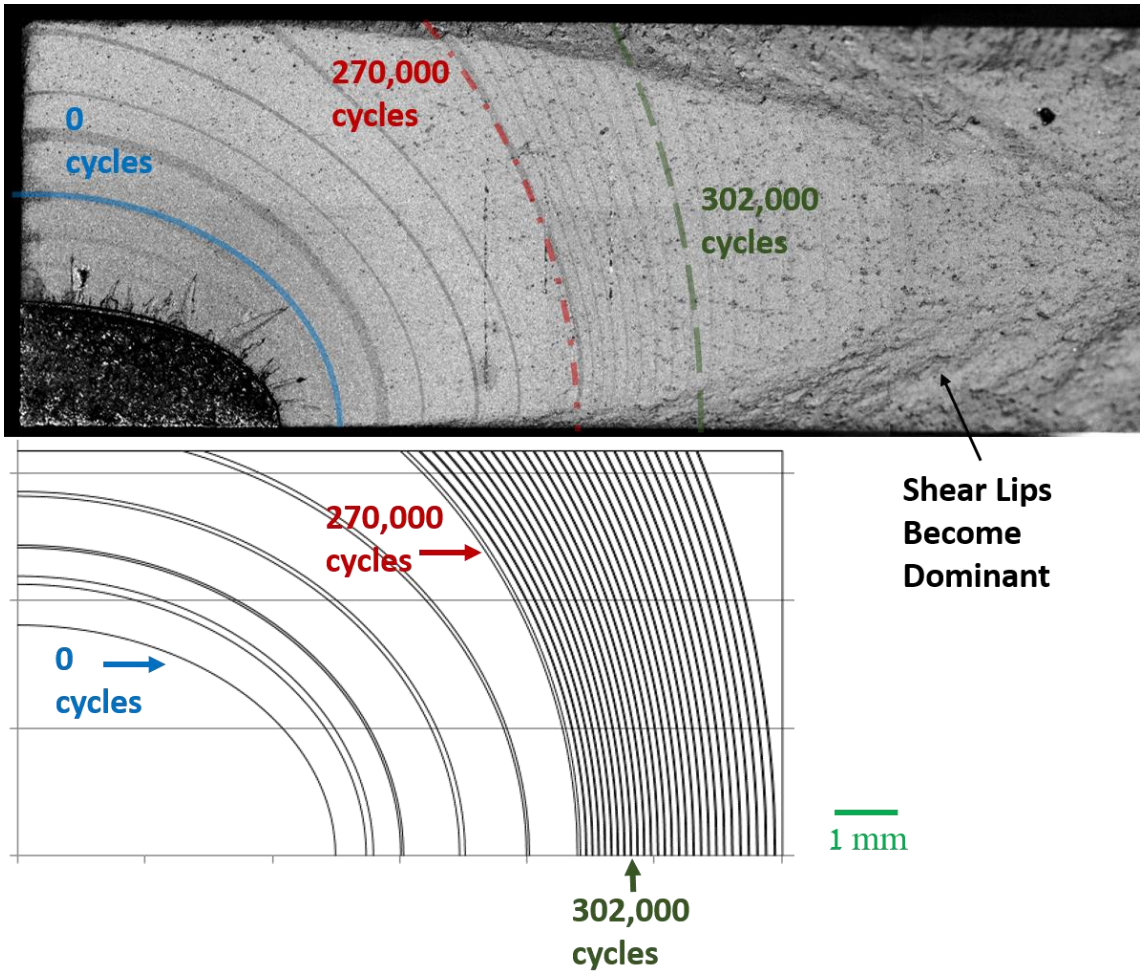

Figure 14: MPYZ-TMF marker band prediction overlay for a/c < 1 (GA-03-02)

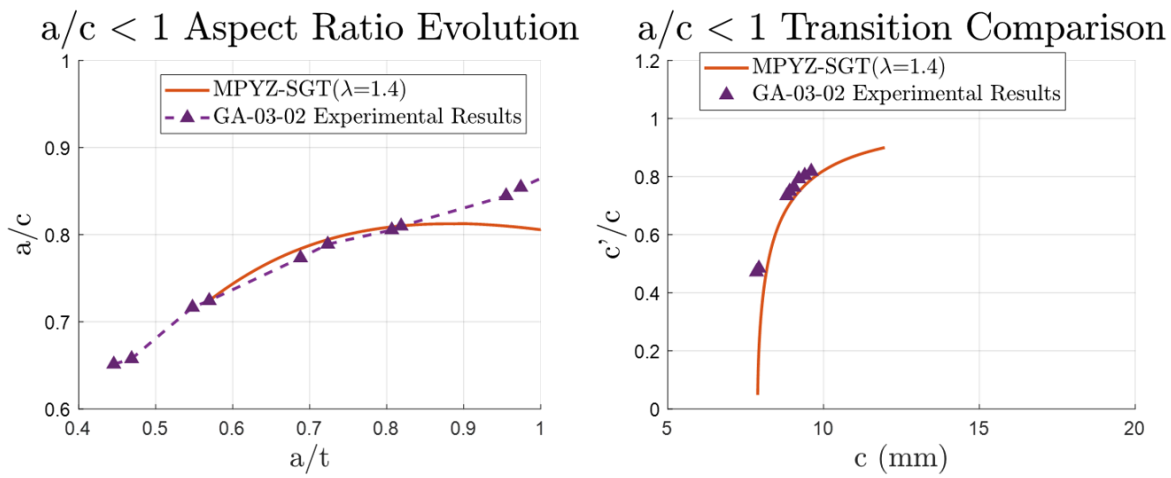

Figure 15: Plots for quarter-elliptical corner crack with starting aspect ratio a/c < 1 (Left) Shape change as a function of crack depth (Right) Transition ratio as a function of front face crack length

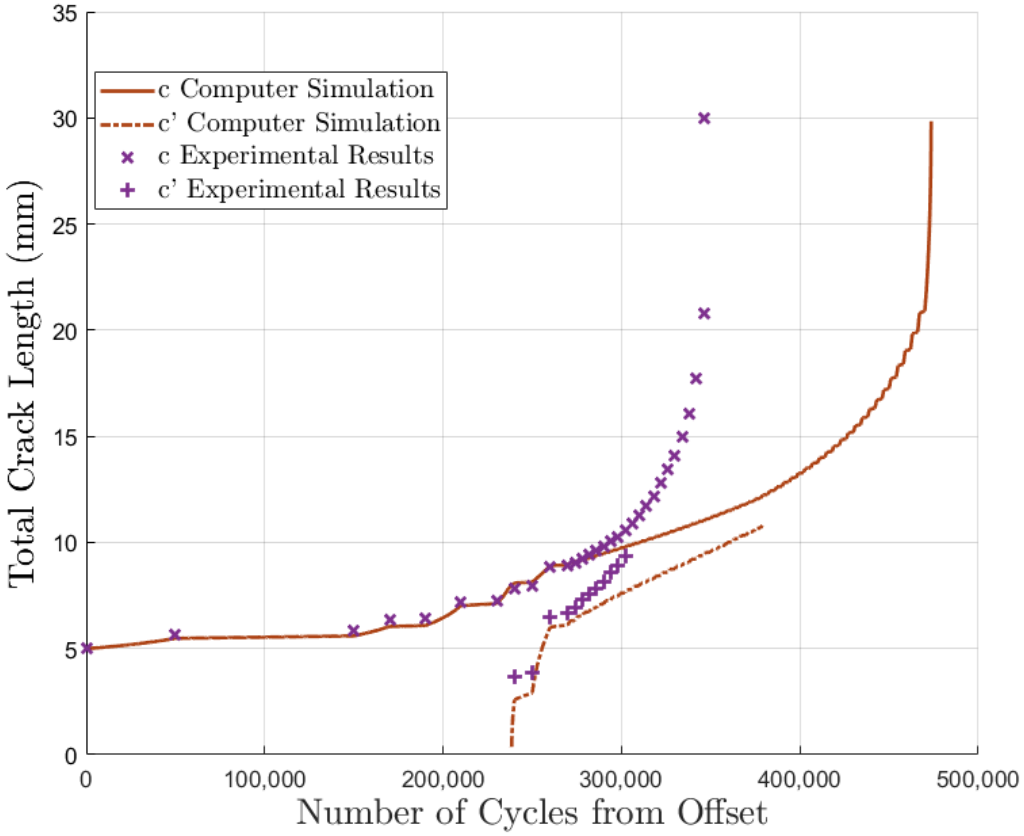

Figure 16: Computer simulation and experimental marker band crack lengths for combined R=0.1 and R=0.7 fatigue and marker cycles for the a/c < 1 quarter-elliptical corner crack

The $a/c > 1$ specimen (GA-04-01) was treated in a similar manner to the previous sample. It was also made of Inconel 718 and had the following inputs:

Table 8: Quarter-elliptical corner crack simulation information for a/c >1 (GA-04-01) sample

Geometry		**Number of Blocks**	**Fatigue**	**Marker**
$a_{initial}$	4.75 mm	First Four	10,000	10,000
$c_{initial}$	4.63 mm	Marker Bands to Failure	1,000	3,000
Gauge Height	54 mm			

Again, the marker band output was overlaid on the experimentally observed fatigue surface to show location and shape matching (Figure 17):

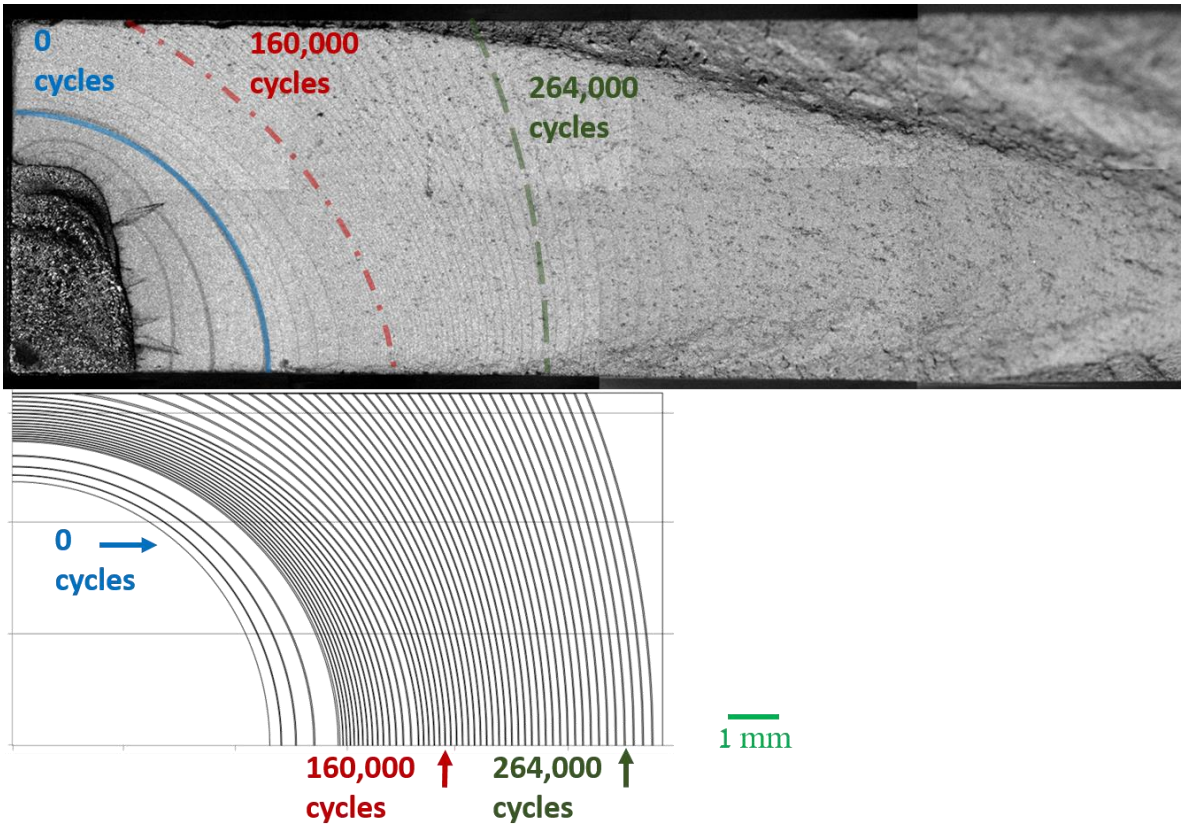

Figure 17: MPYZ-TMF marker band prediction overlay for a/c > 1 (GA-04-01)

For larger starting aspect ratios where a/c > 1, the modified Raju-Newman solution predicts a larger drop in aspect ratio before breakthrough then what is seen experimentally. However, this deviation is slight, and the aspect ratio "recovers" in the transition region where it meets back up to correctly predict the shape and location of the contours at transition.

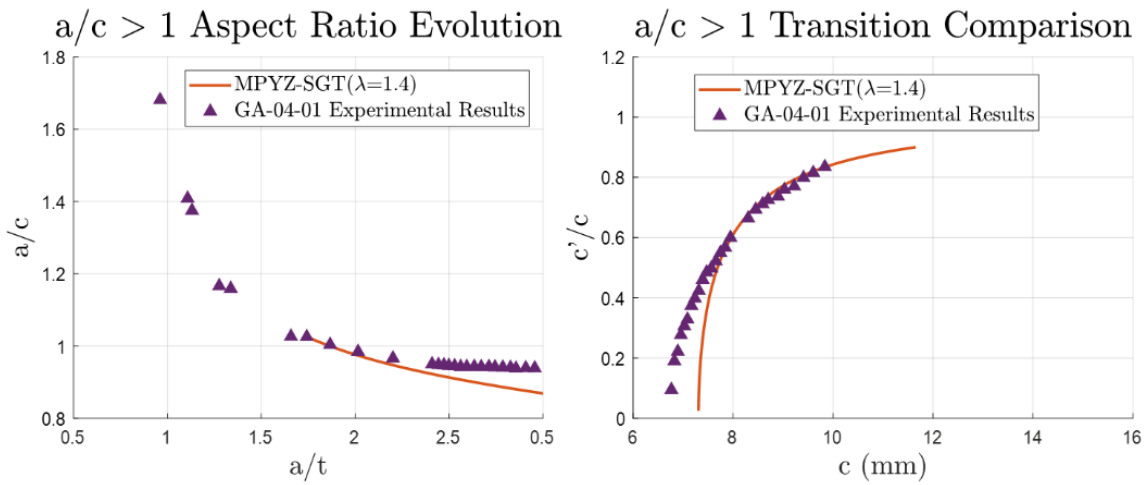

Figure 18: Plots for quarter-elliptical corner crack with starting aspect ratio a/c >1 (Left) Shape change as a function of crack depth (Right), Transition ratio as a function of front face crack length

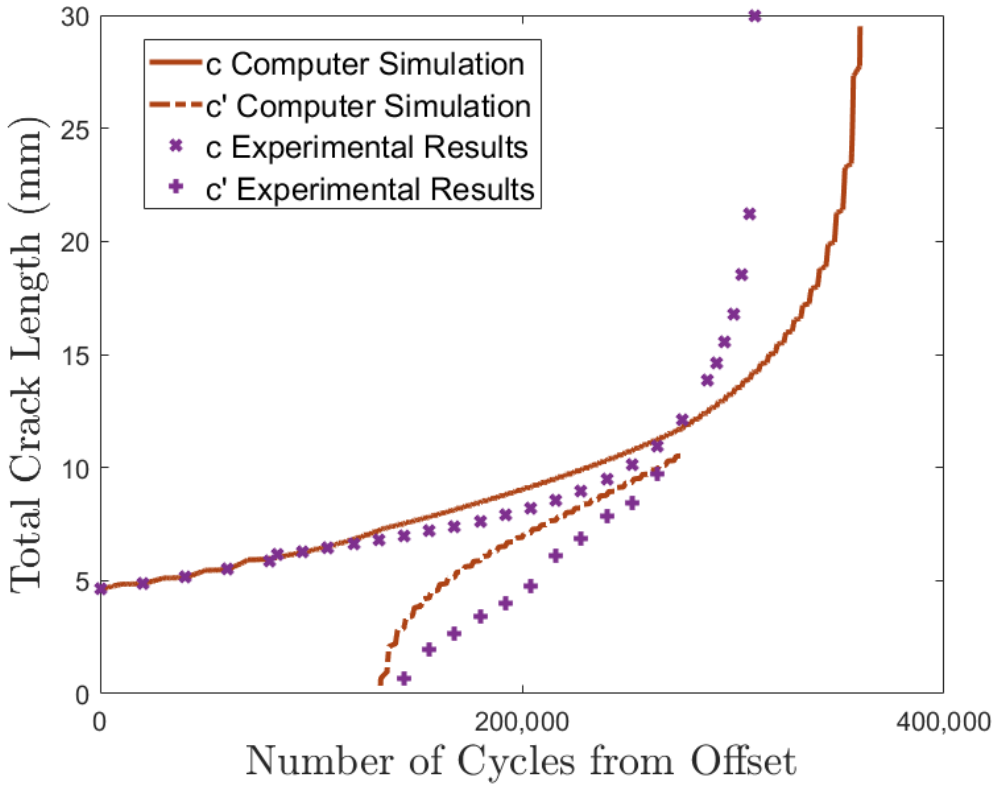

Figure 19: Computer simulation and experimental marker band crack lengths for combined R=0.1 and R=0.7 fatigue and marker cycles for the a/c > 1 quarter-elliptical corner crack

Experiments have also been conducted in the 17-4 H1025 steel material on semi-elliptical surface flaws. An experiment was conducted on a flaw with a starting aspect ratio very close to 1 as well as a flaw with a starting notch of $a/c = 0.5$. However, just as was seen using the corner crack configuration, there is an unpredictable patter of crack growth very close to the EDM starting notch. In the case of the semi-elliptical surface flaw, this caused the experiment with the $a/c = 0.5$ starting aspect ratio to rapidly grow in the depth direction. Although this behavior was unexpected, the experiment still had a starting aspect ratio of less than 1, and was in line with the modeling for data away from the notch.

Simulations were also run using the instant transition method to compare life predictions. The instant transition method estimated the total cycles to failure for the $a/c > 1$ case to be 348,622 and 475,361 cycles for the $a/c < 1$ case. These deviated from the life predictions made using the SGT(λ) method by 3.3% and 2.4% respectively. This means that influence of the transition geometry on the crack's advancement on the front face is very slight and does not make a large difference in the total life to failure. This is largely due to the fact that majority of the crack's life is spent in the pre-transition region before breakthrough. However, the instant transition method may only be accurate in circumstances where the shape of the crack during transition is not important.

1.3.4. Experiment and Model Comparisons – Semi Elliptical Surface Flaws

The $a/c \approx 1$ (174-S-002) experiment was modeled using the following inputs along with the fatigue crack growth law derived for the 17-4 material and the 76.2 mm wide plate geometry discussed above:

Table 9: Semi-Elliptical surface flaw simulation information for a/c ≈ 1 (174-S-002)

Geometry		Number of Blocks	Fatigue	Marker
$a_{initial}$	3.136 mm	First Three	20,000	50,000
$c_{initial}$	2.9885 mm	Next Six	10,000	25,000
Gauge Height	101.6 mm	Next Five	2,000	4,000
		Marker Bands to Failure	1,000	2,000

The experimental and shape overlay are shown in Figure 20. The markings are very close together between the red and green lines but are possible to view if magnified properly.

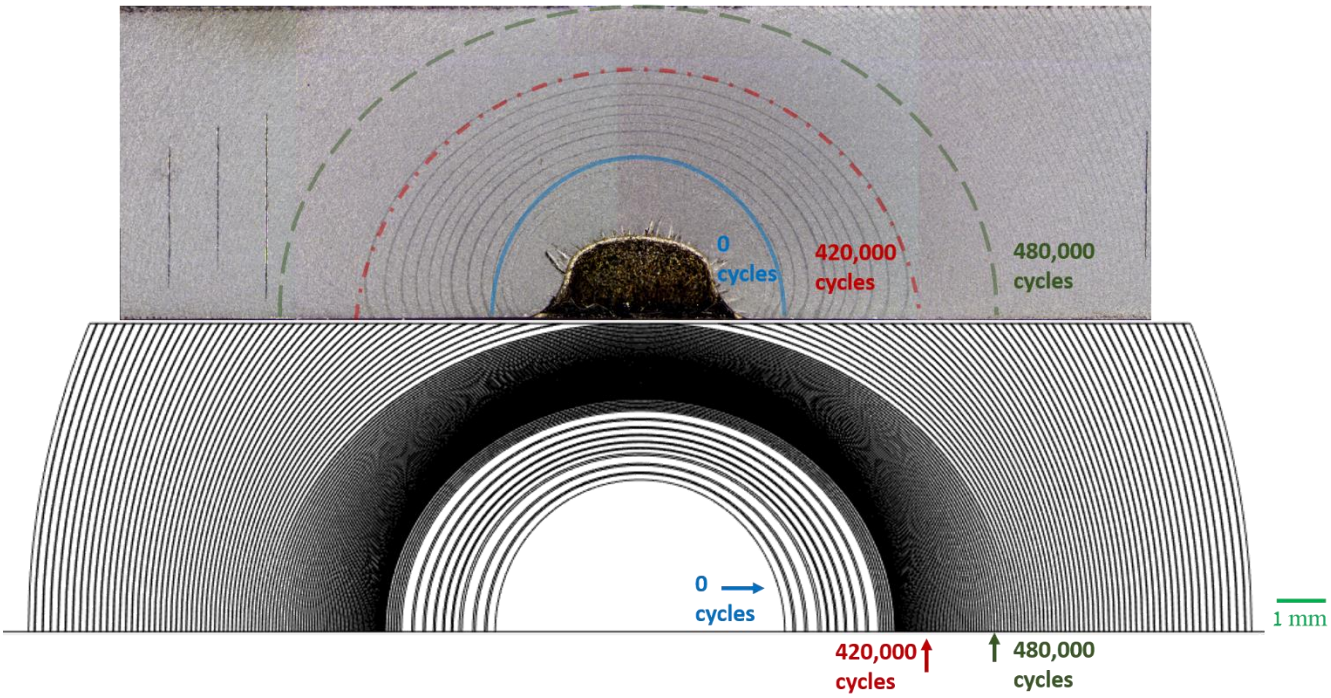

Figure 20: Semi-Elliptical surface flaw marker band prediction overlay for a/c ≈ 1 (174-S-002).

It was found for the semi-elliptical surface flaws a value of λ=1.55 was more appropriate than that of 1.4 seen for quarter-elliptical corner cracks. This transition method again gave a good fit in the shape evolution before and after breakthrough of the crack:

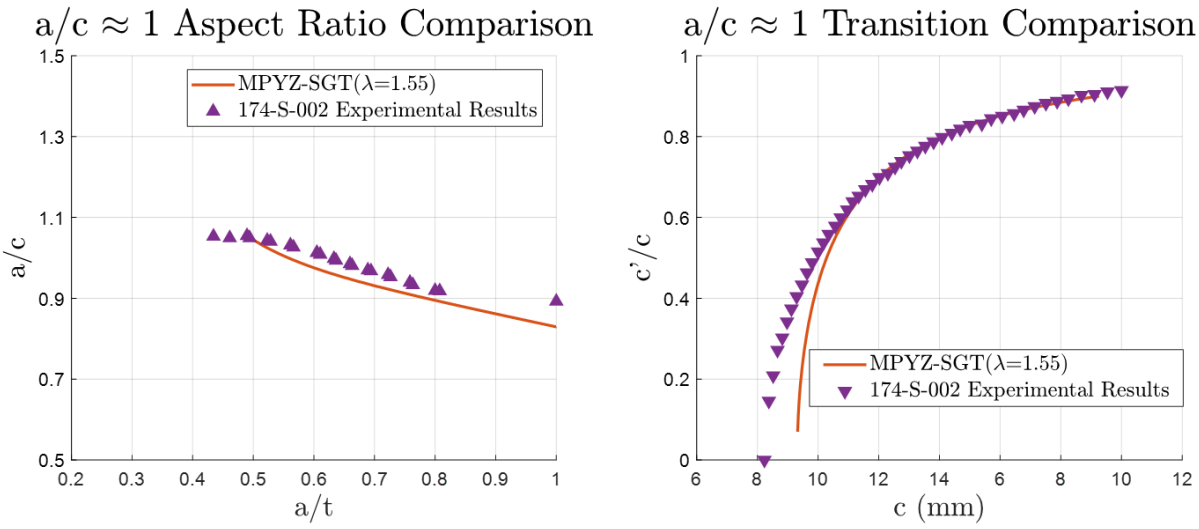

Figure 21: Plots for a semi-elliptical surface flaw with starting aspect ratio a/c ≈ 1 (Left) Shape change as a function of crack depth, (Right) Transition ratio as a function of front face crack length

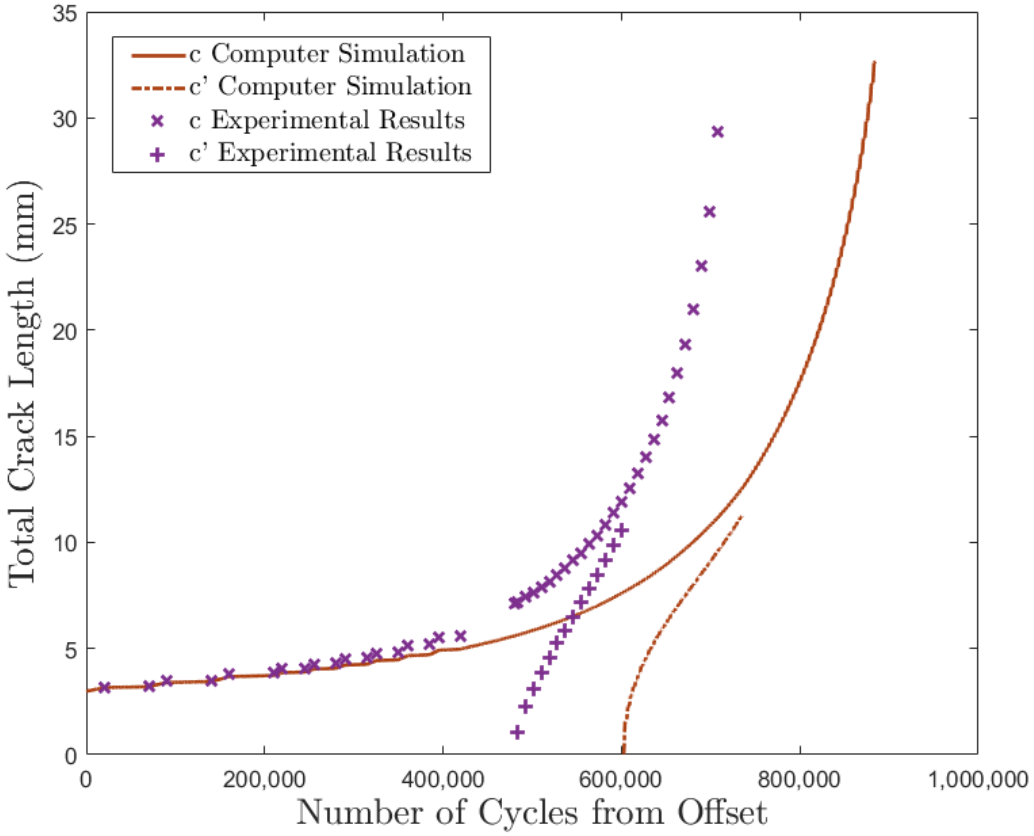

Figure 22: Computer simulation and experimental marker band crack lengths for combined R=0.1 and R=0.7 fatigue and marker cycles for the a/c ≈ 1 semi-elliptical surface crack

For a starting aspect ratio of $a/c < 1$ (174-S-003) the simulation inputs were:

Table 10: Semi-Elliptical surface flaw simulation information for a/c < 1 (174-S-003)

Geometry		**Number of Blocks**	**Fatigue**	**Marker**
$a_{initial}$	3.039 mm	First Three	20,000	50,000
$c_{initial}$	3.2605 mm	Next Twelve	10,000	25,000
Gauge Height	101.6 mm	Marker Bands to Failure	1,000	2,000

This experiment showed a good combination of initial marker bands and bands in the transition region allowing for good resolution data across the entire experiment. Different lighting was needed to show the marker bands in the near notch region, and as such the fracture surface image is comprised of two separate stitched photomontages overlaid on each other:

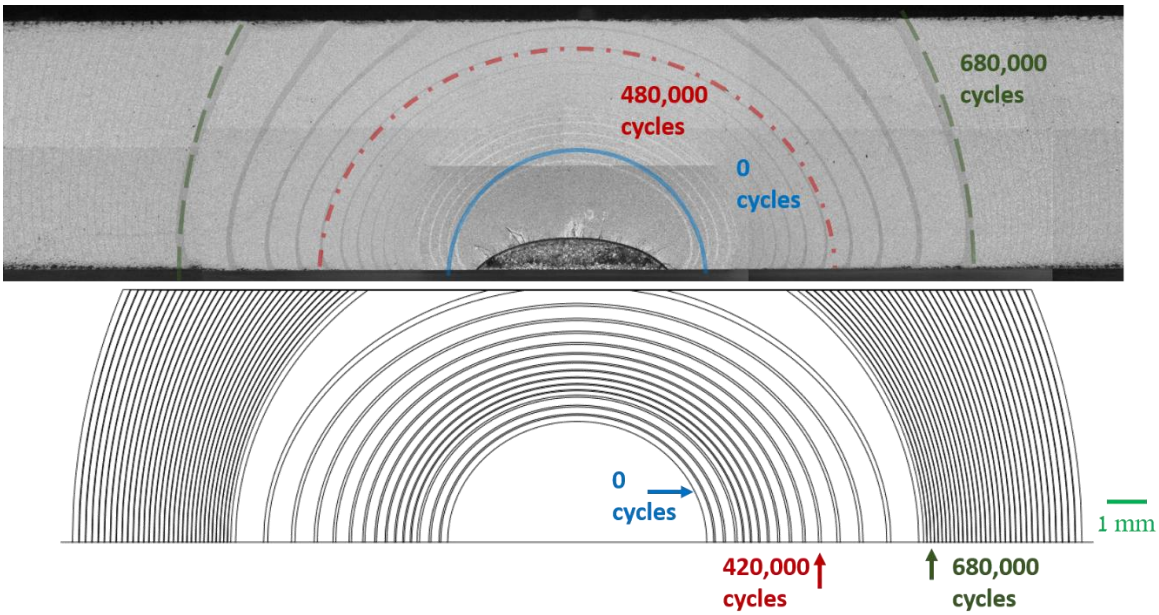

Figure 23: Semi-Elliptical surface flaw marker band prediction overlay for a/c < 1 (174-S-003)

Again, the model shows good agreement in marker band shape and location:

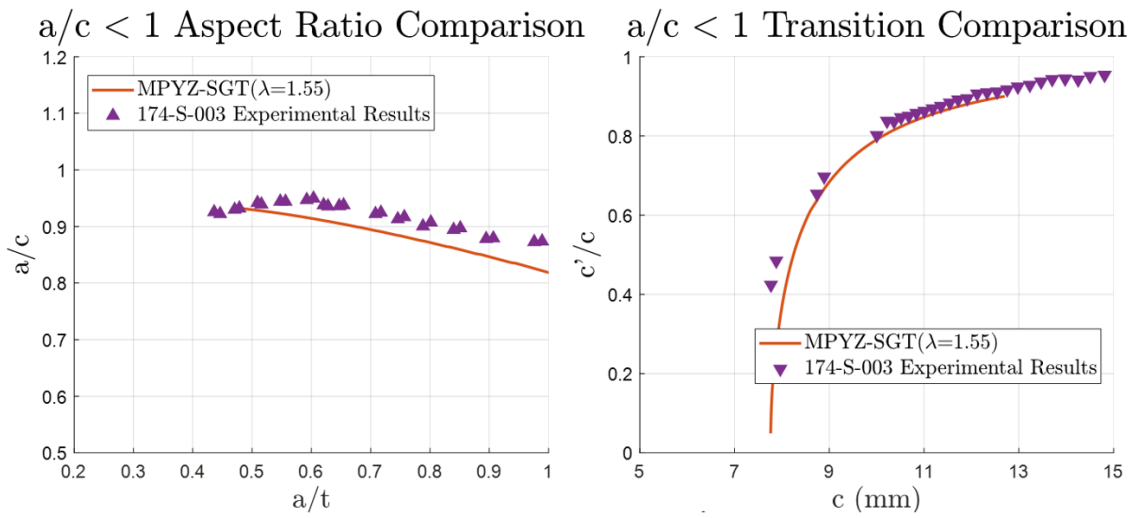

Figure 24: Plots for a semi-elliptical surface flaw with starting aspect ratio a/c < 1 (Left) Shape change as a function of crack depth, (Right) Transition ratio as a function of front face crack length

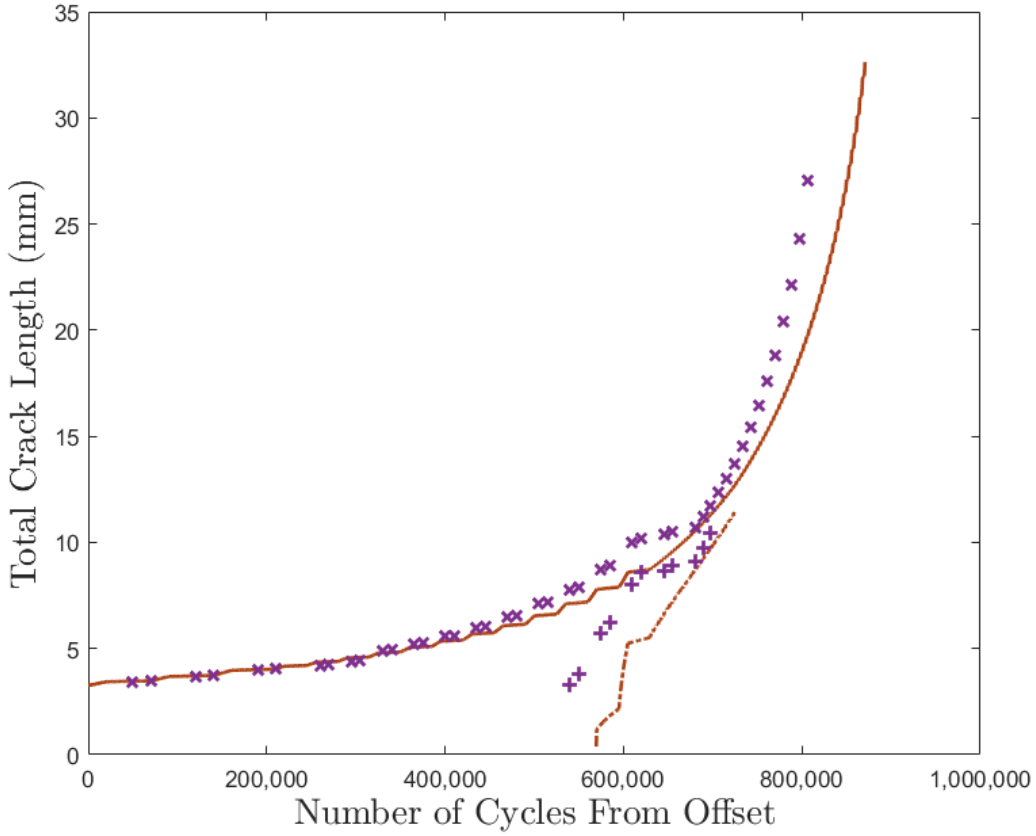

Figure 25: Computer simulation and experimental marker band crack lengths for combined R=0.1 and R=0.7 fatigue and marker cycles for the a/c < 1 semi-elliptical surface crack

1.3.5. Experiment and Model Comparisons – Symmetric Corner Cracks at a Center Through Hole

Experiments were also conducted on symmetric quarter-elliptical corner cracks at a center through hole. These experiments were conducted on 17-4 plates with the same overall dimensions as the semi-elliptical surface flaws (101.6 mm tall x 76.2 mm wide x 6.35 mm thick). These experiments were comprised of two different center hole sizes, and

two different starting aspect ratios as seen below in , with their respective fracture surfaces shown in Figure 26.

Table 11: Table of symmetric quarter-elliptical corner cracks at a center through hole experiments

Hole Radius (mm)	Nominal starting *a* (mm)	Nominal starting *c* (mm)	Designation	Designation Code
3.09	1.5	1.5	Small hole *a*/*c* = 1	174-CH-001
4.975	1.5	1.5	Large hole *a*/*c* = 1	174-CH-002
3.105	1.5	3.0	Small hole *a*/*c* = 0.5	174-CH-003

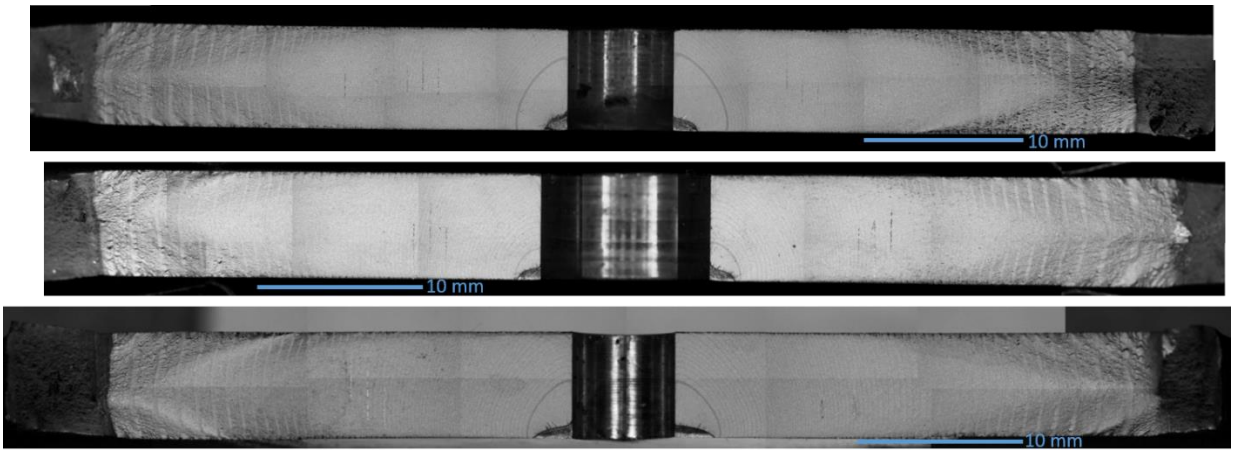

Figure 26: Fracture surfaces of the three symmetric quarter-elliptical corner cracks at a center through hole

Due to the influence of the stress concentration felt at the center hole, the crack fronts regardless of starting aspect ratio tend to see a very rapid increase to a high value of *a*/*c*. However, after this initial rise, the aspect ratio tends to stay at high but stable value (about 1.3) through the transition. Because of this a much lower λ value (1.15) was found to work well with this crack configuration vs the higher values (1.4 for quarter-elliptical corner cracks and 1.55 for semi-elliptical surface flaws) discussed previously.

These experiments had such a quick initial rise in aspect ratio, that the first marker bands recorded on each surface already had *a*/*c* values well over 1.0. This can be seen on the fracture surface in Figure 27 and the initial aspect ratio plot in Figure 28.

Figure 27: Right side fracture surface of the small hole, starting a/c = 1 symmetric corner cracks at a center through hole with the computer predicted marker bands overlaid

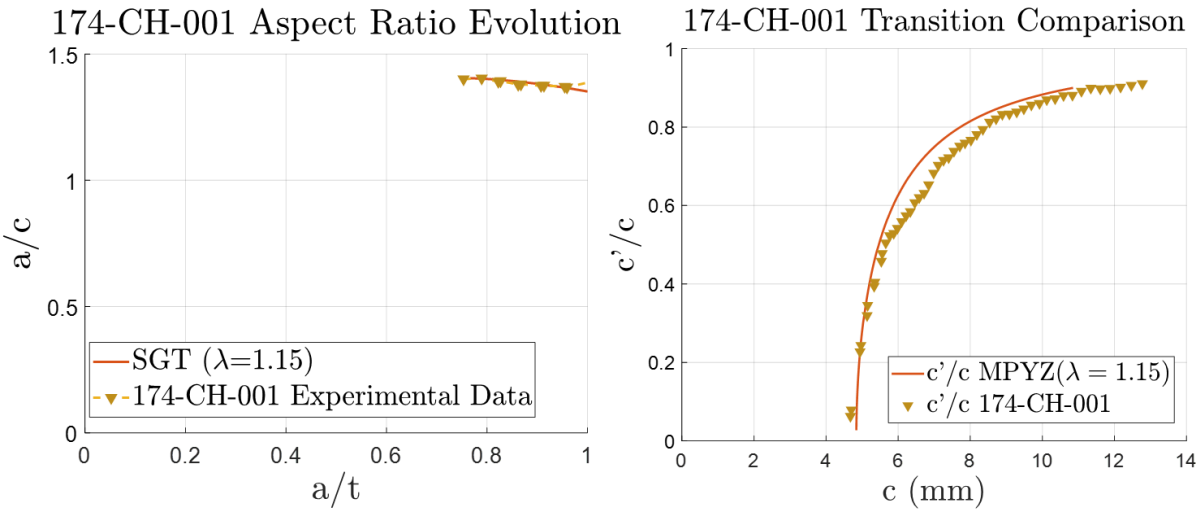

Figure 28: Shape plots for the small hole, starting a/c = 1 symmetric corner cracks at a center through hole with the predicted SGT(λ) values

The low value of λ (1.15) does a good job of maintaining the appropriate aspect ratio through the transition resulting in good agreement on the transition comparison plot on the right hand side of Figure 28. The life predictions for these types of cracks tends to be conservative as can be seen for the first experiment in Figure 29.

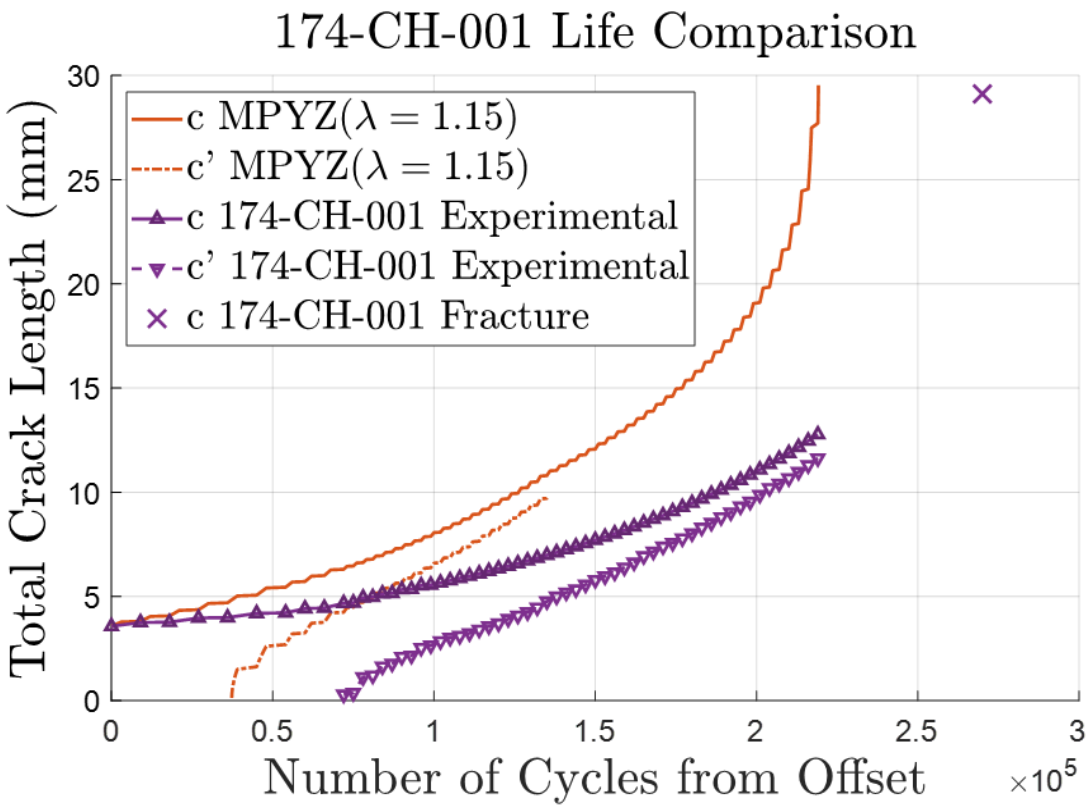

Figure 29: Comparison of Total crack length and offset cycle count for the small hole, starting a/c = 1 experiment with the SGT(λ) life predictions

The large hole experiment shows very similar trends. This experiment had a much closer initial marker band that shows just how quickly the crack aspect ratio increases, even when the nominal starting ratio is $a/c = 1$ (Figure 30). This sample configuration showed the largest deviation in life predictions, although it was still within a factor of 2 as shown in Figure 32.

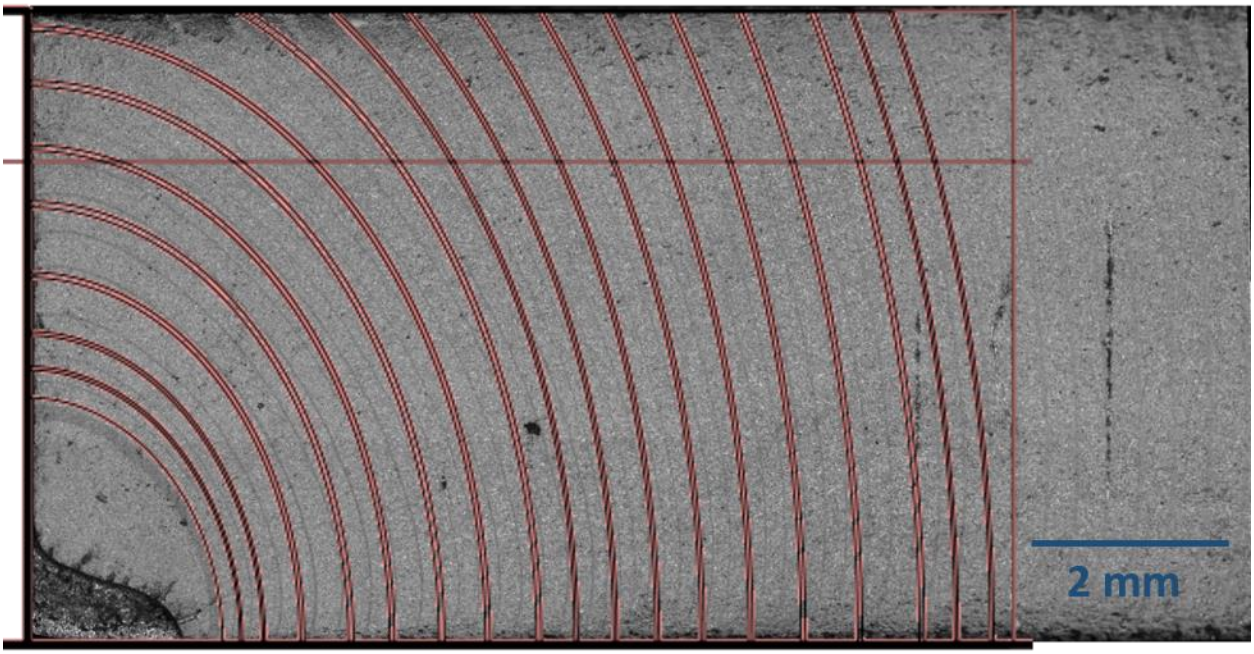

Figure 30: Right side fracture surface of the large hole, starting a/c = 1 symmetric corner cracks at a center through hole with the computer predicted marker bands overlaid

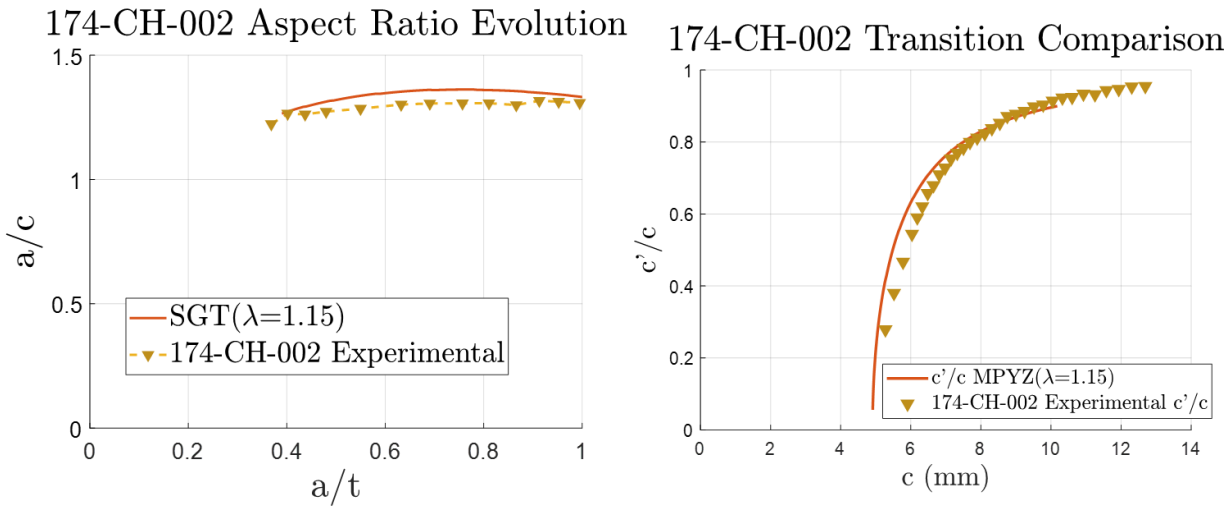

Figure 31: Shape plots for the large hole, starting a/c = 1 symmetric corner cracks at a center through hole with the predicted SGT(λ) values

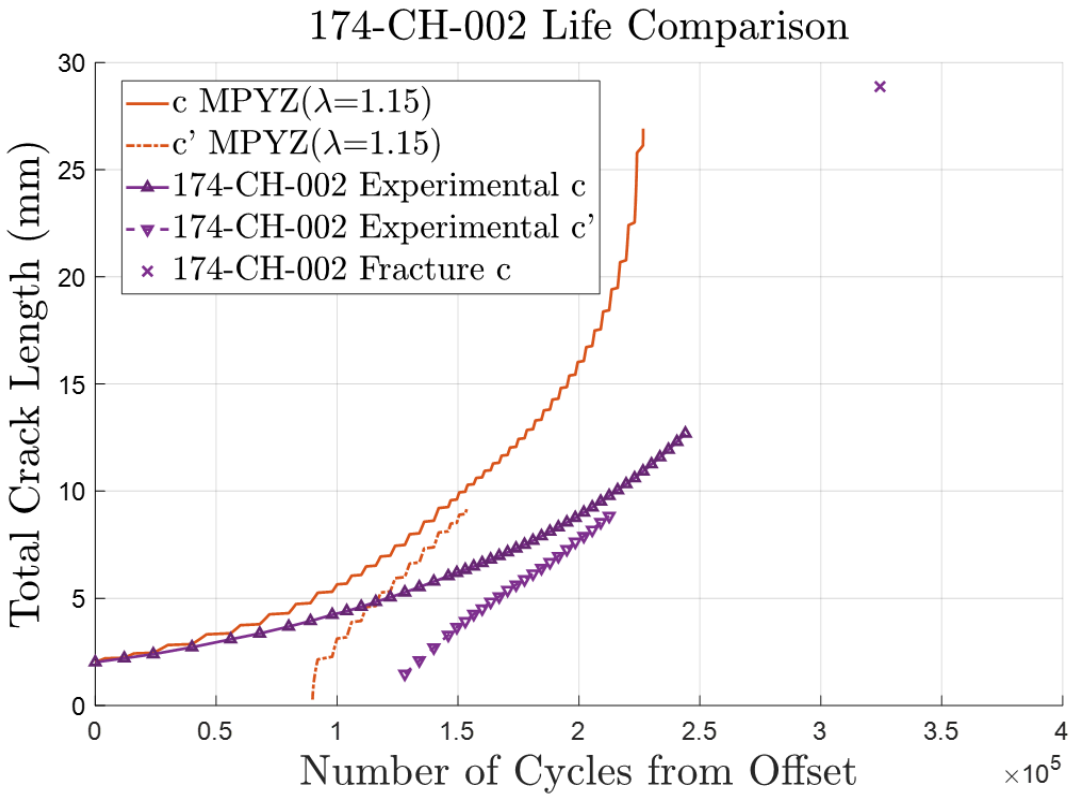

Figure 32: Comparison of Total crack length and offset cycle count for the large hole, starting a/c = 1 experiment with the SGT(λ) life predictions

The small hole, $a/c = 0.5$ experiment shows that even when the starting aspect ratio is very low, it also very quickly rises to the high values seen the other experiments. This combination yielded the best life predictions and a very close shape prediction.

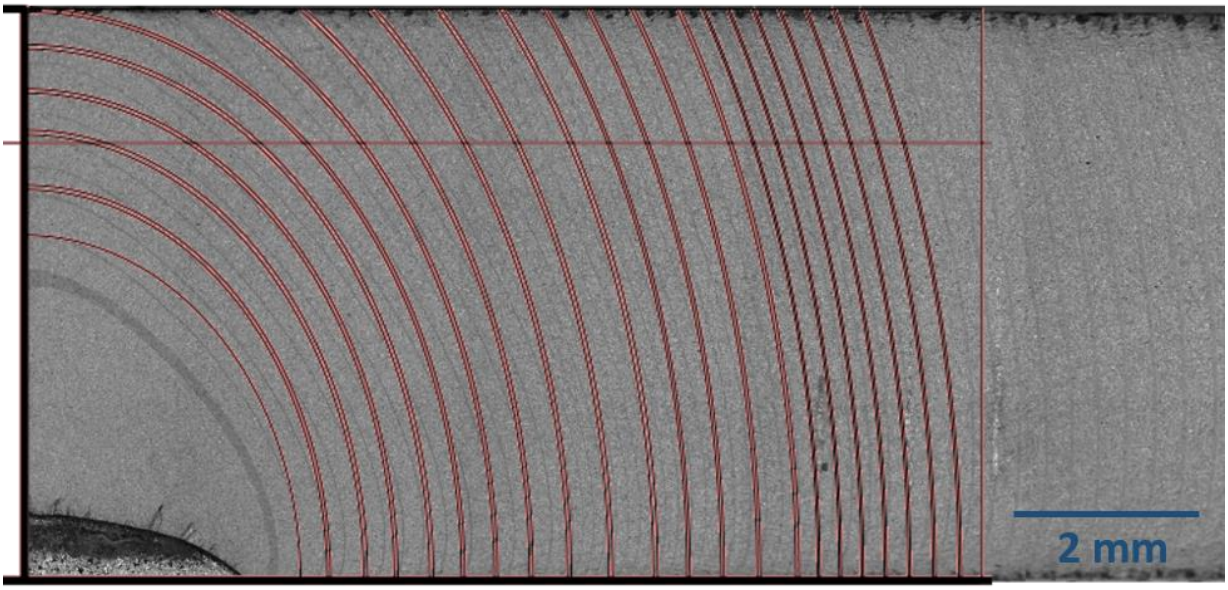

Figure 33: Right side fracture surface of the small hole, starting a/c = 0.5 symmetric corner cracks at a center through hole with the computer predicted marker bands overlaid

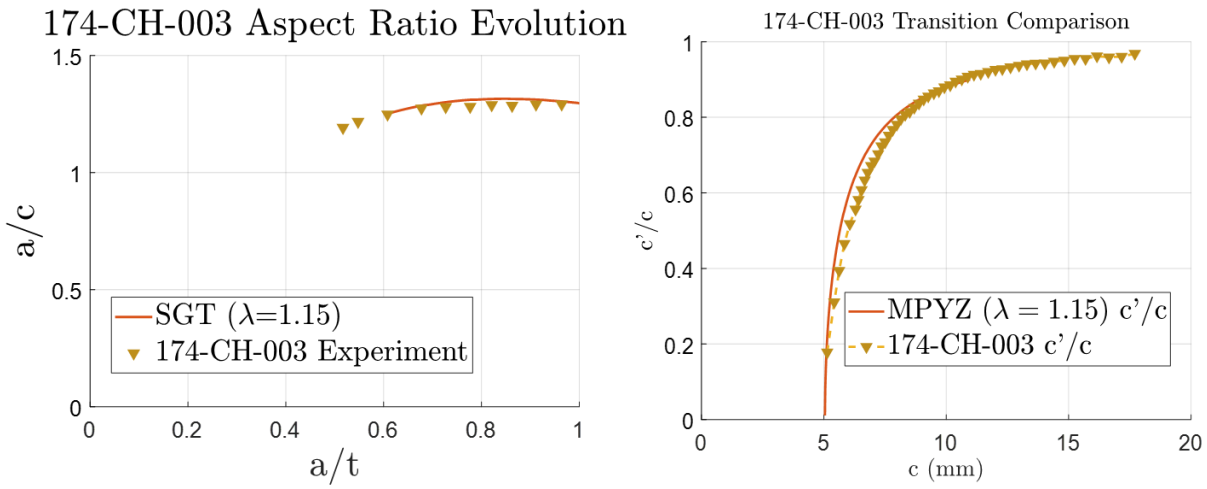

Figure 34: Shape plots for the small hole, starting a/c = 0.5 symmetric corner cracks at a center through hole with the predicted SGT(λ) values

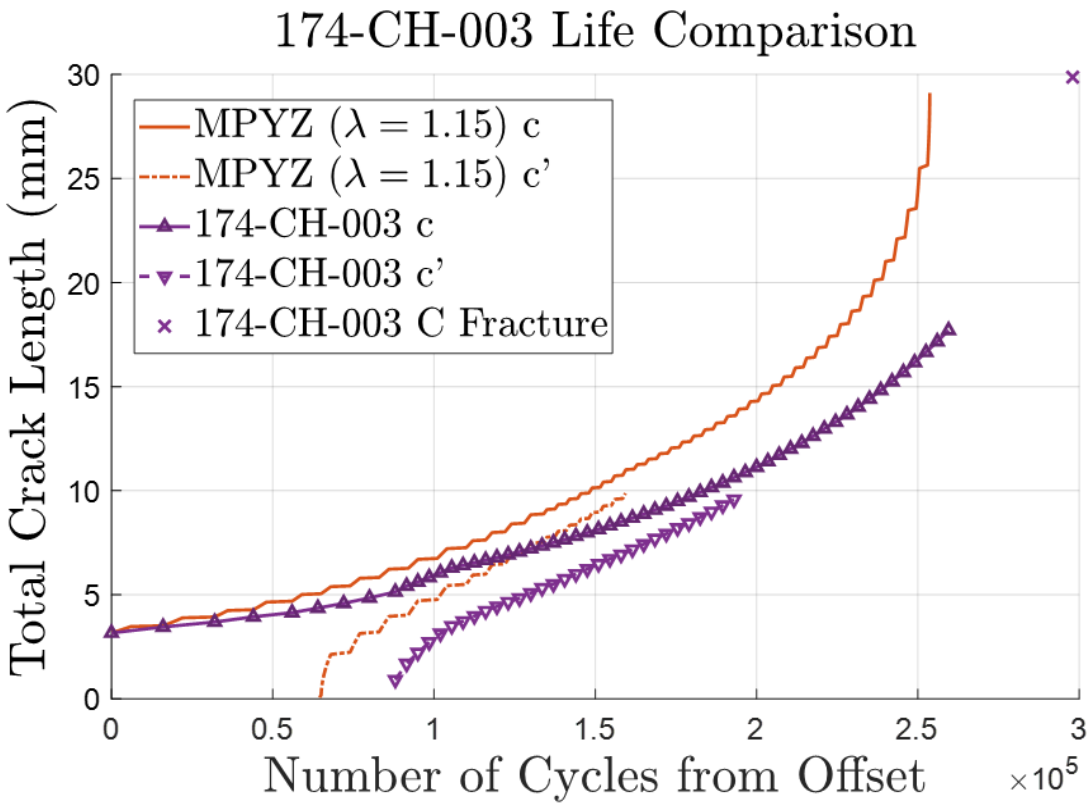

Figure 35: Comparison of Total crack length and offset cycle count for the small hole, starting a/c = 0.5 experiment with the SGT(λ) life predictions

It seems that the model works best for smaller hole sizes. This is likely because the larger center holes push the cracks to a larger crack/width ratio causing edge effects to have more influence.

CHAPTER II

THERMOMECHANICAL FATIGUE OF SURFACE FLAWS IN INCONEL 718

2.1.Background

2.1.1. Inconel 718 Properties and High Temperature Oxidation

Inconel 718 is a polycrystalline nickel based superalloy that has wide ranging applications in industry and is heavily used in jet engines. First introduced in the 1950's by the International Nickel Company [24], the alloy has an attractive combination of good mechanical properties and corrosion resistance at high temperatures (working maximum of 650 ºC) as well as good workability with niobium added to overcome cracking during welding [25]. Inconel 718 is widely used for high temperature applications due to its ability to retain good mechanical properties at relatively high temperatures (Figure 36).

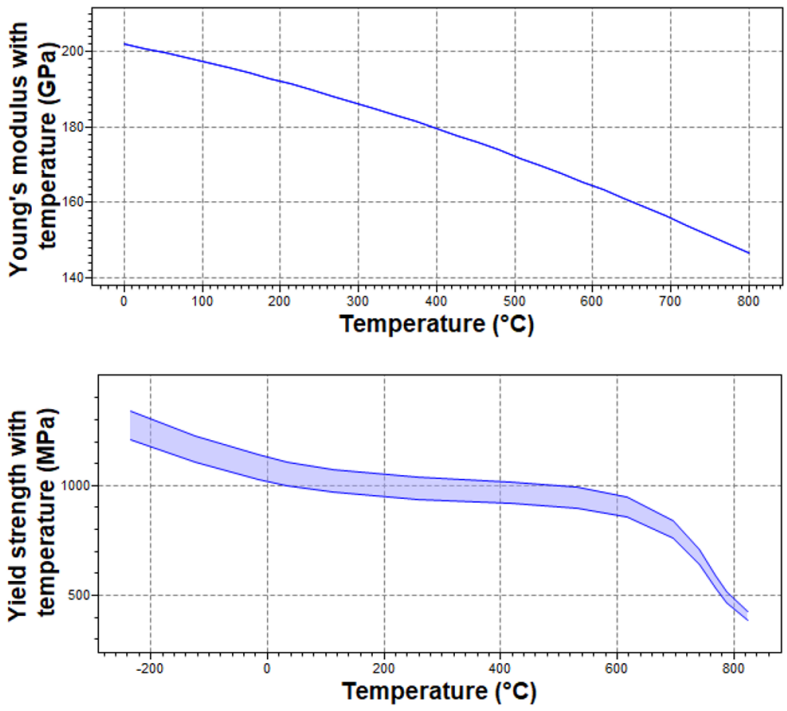

Figure 36: Mechanical properties of wrought solutioned and aged IN718 as a function of temperature [18]

2.1.1.1. Microstructure

Inconel 718 is often referred to as a "nickel-iron superalloy" due to its significant amount of iron [26] (see Table 12). It is primarily comprised of the host γ FCC phase with γ', γ'', and δ phase precipitates. The main strengthening phase in IN718 is metastable γ'' which has a DO_{22} ordered BCT crystal structure and contains Ni_3M where M can be either Nb or Al but is richer in Nb and has disk like morphology. The relatively high strength of IN718 at high temperatures is due to the large coherency strains of the γ/γ'' interface, and the limited number of slip systems in the BCT crystal structure [26]. The metastable γ' phase is an ordered FCC phase with an $L1_2$ structure also composed of Ni_3M but is richer in Al and can be found as a round particle. The incoherent orthorhombic δ phase is the

equilibrium phase of γ' and γ'' but the transition is slow at room temperature and often precipitates on grain boundaries [24]. Because of its incoherency, the δ phase does not strengthen the material, and often forms at the expense of the valuable γ'' precipitates [26].

Table 12: Nominal elemental composition of Inconel 718 [26]

	Cr	**Fe**	**Nb**	**Mo**	**Ti**	**Al**	**C**	**Ni**
Weight %	19.0	18.5	5.1	3.0	0.9	0.5	0.04	Bal

Carbides are also found in IN718 as relatively large particles that are generally considered to be stable and do not change with time at lower temperatures [24]. The carbide composition in IN718 is primarily NbC which when precipitated at temperatures above the working temperature are often found at grain boundaries [27]. In some cases the carbides can form a continuous film at grain boundaries reducing material ductility [24].

Heat treatments include a solutionizing and quenching step followed by an aging process. Depending on the form and use of the alloy, common heat treatments include solutionizing at 954ºC for 1 hr per inch of thickness followed by aging at 718ºC for 8 hours, then furnace cooling to 621ºC for a total precipitation time of 18 hrs; or solutionizing at 1066ºC for 1 hr per inch of thickness followed by aging at 760 ºC for 10 hrs, furnace cooling to 649 ºC and then holding for a total precipitation time of 20 hrs [28]. These treatments put the γ' and γ'' precipitates into solution, then precipitate them a relatively high temperature, with a precipitate growth and coarsening step at a temperature below the 650 ºC maximum working temperature (Figure 37).

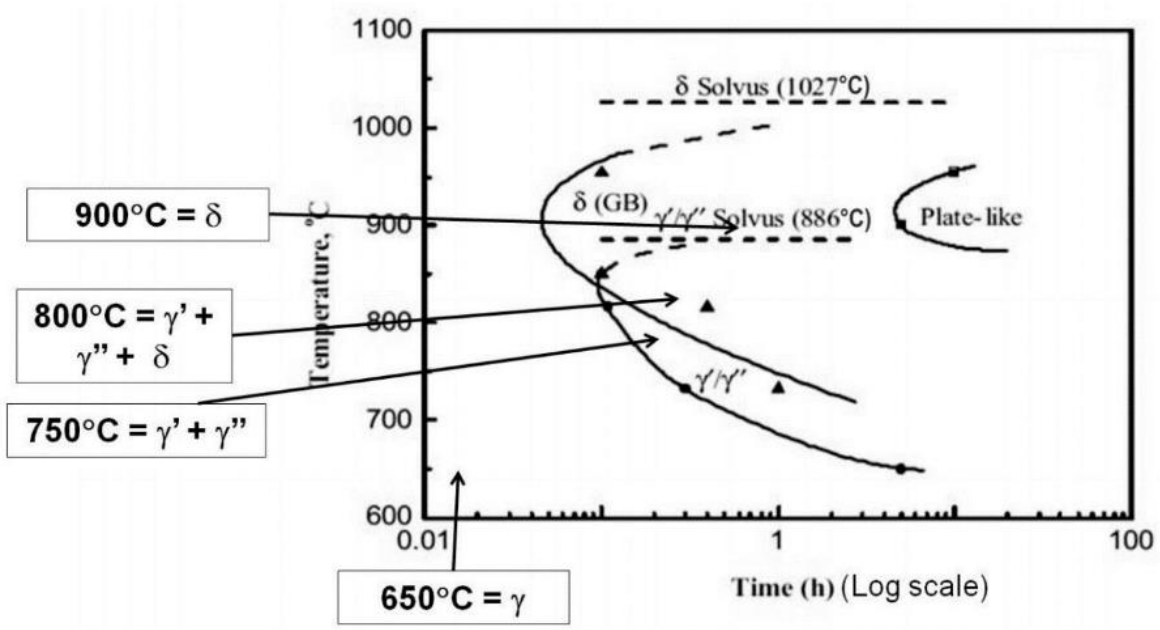

Figure 37: TTT diagram for Inconel 718 [29]

2.1.1.2. Fatigue Behavior

Many features of IN718 affect the elevated temperature fatigue crack growth behavior. It was found that while under low cycle fatigue crack initiation was faster at higher temperatures, for high cycle fatigue, initiation time also decreases with increasing temperature up to 427 ºC, however above this temperature (up to 650 ºC) the fatigue life actually increases with increasing temperature [30]. This behavior is thought to stem from a difference in deformation behavior in these two temperature ranges with the dominant mechanism below 427 ºC being deformation twinning and the dominant behavior above 427 ºC being slip. For intermediate temperatures (350 ºC and 500 ºC) fatigue life was improved my refining the grain size to ASTM 10/11 (approx. 7.9-11.2 μm) [31]. However, for fatigue crack growth at 427 ºC it was found that growth could be slowed by a coarser grain structure (around ASTM 1, approx. 254 μm) [32]. It was also found that for fine

grained (around ASTM 8.5, approx. 18.9 μm) structures fatigue crack growth in Region II could be lowered by large overaged γ'' precipitates, but had very little effect on Region I growth rates [32]. It was found that the size, shape or distribution of δ phase precipitates did not have a significant effect on fatigue but were important in creep [31].

2.1.1.3. Environmental Effects

At high temperatures, atmosphere plays an important role in the fatigue crack growth rate. It's been shown that oxygen and sulphur can increase the fatigue crack growth rate of IN718. A number of different tests were performed at 650 ºC under different atmospheres showing that even lab air can increase the crack growth rate by almost an order of magnitude when compared to helium [33]. It has been postulated that oxygen diffusion down grain boundaries can cause local oxidation leading to increased crack growth [33], [34]. Pedron et al. showed that there is a time-dependent aspect to the effects of air, where crack growth rates were similar between air and vacuum at 20 Hz, but deviated when a tensile hold was applied prior to fatigue. This gives further evidence pointing towards oxidation playing a role in the enhanced crack growth [34].

The work of Ghonem and Zheng defined an Arrhenius relationship to describe the oxygen diffusivity at stressed grain boundaries which was thought to be greater than that of a normal grain boundary [35]. Low frequency loading promotes grain boundary stress concentration, which when combined with the fact that stress relief by grain boundary sliding is not permitted in IN718, leads to an increase in oxygen diffusion aiding intergranular fracture. At high frequencies, cracking occurs in a transgranular fracture mode. The frequency needed to reach this environment-independent behavior has an inverse relationship with ΔK. At lower frequencies the crack growth is governed by a

linear combination of the cyclic fatigue type transgranular cracking and the time-dependent intergranular fracture. At 650 ºC with a grain size of ASTM 3.5 (approx. 106.8 μm) and a ΔK of 40 MPa√m the transition frequency where the time/environmental effect dominates is on the order of 0.1 Hz. Under vaccum the fracture mode under these conditions (but at 0.05 Hz) is completely transgranular unlike the same test done in air. Work was done in other metals where only portions of the loading cycle were important for oxidation effects, but in IN718 it was found that the entire cycle participated in the effective oxidation time [35]. The transition frequencies for these different types of fracture are dependent on temperature, and can be seen in Figure 38. Note that all crack growth in Inconel 718 is transgranular below 400 ºC.

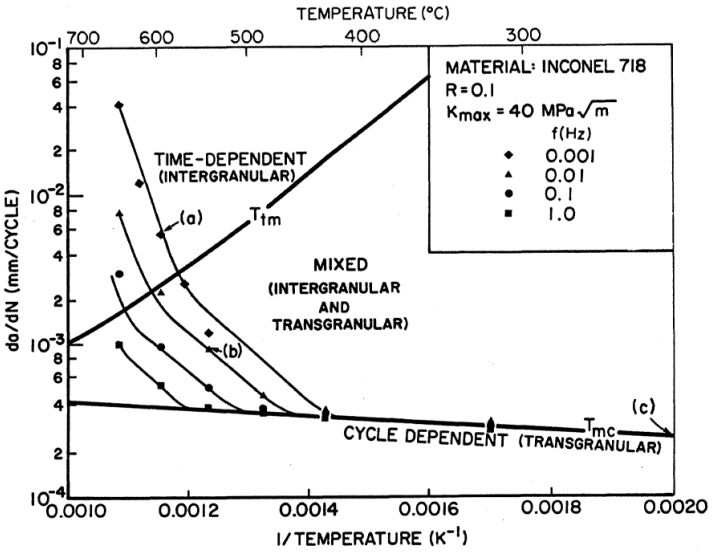

Figure 38: Transition frequencies for crack growth types for different temperatures in IN718 [36]

2.1.1.4. Fatigue Crack Growth Laws

Work was done using the Single Edge Notch Tension (SENT) specimen configuration by Radzicki [1] to find the fatigue crack growth rate of Inconel 718 at three

different temperatures at 8-10 Hz and a loading ratio of R=0.05. This fatigue crack growth was all in the cycle dependent (transgranular) regime and agrees in order of magnitude with the transgranular behavior at 40 MPa√m found in Figure 38. Crack growth is faster at higher temperatures, but does not reach the very high crack growth rates seen in the intergranular regime at low test frequencies.

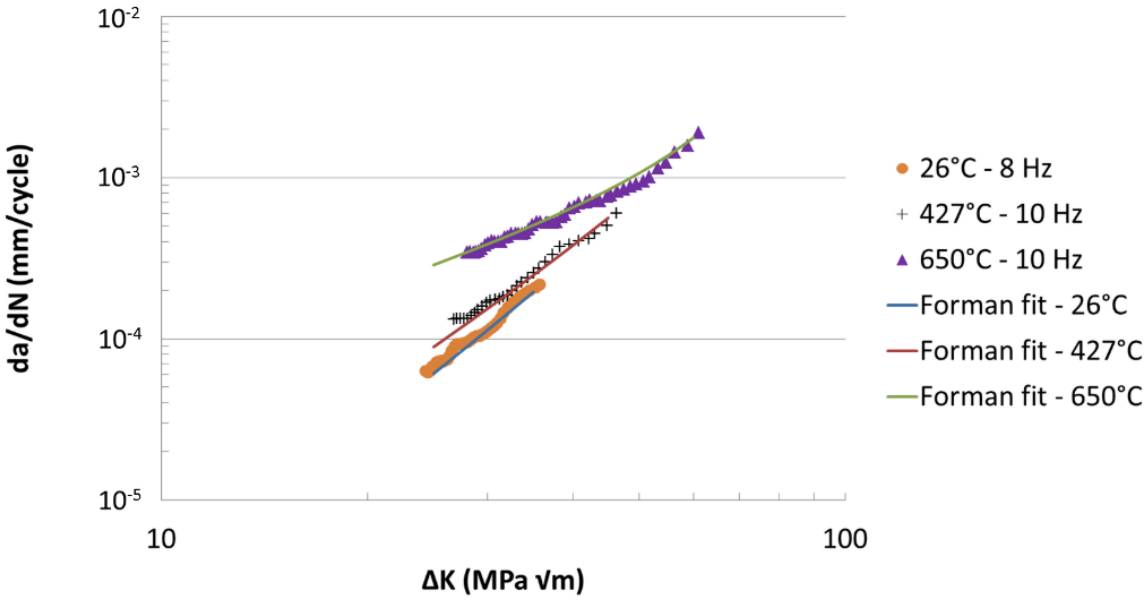

Figure 39: Fatigue crack growth rates for Inconel 718 at three different temperatures at a loading ratio of R=0.05 [1]

The Forman equation used by Radzicki had the following form:

$$\frac{da}{dN} = \frac{C(\Delta K)^n}{\left((1 - R_{eff}\right)^m * K_C - \Delta K)} \qquad (19)$$

The coefficients fit from his data were for da/dN in units of mm/cycle:

Table 13: Forman coefficients for Inconel 718 fit by Radzicki

Temperature	**Forman Coefficients**		
ºC	C	n	K_c (MPa√m)
26	2.40×10^{-7}	3.1	116
427	1.31×10^{-6}	2.7	119
650	3.93×10^{-4}	1.2	95

This equation with these coefficients were used for the predictions found in Chapter II of this document.

2.1.1.5. Oxidation Mechanisms in IN718

This time dependent behavior would usually be interpreted as time dependent crack growth as oxidation penetrated into the material. However it was found that under tensile holds at high temperatures no crack growth was observed [37]. Instead it is thought that oxidation weakens the material ahead of the crack tip, resulting in enhanced crack growth once cycling is resumed. The work of Mollins et al. explored the oxidation mechanisms in Inconel 718 [38]. They found there is a step change in crack growth rate when the partial pressure of oxygen reaches 10^{-1} Pa at 650 ºC. This transition pressure was independent of applied ΔK, frequency, or applied wave shape and increasing the partial pressure after transition had minimal effect on the growth rate (Figure 40). Mollins et al. found that the intergranular embrittlement resulted from NiO nuclei at the crack tip. Fractured surfaces analyzed with an elemental linescan in TEM were found to be primarily nickel followed by a primarily chromium layer which covered the nominal alloy composition. This showed that oxidation penetrated until a layer rich in chromium could stop the damage.

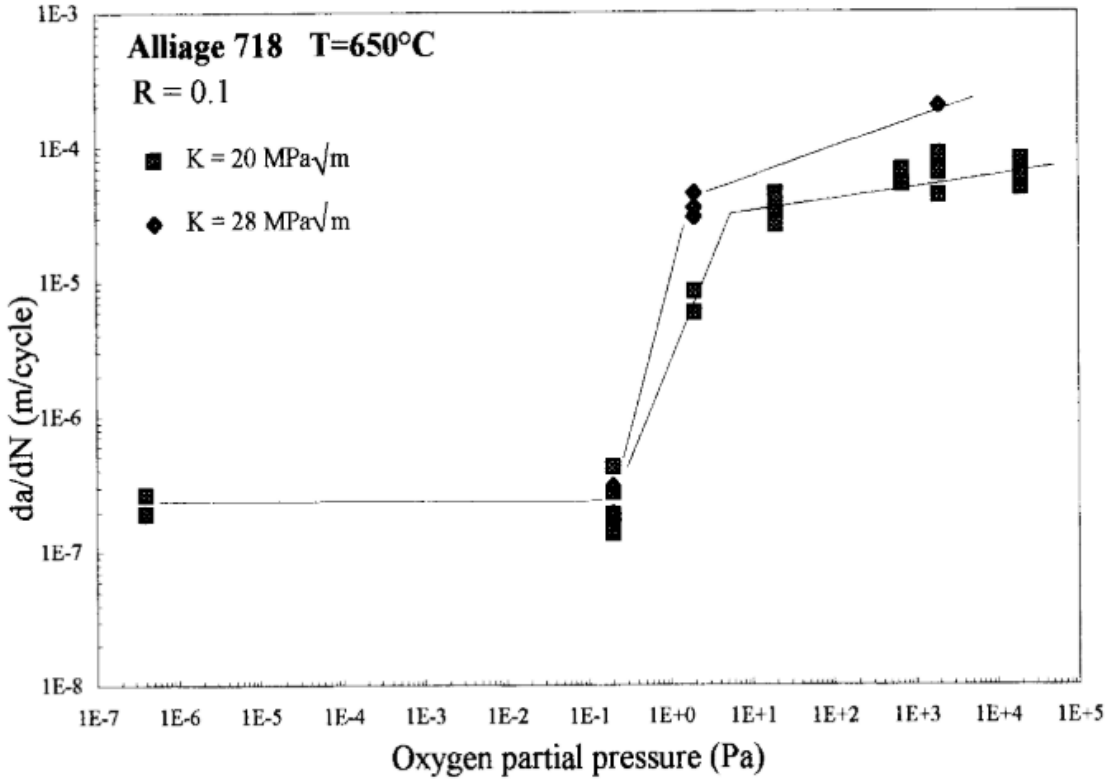

Figure 40: Effect of oxygen partial pressure on crack growth rate at 650 ºC [38]

The Mollins group further asserted that as long as the deformation rate at the crack tip is positive, NiO will continue to form on new crack surfaces. As nickel cations are removed from oxidation, vacancies are formed deeper in the material. Vacancies are injected into the material along the grain boundaries further embrittling those interfaces leading to the intergranular cracking. Chromium is attracted to the zone ahead of the crack tip rich in oxygen where it forms a protective chromia barrier, however this reduces ductility creating a further embrittled zone around the crack tip. In addition they found that once the crack tip reaches relaxation conditions (if at all) the damage from the environment stops. This means under creep-fatigue conditions a quickly relaxing material would have increased resistance to embrittlement.

Later work by Miller et al. [39] attempted to explain differences in crack growth responses between different superalloys by focusing on mechanisms involving niobium which is a major constituent of Inconel 718. Specimens were polished and then heated to 700 ºC under either ultra-high vacuum or an atmosphere containing oxygen. The samples that had only been heated under ultra-high vacuum showed that less than 20% of the surface Cr had become Cr_2O_3 but 75% of the Ti, Al, and Nb had become TiO, Al_2O_3, and Nb_2O_5 respectively. Samples that had been heated in the oxygen containing atmosphere showed that Cr, Fe, and Nb preferentially oxidized, showing that Nb is a highly reactive component of IN718 when exposed to oxygen at high temperatures. Specimens of carefully prepared Inconel 718 were exposed to a controlled atmosphere of high-purity oxygen at a sustained load at 700 ºC until cracks reached a stress intensity of 60 MPa√m. The specimens were then allowed to furnace cool in the test chamber under high-purity argon that had been passed through a gettering furnace. The sample was sectioned, polished, and then fractured before being analyzed using X-ray photoelectron spectroscopy (XPS). They found an area ahead of the crack tip that had not yet been cracked through but was affected by oxygen called the Oxygen Affected Region (OAR). XPS showed that oxygen penetration ahead of the crack tip oxidized Nb and Cr even in unexposed areas and Nb oxidized further ahead than Cr at lower levels of oxygen (Figure 41). Because of this, older theories of Ni and Fe oxidation causing the intergranular embrittlement were thought to be incorrect.

Perhaps the most compelling evidence that Nb was involved in this effect was a study on the high temperature fatigue of a ternary Ni-18Cr-18Fe alloy [40]. While oxygen had a small influence on crack growth rate it was nowhere near the acceleration seen in Inconel 718. This shows that one of the minor alloying elements in Inconel 718 is

responsible for a large portion of the acceleration effect. When combined with the findings of Miller et al., it becomes likely that Nb is responsible.

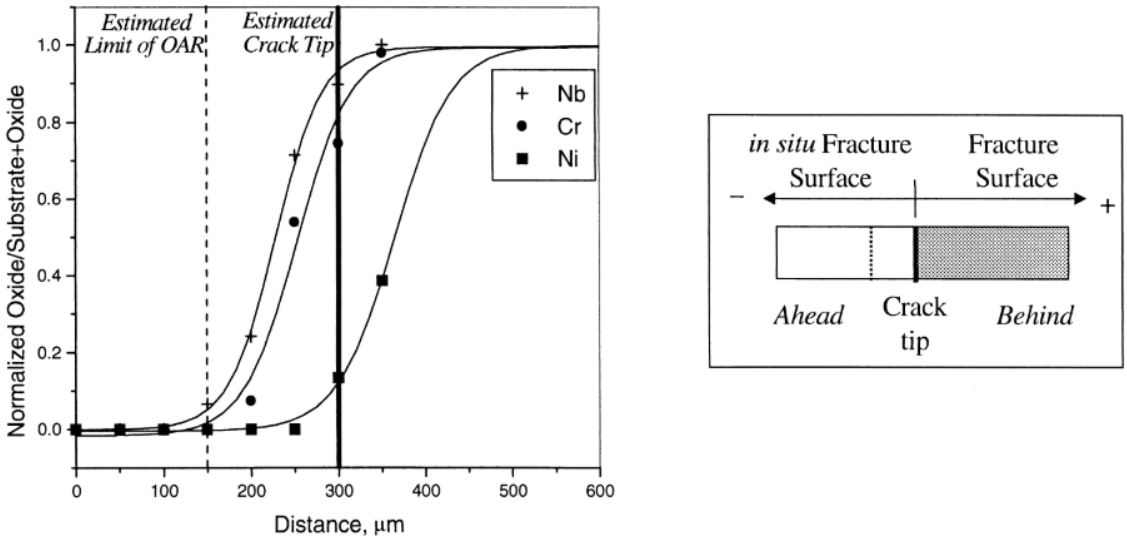

Figure 41: Metal oxides found in cracked region (fracture surface >300 μm), in the OAR ahead of the crack tip (< 300 μm and > 150 μm), and in the bulk material (< 150 μm)

2.1.2. Thermomechanical Fatigue of Inconel 718

Thermomechanical fatigue (TMF) is a process where fatigue damage occurs as a combination of mechanical cycling and thermal cycling. TMF is commonly divided into two sub-classifications in-phase TMF (IP TMF) and out-of-phase TMF (OP TMF) (Figure 42). IP TMF refers to situations where the maximum mechanical strain occurs simultaneously with the maximum thermal strain (maximum temperature). OP TMF is the opposite case where maximum mechanical strain occurs when temperature is at a minimum. It is thought that OP TMF is usually the more damaging situation where environmental damage can occur at high temperature and the weakened material will crack more easily when higher loads are applied later at subsequent lower temperatures [41]. However Nicholas et al. found that for Inconel 718, IP TMF was more damaging then OP

TMF when cycled between 427 ºC (the minimum temperature for intergranular cracking) and 649 ºC [42]. They also found through various experiments at different phase angles between the mechanical and thermal cycling that TMF damage only occurs during the increasing load portion of the cycle and "only when the instantaneous contribution to time-dependent damage is an increasing function".

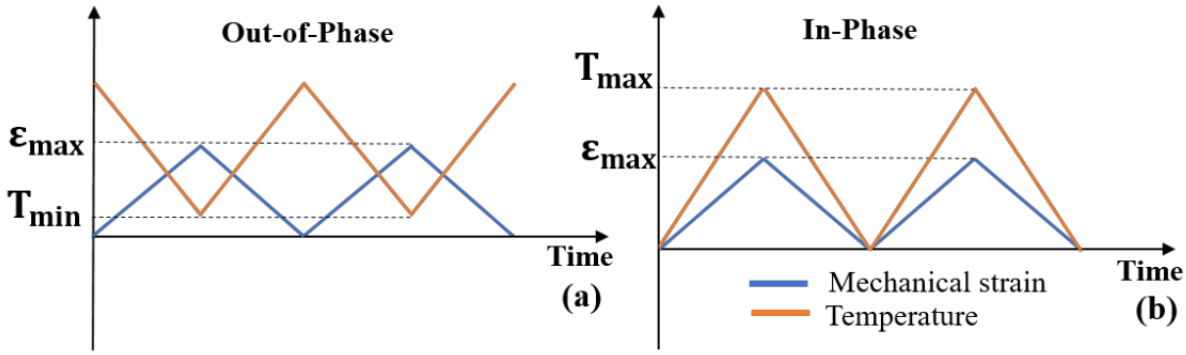

Figure 42: (a) Out-of-Phase TMF where the peak temperature coincides with the minimum mechanical strain. (b) In-Phase TMF where the peak temperature coincides with the maximum mechanical strain [43]

The term Temperature Affected Zone (TAZ) was used by Radzicki et al. [1] to describe the damage zone ahead of the crack tip that is not caused by fatigue or plasticity under TMF. The idea is that the TAZ grows ahead of the crack tip during certain regions of the TMF loading spectrum. While the crack is in the TAZ regardless of temperature there will be an increased Fatigue Crack Growth Rate (FCGR) until the crack has broken through the entirety of the TAZ. Once the TAZ is fully depleted, the FCGR reverts to whatever is would have been at the current temperature without environmental degradation.

The work by Molins et al. [38] mentioned earlier in this paper supports this theory, showing that a high temperature hold increases subsequent crack growth rates. Work by

Gustafsson et al. created a time based function to describe the depth of the "damage zone" (TAZ) at 550 ºC [44]. The damage ahead of the crack tip can be quite complex with channels of broken grain boundaries in between unbroken "islands" and "ligaments" as observed by Lundstrom et al. (Figure 43) [45]. Lundstrom introduced a model where TAZ is developed and then consumed by subsequent crack growth with a focus on IN718 at 550 ºC.

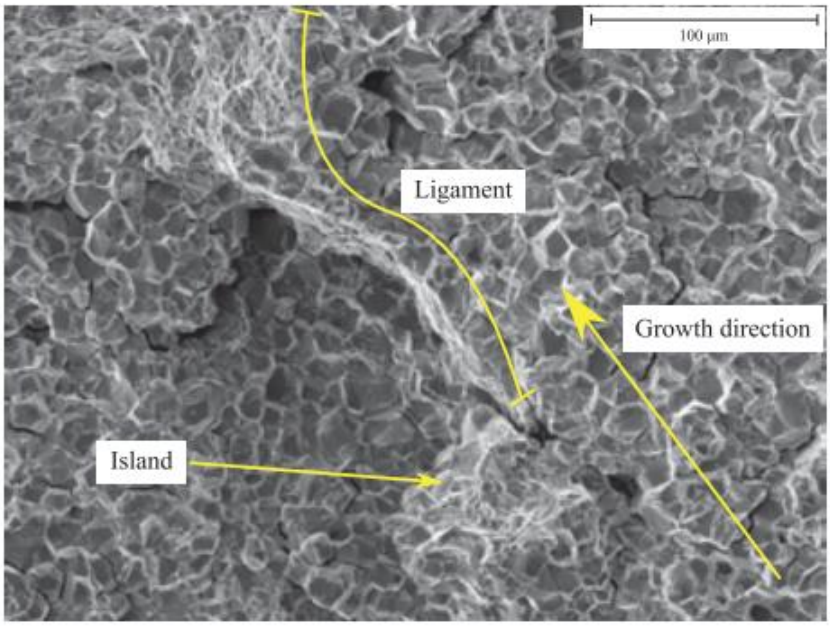

Figure 43: SEM micrograph showing islands and ligaments of ductile fracture surrounded by channels of intergranular fracture [45]

Lundstrom showed that quite a bit of time dependent growth occurred in the material at 550 ºC which was ringed by a "damaged zone". This zone was shown to be at least partially intact by EPD measurements, but was dominated by intergranular fracture and was visibly oxidized. Note that this observation of time-dependent crack growth is at odds with other reports from Radzicki, Barker, and Andersson et al. [1], [17], [37].

Radzicki et al. noted that TAZ development is more significant in areas away from the specimen surface. He asserted that more significant tensile dilatational forces exist in the plane strain dominated region, leading to increased oxygen penetration and additional TAZ. In addition he found that even for a constant thickness specimen, TAZ size varied based on crack length in a SENT specimen for equivalent stress intensities. Because of this, he found that TAZ size is 2 times larger in "plane strain dominated" region of the SENT specimen then in the "plane stress dominated" region. This idea will be explored in the current work through TMF testing on the surface crack configuration to highlight differences in the plane stress and plane strain regions of the crack front.

Radzicki et al. tested both the effects of tensile and compressive holds at high temperatures followed by isothermal cycling as well as the effect of tensile holds in an OP TMF loading. In the tensile hold testing, it was found that TAZ occurred only when the tensile hold was greater than 75% of the cyclic maximum load. No effects were found for the compressive holds. Though FEA simulation, it was found that stresses immediately ahead of the crack tip did not reach yield for holds of 75% or less. From this, Radzicki postulated that tensile stresses must be at least at the yield strength for TAZ to develop. As hold duration increased, not only did the TAZ size increase, but also the amount of secondary (out of plane) cracking and oxidation.

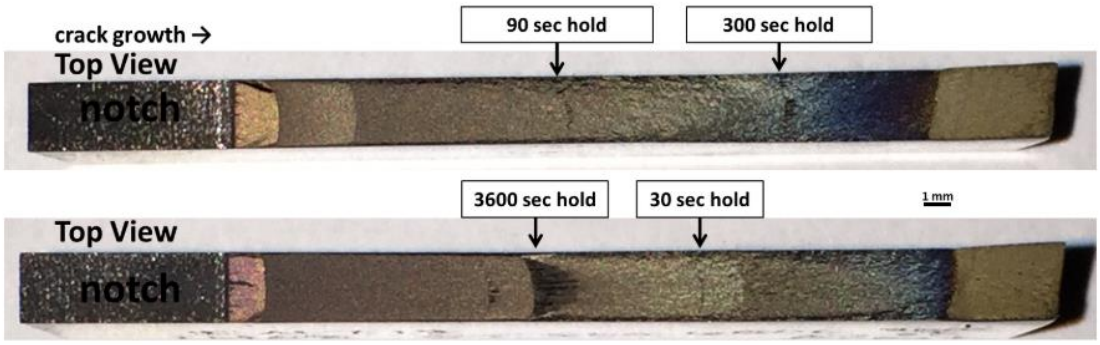

Figure 44: Isothermal tensile hold testing (100% load$_{max}$) at 650 ºC on single edge notch tension (SENT) specimens [1]

Like Lundstrom, Radzicki found that the TAZ region was composed of "fingers" of weakened material with ligaments (or ridges) of transgraular crack growth in between (Figure 45 and Figure 46).

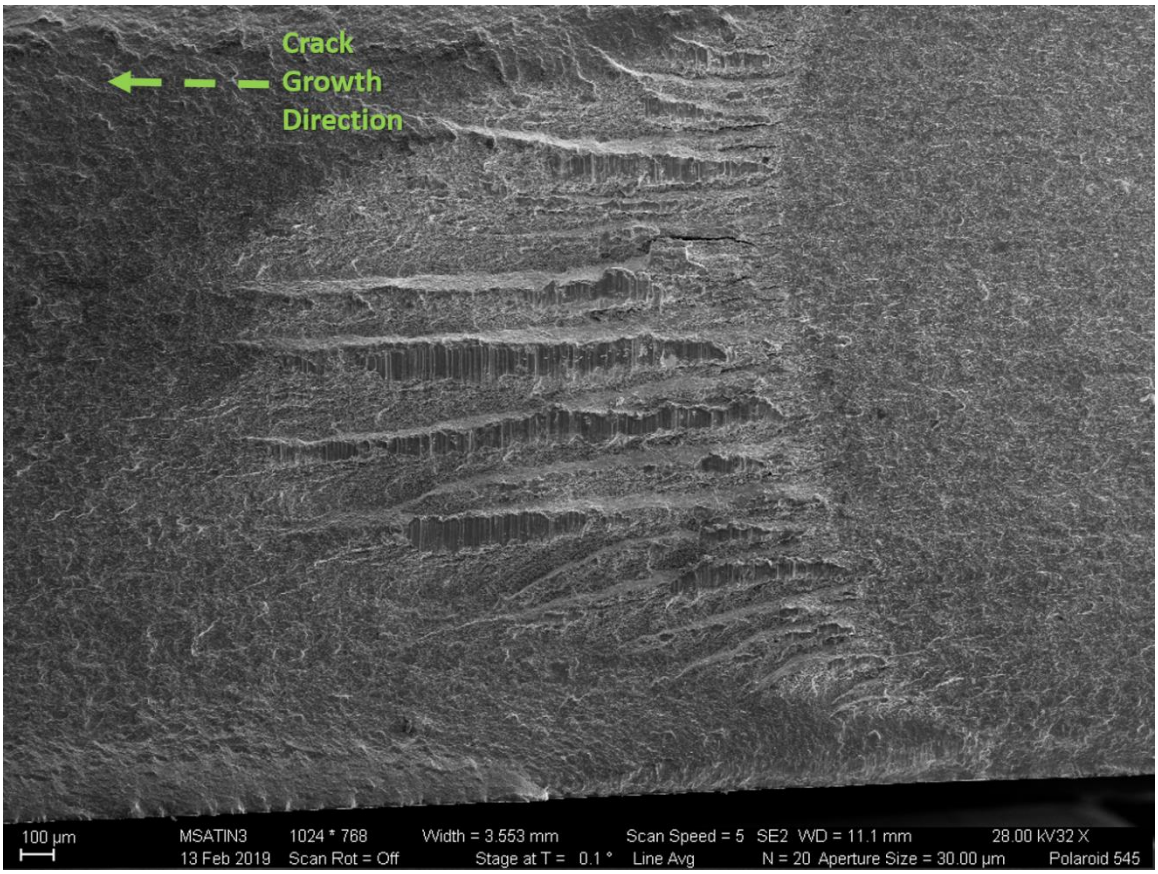

Figure 45: SEM fractograph of Radzicki's 3600 second 650 ºC K-hold showing transgranular ridges

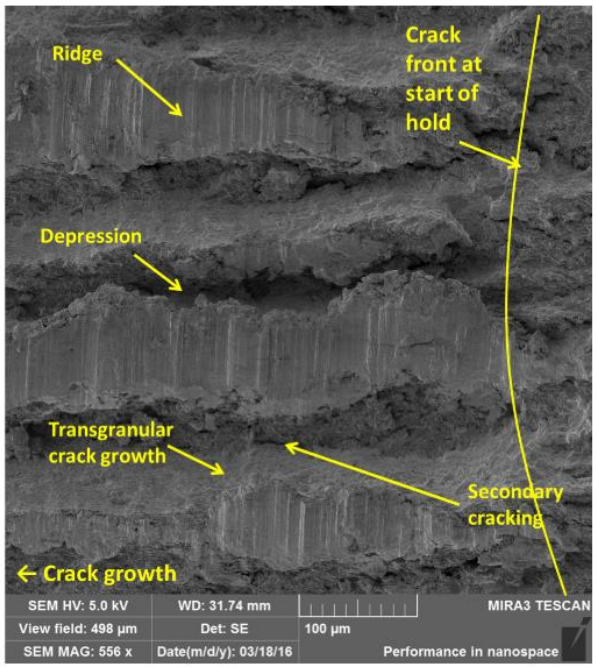

Figure 46: SEM micrograph showing TAZ region and constitutive features [1]

Another test was conducted where TAZ was grown ahead of a crack tip and then monotonically pulled to fracture. In this case the damage in the TAZ area was evident, but the ligaments of what would have been transgranular striated crack growth showed ductile rupture dimples instead. This indicated to Radzicki that there is no traditional "time dependent" crack growth in Inconel 718. Instead there is complex time dependent component that grows the TAZ, but does not actually grow the crack until subsequent mechanical cycling.

Using the TAZ measurements corrected for plane strain and plane stress dominated regions and the hold time, temperature, and applied K, Radzicki developed the following relationship to describe the size of the TAZ region ahead of a crack tip:

$$TAZsize = Ct^{n_1} K_{hold}^{n_2} e^{n_3 \frac{-Q}{RT}} \qquad (20)$$

Where TAZ size is in mm, t is the duration in seconds, K_{hold} is the stress intensity in MPa√m, T is the absolute temperature (Kelvin), R is the universal gas constant, and Q is the activation energy for high temperature oxidation of nickel superalloy from Chang [46]. The parameters were empirically fit using regression analysis of the experimental data and were:

Table 14: Empirically fit values for Equation (20)

C	0.291	$(sec)^{-n1}(MPa\sqrt{m})^{-n2}$
$\mathbf{n_1}$	0.48	
$\mathbf{n_2}$	2.6	
$\mathbf{n_3}$	0.38	
Q	25000	J/mol
R	8.31446	J/mol*K

To account for the acceleration in crack growth due to growing through the TAZ, a TAZ acceleration factor (TAF) was developed which is dependent on the remaining TAZ size, the plastic zone size ahead of the crack tip, and some fitting parameters. This allows the effect of TAZ to be reduced as stress changes from plane strain dominated to plane stress dominated.

For the OP TMF spectra tested with included tensile holds it was shown that the "forward" waveform with an increase in load prior to a tensile hold caused faster crack growth then a "backward" waveform with a tensile hold following an unload (Figure 47). Radzicki's work showed a 30% increase in crack growth for the forward spectrum. The forward spectrum has an underload just prior to the tensile hold, reducing the retardation effect from the previous overload. The underload also paves the way for a greater tensile dilatational force at the crack tip during the hold leading to further embrittlement.

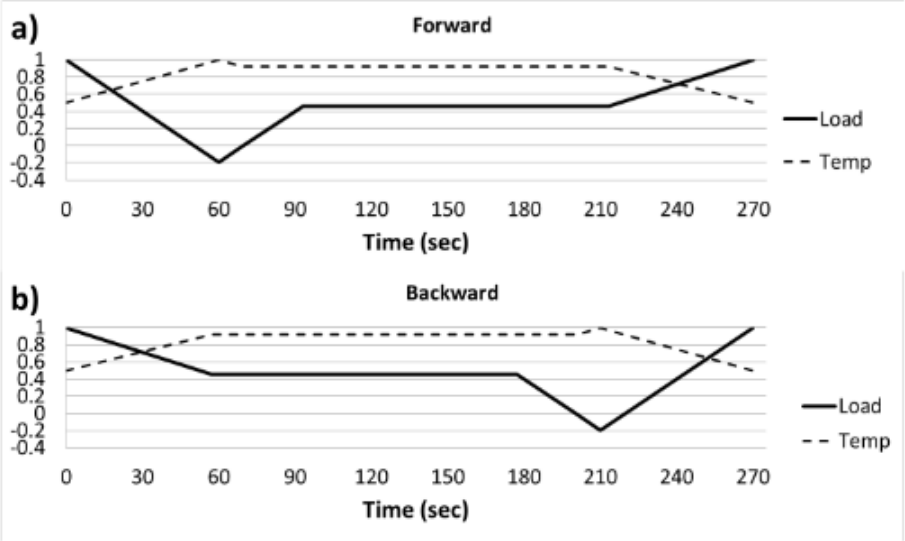

Figure 47: OP-TMF spectra with tensile holds [1]

The final set of experiments conducted by Radzicki et al. used two representative TMF spectra. One that used a representative "flight" of a transport aircraft and one of a fighter aircraft (the same but with two maneuvering subcycles) (Figure 48). The fighter spectrum had a noticeable drop in life when compared to the transport spectrum. These tests were the main objects of testing the prediction capabilities of the improved MPYZ-TMF code.

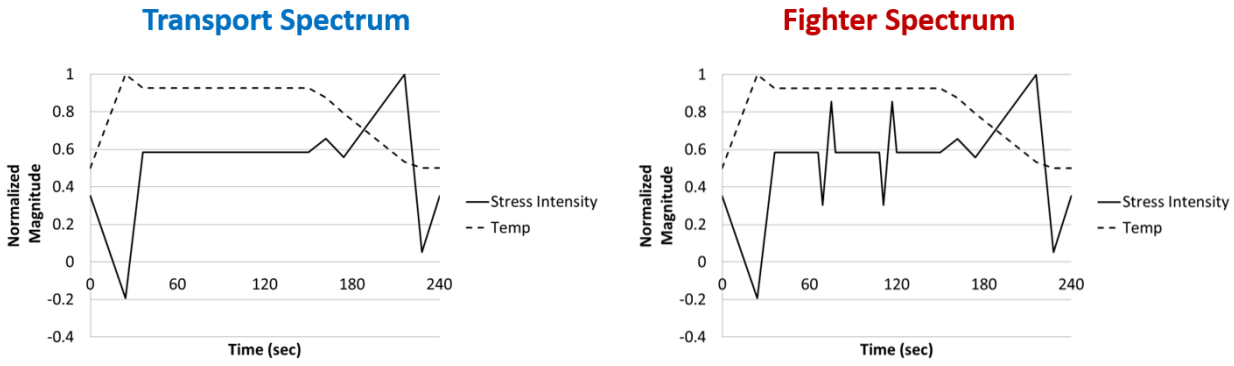

Figure 48: Representative TMF spectra of a transport aircraft and a fighter aircraft [1]

2.1.3. Multi-Parameter Yield Zone – Thermomechanical Fatigue Model and Code

The Multi-Parameter Yield Zone model (MPYZ) was originally developed by William S. Johnson while at NASA, and written in the FORTRAN computer language [15]. This model was developed to account for crack growth retardation and acceleration due to load interactions such as overloads and underloads. In the model a residual stress intensity factor, K_R is calculated and used to find effective K values by subtracting K_R from both K_{max} and K_{min}.

$$R^{eff} = \frac{K_{min} - K_R}{K_{max} - K_R} = \frac{K_{min}^{eff}}{K_{max}^{eff}} \qquad (21)$$

In 2011 Vince Barker re-wrote the MPYZ model in C++, added a system for interpolating material fatigue data at different temperatures, and added the capability for cycling in both stress and temperature resulting in an early form of the MPYZ-TMF code used in the present work [17]. He showed that load and temperature interactions in the nickel based superalloy Inconel 100 could be successfully modeled and predicted using MPYZ-TMF [16], [17]. However, this version of MPYZ-TMF could only use isothermal constant amplitude cycles before moving on to the next cycle at a different temperature.

The Barker version of MPYZ used the following scheme for dealing with the retardation of crack growth due to overloads. K_R is a parameter calculated using the plastic zone size of the preceding overload (Z_{OL}), the current plastic zone size ahead of the crack tip (Z), and a parameter α which describes the stress state at the crack tip. The Z parameter and α parameter are iteratively derived with the following logic:

- The value of α is set to √3
- The value of Z is set to 0
- The increment ΔZ is set to 1
- A precision variable is set to 0.05
- While the ΔZ increment is larger than the precision:

$$Z_{new} = \frac{1}{\alpha\pi\left(\frac{K_{max}}{\sigma_{yield}}\right)^2} \qquad (22)$$

- The increment ΔZ is then described as:

$$\Delta Z = \frac{Z_{new} - Z}{Z_{new}} \qquad (23)$$

- If Z_{new} is ≥ t/4 (plane strain like condition) then α=1
- If Z_{new} is ≤ t/6 (plane stress like condition) then α=3
- For values in between the following equation is used to calculate α:

$$\alpha = \sqrt{\frac{t}{2Z_{new}}} \qquad (24)$$

This loop is repeated until the desired precision is reached and the values of Z and α are fixed

The temperature dependent value K_R can then be calculated after an overload by:

$$K_R = \sigma_{yield}\sqrt{\left(Z_{OL} - (\Delta a + Z)\right)\pi\alpha} \qquad (25)$$

This is used in combination with the experimentally fitted constants C_1, and C_2 as well as the no retardation overload ratio A, and the cut-off overload retardation ratio B to find the R_{eff} ratio to be used in the fatigue crack growth law:

$$R_{eff} = C_1 \left(\frac{1}{\frac{K_{OL}}{K_{max}} - \frac{B}{A}} \right) K_R^{C_2} + \frac{K_{min}}{K_{max}} \qquad (26)$$

The no retardation overload ratio (overload with no effect on crack growth rate) is found for a certain temperature by:

$$B = B_a * T + B_b \qquad (27)$$

Where B_a and B_b must be fit to experimental data.

Underloads are also accounted for in the model by reducing the magnitude of the previous overload to get a new overload stress intensity factor and is found with the following equations where K_{pr} is the minimum stress intensity factor for the cycle that produced the overload, K_{UL} is the stress intensity of the underload, K_{OLeff} is the effective overload ratio, and Y & Z are material fitting parameters:

$$\beta = \frac{K_{pr} - K_{UL}}{K_{eff}^{OL} - K_{UL}} \qquad (28)$$

$$K_{max}^{OL} = \frac{\left(K_{eff}^{OL} - K_{max}\right)}{(Z - Y)} (Z - \beta) + K_{max} \qquad (29)$$

Radzicki made several important changes to the code and the way it handles material under TMF. Radzicki's implementation of a TMF spectrum into MPYZ-TMF consisted of loading in a table of temperature and load "points". As the model goes from

point-to-point in the spectrum it assigns a maximum and minimum stress intensity for that segment. It then adjusts for load interaction effects using Barker's method, and then uses the fatigue crack growth law to calculate a crack growth increment. However, the calculated crack growth increment only contributes to the growth in the model if the load is increasing in the current segment. Radzicki had found that for an OP TMF cycle the temperature at the maximum of a segment is not representative of the crack growth response. Instead, the model uses the average temperature of the segment for the calculation.

TAZ development in the model is expected to occur in certain situations. In order to ensure TAZ was grown realistically TAZ is not allowed to develop when the temperature is below 500 ºC, the stress intensity is ≤ 0, or the stress intensity is ≤ 75% of any of the previous three spectrum points. The model also takes the previous three segments of the spectrum into account to see if any portions of the loading spectrum may have a general downward trend over several points to ensure unloading effects are accounted for in retarding TAZ growth. Each loading segment is portioned into 5 sub-segments by time to try to capture portions where TAZ can develop. This ensures that if a point-to-point segment on the TMF spectrum only qualifies for TAZ development for part of the time, it will still be accurately represented.

The empirical model for TAZ growth is based on the underlying assumption that the crack tip does not already have existing TAZ. In order to account for this Radzicki modified a parabolic oxygen diffusion law since the embrittling species must diffuse through the existing TAZ to develop the new TAZ region:

$$TAZsize_{newtotal} \qquad (30)$$

$$= TAZsize_{existing} + \frac{TAZsize_{newsegment}}{\left(TAZsize_{existing} + 1\right)^{TAC}}$$

Where TAC is the TAZ accumulation coefficient which is equal to 2.0. Radzicki does note that this approach does make the resulting TAZ size dependent on the number of sub-segments (5) in a TAZ development segment since a smaller percentage of new TAZ gets applied when the existing TAZ is thicker. As a crack grows through the accumulated TAZ region, the TAF is applied speeding that growth and an equivalent amount of TAZ is subtracted from the accumulation.

Radzicki used the TAZ Acceleration Factor (TAF) to describe how much faster crack growth is when consuming TAZ:

$$TAF = 1 + D\left(\frac{TAZsize_{current}}{r_p}\right)^p \qquad (31)$$

In this equation, acceleration increases as the current TAZ size increases, and is adjusted with the plastic zone size r_p to account for the slowing effect seen in plane stress conditions. The values of D and p were empirically fit to crack growth data taken following K-hold experiments and had values of 6.0 and 0.5 respectively.

2.2.Base Material Characterization

A metallographic mount was prepared using a portion of material from the Pratt & Whitney provided Inconel 718. This material was polished to a 1 μm surface finish with a Struers Roto-Pol15 automatic polishing system and progressively finer diamond suspension slurry. The mount was then etched with P&W #17 etchant [47] consisting of the following:

Table 15: P&W #17 etchant recipe

Chemical	Quantity per 75 ml
Hydrochloric Acid (HCl)	25 ml
Nitric Acid (HNO_3)	25 ml
Water (H_2O)	25 ml
Molybdic Acid ($MoO_3 \cdot H_2O$)	0.75 g

The mount was imaged with a Phenom Pro bench-top scanning electron microscope using a backscatter electron detector along with the Zeiss Ultra-60 FE-SEM and several optical microscopes. Additional information about the microstructure and its constituents were found using the included energy dispersive x-ray spectroscopy (EDS) detector to do elemental analysis on etched features.

More microstructural analysis was conducted using Kalling's II etchant consisting of the following:

Table 16: Kalling's II etchant recipe

Chemical	Quantity per 100 ml
Methanol (CH_4O)	50 ml
Hydrochloric Acid (HCl)	50 ml
Copper II Chloride ($CuCl_2$)	5 g

The etchant was applied by polishing with a final step of 1 μm diamond slurry, and then brushing the etchant lightly across the surface with a cotton ball for no less than one minute. Samples were analyzed using a Zeiss Ultra 60 Field Emission Scanning Electron Microscope (FE-SEM) with an equipped EDS detector.

Hardness testing was performed on IN718 specimens at various locations to check for any inhomogeneities in heat treatment or processing. Indentation was performed using the Rockwell "C" scale measurement on a Riehle 3-1920 portable hardness tester. Each

testing session was immediately preceded with testing of a calibration block to ensure proper indenter seating and diamond condition.

Characterization was not performed on the 17-4 steel material since use of that material is restricted to room temperature testing and will not be part of the TMF study. Hardness testing was performed to verify that heat treatment had the desired effect on mechanical properties.

2.2.1. Base Material Characterization – Fine Grained Inconel 718

The IN718 material supplied by Pratt & Whitney appeared to have an equiaxed grain structure of similar size to the material used by Radzicki [1] of ASTM grain size 13 (mean diameter approx. 4 μm) (Figure 49). Measurements were performed by, a colleague Jonathan Leung, per ASTM E112[48]. Measurement was conducted using 5 images at 1262 x magnification with four fields of view selected per image for a number of test frames (n) of 20. Each frame consisted of 5, 50 μm length lines for a total length per measurement of 250 μm (Figure 50). The mean intercept grain size was 3.38 ± 0.18 μm. The quantification was based on the assumption that the grain structure was isotropic from visual inspection of the micrographs.

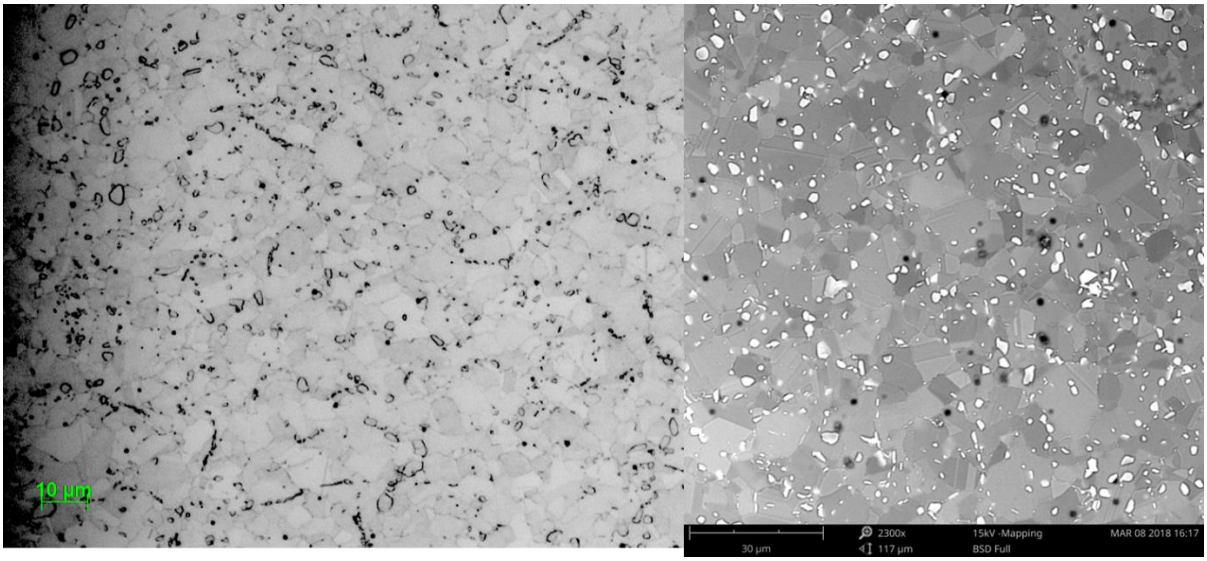

Figure 49: Comparison of Radzicki's IN718 microstructure imaged in an optical microscope (left) and the current material provided by Pratt & Whitney in SEM (right)

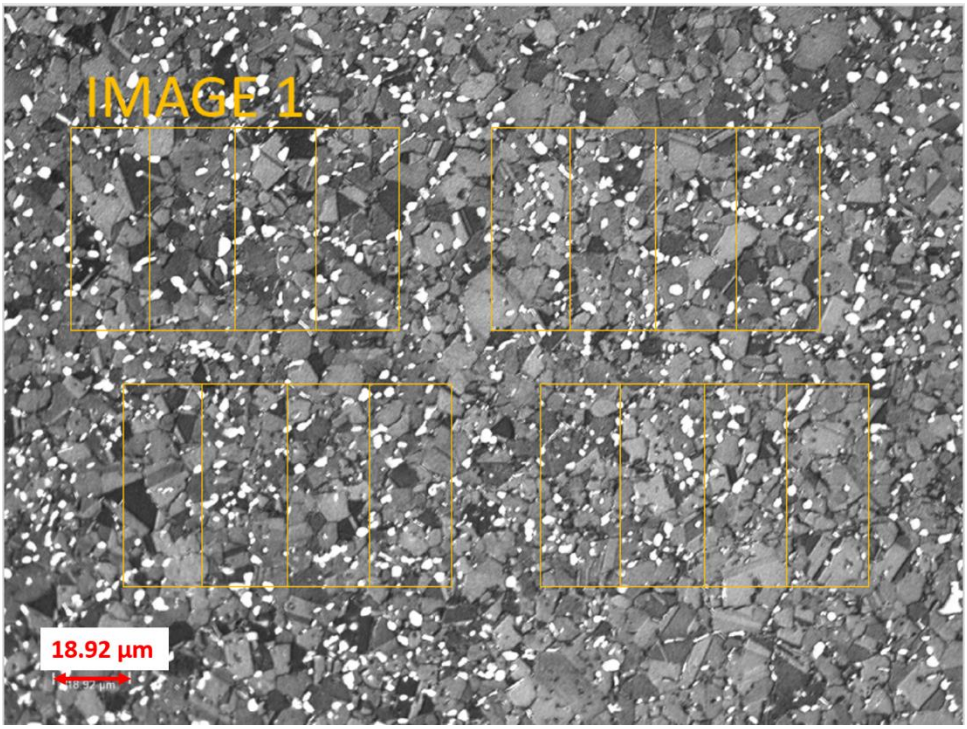

Figure 50: Optical micrograph of IN718 grains with counting frames shown used for grain size measurement

This material showed relatively large carbides (on the order of 10 µm) that were relatively rare and were segregated into NbC (with some Mo) and TiC. These carbides are

easily identified with EDS by showing a large concentration of Nb and Mo (and to a much lesser extent Ti) but are nearly devoid of Inconel 718's primary constituents Ni, Cr, and Fe.

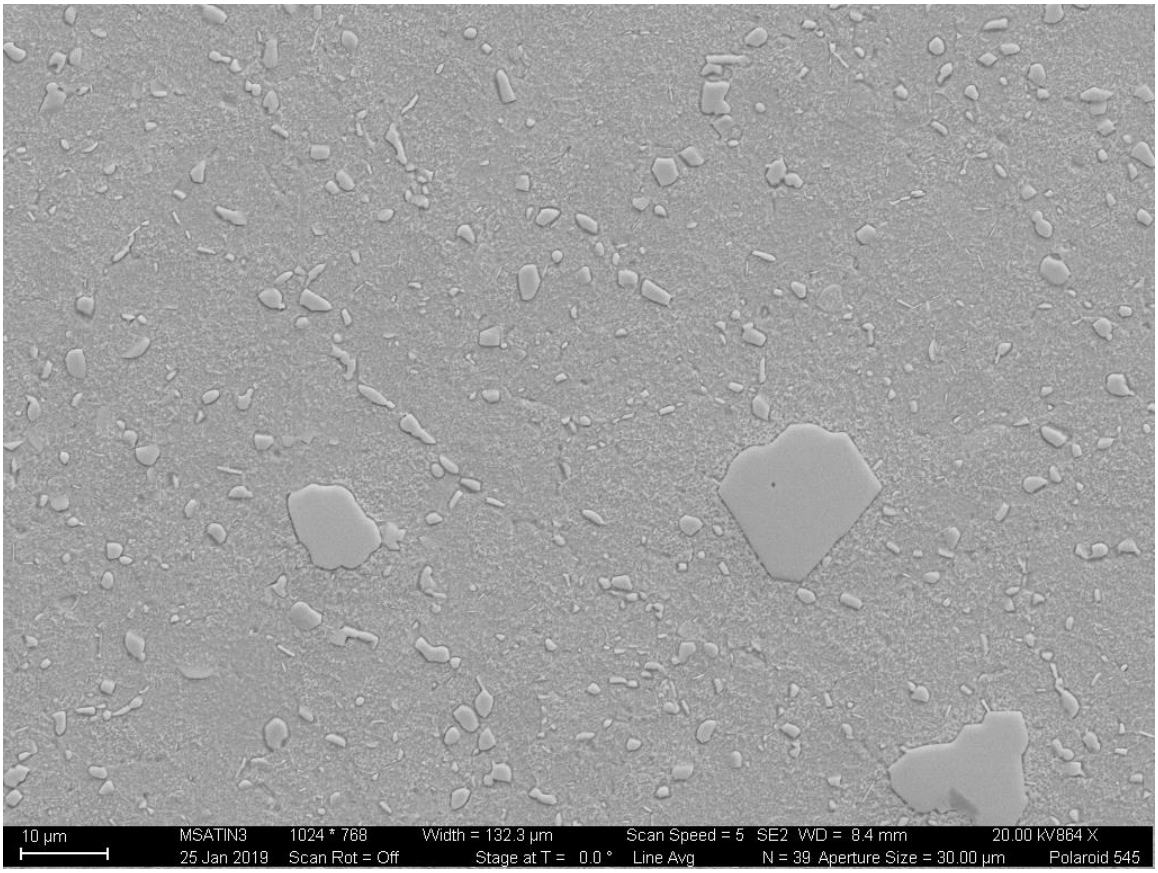

Figure 51: Precipitates in Inconel 718 etched with P&W #17 showing spheroidized δ partiuclates as well as much larger NbC particles

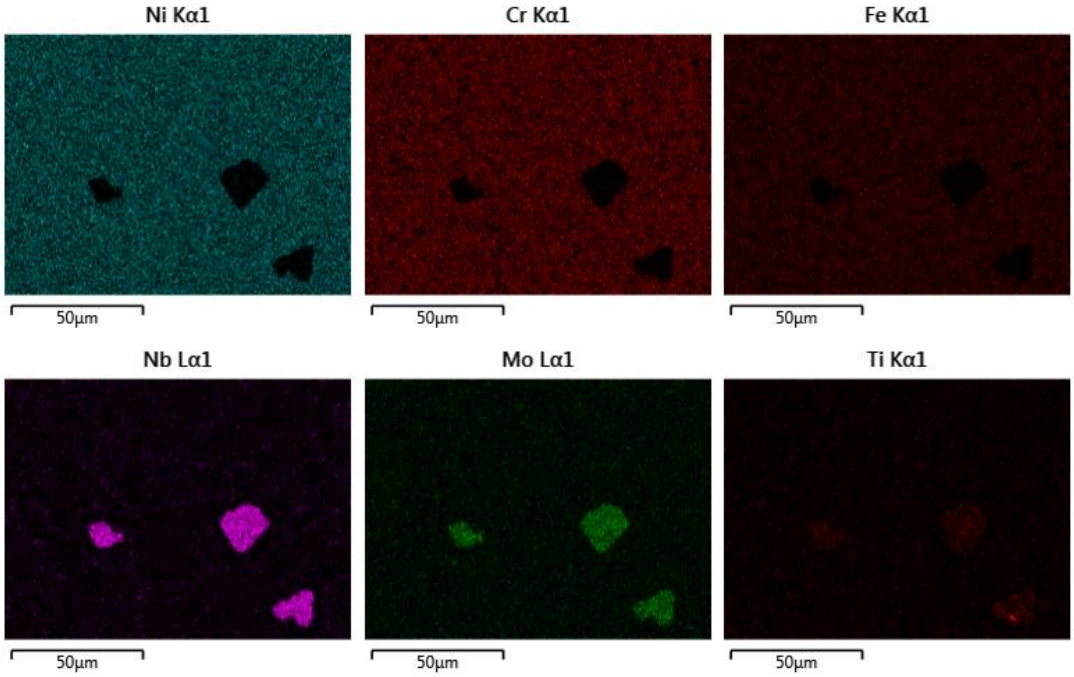

Figure 52: EDS map of micrograph in Figure 51, showing a concentration of Nb and Mo without Fe, Cr, and Ni

Other, rarer carbides in the material are nearly pure TiC. These particles usually present with more rectangular shaped cross sections and typically are darker in appearance when etched with P&W #17 then the NbC's. An example can be seen below in Figure 53.

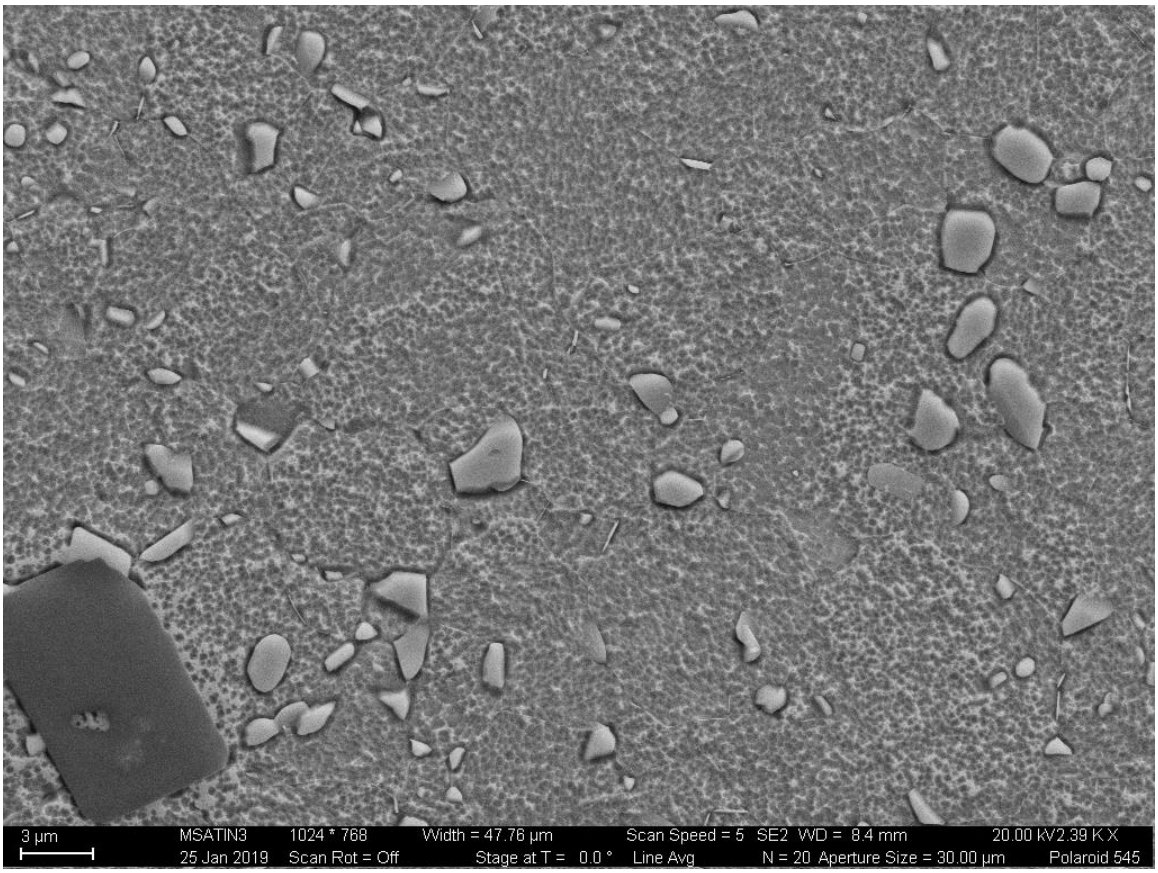

Figure 53: Etched Inconel 718 microstructure showing a dark TiC particle in the lower left

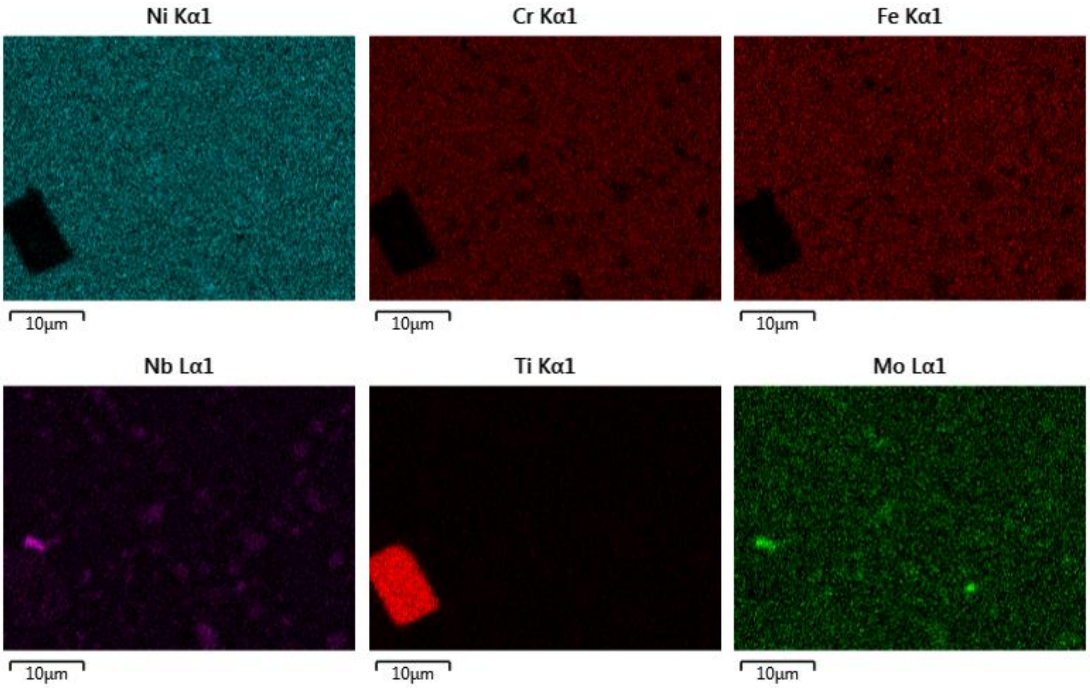

Figure 54: TiC can be identified by the lack of Ni, Cr, and Fe as well as Nb and Mo, and the high concentration of Ti.

Unlike carbides, δ is smaller and is present in two morphologies in this material. Most of the δ has been spheroidized using a heat treatment process and are found as rounded precipitates with no relationship to currently existing grain boundaries (Figure 55).

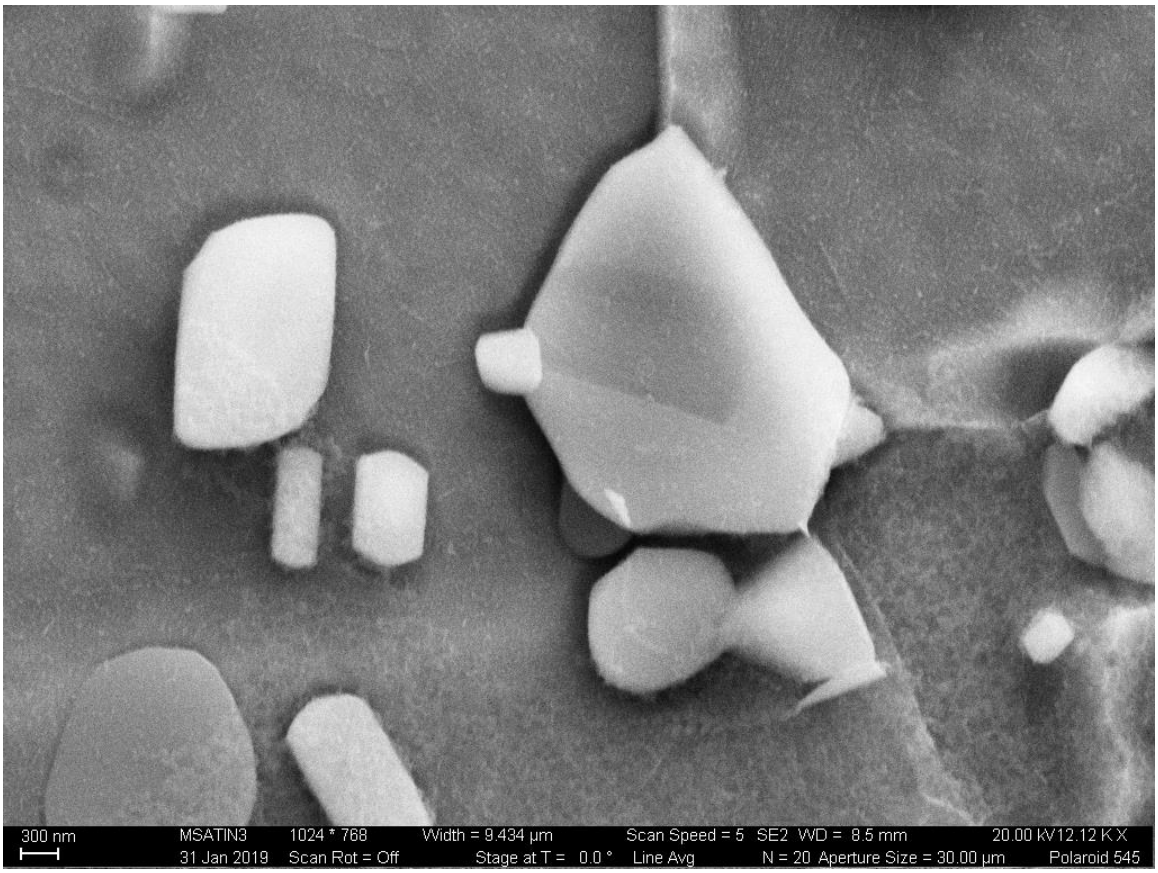

Figure 55: Spheroidized δ precipitates

More typical δ precipitates that formed later in the heat treating process can be seen on grain boundaries with a needle like morphology.

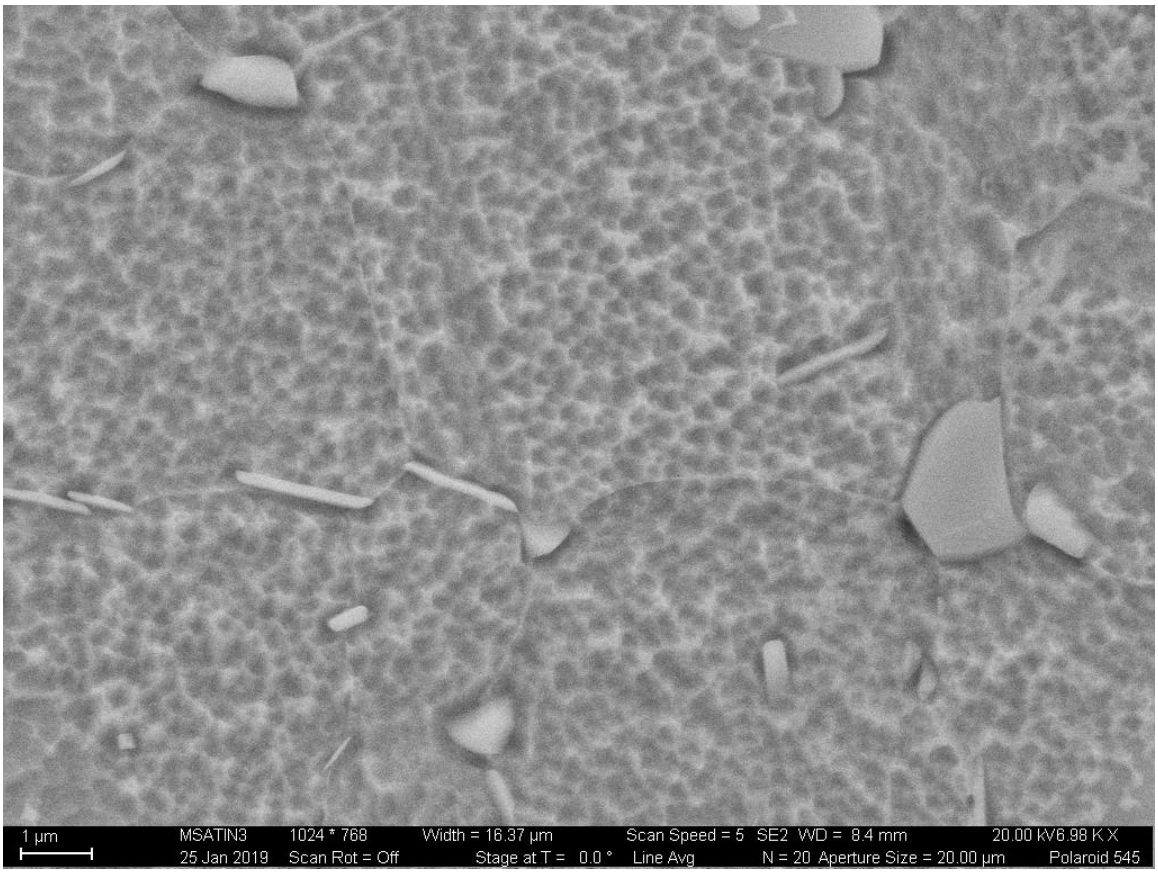

Figure 56: Grain boundaries showing needle like δ precipitates

In general δ precipitates are detrimental to the mechanical properties of Inconel 718. δ is the equilibrium phase of the metastable γ'/γ'' phases that act as the main strengthening agents in Inconel 718. Because of this, δ is often formed at the expense of γ'/γ''. In addition, δ often precipitates on grain boundaries, and the needle like morphology acts as a stress concentrator. In this alloy much of this has been alleviated by reprocessing the δ into a rounder shape to mitigate these effects.

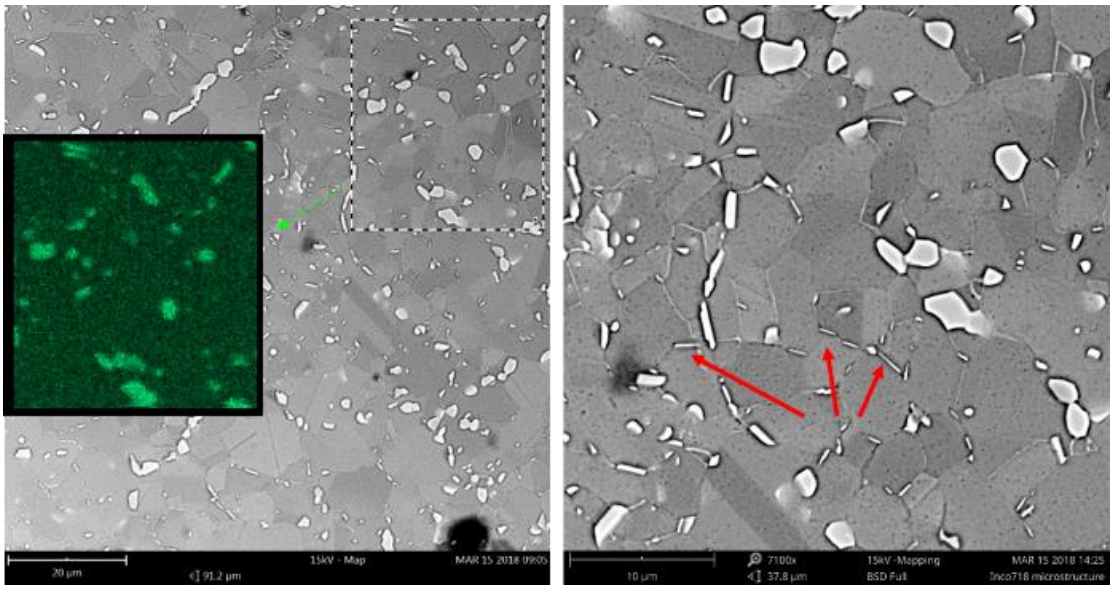

Figure 57: (left) Niobium mapping of microstructure using EDS showing spheroidized δ in IN718, (right) high aspect ratio δ phase precipitates along grain boundaries

An Inconel 718 bar was selected for hardness testing to test for material inhomogeneity across the specimen. The specimen was tested near the center of the front face at ¼, ½, and ¾ of the specimen height. Each test yielded a result of 44 HRC, which is in line with expected values for heat treated IN718 of greater than 38 HRC (per SAE AMS2774E [28]).

2.2.2. Base Material Characterization – Coarse Grained Inconel 718

Additional material was provided by Pratt & Whitney for high temperature testing. However, this material was commercially sourced and had a very different structure from the original material used by Radzicki [1] and used in the room temperature portion of this project. The properties of this material do not represent any Pratt & Whitney hardware or intellectual property. This new material had a much coarser microstructure and did not have the spheroidized δ microstructure. For the purposes of this paper the original material will be referred to as Fine Grained Inconel 718 (FGIN718), and the newer material will be

referred to as Coarse Grained Inconel 718 (CGIN718). Unless otherwise noted, all high temperature testing was performed on the CGIN718 material.

The CGIN718 was heat treated per AMS 5663M [49] which involves a solutionizing step, a precipitation initiation step, and an aging step. Solutionizing involves heating to 941-1010 ºC and holding for a time commensurate with cross-sectional thickness. The material is then quenched by air cooling or faster. The precipitation initiation involves heating to 718-760 ºC for 8 hours and then is immediately followed by aging by cooling at 56 ºC per hour to 621-649 ºC and then holding for a combined total of 18 hours.

AMS 5663M requires that the material have an ASTM grain size of 5 or finer but may have up to 20% of grains with an average of 3-5. The hardness is required to be 331 HB (35-36 HRC) or higher. The measured hardness for the CGIN718 material was 42 HRC.

Again, the material was polished, etched, imaged and counted using the line intercept method per ASTM E112 [48] assuming an equiaxed grain structure. Measurements were taken in 5 fields of view with five lines per counting frame. The total length per test frame was 3.15 mm for a total line length of 15.75 mm. In CGIN718, the ASTM grain size was found to be 5 with a mean intercept grain diameter of 61 μm. Grains in this material are over an order of magnitude larger than the FGIN718.

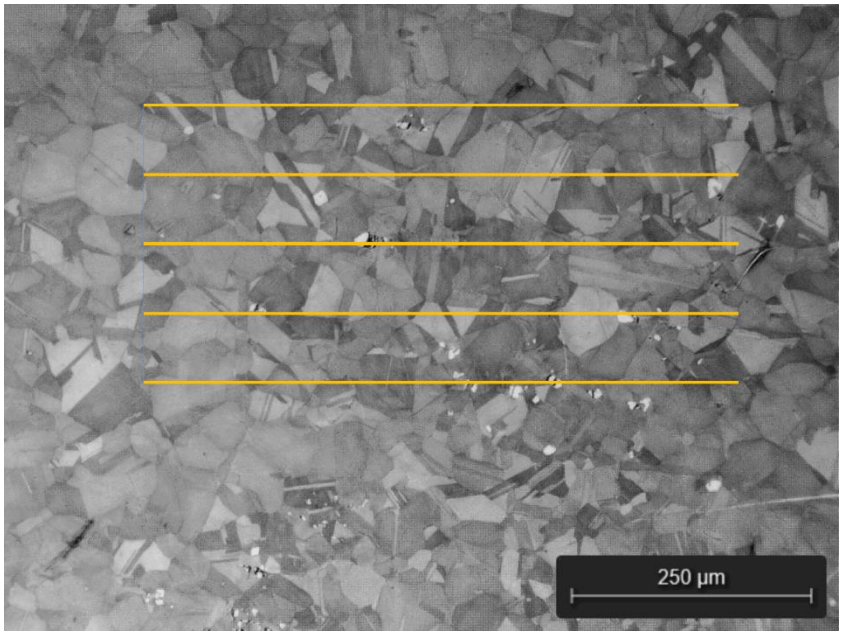

Figure 58: Optical micrograph showing grain boundaries etched with P&W #17 in CGIN718. The dispersed white particulates are carbides.

Carbides in CGIN718 can be found in clusters and do not necessarily lie on grain boundaries. Again, these carbides are characteristically deficient in Ni, Cr, and Fe. However, in this material there does not seem to be a delineation between Nb(Mo)C and TiC particles (Figure 60). Additional particulates can be seen with SEM that are less than 1 µm primarily lying on grain boundaries. These particulates are thought to be δ precipitates, but they do not show the characteristic concentration of Nb and Mo that is seen in δ in FGIN718 (Figure 61). This could be due to limitations in EDS resolution.

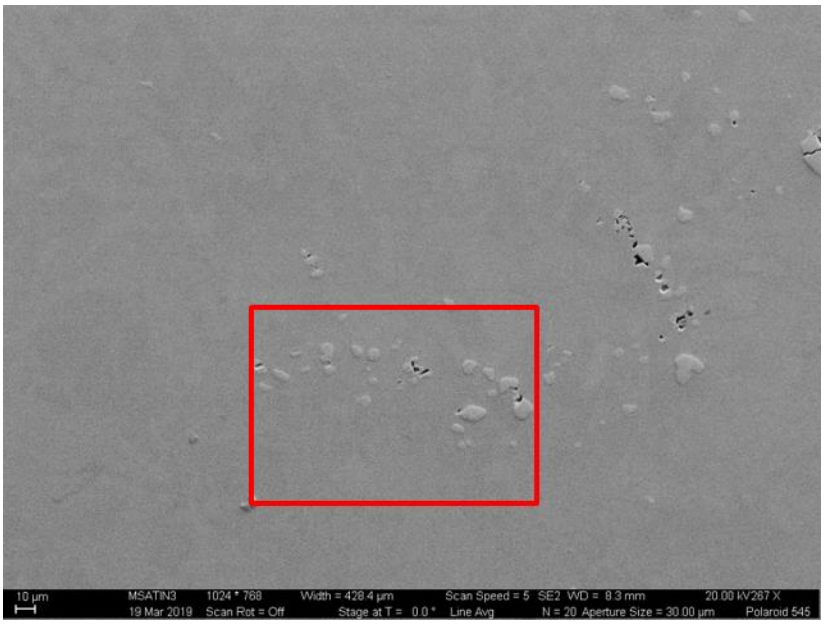

Figure 59: CGIN718 showing a carbide cluster. The area shown in the EDS map below is highlighted in red.

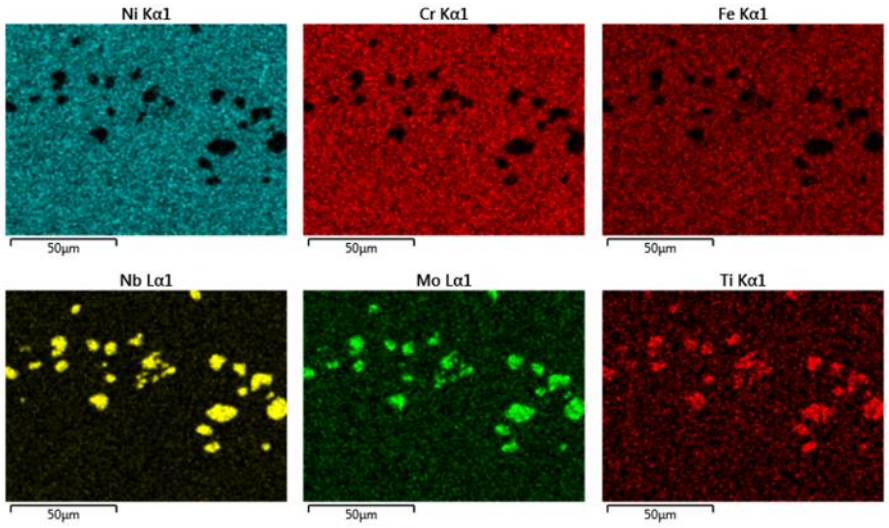

Figure 60: EDS composition map showing that carbides in CGIN718 can be characterized by their deficiency in Ni, Cr, and Fe and contain both Nb and Mo as well as Ti.

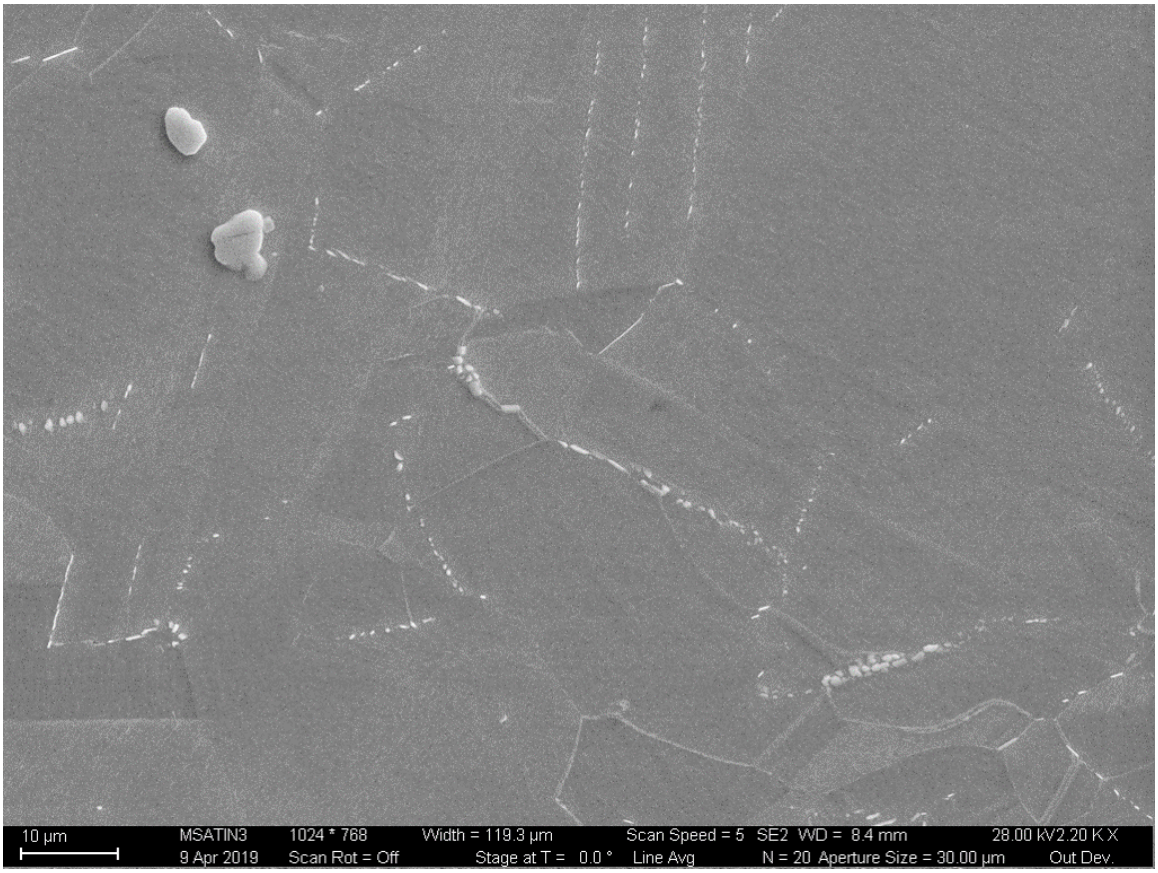

Figure 61: Micrograph of CGIN718 showing small white precipitates lying primarily on grain boundaries.

This difference in material introduces some uncertainty in the experimental process when compared to the data prepared by Radzicki [1]. The measured hardness values are comparable (44 HRC for FGIN718 and 42 HRC for CGIN718). However, the difference in grain size could have a significant effect on the way the material interacts with a grain boundary driven weakening mechanism like TAZ. There is some indirect evidence that the FGIN718 may have a lower yield strength as it seems to be more susceptible to forming shear lips then CGIN718. Further work in the future may be warranted to study the differences between these two materials in detail.

2.3.Experimental Methods

2.3.1. High Temperature Testing

Experiments were conducted in rectangular flat plate specimens of a similar geometry to those used in the corner crack specimens at room temperature but slightly thinner. All specimens except those that are specially designated, were 203.2 mm tall x 38.1 mm wide x 5.15 mm thick. These specimens were again clamped in hydraulic wedge grips so that the sample height between the grips was 101.6 mm. The material for these experiments was made of CGIN718 with the exception of 718-KH-006 (see Table 17). The plate geometry for that experiment was 203.2 mm x 38.1 mm x 5.85 mm.

As with the room temperature testing, Inconel 718 plates had semi-elliptical starter notches inserted with a plunger style EDM, or for the case of SENT specimens, wire EDM. The front faces of the plates were polished with a finishing step of 1 μm diamond slurry. The plates were then scored with a carbide tipped tool at 1 mm intervals to make measurements and tracking easier during the experiment. All specimens were heated in an environmental chamber set to 80 ºC and 0% relative humidity for at least 4 hours to ensure that all residual liquid from EDM and polishing had evaporated prior to testing. A K-type control thermocouple was spot welded onto the center of the front face just blow the crack plane, and in most cases a second thermocouple was spot welded off to the side as a way to independently confirm temperature readings. These plates were then placed in a servo-hydraulic load frame equipped with an Ameritherm Hot-Shot induction heating system for testing. Because induction heating was used, EPD was not an option for these tests as the interference from the heating coil introduces too much noise for EPD to be useful.

2.3.2. Experimental Methods – K Hold

A series of experiments were conducted to determine the effects of holding the semi-elliptical surface flaws in Inconel 718 at a high temperature under tensile loading. These experiments are called "K-holds" due to the material being held at a constant force (or starting K) for a fixed period of time at a high temperature. These experiments attempted to replicate experiments done by Radzicki [1] in which he developed the equations that predict the size of TAZ.

Samples were fatigued at constant amplitude R=0.1 at 15 Hz until a crack initiation event was confirmed with the Questar long focal length traveling microscope. The samples were then subjected to the same constant amplitude R=0.1 waveform at 5 Hz until the desired pre-crack length was reached.

Once an appropriate crack length was confirmed with the microscope, the K-hold was conducted. Each K-hold was started by holding the sample at the minimum force from the preceding fatigue waveform. The temperature was then ramped to 426.7 ºC (800 ºF) over 60 seconds. The force was then ramped to the holding force and the temperature was raised to the holding temperature of 650 ºC (1202 ºC) simultaneously over the next 60 seconds. The sample was held at these conditions for the duration of the K-hold. The force was then lowered back to the minimum fatigue force and the sample was forcibly air cooled with fans. The forced air cooling was continued for a minimum of 10 minutes before room temperature cycling was continued. The sample was then fatigued until failure at room temperature, at 5 Hz, and R=0.1 so that the fracture surfaces could be examined.

A variety of different K-hold conditions were tested to evaluate trends in size and shape of the resulting TAZ. These differences are summarized in Table 17 below:

Table 17: List of K-hold experiments

Experiment Label	Description	Starting Aspect ratio (*a*/*c*)	Aspect ratio (*a*/*c*) at start of hold	K_a (MPa√m) at start of K-hold	K_c (MPa√m) at start of K-hold
718-KH-001	35 MPa√m	1	0.75	34.6	33.3
718-KH-002	Low K	0.5	0.6	18.9	15.6
718-KH-003	30 MPa√m	0.5	0.6	31.7	26.0
718-KH-004	High K (after breakthrough)	1	0.75	N/A	41.8
718-KH-005	SENT	N/A	N/A	N/A	27.7
718-KH-006	FGIN718	1	0.8	31.0	31.7
718-KH-007	Interrupted K-hold Experiment	0.5	0.71	37.4	36.9
718-KH-008	Long SENT	N/A	N/A	N/A	53.8 and 64.5

2.3.3. Interrupted K-hold Experiment

In one of the K-hold experiments used for this work (718-KH-007), the procedure was changed slightly. In the majority of experiments after the K-hold was performed, the material was fatigued at room temperature to failure for examination. However, in this experiment the piece was removed after cooling and cut in half along its vertical axis with wire EDM (Figure 62). This allowed for one half of the piece to be remounted in the fatigue fixture and broken so that the fracture surface could be seen. The other half was reserved for metallographic examination of the unbroken intergranular region.

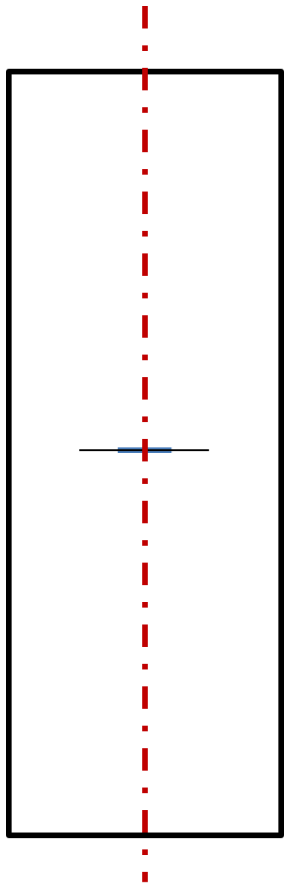

Figure 62: Wire EDM sectioning path for the interrupted K-hold experiment

The unbroken section was diamond sectioned into two pieces so that metallographic mounts could be prepared in both the *a* and *c* directions. Mounts were ground and polished, and the microstructure and crack profiles were examined at various different depth planes into the mounts. This allowed for an idea of what the time dependent material damage and cracking looked like without subsequent fatigue cycling. A schematic of the sectioning plan can be seen in Figure 63. Approximate section depths are 10, 260, 510, and 1010 μm respectively.

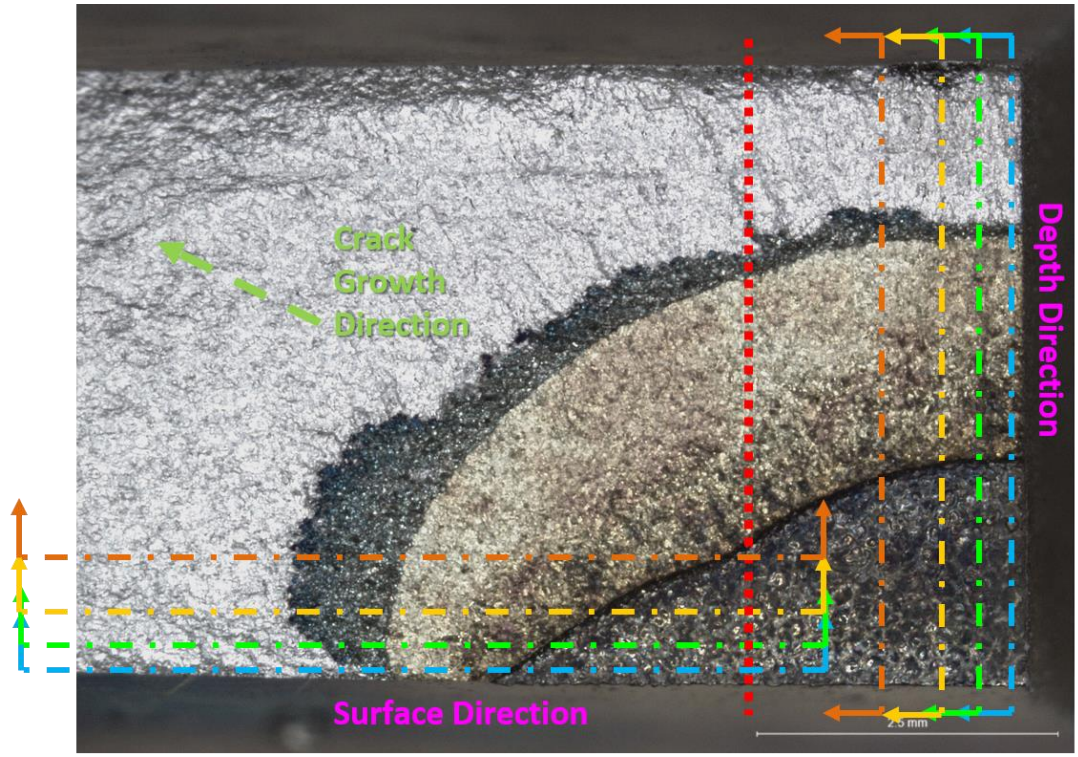

Figure 63: Sectioning plan for unbroken K-hold superimposed on the broken half's fracture surface.

In addition a mount was prepared in the surface direction of the broken half to look at the profile's microstructure and crack path. This mount was also sectioned on several planes to see how the profile evolved as more material was removed. Its sectioning plan can be seen below in Figure 64. Sectioning depths were approximately 10, 510, and 1010 μm respectively. The mount was also ground and polished to a 1 μm diamond slurry finish and was analyzed both unetched, and etched with Kalling's II.

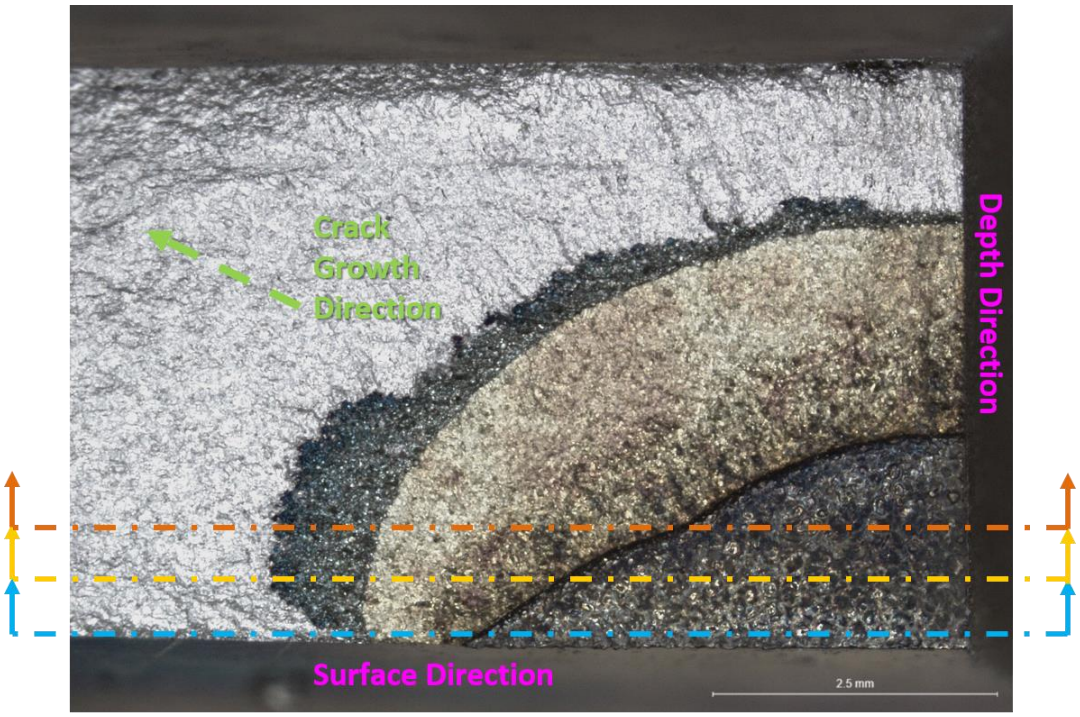

Figure 64: Sectioning plan for the profile sections of the interrupted K-hold experiment (718-KH-007) done on the broken half (pictured)

2.3.4. Isothermal High Temperature Testing

A fatigue test was prepared at 650 ºC to test the feasibility of marking techniques at high temperatures. In addition, shape and crack growth information could be extracted to evaluate the effect of acceleration due to material degradation in different directions. An a = 1.5 mm x c = 3.0 mm semi-elliptical notch was cut with EDM as described previously.

A maximum load of 60 kN was selected for the experiment to ensure that K values for the test stayed out of the threshold region of crack growth. Because of this, a maximum frequency of 2 Hz was used due to machine limitations at high forces. The base waveform used had a maximum of 60 kN, an R ratio of R=0.1, and a frequency of 0.1 Hz. The 0.1 Hz frequency was selected based on the information in Figure 38 in an attempt to keep the base crack growth completely within the intergranular regime.

Two marking methods were evaluated during the experiment. In the first method, an R=0.7 waveform was used to mimic the marking method found to be effective at room temperature in the crack transition portion of this project. In the second method, the base waveform with a maximum load of 60 kN and an R ratio of R=0.1 was used, but instead of a frequency of 0.1 Hz, a frequency of 2 Hz was used. This waveform was selected in order to land in the mixed inter/transgranular regime in Figure 38. In this way, a difference could be seen with either optical microscopy or SEM examination.

The sample was pre-cracked using a combination of max load 44 kN, R=0.1, 15 Hz fatigue cycles and 60 kN, R=0.1, 1-2 Hz cycles. The initial 0.1 Hz loading was started at too low a K value, and the crack did not grow at an acceptable rate. Because of this, room temperature cycling was resumed to enlarge the crack. These cycles along with the rest of the experiment can be seen in the loading history table below:

Table 18: Isothermal high temperature fatigue test loading history

Step Label	Max Load (kN)	Temperature (^{o}C)	R	Frequency (Hz)	Cycles
Initiation	44	RT	0.1	15	300000
Precracking	60	RT	0.1	1	10000
Slow 1	60	650	0.1	0.1	8297
Fast 1	60	650	0.1	2	40000
Back to Room Temp	60	RT	0.1	2	65028
Slow 2	60	650	0.1	0.1	1561
Fast 2	60	650	0.7	5	17136
Slow 3	60	650	0.1	0.1	1178
Fast 3	60	650	0.1	2	2225
Slow 4	60	650	0.1	0.1	972
Fast 4	60	650	0.7	5	6006
Slow 5	60	650	0.1	0.1	417
Final	60	RT	0.1	2	17422

The test concluded with a final application of room temperature cycling. This allowed for one final data point to be captured that can be seen on the fracture surface where the high temperature oxide ends.

2.3.5. TMF Testing

A thermal-mechanical fatigue test was devised to test how cracks grow in a more realistic scenario in surface flaws in Inconel 718. The CGIN718 material was prepared in a similar manner to the other high temperature tests and the initial notch had dimensions of a = 1.5 mm and c = 3 mm. The TMF spectrum was loosely based on the "fighter spectrum" developed by Radzicki [1] seen in Figure 48. However, the spectrum needed to be modified to ensure that K values remained above threshold and the total test run time could be completed in a functional amount of time.

The load and temperature spectrum can be seen below in Figure 65. The spectrum oscillated between 400 ºC and 650 ºC. This ensures that portions of the waveform would produce TAZ while others are below the 500 ºC threshold for TAZ formation. A peak load of 80 kN is applied during the cooler portion of the waveform, while a 70 kN hold is applied for 20 seconds during the high temperature portion.

The test began with a room temperature pre-cracking step to grow the crack to a = 2.8 mm, c = 4.5 mm to further increase the stress intensity during the TMF cycling. The TMF waveform was periodically interrupted with a 2 Hz sine wave with a loading ratio of R=0.1 and a maximum force of 60 kN. These formed visible marker bands on the fracture surface of the material to be used for measuring and recording the crack shape and location during the experiment. Once the TMF testing was complete, the temperature was lowered

to room temperature in order to create a last data point where the high temperature oxide ended. The complete loading history can be seen in Table 19 below.

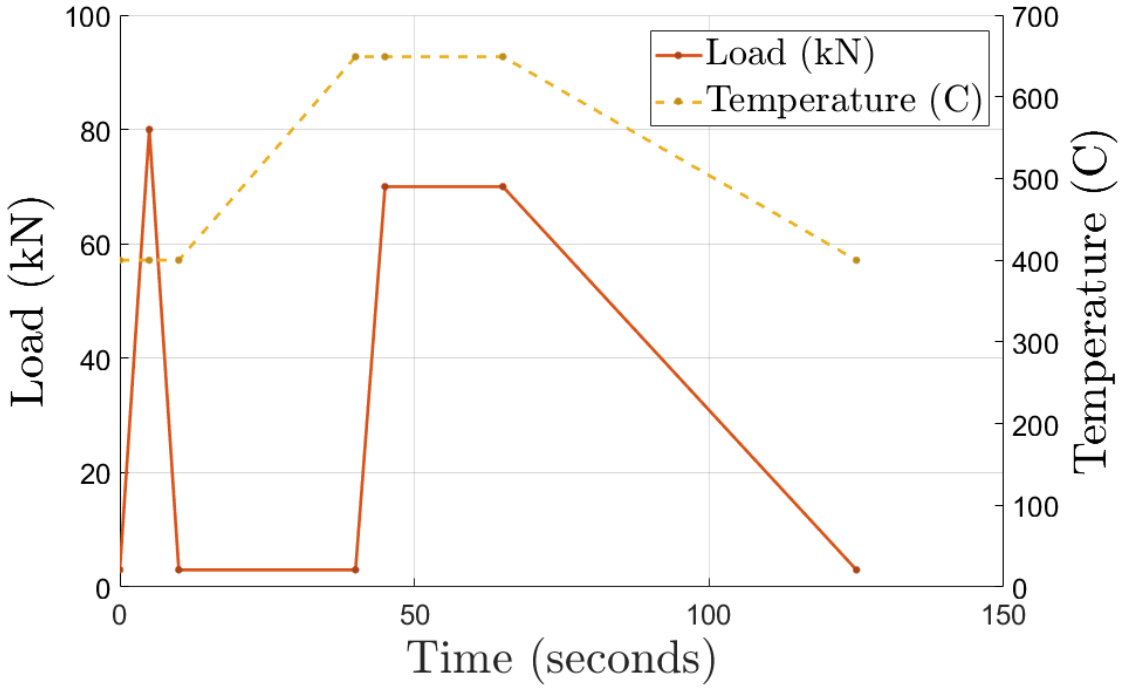

Figure 65: 125 second thermomechanical fatigue spectrum used in the TMF experiment

Table 19: TMF test loading history

Step Label	Max Load (kN)	Temperature (°C)	R	Frequency (Hz)	Cycles
Initiation	44	RT	0.1	15	300000
Pre-Cracking	44	RT	0.1	15	285000
TMF-1	80	TMF	TMF	TMF	791
Marker-1	60	650	0.1	2	3245
TMF-2	80	TMF	TMF	TMF	648
Marker-2	60	650	0.1	2	2078
TMF-3	80	TMF	TMF	TMF	661
Marker-3	60	650	0.1	2	2000
TMF-4	80	TMF	TMF	TMF	167
Final	60	RT	0.1	2	22507

2.4.Results

2.4.1. K-Hold Experiments

Although the K-hold experiments had varied loads, shapes, and conditions, there were some general similarities that could be found across them. Each (with the exception of the low K test 718-KH-002) grew an intergranular region which could be plainly seen with SEM examination. Many of them showed obvious oxidation in this region which if large enough had a distinct blue color that was immediately identifiable. This blue region is a mixture of time dependent crack growth and TAZ formation, and the size of this region varied with applied K and flaw shape.

Actual K values in the tables in the following sections were calculated using the Raju-Newman solutions. Crack lengths were measured from the fracture surfaces using the methods outlined in section 1.2.1.5.

2.4.1.1. 35 MPa√m Test

The 35 MPa√m test (718-KH-001) had the following attributes:

Table 20: Experimental parameters for 35 MPa√m (718-KH-001) test

Starting aspect ratio (*a*/*c*)	1
Fatigue precracking R=0.1 max load (kN)	35.34
Khold starting dimensions (mm)	*a*=3.0 *c*=3.98
Khold starting aspect ration (*a*/*c*)	0.75
Khold force (kN)	81.44
Khold stress intensity *a* direction (MPa√m)	34.6
Khold stress intensity *c* direction (MPa√m)	33.3
Khold temperature (ºC)	650
Khold duration (seconds)	3600
Maximum horizontal depth of intergranular region (mm)	4.7
Fatigue postcracking R=0.1 max load (kN)	50

This experiment was primarily constructed to set expectations for how K-holds work with semi-elliptical surface flaws and with the CGIN718 material. The resulting fracture surface can be seen in Figure 66 below:

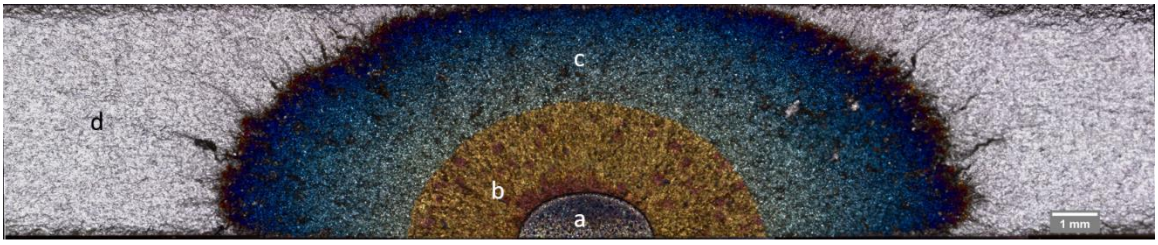

Figure 66: Optical micrograph of 35 MPa√m (718-KH-001) K-hold test. (a) EDM notch. (b) Room temperature pre-crack. (c) K-hold time dependent growth and subsequent room temperature cycling. (d) Room temperature fatigue cycling to failure.

In-situ observations with the Questar long focal length traveling microscope showed a relatively thick, black network of damage growing in a time dependent manner from the room temperature pre-crack. This growth was very different from what is usually seen at room temperature. A picture of the room temperature pre-crack in this experiment can be

seen below in Figure 67. The black damage network forms first at approximately 45º angles from the crack plane and then is progressively filled in with further damage (Figure 68). This time-dependent nature shows an early difference between the present work and Radzicki's SENT samples [1] where no time dependent growth was ever observed on the surface.

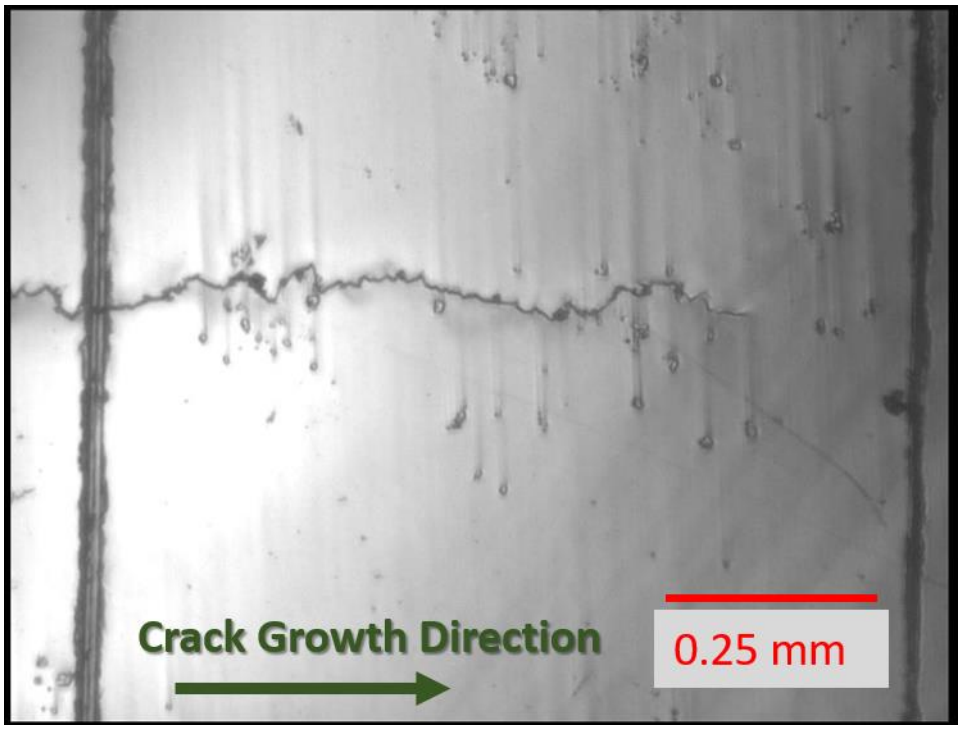

Figure 67: Typical form of room temperature crack growth as seen from the surface in CGIN718. Vertical marks were inscribed prior to testing at 1 mm intervals

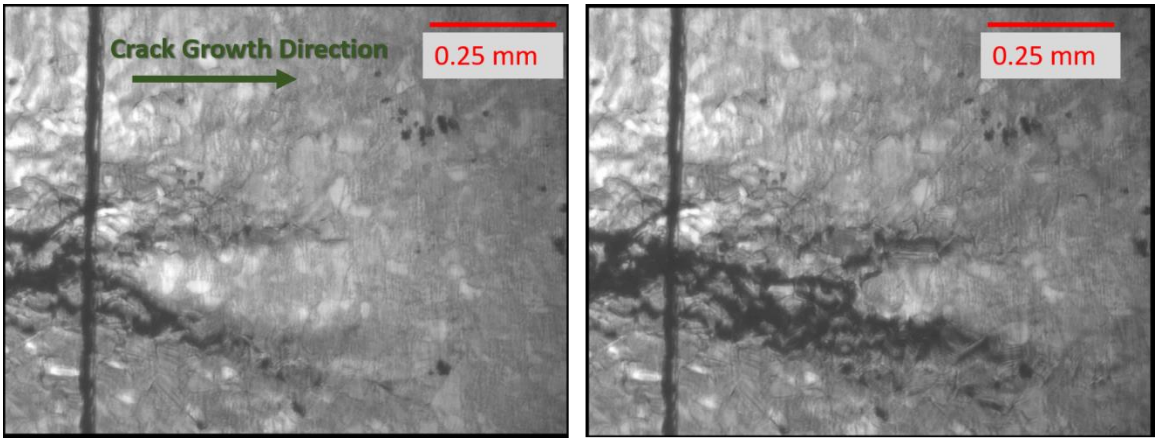

Figure 68: High temperature, time-dependent growth during 180 seconds of the 650ºC K-hold in experiment 718-KH-001

It is not always clear during in-situ observations where the crack plane is within the spreading damage, or if the crack has extended fully into this time-dependent region. As can be seen in Figure 69 below, in this case the crack plane grew along the upper black bar seen in Figure 68. In addition, the crack is not seen emerging from the damaged region immediately after the K-hold once room temperature cycling resumes. Eventually after many cycles the crack grows from this damaged region with the normal room temperature morphology.

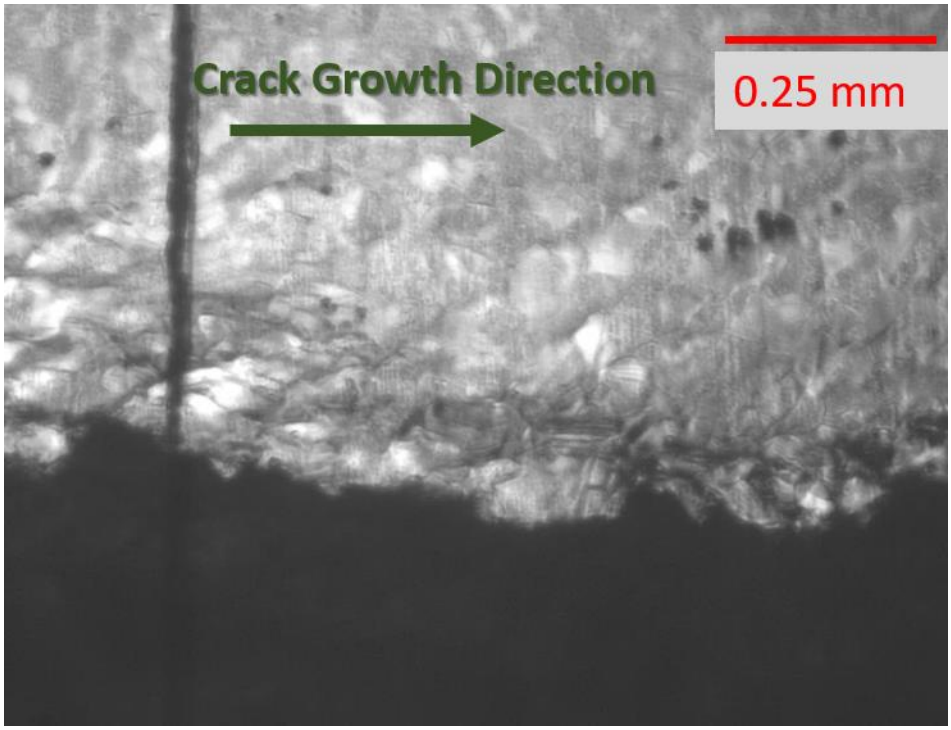

Figure 69: Experiment 718-KH-001 after fracture showing the final crack plane

In SEM it becomes very clear that there is a sharp transition from transgranular crack growth to intergranular growth at the start of the K-hold (Figure 70). The transgranular regime is dominated by fatigue striations appearing in a stair-step pattern. The intergranular regime has a "rock candy" like appearance where the smooth surfaces of individual grains can be easily seen.

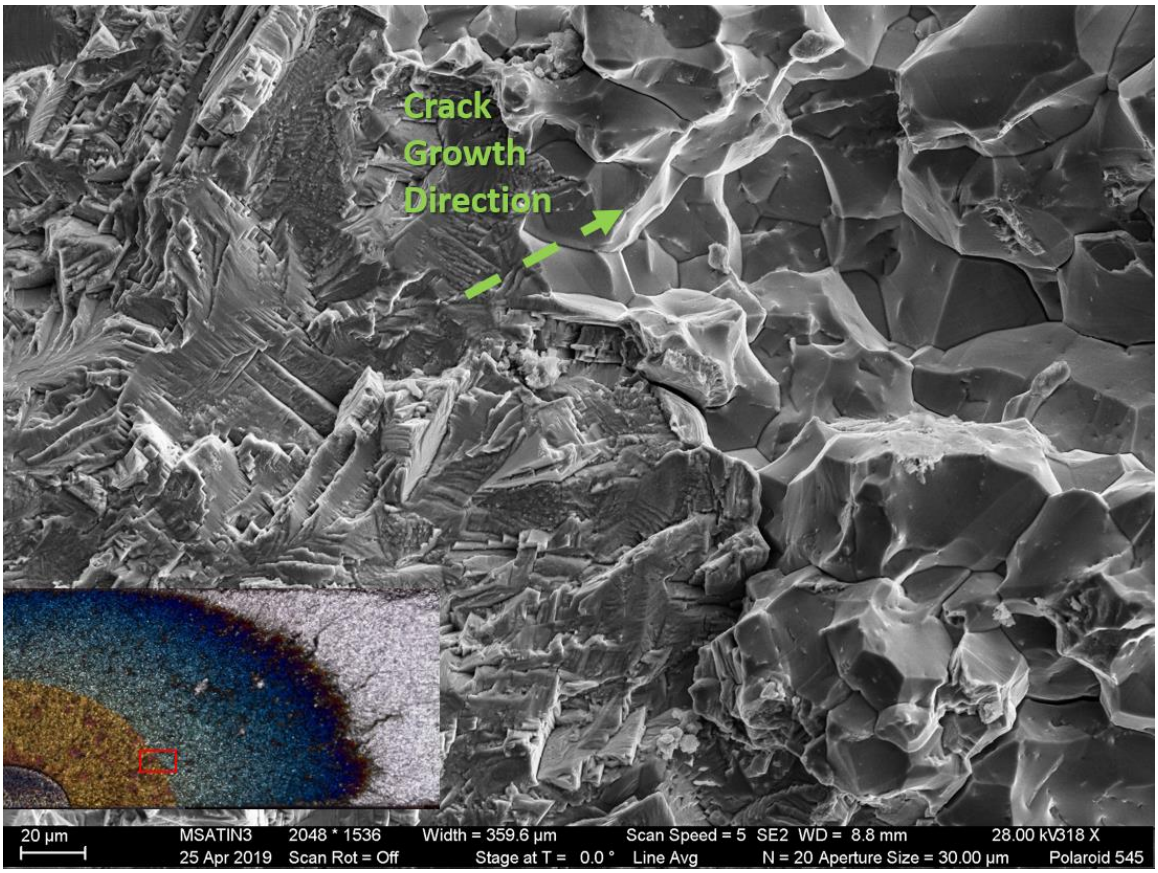

Figure 70: SEM fractograph of the start of the K-hold region. A clear dividing line between transgranular crack growth on the left and intergranular crack growth on the right can be seen.

Another noticeable feature is the undulating ridges and valleys propagating radially and becoming prominent in the K-hold region (Figure 71). A similar arrangement can be seen in Figure 46 with some notable differences. The ridge and valley pattern in this experiment seems to be more spaced out then in Radzicki's specimen. However the most noticeable difference is the lack of the transgranular flat ridges that were characteristic of the TAZ damage in Radzicki's SENT samples. The white step like features on the edge of the ridges are thought to be transgranular ligaments similar to what was seen by Lundstrom [45] in his work.

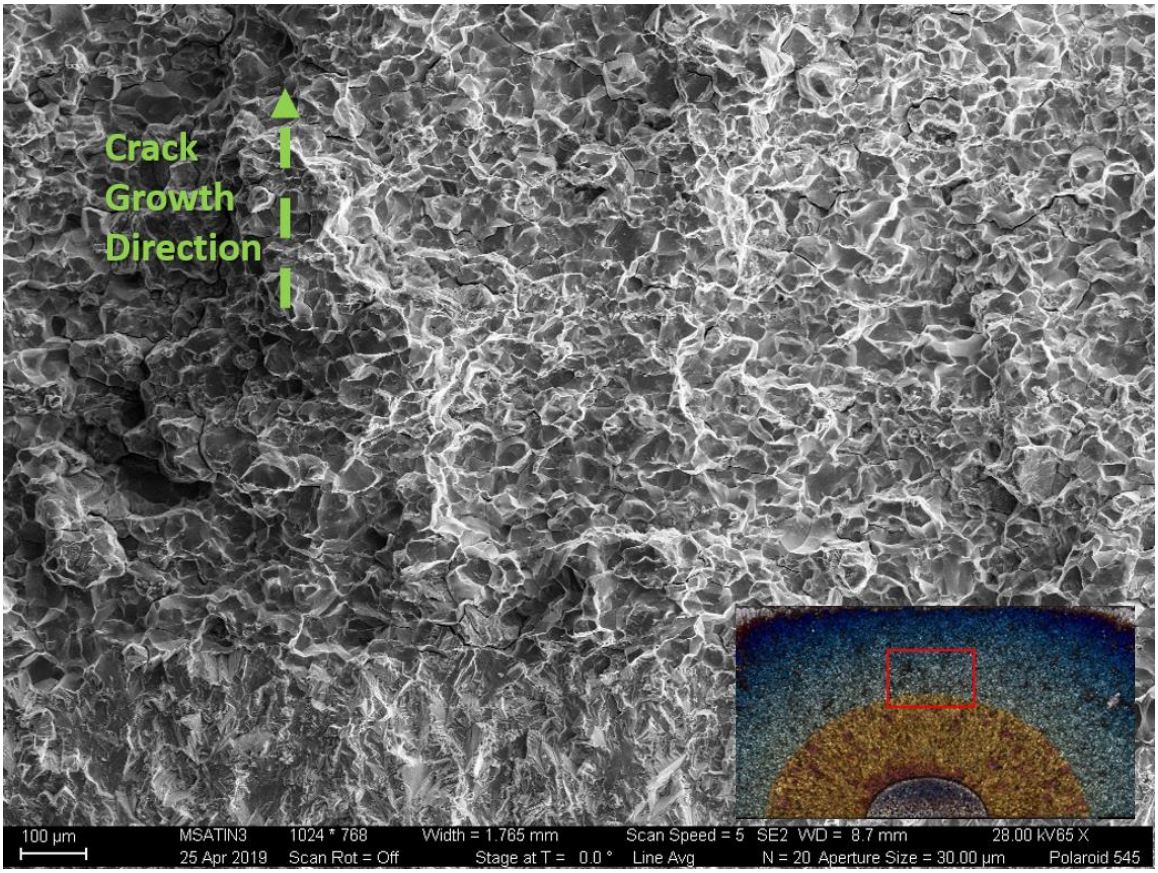

Figure 71: SEM fractograph of sample 718-KH-001 showing a radial ridge and valley pattern, that is nearly fully intergranular

In some cases these valleys and ridges extend into the post K-hold region, however they transition to fully transgranular in nature and do not seem to represent a channel for further oxygen diffusion.

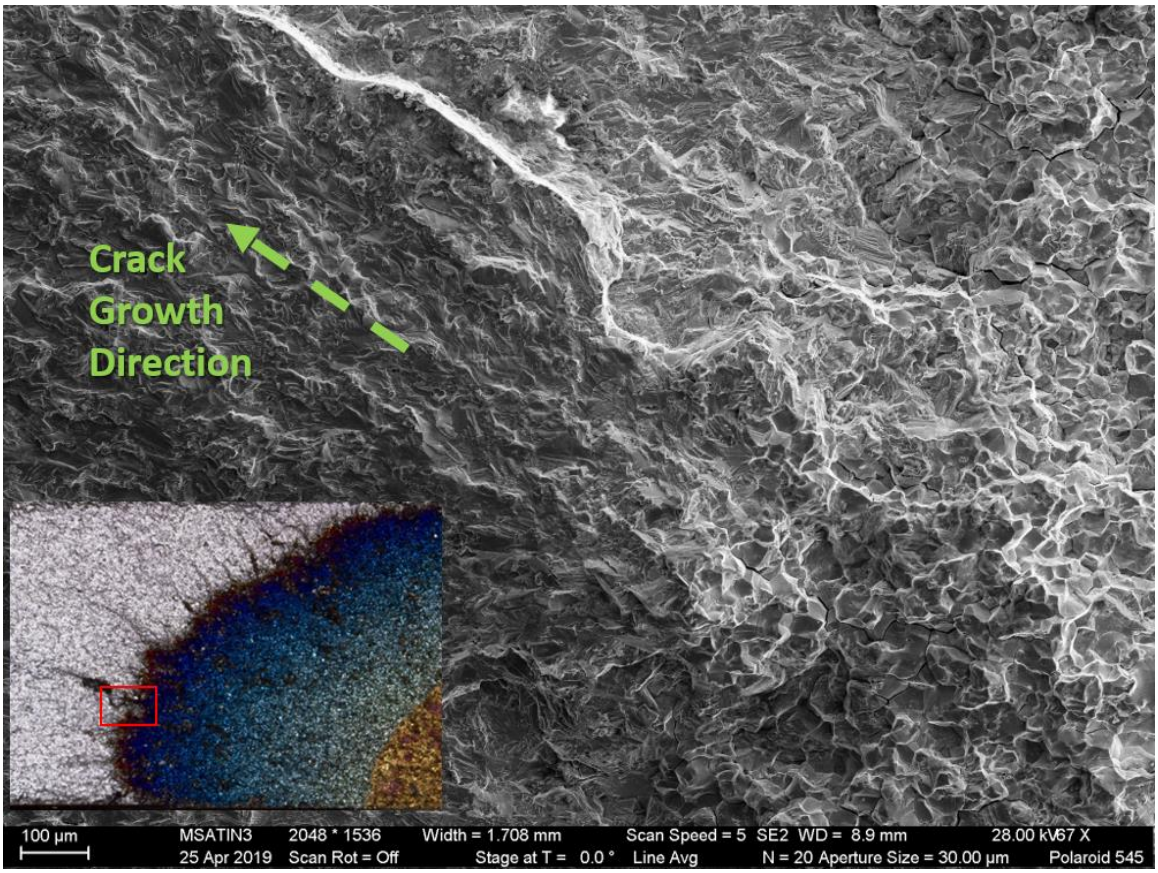

Figure 72: SEM fractograph of sample 718-KH-001 showing a ridge/valley combination extending from the intergranular region to the transgranular fatigue region

Islands and ligaments such as those seen by Lundstrom [45] in Figure 43 can be found close to the transition back to transgranular at the end of the K-hold region. Some examples are pictured in Figure 73 and Figure 74 below. Lundstrom theorized that this represents portions of the material that were not broken in a time dependent fashion and instead broke later during cycling.

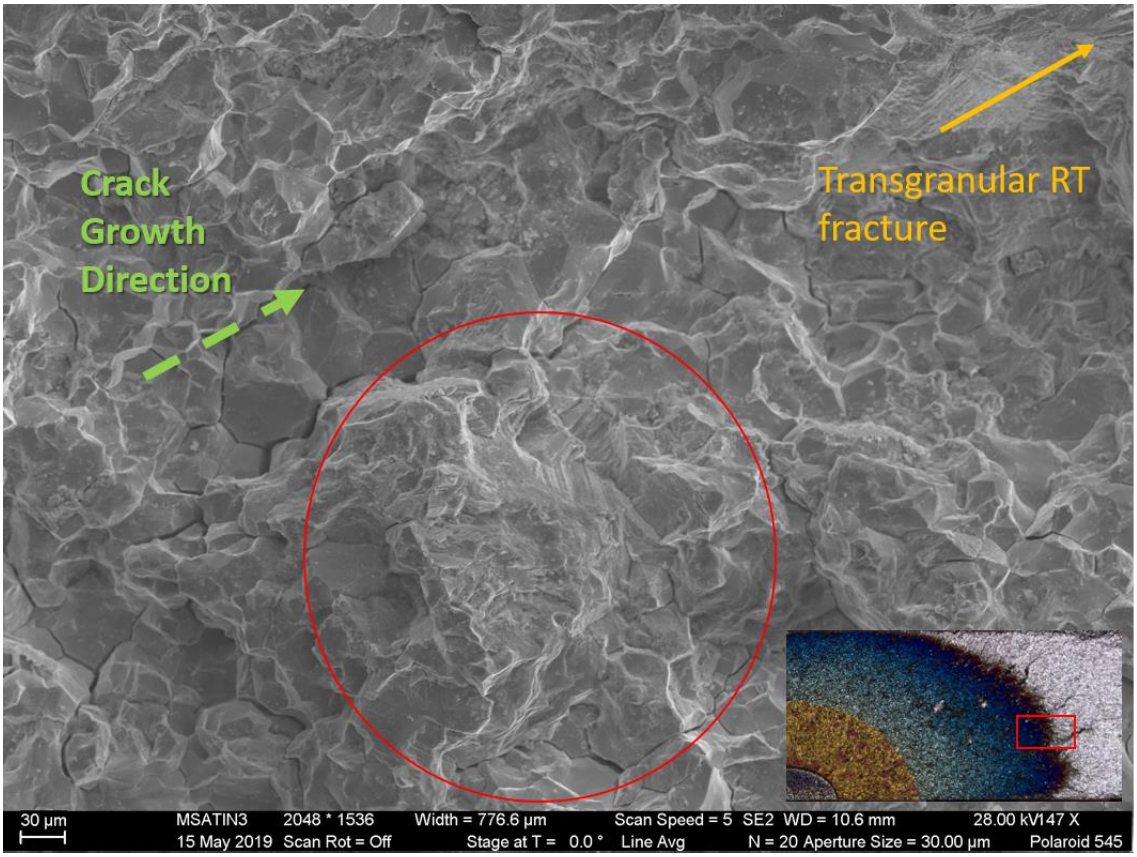

Figure 73: SEM fractograph of a transgranular island near the edge of the intergranular K-hold region in sample 718-KH-001

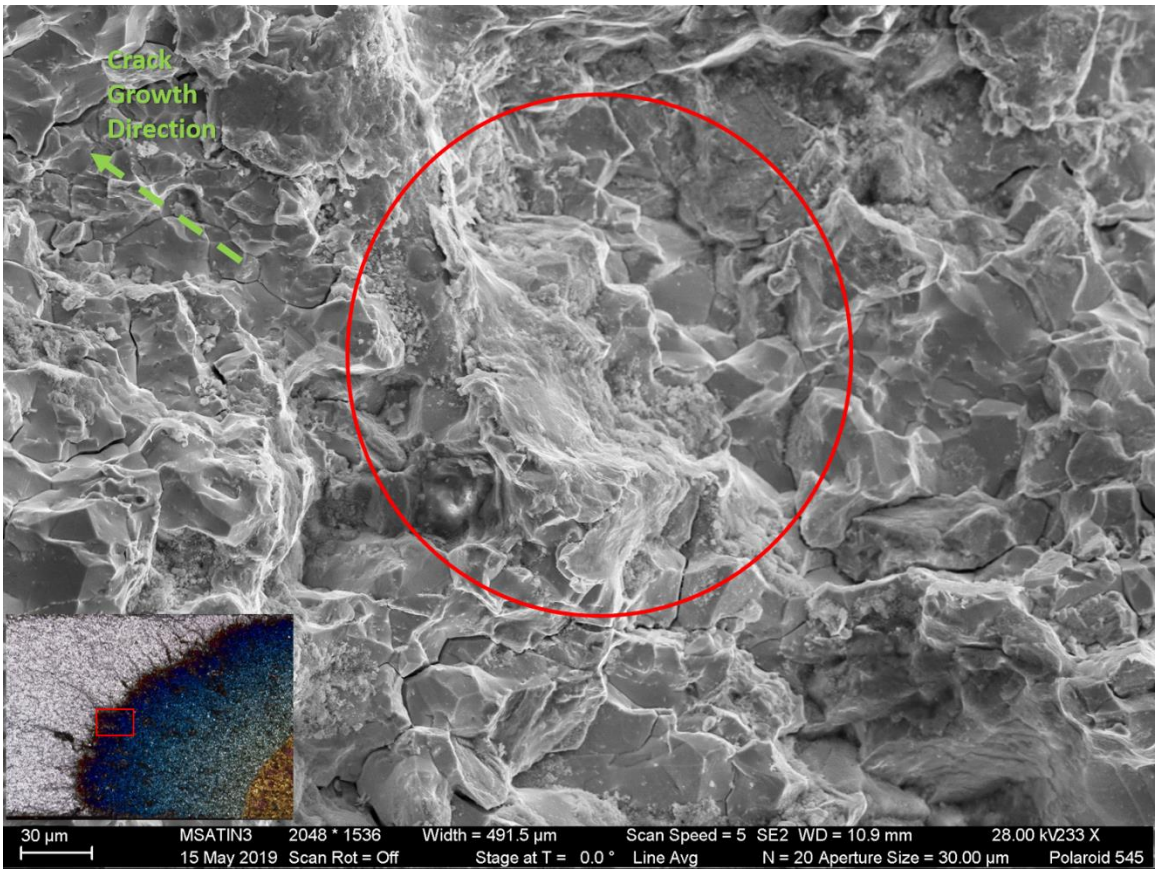

Figure 74: SEM fractograph showing a transgranular ligament within the intergranular field in sample 718-KH-001 near the edge of the K-hold region

2.4.1.2. Low K Test

The next test (718-KH-002) was designed to test the growth of the time dependent/damage region under low K conditions. The sample tested had the following parameters:

Table 21: Experimental parameters for the low K (718-KH-002) test

Starting aspect ratio (*a/c*)	0.5
Fatigue precracking R=0.1 max load (kN)	48
Khold starting dimensions (mm)	a=2.22 c=3.67
Khold starting aspect ration (*a/c*)	0.60
Khold force (kN)	48
Khold stress intensity a direction (MPa√m)	18.9
Khold stress intensity c direction (MPa√m)	15.6
Khold temperature (ºC)	650
Khold duration (seconds)	3600
Maximum horizontal depth of intergranular region (mm)	0
Fatigue postcracking R=0.1 max load (kN)	48
Marker Band	An additional R=0.7 marker band was inserted after 120,000 room temperature cycles at R=0.1 for 50,000 cycles before resuming R=0.1 until failure

Using Equation (20), the expected TAZ length would be 61 μm. However, the minimum K value used to calibrate Radzikci's TAZ model was 25 MPa√m, which is well above the values of 15.6 and 18.9 present in this sample. No blue or discolored region can be seen on the fracture surface outside of the room temperature pre-crack region Figure 75.

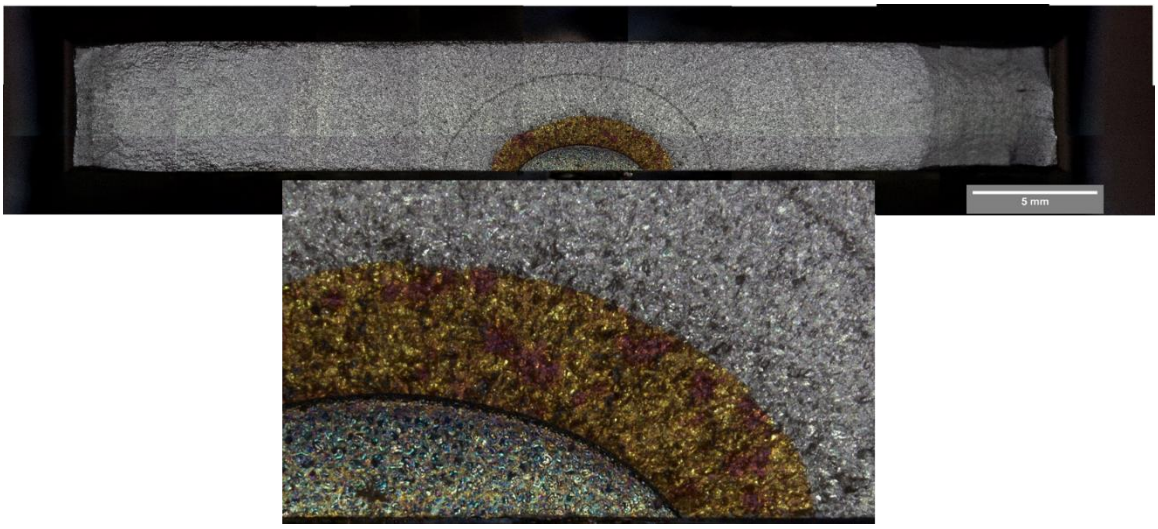

Figure 75: Optical fractograph of low K (718-KH-002) sample showing no visible intergranular or discolored region outside of the room temperature pre-crack

SEM was used to confirm that no intergranular region could be observed. A subtle difference in shading can be seen with a secondary emission detector between the oxidized room temperature pre-crack region and the room temperature post cycling region. No region could be observed in between that could be attributed to the K-hold. Because of this, it may be advisable to set a lower limit or threshold for a stress intensity below which no TAZ is expected to form even at high temperatures.

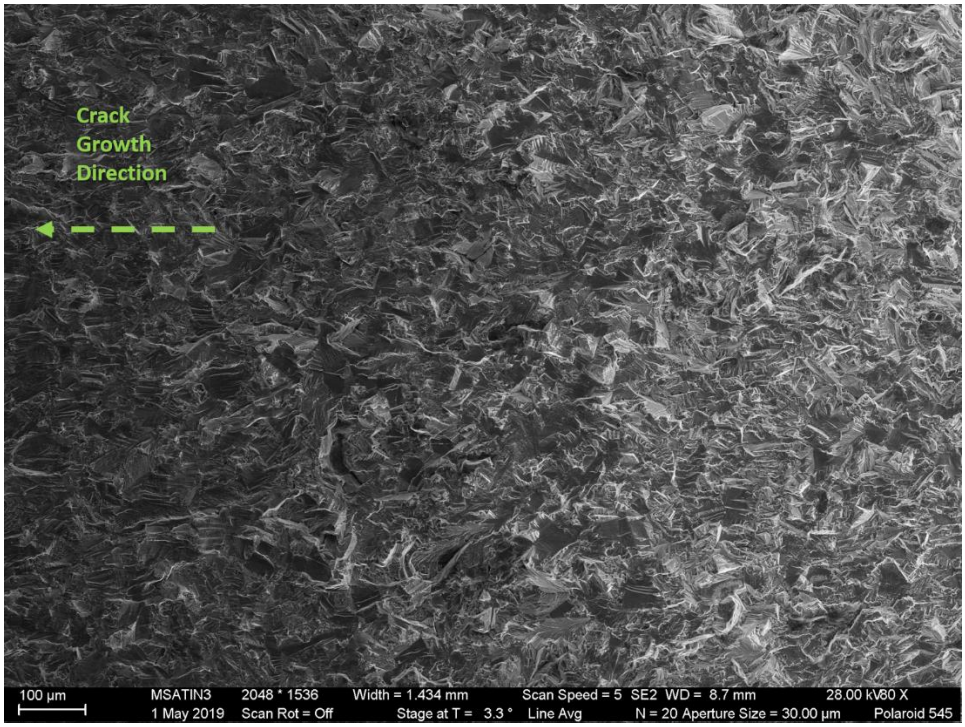

Figure 76: SEM fractograph of the low K (718-KH-002) sample. The lighter region on the right is the oxidized room temperature pre-crack region.

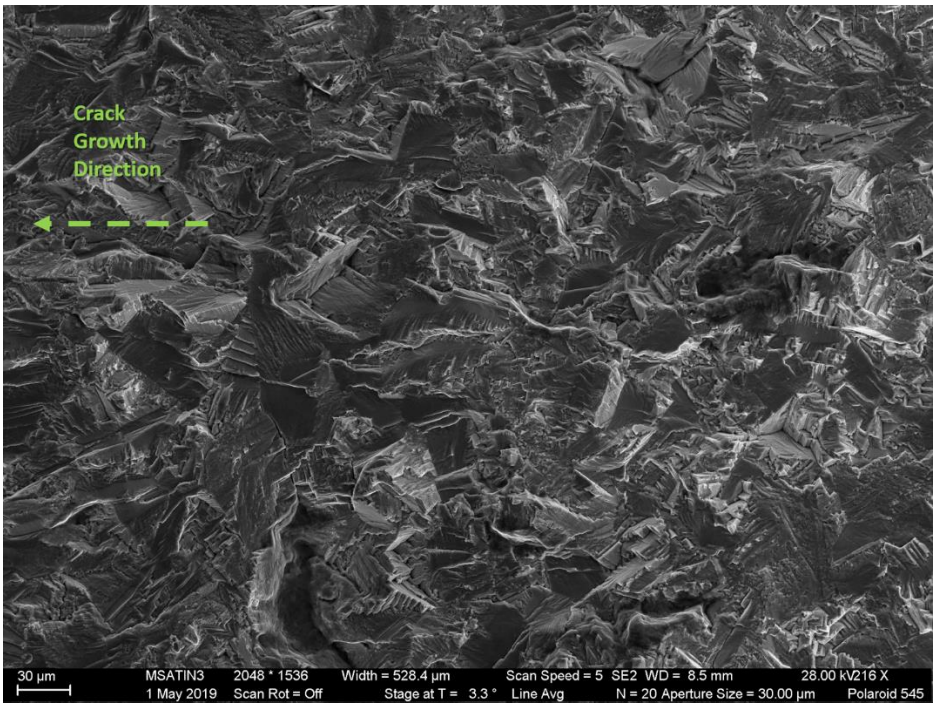

Figure 77: A higher magnification image of the interface between the pre-crack and post-crack regions with no obvious intergranular region present in sample 718-KH-002

2.4.1.3. 30 MPa√m Test

The 30 MPa√m test (718-KH-003) appeared to be right at the threshold for the intergranular phenomenon to occur. It had the following attributes:

Table 22: Experimental parameters for the 30 MPa√m (718-KH-003) test

Starting aspect ratio (*a/c*)	0.5
Fatigue precracking R=0.1 max load (kN)	48
Khold starting dimensions (mm)	*a*=2.15 *c*=3.58
Khold starting aspect ration (*a/c*)	0.60
Khold force (kN)	82
Khold stress intensity *a* direction (MPa√m)	31.7
Khold stress intensity *c* direction (MPa√m)	26.0
Khold temperature (ºC)	650
Khold duration (seconds)	3600
Maximum horizontal depth of intergranular region (mm)	0.22
Fatigue postcracking R=0.1 max load (kN)	48

The in-situ surface observation of this material showed a much smaller area of effect then what was seen in Figure 68. The "bifurcation" seen in Figure 78 is the result of the much larger plastic zone at 82 kN 650 ºC then the preceding plastic zone formed at 48 kN at room temperature. This bifurcation grew very slightly and darkened as the experiment proceeded. Upon subsequent cycling the fatigue crack did not emerge from the tips of the damaged area, but instead from the root of the bifurcation, growing through the center of the area.

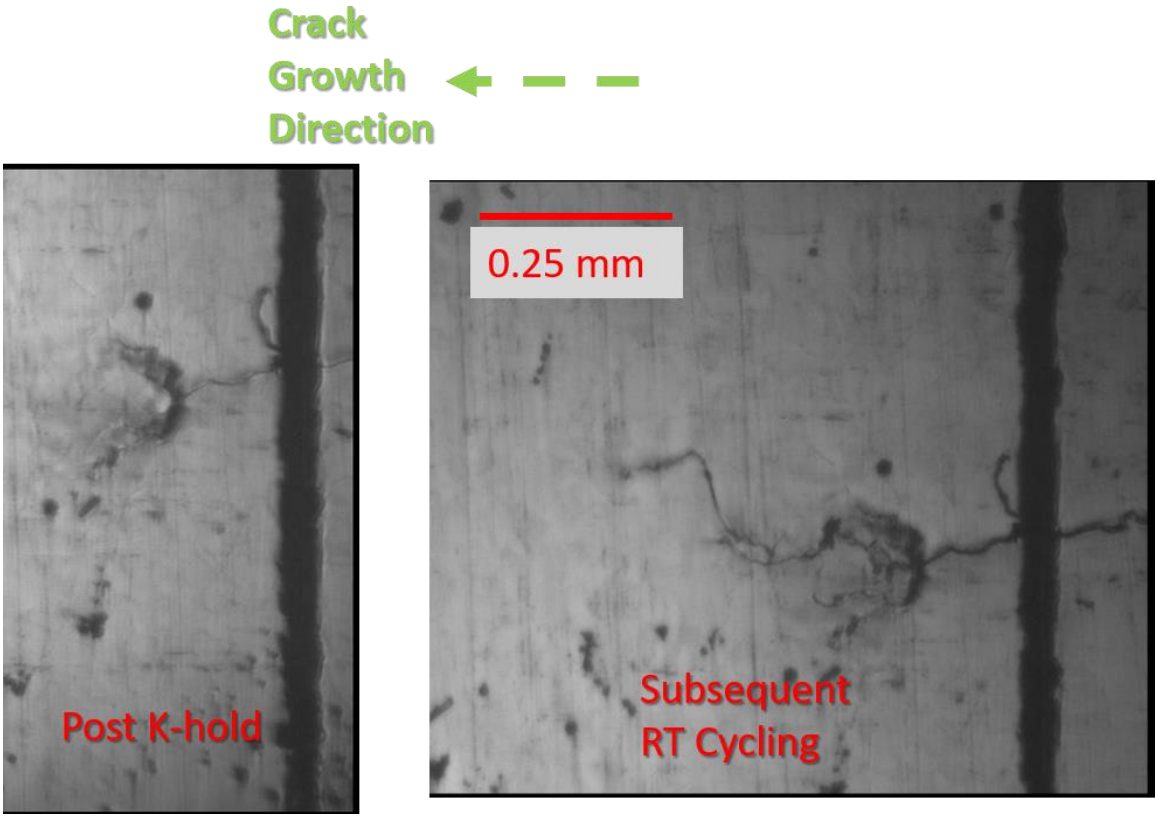

Figure 78: In-situ observation of the 30 MPa√m (718-KH-003) experiment showing a much smaller area of effect from the K-hold

Careful examination of the fracture surface (Figure 79) shows a very thin band of darkened material around the room temperature pre-crack region. That area is surrounded by non-uniform dark grey material that represents a sloped area where the crack plane changes from the pre-crack level to the post K-hold level.

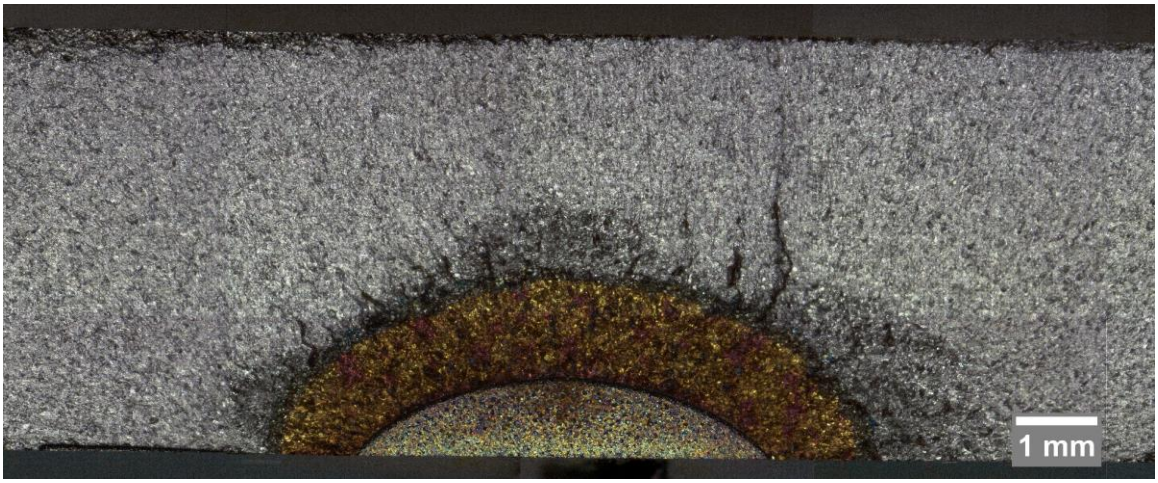

Figure 79: Optical fractograph of the 30 MPa√m (718-KH-003) sample

SEM examination reveals that the darkened material is a thin ribbon of intergranular material with a maximum thickness of about 220 μm (Figure 80 and Figure 81). In certain sections, especially where the intergranular region is thin, transgranular bridges can be seen that extend across the area such as Figure 82. These bridges are relatively rare. The areas that appear as dark grey in optical microscopy also appear slightly different in the SEM. However, these regions are still transgranular in nature and likely show contrast in secondary emission due to their orientation.

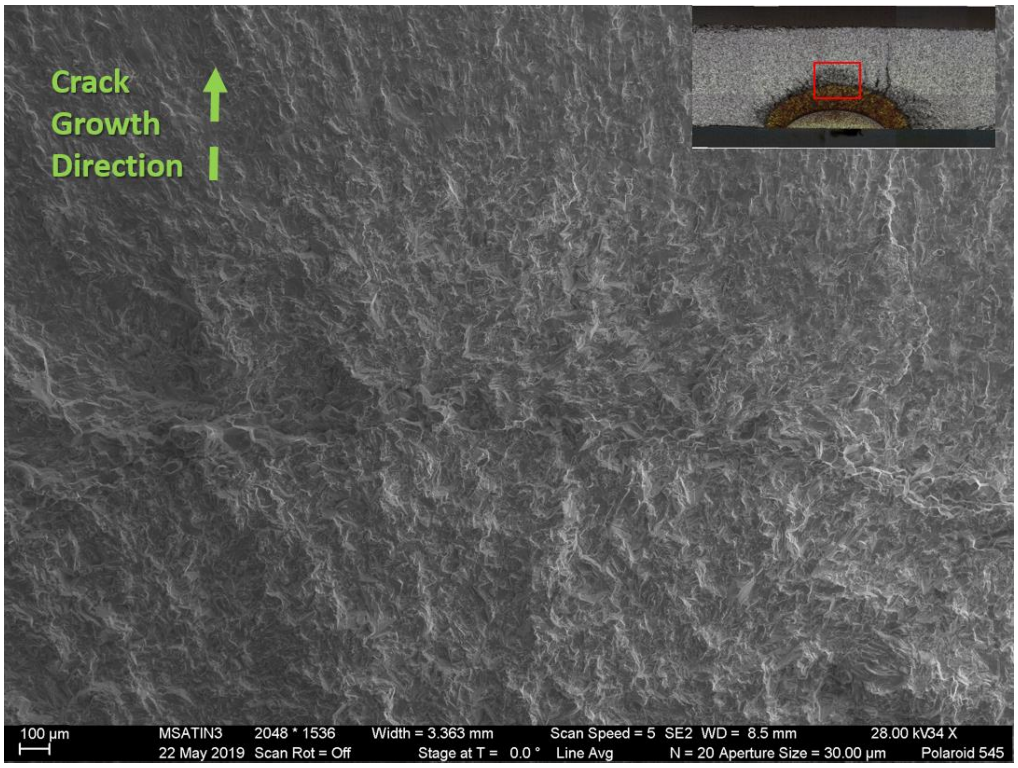

Figure 80: SEM fractograph of the 30 MPa√m (718-KH-003) showing a thin ribbon of intergranular fracture between two transgranular regions.

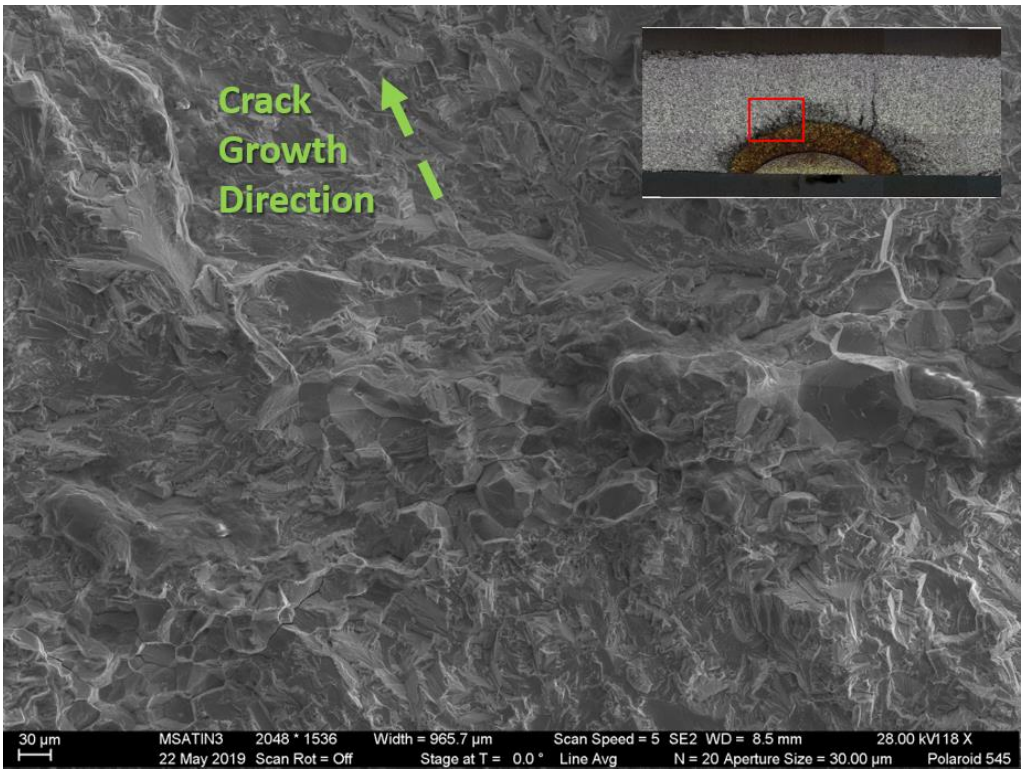

Figure 81: SEM fractograph of the 30 MPa√m (718-KH-003) showing that the intergranular region is 2-5 grains wide

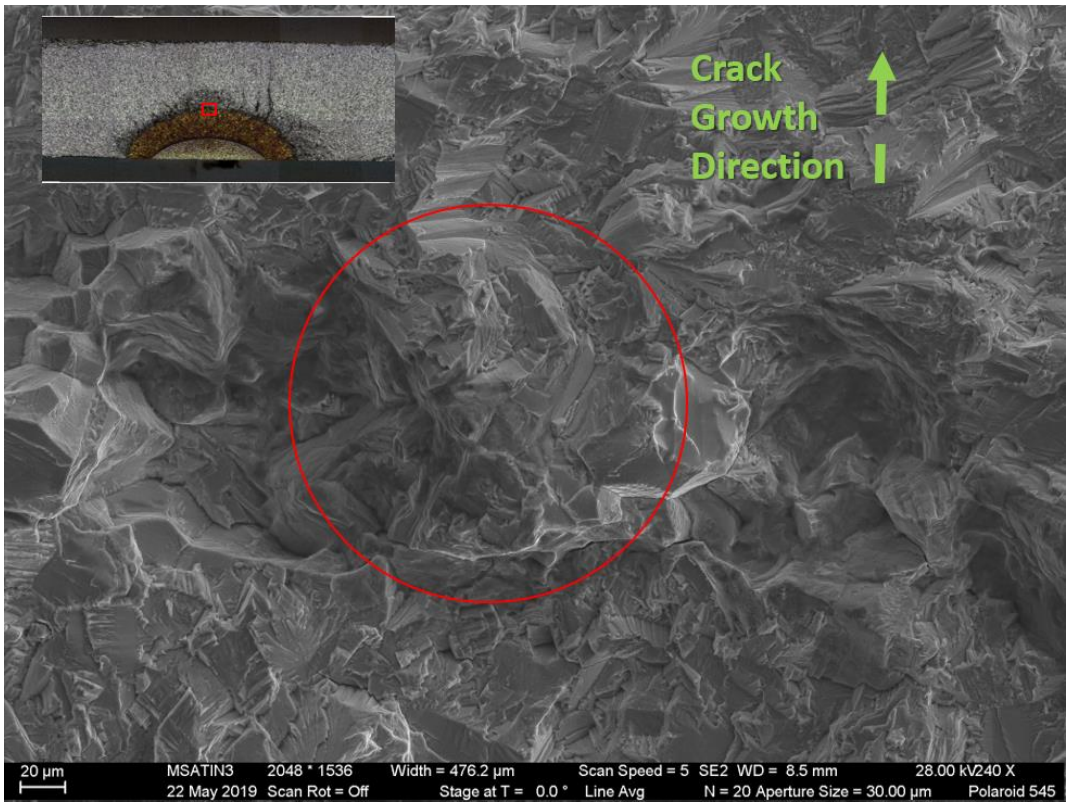

Figure 82: SEM fractograph of the 30 MPa√m (718-KH-003) showing transgranular bridging across the intergranular region

2.4.1.4. High K Test

The fourth experiment (718-KH-004) was aimed at looking at the effects of a relatively high K value. In order to achieve this the crack was grown past the breakthrough point and was effectively half way to becoming a center through crack (Figure 83). In addition the crack took on a noticeably asymmetric character as it grew to longer crack lengths. Because of this its crack length is represented by the average length at midthickness, and aspect ratios are represented by *a'* instead of *a* using the definition pictured in Figure 3. The parameters for the experiment were:

Table 23: High K (718-KH-004) experimental parameters

Starting aspect ratio (*a/c*)	1
Fatigue precracking R=0.1 max load (kN)	55
Khold starting dimensions (mm)	*c*=6.79
Khold starting aspect ration (*a/c*)	0.71
Khold force (kN)	55
Khold stress intensity *a* direction (MPa√m)	N/A
Khold stress intensity *c* direction (MPa√m)	41.8
Khold temperature (ºC)	650
Khold duration (seconds)	3600
Maximum horizontal depth of intergranular region (mm)	2.2
Fatigue postcracking R=0.1 max load (kN)	55

Figure 83: High K (718-KH-004) sample showing K-hold initiated after breakthrough

As can be seen in Figure 83 above, the crack was not only asymmetric in size, but also in character in the K-hold zone. On the left, the blue color can be seen extending all the way to the free surface with a slight ducking in at the end of the K-hold. On the right, the blue zone seems to completely miss the surface ducking in almost all the way to the room temperature pre-crack region. This observation shows a consistency with Radzicki's observations where TAZ did not form at the free surfaces in SENT specimens. The in-situ surface observations are also different. The left side (Figure 84) begins with the bifurcation pattern (180 seconds pictured), but then fills in and grows a black network like what was seen in Figure 68 (1020 seconds pictured). On the right side, the bifurcated pattern forms

but instead of growing into a complete network, the damage propagates as a light feathery pattern from the tips of the forks.

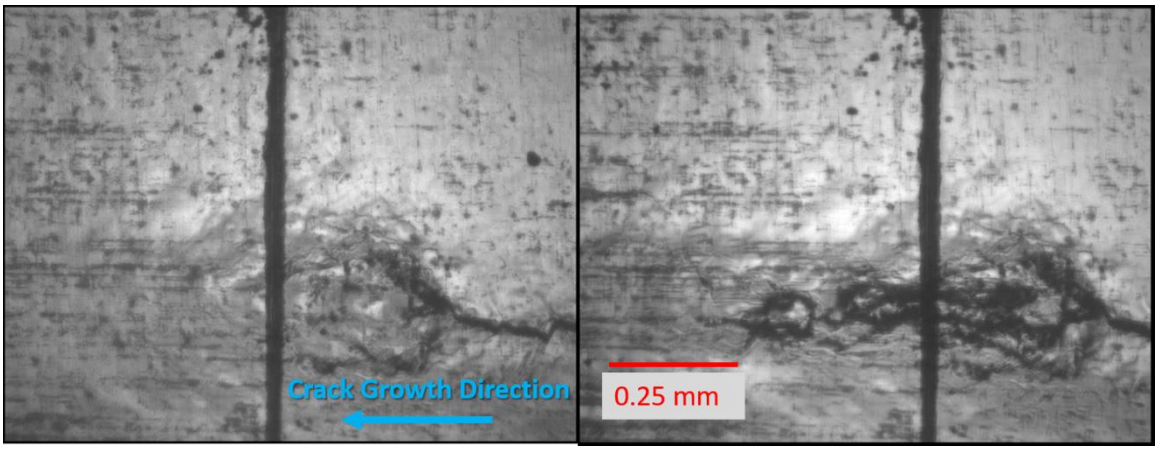

Figure 84: In-situ surface measurements of time-dependent crack extension on the left side of the high K (718-KH-004) experiment after 180 seconds (left) and 1020 seconds (right)

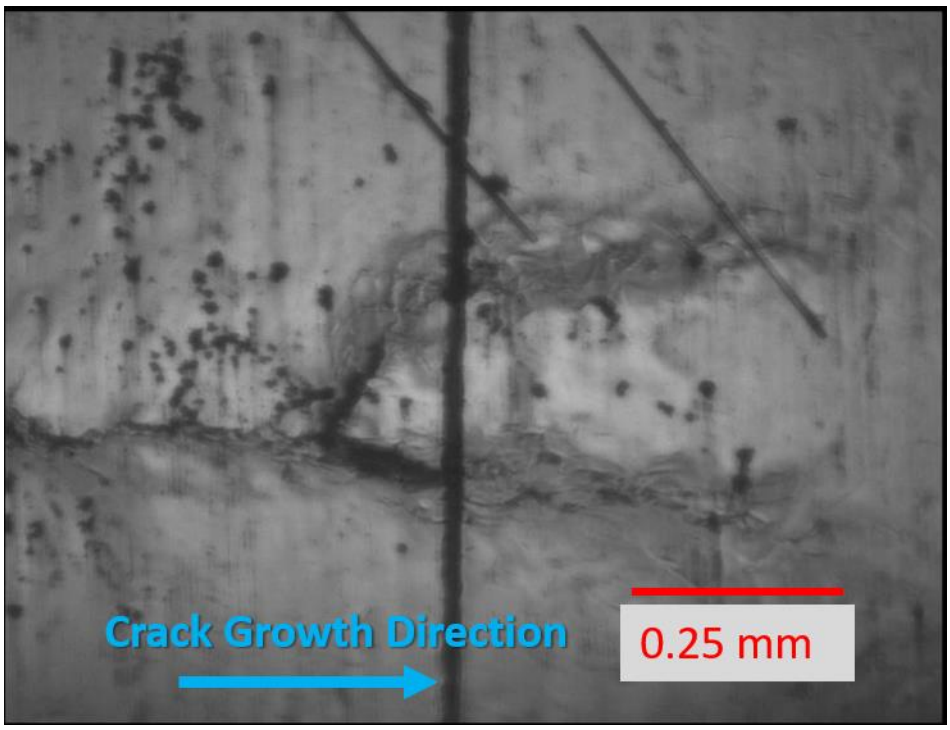

Figure 85: In-situ surface measurements of time-dependent crack extension on the right side of the high K (718-KH-004) experiment after 3600 seconds

Surface measurements were made with the long focal distance traveling microscope during the K-hold test in order to record the rate of time-dependent damage accumulation. Since this type of damage is difficult to measure to a unique point like a room temperature crack tip, the measurements were made using the maximum horizontal distance to the edge of the darkened region. These measurements are recorded in Figure 86 and range in growth rate from 2.22×10^{-4} to 6.07×10^{-4} mm/sec.

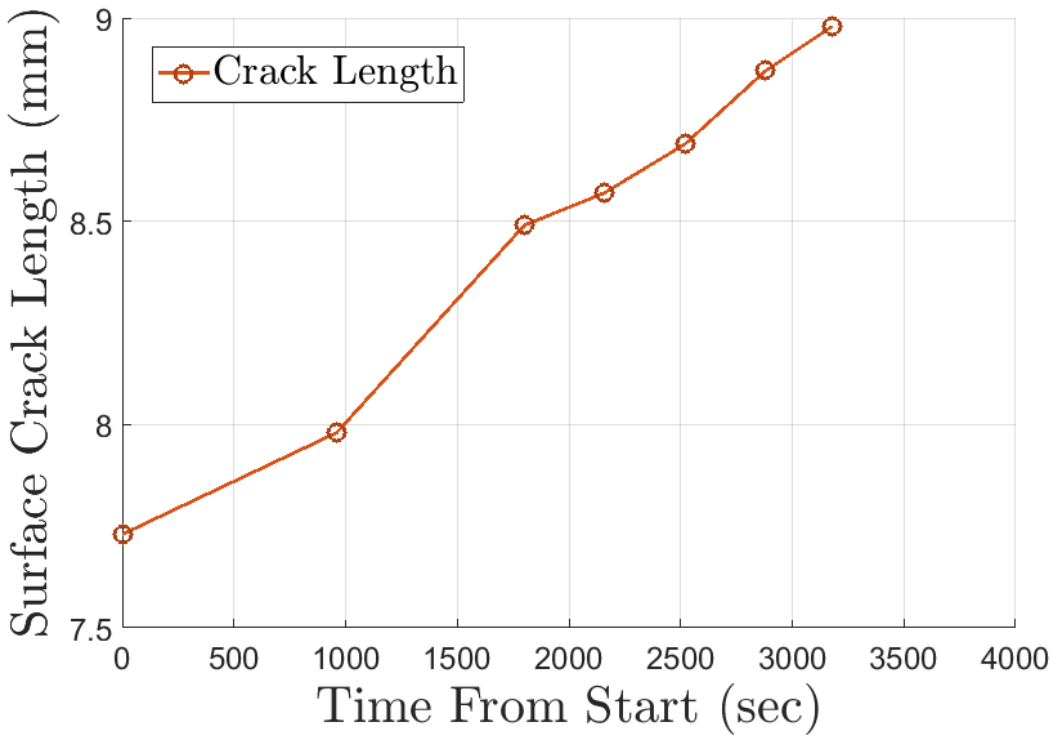

Figure 86: Time-dependent growth from in-situ crack growth observations on the surface of the high K (718-KH-004) K-hold sample

SEM examination shows the typical region of intergranular growth with some notable features. In Figure 87 the region in blue shows what appears to be a shear lip (region of slant growth) reaching back nearly all the way to the room temperature pre-crack region. In addition a well-defined ridge and valley pattern can be seen crossing the trans

and intergranular regions in a radial pattern. One of these regions highlighted in red is shown in Figure 88. Upon close examination, it becomes obvious that these features extend through the K-hold region and into the rest of the crack plane but appear much more obvious in the intergranular region. It can also be seen that although there is a sharp transition from transgranular to intergranular at the start of the K-hold zone, the transition and the end of the K-hold zone shows pockets of intergranular fracture adjacent to pockets of transgranular fracture.

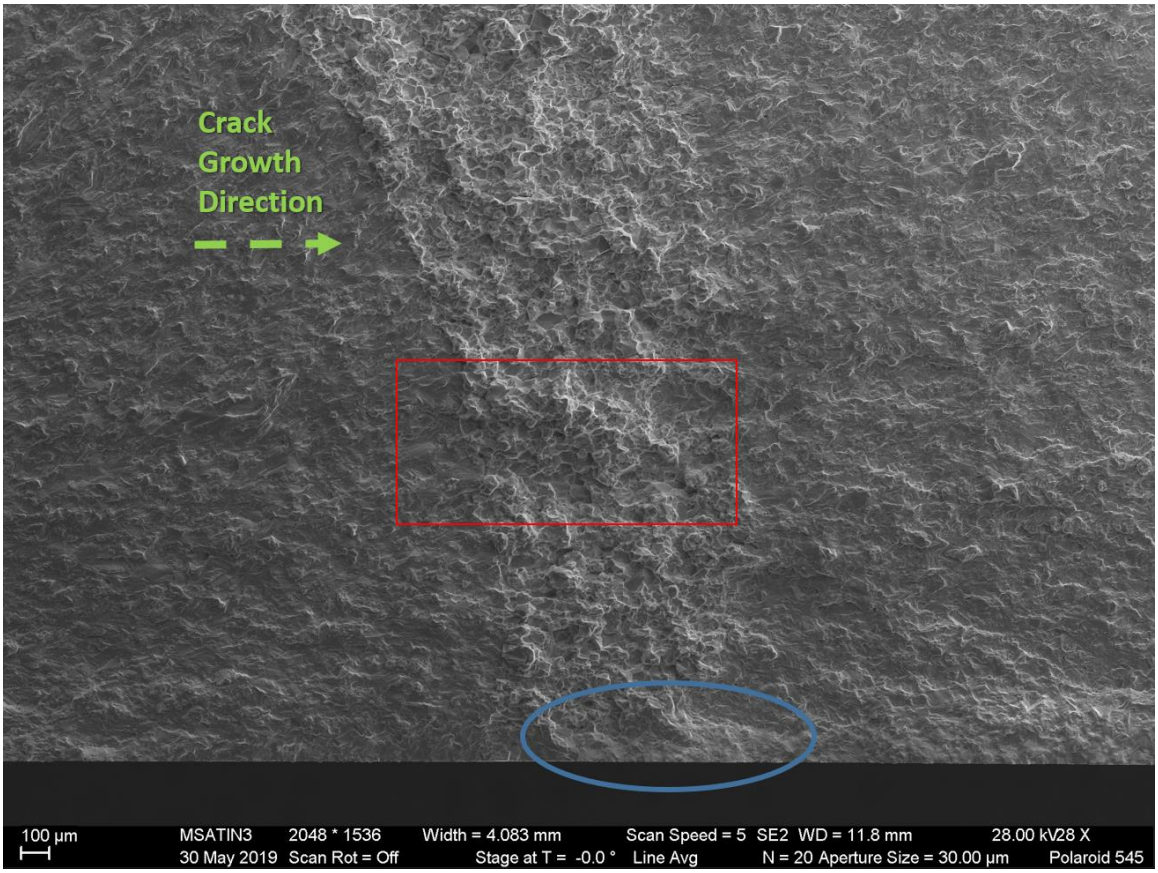

Figure 87: SEM fractograph of the high K (718-KH-004) sample's right side showing the field of view of Figure 88 in red and the surface lip in blue

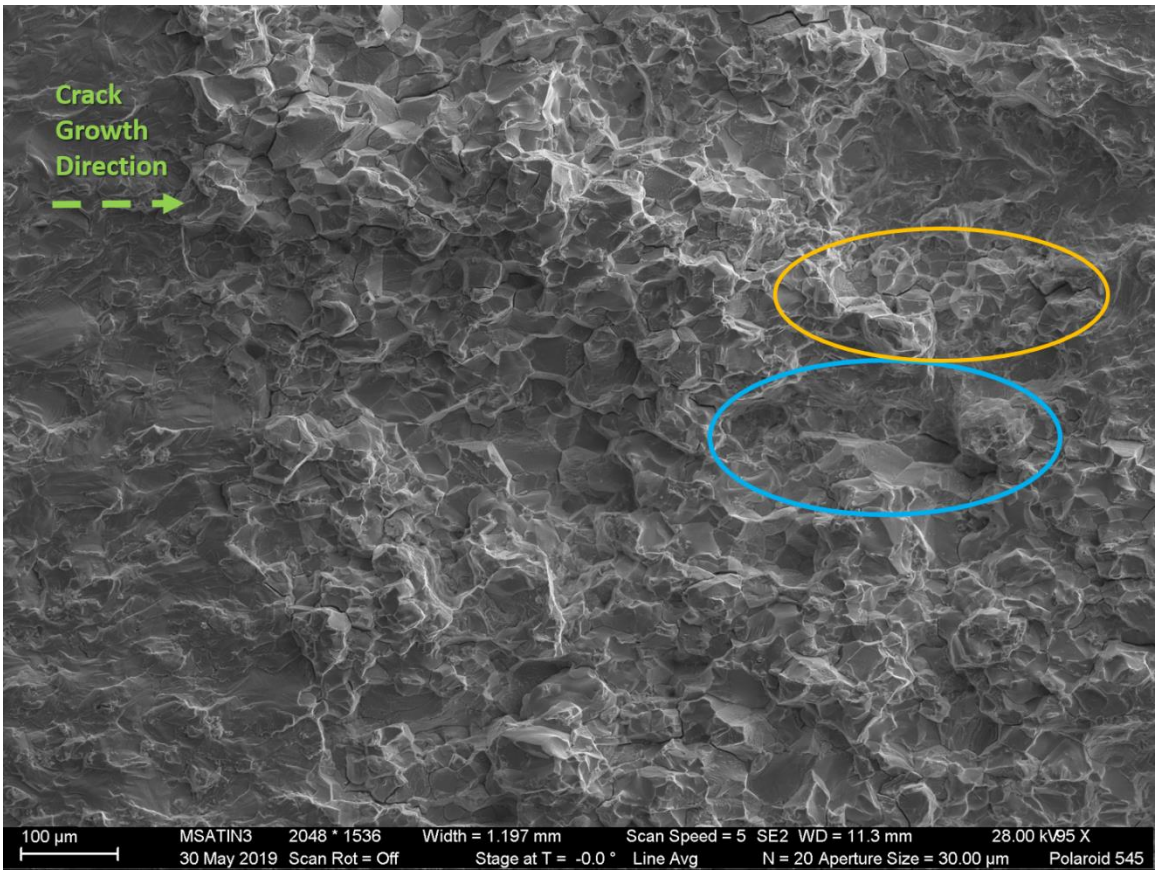

Figure 88: SEM fractograph of the high K (718-KH-004) sample showing a valley feature extending through the K-hold region. Regions of mixed character can be seen at the end of the K-hold with transgranular (blue) and intergranular (orange) regions adjacent

2.4.1.5. SENT K-hold Test

The first four K-hold tests had failed to replicate the signature pattern of Radzicki's TAZ region pictured in Figure 46 with intergranular valleys separated with transgranular ridges. A test was devised to see if the pattern was geometry dependent. All of Radicki's samples were single edged notch tension (SENT) cracks. The SENT test (718-KH-005) had the following parameters:

Table 24: Experimental parameters for the SENT (718-KH-005) K-hold test

Fatigue precracking R=0.1 max load (kN)	35
Khold starting dimensions (mm)	*a*=4.8 (furthest extents as measured from EDM notch)
Khold force (kN)	35
Khold stress intensity (MPa√m) at start	27.7
Khold temperature (ºC)	650
Khold duration (seconds)	3600
Maximum horizontal depth of intergranular region (mm)	4.1
Fatigue postcracking R=0.1 max load (kN)	35

Within the 3600 seconds of the K-hold, a very large area of damage formed resulting a very large (4.1 mm wide) intergranular zone (Figure 89). There is some amount of ducking in the surface at the maximum extent of the K-hold zone with a maximum difference of about 700 μm in width when compared to the center.

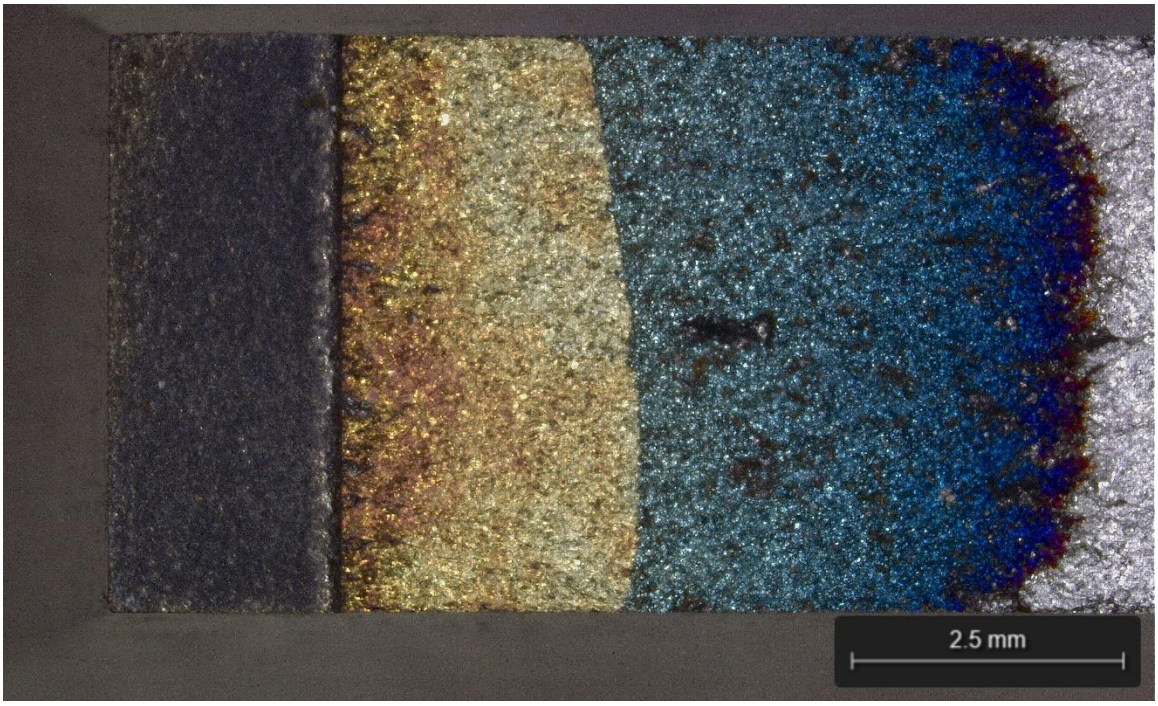

Figure 89: Optical fractograph of the SENT (718-KH-005) K-hold test

SEM examination found the typical intergranular fracture morphology expected in this type of K-hold region. A few notable features can be seen in Figure 90. In red is an abnormally large island of transgranular fracture surrounded by intergranular fracture. In addition colorless regions can be seen in Figure 89 which correspond to rounded intergranular nubs surrounded by pits. One of these is highlighted in blue in Figure 90. It is probable that these regions represent relatively large amounts of material that fell out of the surface after the K-hold had completed. This is why they appear as non-oxidized material and pits in SEM.

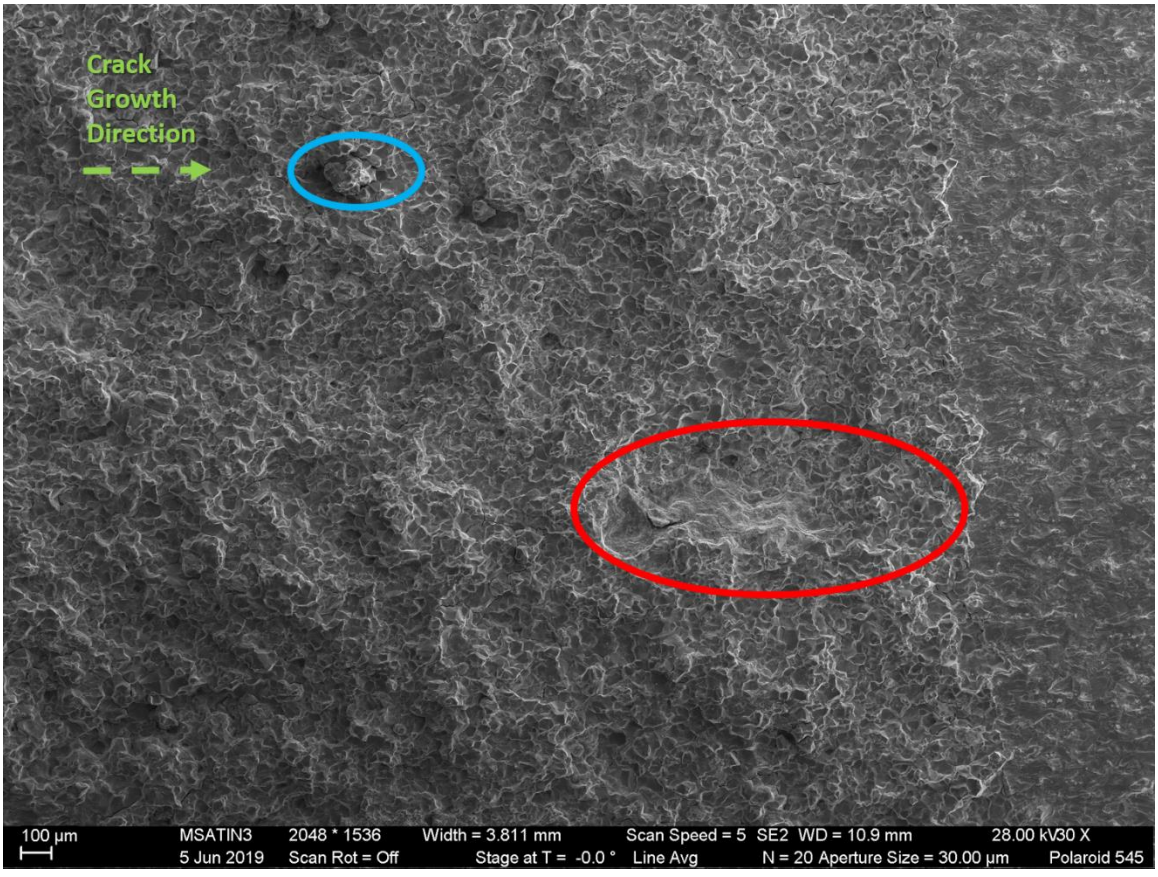

Figure 90: SEM fractograph of the trailing edge of the K-hold region in the SENT (718-KH-005) sample

From these results it is evident that the characteristic morphology seen in Radzicki's work is not purely driven by the SENT configuration. A large amount of time-dependent growth was observed in-situ from surface measurements during the test. This too had the black network morphology that accompanies this amount of time-dependent growth and is charted in Figure 91. The growth rate ranged from $5.00x10^{-4}$ to $3.61x10^{-3}$ mm/second. This is faster than the rates recorded in the previous sample (718-KH-004) even though the applied stress intensity was lower. This suggests that this time dependent behavior is not purely K-dependent and may be partially driven by the stress state at the crack tip. This is an idea that will be carried forward and may be related to why Radzicki did not observe time-dependent crack growth.

Although the SENT geometry was tested to be comparable to Radzicki's specimens, there were still major differences in materials and specimen dimensions. As will be discussed later, the TAZ phenomenon is a grain boundary effect, resulting in different behavior in FGIN718 and CGIN718. In addition, this test had a much larger specimen thickness then the thin plates used in Radzicki's work. Since TAZ has been shown to be somewhat dependent on stress state, this difference in thickness could also play an important role in why a different behavior was seen.

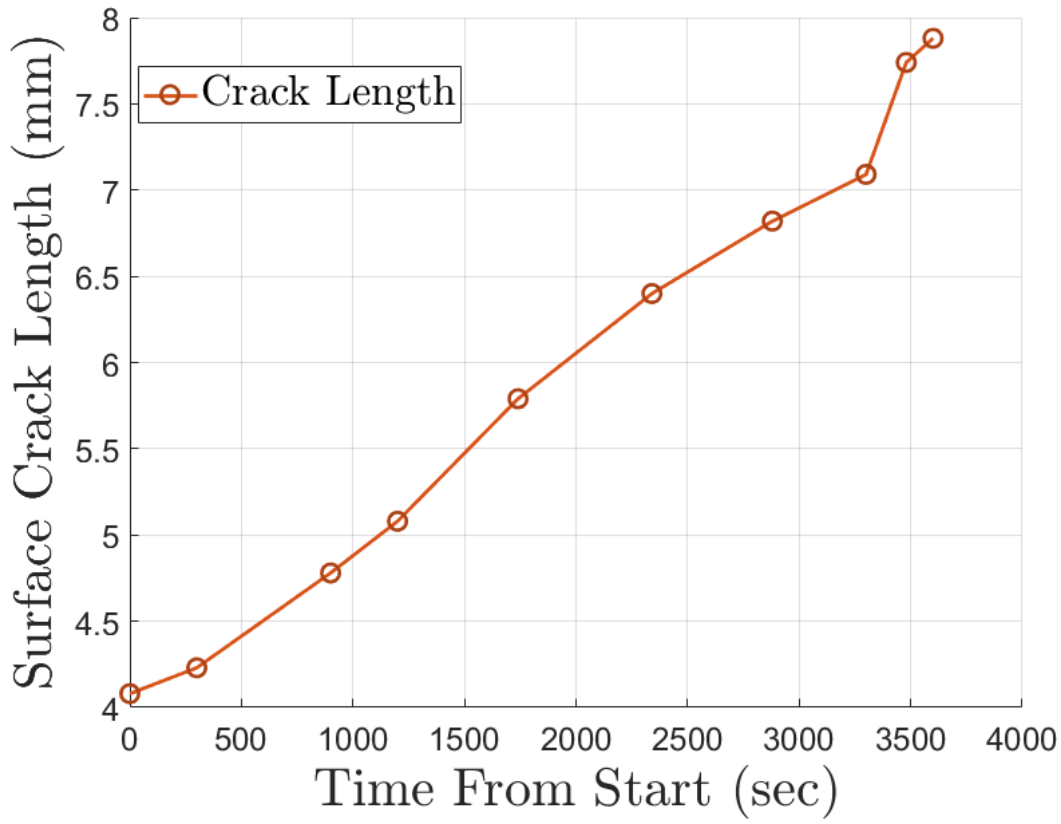

Figure 91: In-situ time-dependent surface crack growth observations of the SENT (718-KH-005) sample

2.4.1.6. FGIN718 K-hold Test

A single additional sample made of the original FGIN718 material was obtained. This sample was used to determine if the material structure itself was the source of the discrepancy between Radzicki's TAZ morphology and the time-dependent damage seen in the CGIN718 samples used in this project. An important difference in this sample was that the geometry was slightly thicker than that of the rest of the high temperature tests done. While all other tests in this section were 5.15 mm thick, this sample was slightly thicker at 5.85 mm. It also had the following experimental attributes:

Table 25: Experimental parameters for the FGIN718 (718-KH-006) test

Starting aspect ratio (*a/c*)	1
Fatigue precracking R=0.1 max load (kN)	50
Khold starting dimensions (mm)	*a*=3.97 *c*=4.99
Khold starting aspect ration (*a/c*)	0.8
Khold force (kN)	72
Khold stress intensity *a* direction (MPa√m)	31.0
Khold stress intensity *c* direction (MPa√m)	31.7
Khold temperature (ºC)	650
Khold duration (seconds)	3600
Maximum horizontal depth of intergranular region (mm)	1.12
Fatigue postcracking R=0.1 max load (kN)	72

In-situ observations show the bifurcation with feathery extension morphology that was seen on the right side of the high K (718-KH-004) sample in Figure 85. Three pictures of this growth at 840 seconds (14 minutes), 2640 seconds (44 minutes), and 3600 seconds (1 hour) are shown in Figure 92 below. A similar (although straighter) morphology can be seen on the right side in Figure 93.

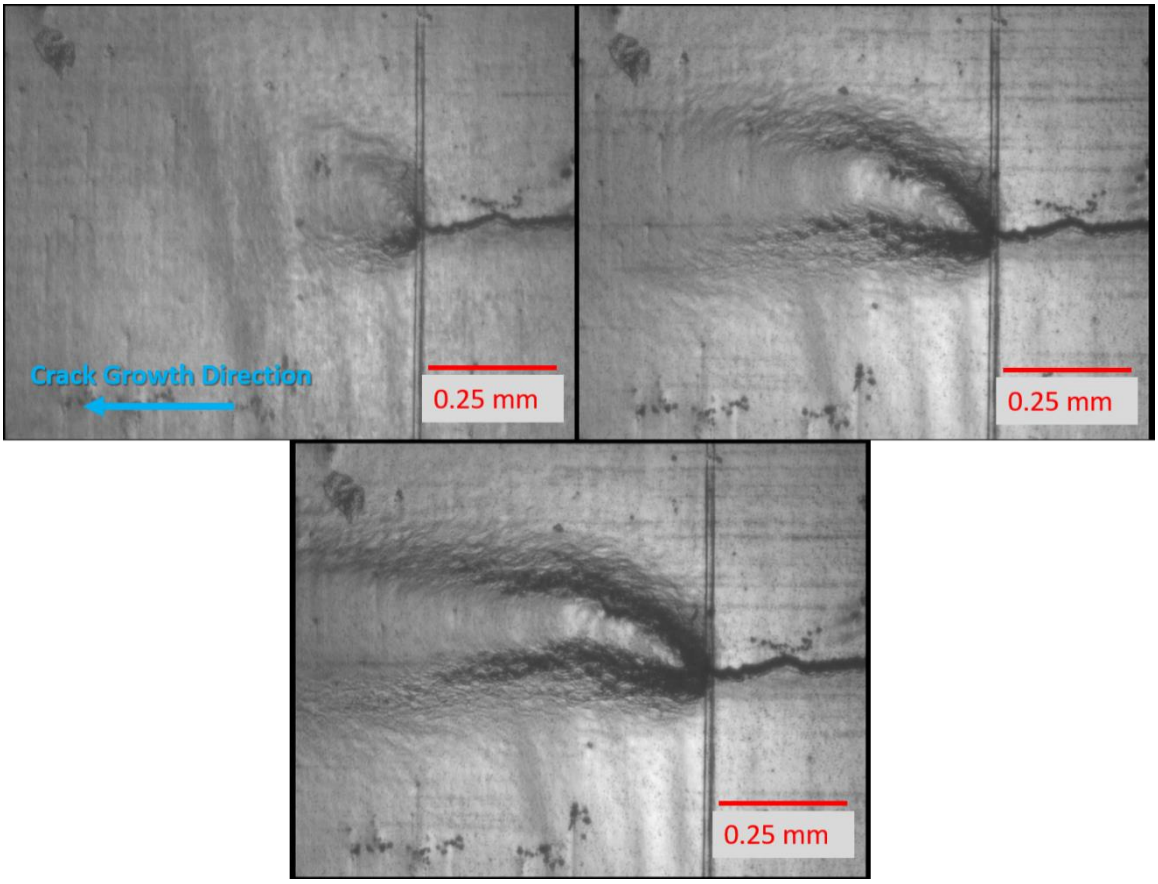

Figure 92: In-situ observations of the FGIN718 (718-KH-006) sample during the K-hold at (clockwise from top right) 840 seconds, 2640 seconds, and 3600 seconds

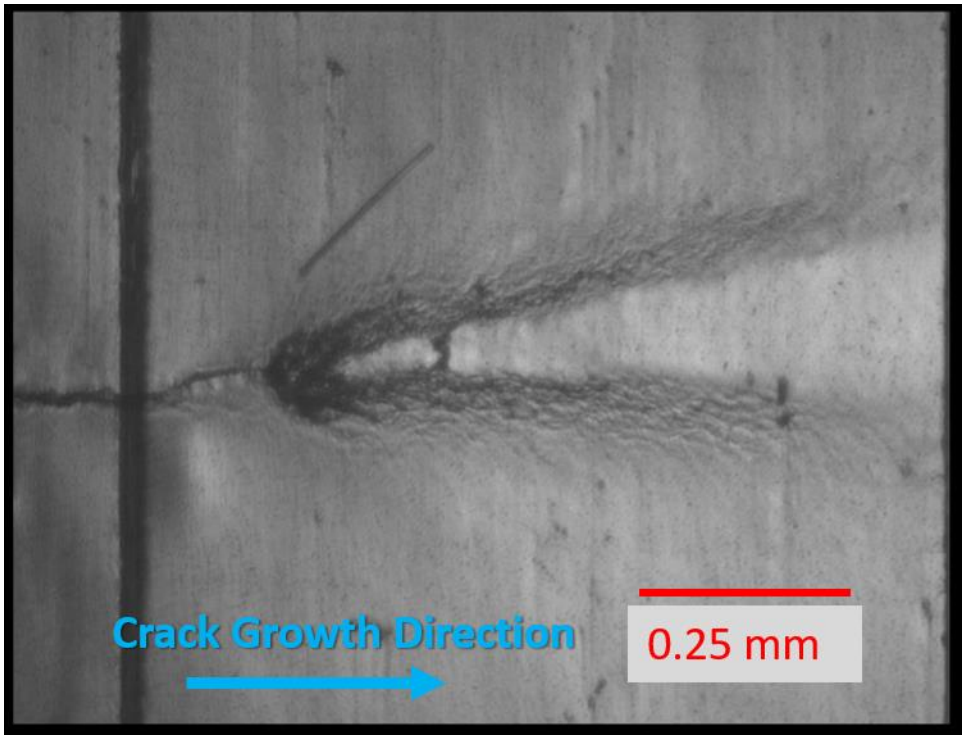

Figure 93: In-situ observation after the 3600 second K-hold on the right side of the FGIN718 (718-KH-006) sample

In-situ observations were gathered within a few minutes of resuming room temperature cycling at 5 Hz and pictures were taken every 60 seconds or 300 cycles. The first thing to note is that over the four observations in Figure 94, the crack grows at an average rate of 4.86×10^{-4} mm/cycle which is 4-5 times faster then what is predicted by the Modified Forman fit for IN718 at room temperature in Table 3 for a K value of 31.7 MPa$\sqrt{m}$ corresponding to a TAZ acceleration effect. Other interesting features can be seen upon close inspection. In picture a, the crack plane can be seen propagating between the two damaged regions. Picture b shows that the black/darkened region is not permanent, aspects of this black region associated with the crack tip itself in picture a are missing 300 cycles later in picture b. It also shows that crack plane shifts and begins to follow the bottom of the region damaged from the K-hold. This trend is continued in pictures c and d.

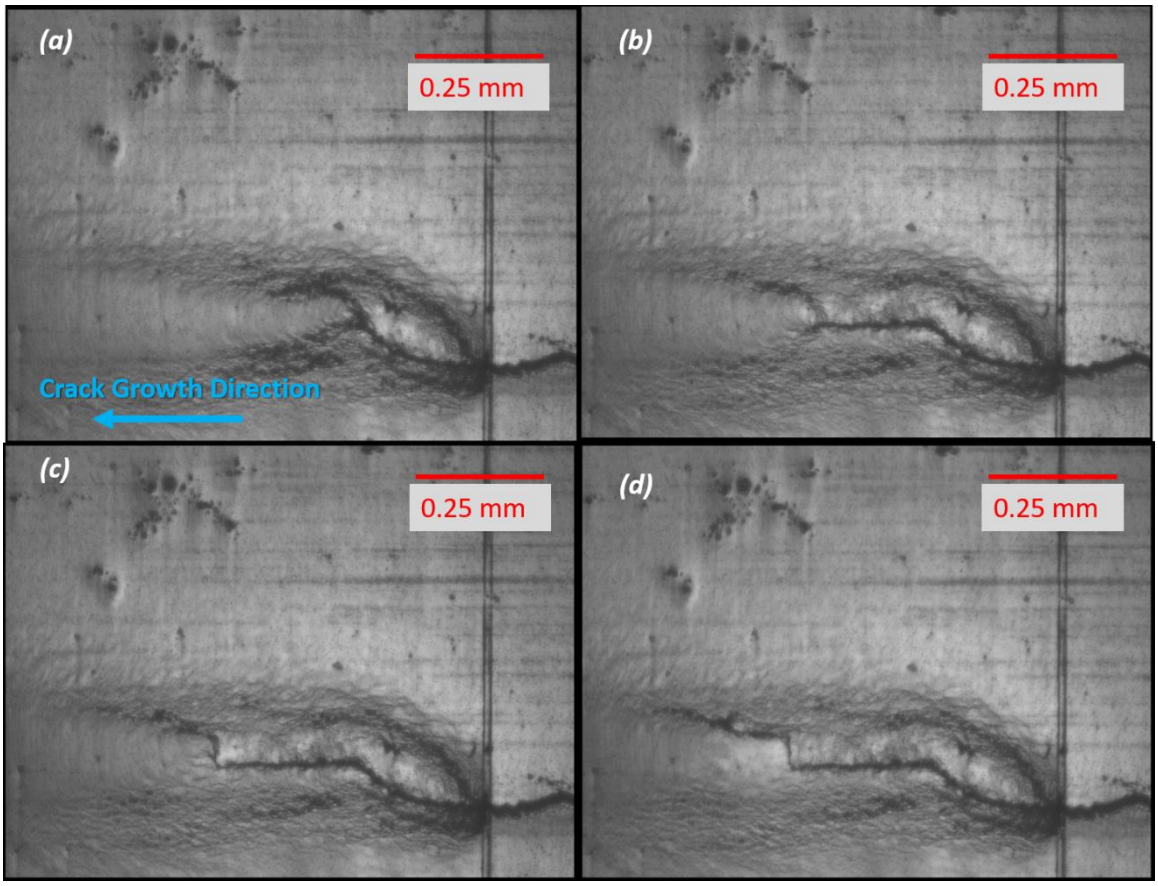

Figure 94: In-situ observations of the crack front propagating on the surface of the FGIN718 (718-KH-006) sample at 60 second (300 cycle) intervals

This bifurcation pattern is associated with a ducking in of the K-hold zone on the fracture surface. This can plainly be seen on both sides of the crack in Figure 95. It also appears that this ducking in phenomenon is directly related to the generation of shear lips at the free surface. When this sample is compared to the other samples made of CGIN718 it appears that this material is much more susceptible to shear lip formation. This could indicate a lower yield strength at room temperature using the model developed by Schuve [50], however it has also been noted in the literature by Loo-Morrey and Reed [51] that very fine grained materials seem to be susceptible to shear lip formation.

It also should be noted that the greatest extent of intergranular growth is in the surface direction (though not on the free surface), with less growth in the *a* direction. This pattern is seen again in other samples which have their K-hold regions ending before breakthrough. This matches the observations by Radzicki where he found that TAZ extends more in areas of plane strain vs plane stress. If we rephrase the problem as a constraint based phenomenon we can imagine that the level of constraint felt at the crack tip can be related to the remaining uncracked material along a radial line running through that point on the crack contour. In this way, the maximum constraint is felt just a little away from the surface with minimum constraint on the free surface, and also in the depth direction where there is a shrinking uncracked ligament.

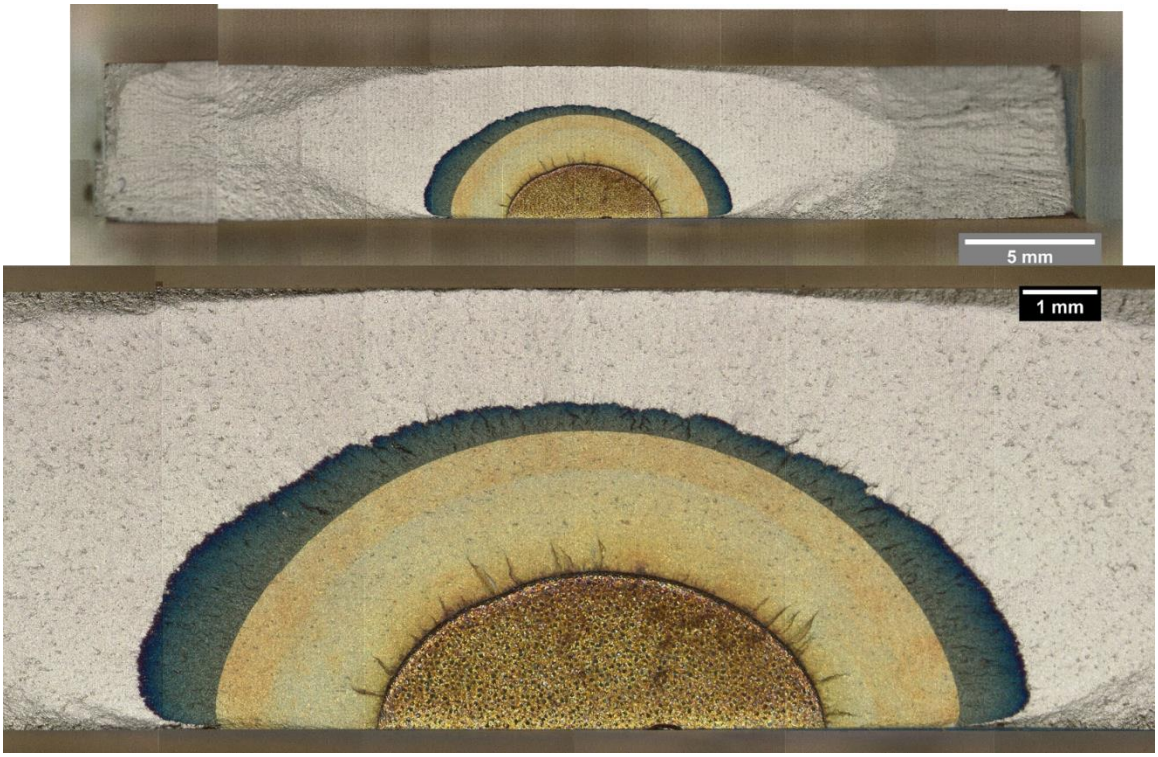

Figure 95: Optical fractograph of the FGIN718 (718-KH-006) sample

SEM examination shows the expected intergranular region. This region has ridges and valleys, with some of those ridges being very well defined. However, this still does

not show the alternating inter and transgranular ridges seen in Radzicki's work. Figure 96 shows the intergranular region in the *a* direction with a distinctive ridge and valley pattern. Figure 97 shows a highly magnified region showing the fine microstructure present in the material. Spheroidized δ precipitates can be seen covering the structure, however on the "cliff face" between the valley and ridge these features are conspicuously absent. As will be explained later, this cliff face phenomenon is thought to be from subsequent cycling where cracks very quickly grow across disconnected damage regions to create a continuous crack plane and take the shortest path available, possibly even traveling through the precipitates.

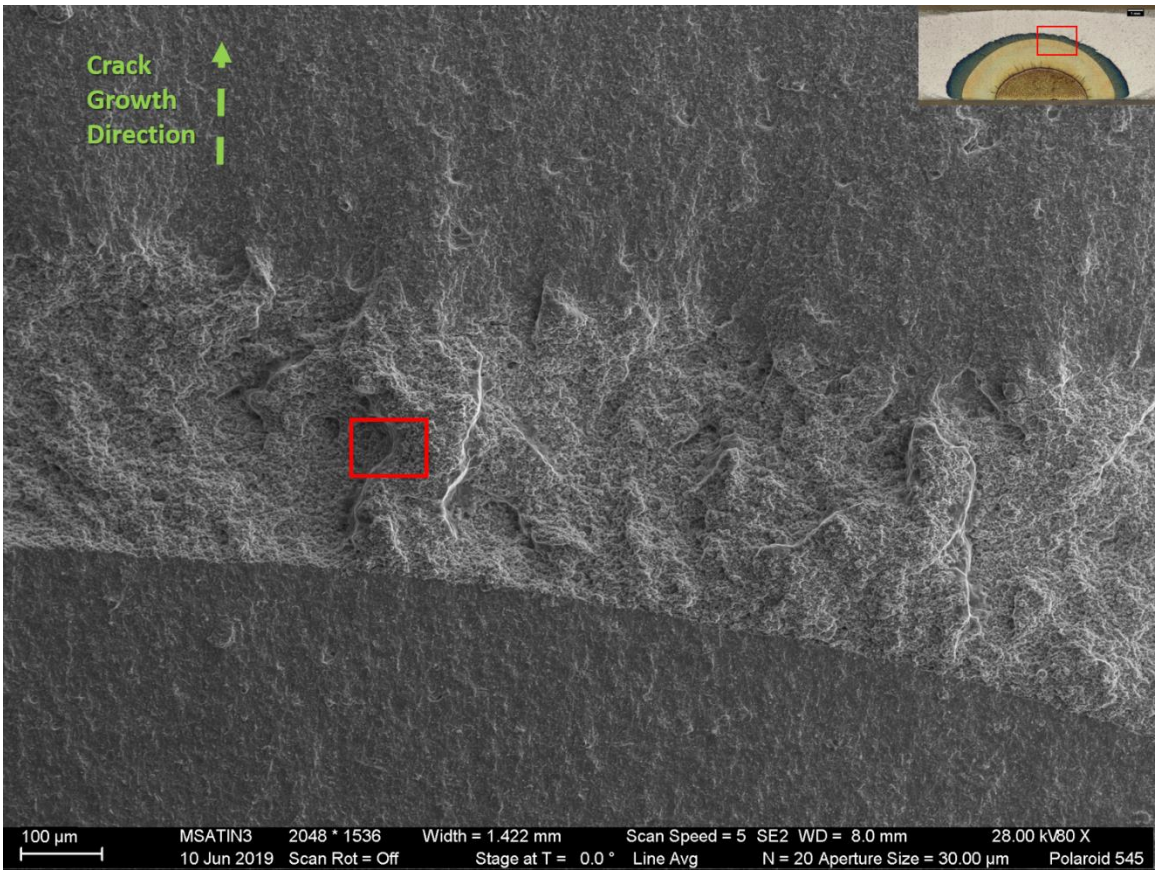

Figure 96: SEM fractograph of the FGIN718 (718-KH-006) material showing ridge and valley pattern with the area shown in Figure 97 highlighted in red

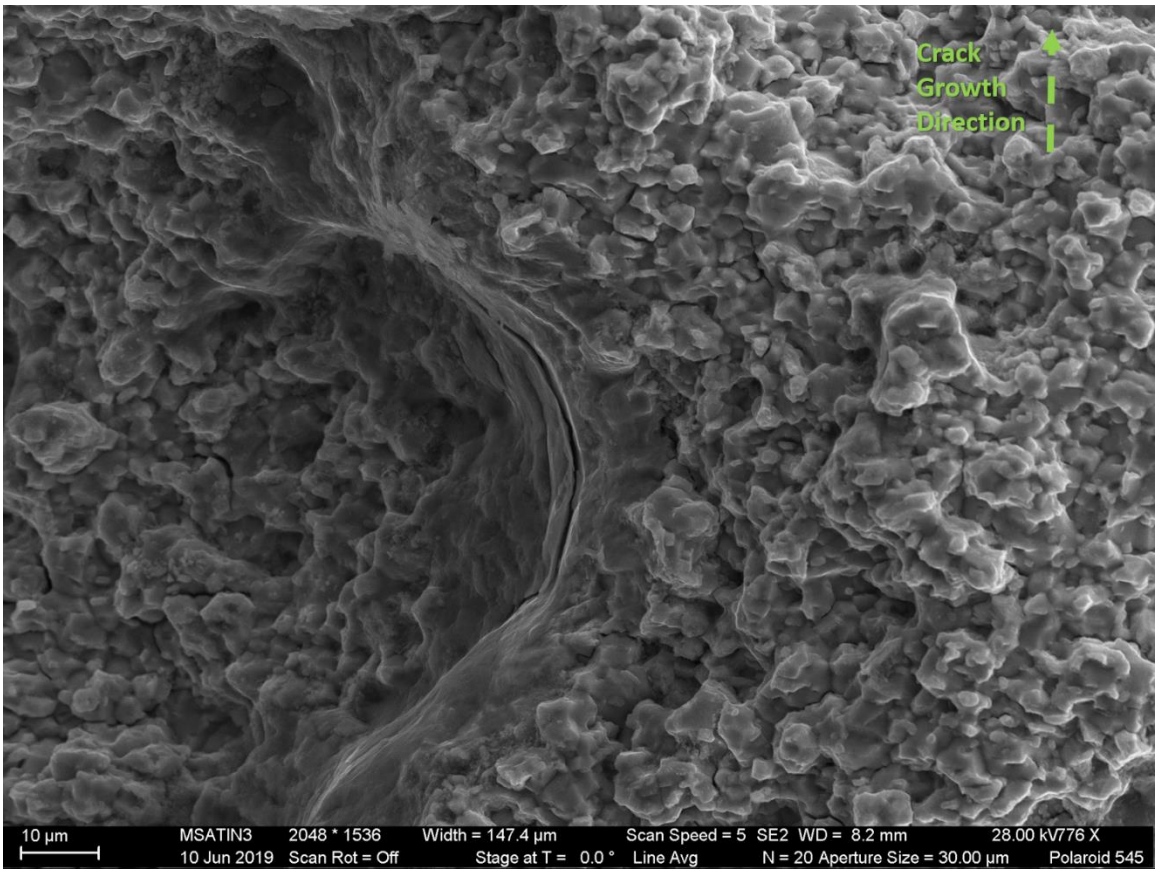

Figure 97: High magnification SEM fractograph showing the edge of a ridge covered in intergranular fracture and homogenously dispersed spheroidized δ precipitates

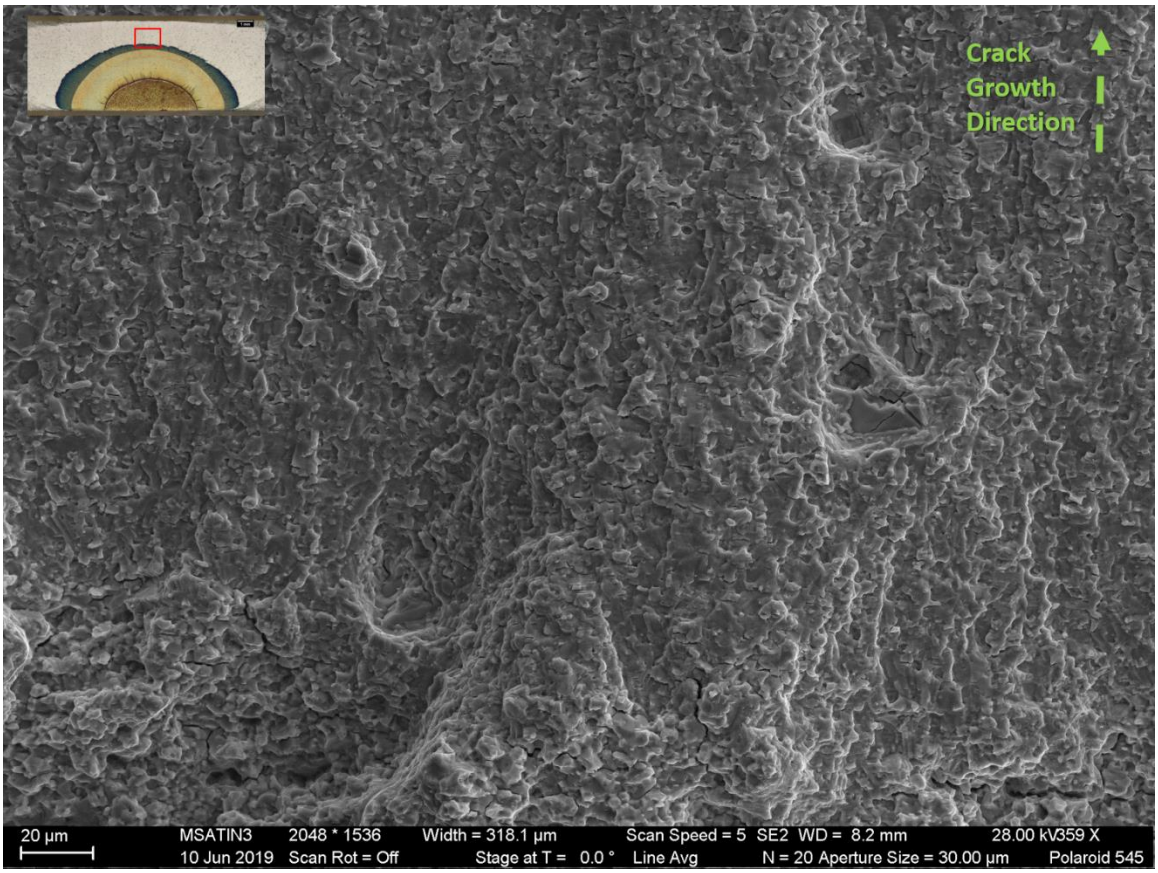

Figure 98: SEM fractograph of FGIN718 (718-KH-006) sample showing the transition back to transgranular fracture at room temperature

What is immediately apparent is that the difference in TAZ morphology between Radzicki's observations and the K-hold experiments seen in this work cannot be explained by material microstructure or specimen geometry alone. It's possible that some unique combination of specimen geometry, microstructure, and thickness (Radzicki's specimens were approximately half the thickness) resulted in the morphology seen by him.

2.4.1.7. Long SENT Experiment

The interrupted K-hold experiment (718-KH-007) will be discussed in the following section due to the larger amounts of observations associated with it. The final K-hold experiment, the long SENT (718-KH-008) experiment was designed to try to test a

hypothesis on why time-dependent crack growth had not been observed by Radzicki. It is thought based on evidence from Figure 95, and the bifurcated/lighter surface indications on some samples that shear lips may have a major role in deciding if the intergranular region reaches the surface of the material or not. It already seems that the FGIN718 material is more susceptible to shear lip formation based on both the room temperature corner crack specimens (see Figure 14), and the FGIN718 K-hold test (Figure 95). The long SENT specimen was an attempt to grow shear lips by having a very high K and long crack scenario and then observe whether a K-hold intergranular region could be observed growing on the surface in a time-dependent manner.

This sample had a slightly different procedure consisting of 2 separate K-holds. In addition these K-holds were not the standard 3600 seconds (1 hour). Because they were at much higher K values, they were held for shorter durations to ensure the K-hold region did not result in fracture. Room temperature cycling between the K-holds was complicated by the fact that the load needed to be reduced for the second K-hold due to the very long crack length. Initially the crack was grown out of the first K-hold region using the 35 kN max R=0.1 waveform. Once the crack was clear of that area, the load was reduced to 10 kN maximum. However, this resulted in what appeared to be a crack arrest event, the load was raised to 20 kN maximum, and then again to 30 kN maximum before the crack began moving again. The load was then again lowered to 20 kN maximum, and then raised again to 25 kN maximum. Finally the load was successfully lowered to the 20 kN maximum to match the load of the second K-hold and the crack was grown to the second K-hold's starting dimension. The experiment had the following attributes:

Table 26: Experimental parameters for the long SENT (718-KH-008) sample

Initial wire EDM notch (mm)	7.0
Fatigue precracking R=0.1 max load (kN)	35
Khold 1 starting crack length (mm)	14.14
Khold 1 force (kN)	35
Khold 1 stress intensity (MPa√m)	53.8
Khold 1 temperature (ºC)	650
Khold 1 duration (seconds)	1740
Maximum horizontal depth of intergranular region 1 (mm)	5.67
Khold 2 starting crack length (mm)	28.76
Khold 2 force (kN)	20
Khold 2 stress intensity (MPa√m)	64.5
Khold 2 temperature (ºC)	650
Khold 2 duration (seconds)	840
Maximum horizontal depth of intergranular region 2 (mm)	2.37

Figure 99 shows the fracture surface of the sample with the different regions labeled. In addition it is important to note which side of this sample (top in the picture) was the viewing side during the experiment. Although the crack was grown to very long lengths, obvious shear lips were never visible in the in-situ measurements. Because of this large amounts of time-dependent growth were always evident during the K-holds. It does appear that a shear lip did form on the back side of the plate which greatly reduced the effect of the second K-hold at that surface. However, this was not visible during the experiment and cannot be used to prove the hypothesis that this was the reason for Radzicki failing to observe time-dependent growth at the surface.

Two other features stand out in this sample. In the first K-hold the amount of tortuosity seen on the surface at the end of the K-hold and the room temperature region immediately after is much greater then what has been seen previously. This is probably

due to the very high stress intensity (53.8 MPa√m) and may be why the crack appeared to get "stuck" after that step. The other feature of note, is the much larger color gradient at the end of the second K-hold. This was the highest K of any high temperature experiment in this project (64.5 MPa√m). The relatively large purple region at the end of the K-hold shows that an extensive region of up to 0.7 mm was partially exposed to oxygen but either at lower concentrations, or for a much lower amount of time then the saturated blue color associated with the K-hold area.

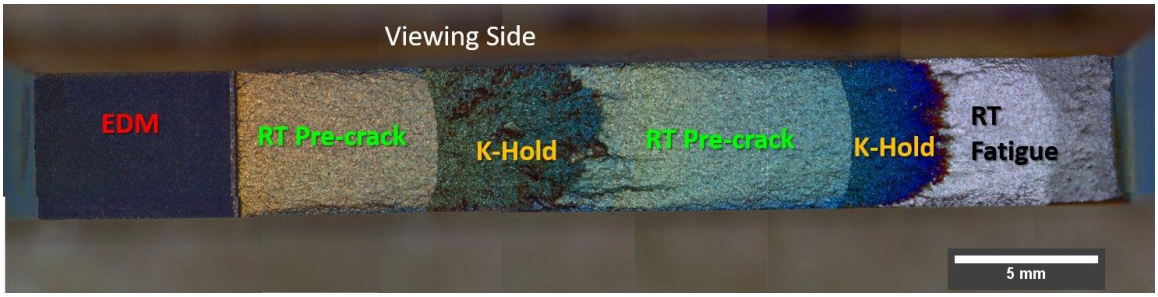

Figure 99: Optical fractograph of the long SENT (718-KH-008) sample showing the different experimental regions and the surface (top) that was visible for in-situ measurements during the experiment

SEM examination shows the typical intergranular and transgranular regions albeit with much more tortuosity. A demarcation can be seen near the bottom edge of Figure 100 where the shear lip keeps the intergranular region from reaching the surface. This transgranular fracture grew in cycle dependent manner after room temperature cycling resumed, and lends support to the theory that shear lips prevent time-dependent growth from being observed from the free surface in-situ.

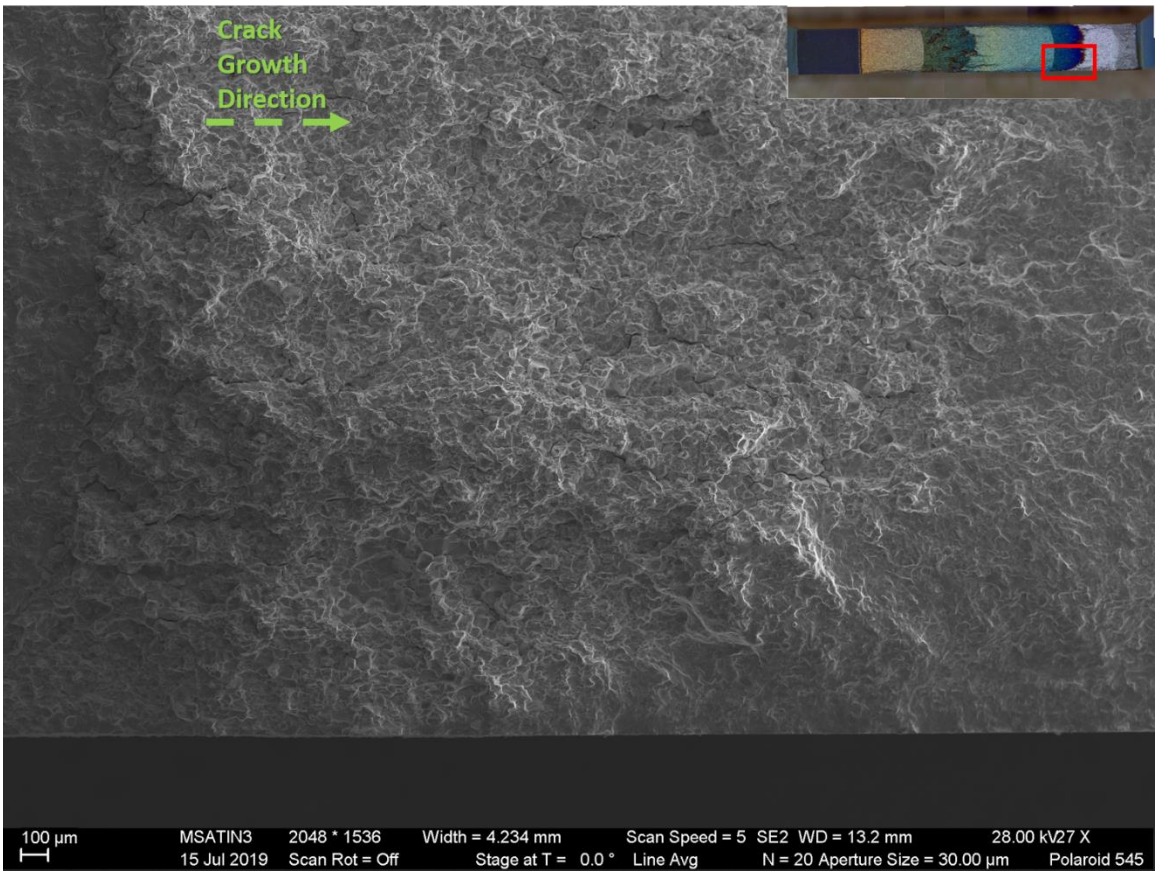

Figure 100: SEM fractograph of the long SENT (718-KH-007) sample showing the non-viewing side with a shear lip bounding the second K-hold region

2.4.2. Interrupted K-hold Experiment

The interrupted K-hold experiment is a novel way of observing how the time-dependent damage at high temperatures in Inconel 718 evolves without the influence of subsequent cycling. When looking at the fracture surfaces from the K-hold experiments, it is not apparent if the time-dependent damage is true time-dependent crack growth or if it is simply damage that is then exposed upon subsequent cycling (Radzicki's TAZ model). Arguments could be made for either as there is an obvious time-dependent extension that for large K-hold areas appears to partially open and close with cycling indicating the region is fully cracked. However when cycling at room temperature, the crack tip does not simply

begin at the edge of the damage zone, but instead takes some time to emerge from the zone as if it had to work its way through the damage from the pre-K-hold crack tip.

2.4.2.1. In-Situ Observations

This experiment was run in a similar manner to the other K-hold experiments, and was again on the CGIN718 material. The sample was cycled at room temperature until the desired crack dimensions were reached. A K-hold was then applied for 3600 seconds at 650 ºC. However, the sample was then removed from the fatigue fixture and cut in half along the vertical axis with wire EDM in the manner shown in Figure 62. Half the sample was re-placed in the frame and cycled to failure at room temperature. The test had the following parameters, Table 27, (assuming the wire EMD cut was exactly in the center and material removal was negligible):

Table 27: Experimental parameters of the interrupted K-hold (718-KH-007) experiment

Starting aspect ratio (*a/c*)	0.5
Fatigue precracking R=0.1 max load (kN)	40
Khold starting dimensions (mm)	*a*=3.74 *c*=5.25
Khold starting aspect ration (*a/c*)	0.71
Khold force (kN)	72
Khold stress intensity *a* direction (MPa√m)	37.4
Khold stress intensity *c* direction (MPa√m)	36.9
Khold temperature (ºC)	650
Khold duration (seconds)	3600
Maximum horizontal depth of intergranular region (mm)	0.95
Fatigue postcracking R=0.1 max load (kN)	35

Once again this experiment showed the bifurcated pattern with the feathery growth extending from the forks (Figure 101).

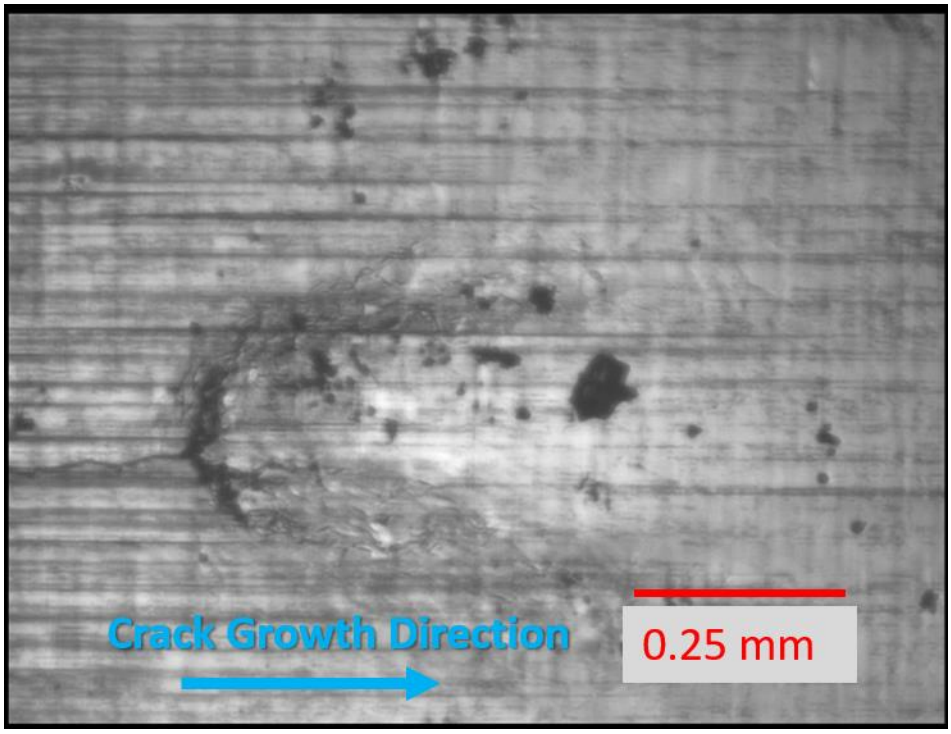

Figure 101: In-situ observation of the interrupted K-hold (718-KH-007) experiment at the end of the K-hold

2.4.2.2. Fracture Surface Observations

The broken half of the experiment can be seen in the fractograph in Figure 102. Due to an error in the plunger EDM process, the starting notch is not elliptical. However, after pre-cracking, the contour reached the typical elliptical shape for a surface flaw. Like in Figure 95, the greatest extent of the intergranular region is just beyond the surface starting at about 0.36 mm from the free surface. Just as the form in Figure 101 suggest, the fracture surface shows a ducking in of the intergranular region at the surface (plane stress region).

Figure 102: Optical fractograph of broken half of the interrupted K-hold (718-KH-007) test

The fracture surface in this specimen takes on a lot of meaning when compared to the micrographs taken of the unbroken half. This fracture surface is assumed to be equivalent to the features on the unbroken section which can be thought of as the mirror image of this surface. Figure 103 shows the largest portion of the K-hold zone. In this region the intergranular zone is mostly uninterrupted with transgranular ridges linking sections of intergranular fracture becoming more common on the left hand side as it approaches the end of the K-hold.

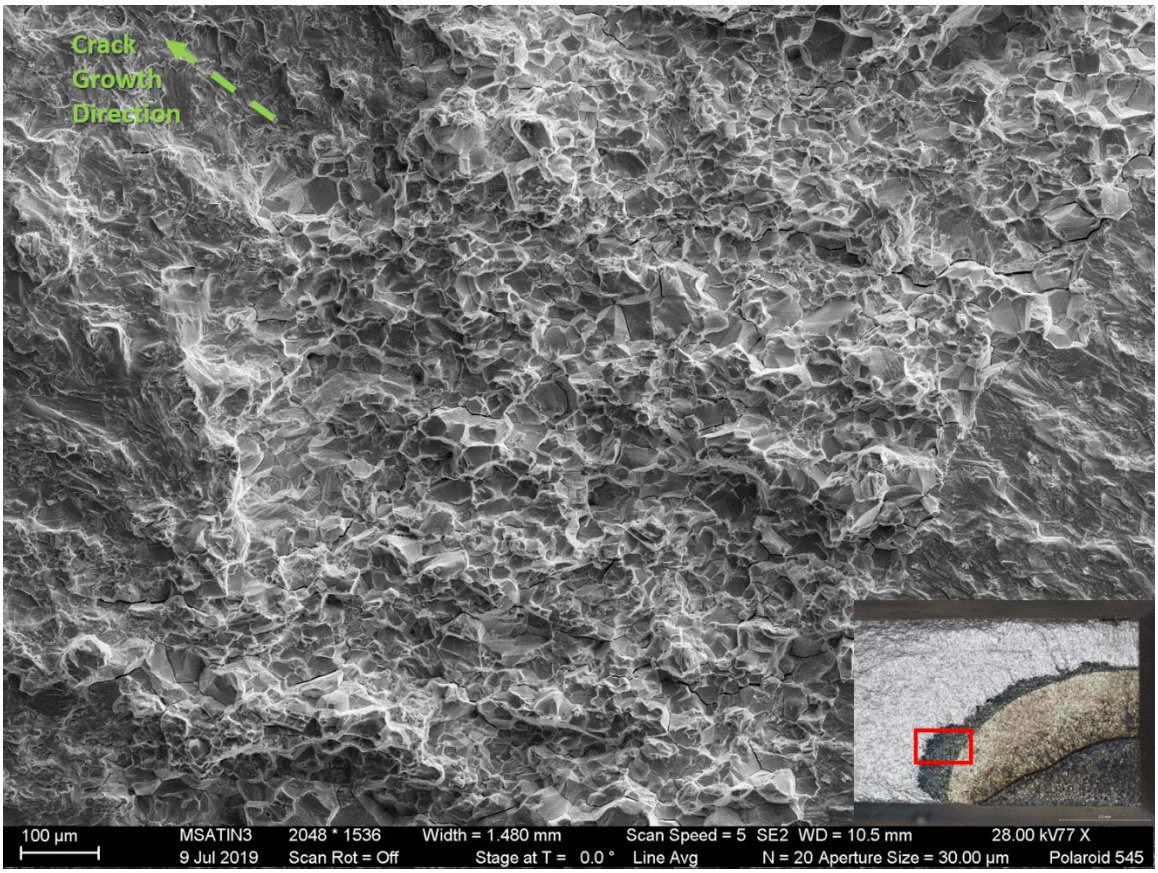

Figure 103: SEM fractograph showing the bulk fracture surface on the broken half of the interrupted K-hold experiment

The *c*-direction free surface is shown in Figure 104. A relatively small (≈100µm) section of intergranular fracture is all that reached the surface on this side. This region seems to be flanked on either side by transgranular fracture that is raised out of plane from the material around it possibly signifying the start of slant growth (shear lips).

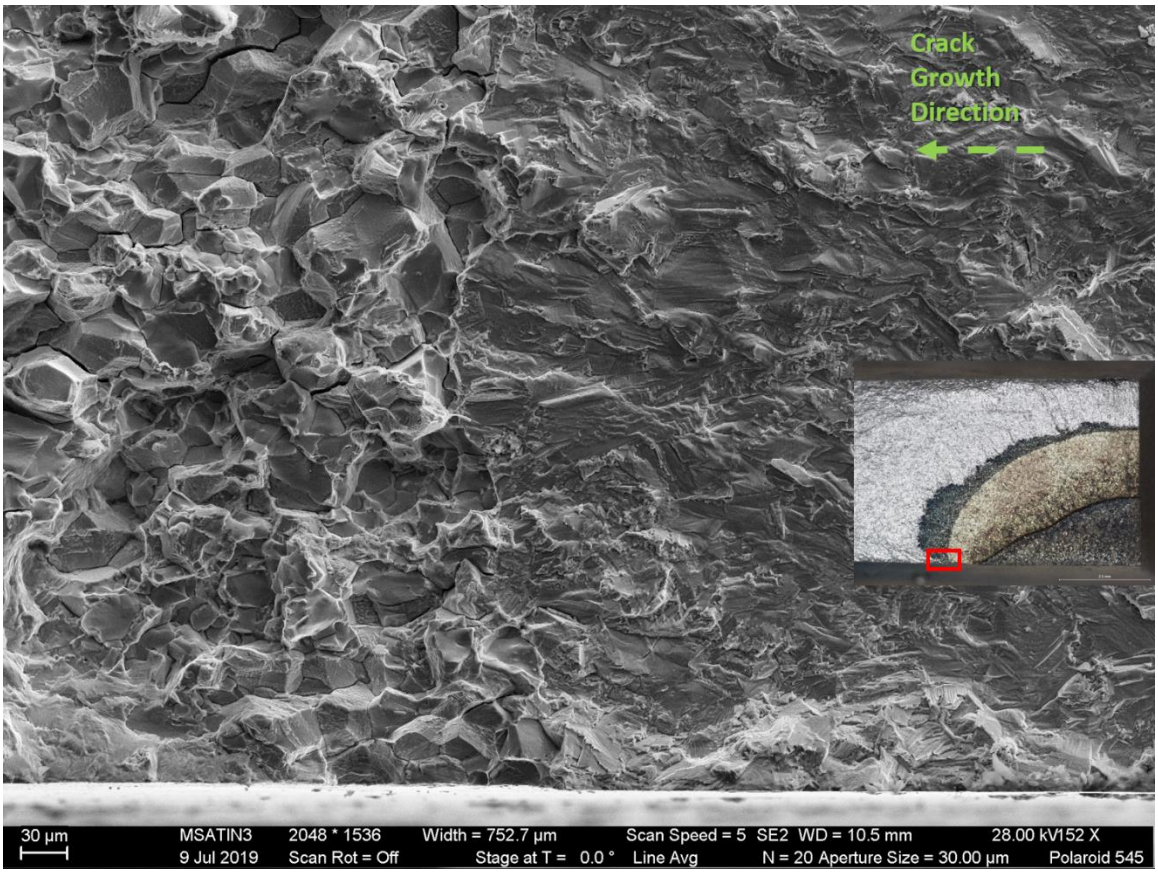

Figure 104: SEM fractograph showing the small intergranular section on the surface of the broken half of the interrupted K-hold experiment

Figure 105 and Figure 106 show the *a*-direction, or depth direction K-hold. This direction saw a much thinner section of growth especially very close to the *a* axis. Although that thin ribbon is intergranular, transgranular linkages can be seen between almost every grain. These linkages form when the crack plane is discontinuous at the end of the K-hold and quickly break upon subsequent cycling. Because these are so prevalent in this region, it is expected that the unbroken sections of this material will have many in-plane discontinuities.

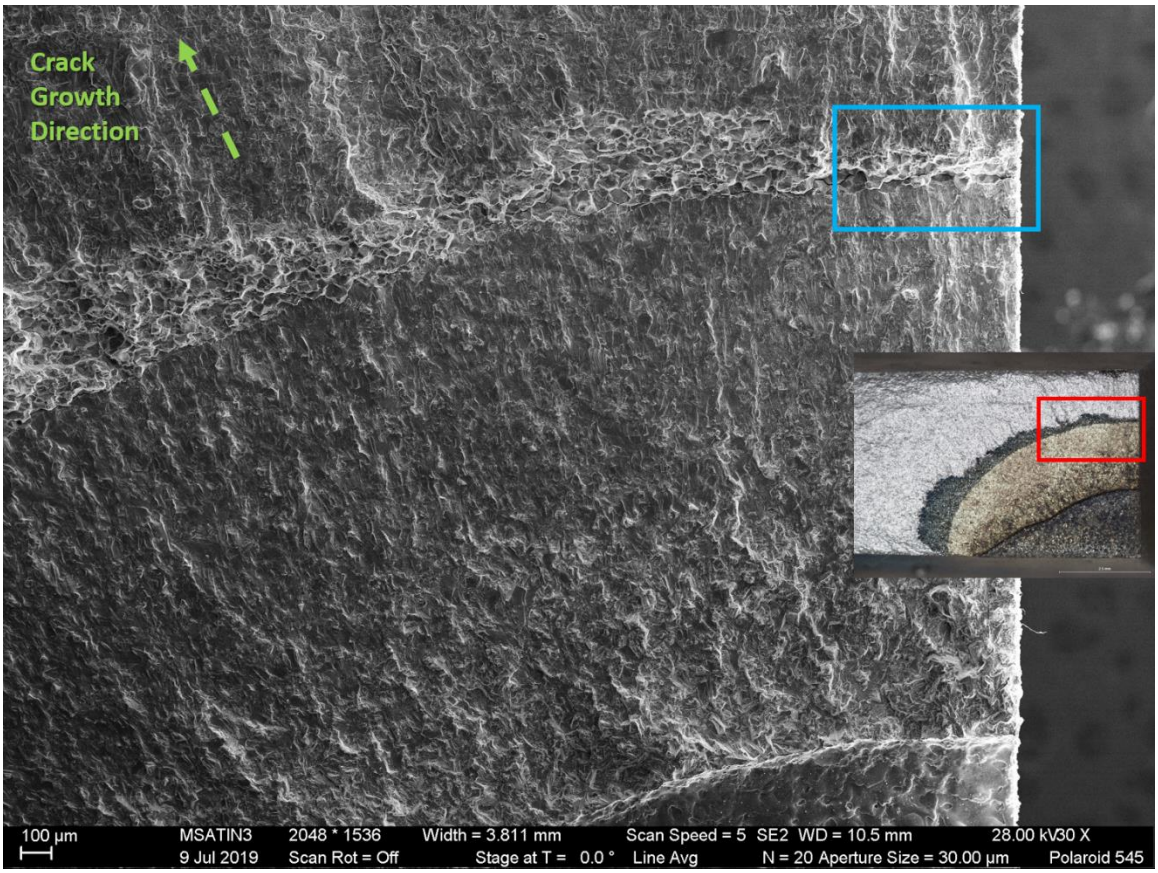

Figure 105 : SEM fractograph showing a direction intergranular ribbon on the broken half of the interrupted K-hold experiment. The area highlighted in blue is shown magnified in Figure 106.

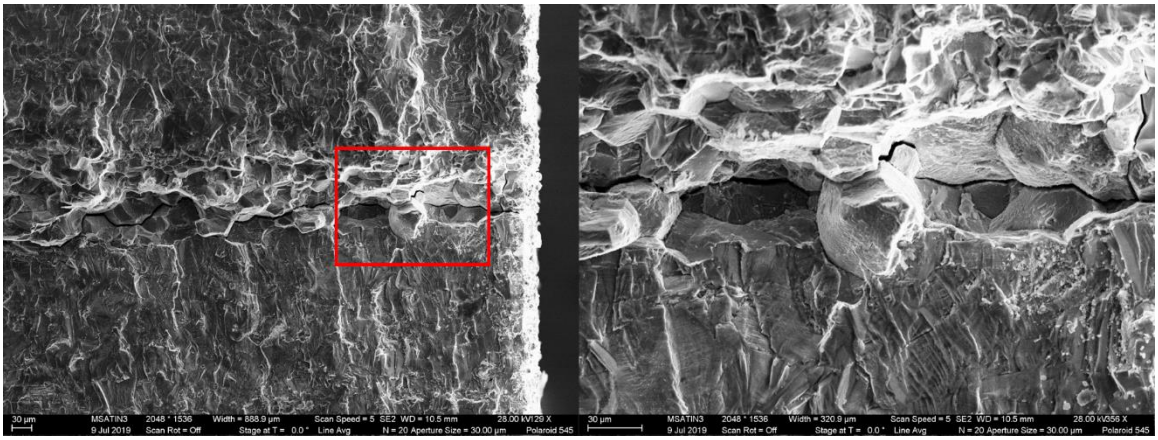

Figure 106: Magnified fractograph of the a-direction K-hold region showing transgranular linkages between intergranular failures

2.4.2.3. Profile Observations

The profile mount of the broken section was ground and polished to three depths of approximately 10 (I), 510 (II), and 1010 (III) μm as seen in Figure 107 below.

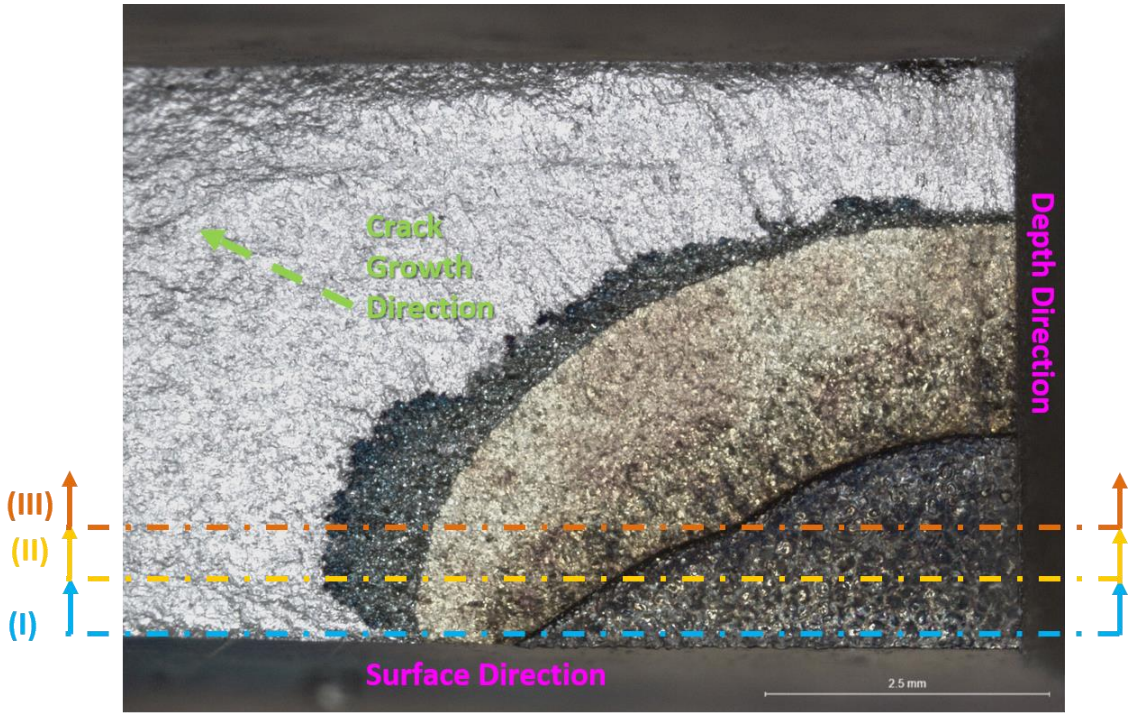

Figure 107: Sectioning plan of profile mount of broken half of the interrupted K-hold experiment with sections at 10 (I), 510 (II), and 1010 (III) μm marked.

Figure 108 shows the near surface (≈10μm deep) profile section (section I). As expected from Figure 104, the intergranular region is very small and relatively featureless. A single intrusion can be seen in blue where secondary cracking has infiltrated the material following a grain boundary. As expected the region that is tinted blue in Figure 107, is indeed intergranular, which agrees with the SEM fracture surface observations.

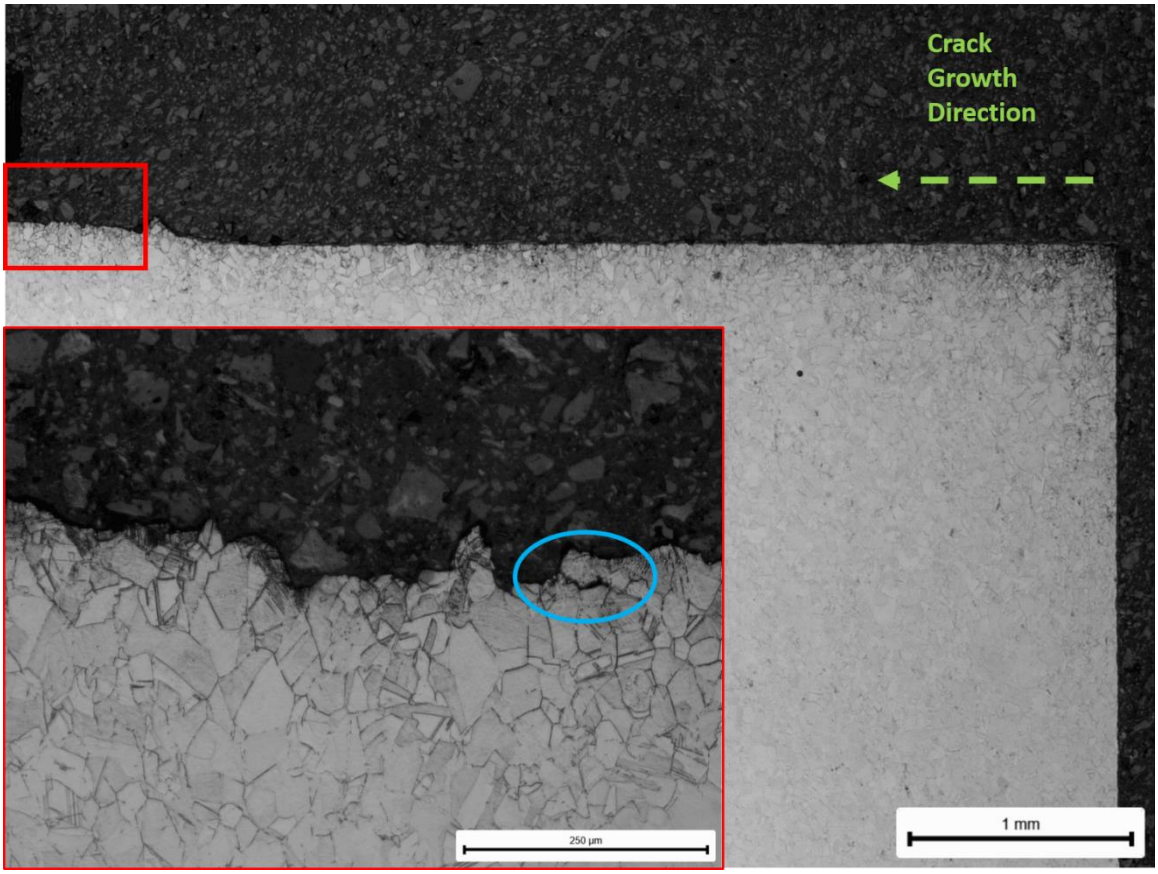

Figure 108: Section (I) of the broken profile showing the etched small intergranular region (highlighted in red and magnified), and a single intrusion highlighted in blue

Section II is pictured below in Figure 109. It shows a pattern which is consistently repeated through the rest of the mounted sections in this material. Each segment is underlined in the figure to show its extent. Segment 1 shows the extent of the original EDM starter notch. Segment 2 shows a somewhat tortuous crack path which is dominated by short crack behavior and is influenced by material damage imparted by the EDM notch. This effect can be seen on the optical fractographs of many of the K-hold tests (such as Figure 102) as the textured darker region in the room temperature pre-crack regime. The crack here is mostly transgranular but occasionally will follow grain boundaries. Segment 3 is planar, transgranular growth at room temperature where the long crack behavior dominates and the crack is kept in-plane by LEFM. Segment 4 shows the area of interest

corresponding to the K-hold intergranular region. Segment 5 and beyond shows the room temperature crack growth to failure which again seem tortuous in nature but is primarily transgranular.

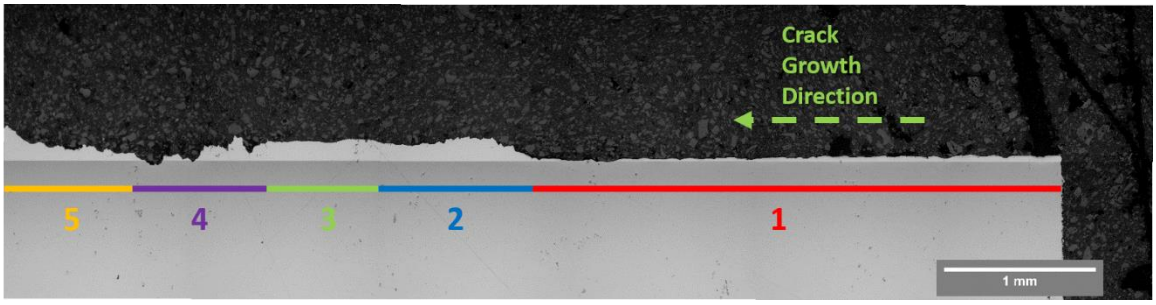

Figure 109: Composite photo of un-etched section II of the profile mount at approximately 510 μm deep. Note color change from top to bottom is an artifact from the image acquisition.

Section II has a much larger intergranular region with more features. Figure 110 shows the intergranular section with relatively short intrusions extending down from the surface along grain boundaries. In addition an oxidized carbide can be seen along the crack path as a dark grey particle touching the fracture surface. These are distinct from the lighter grey carbides, and are identified with EDS later in this paper.

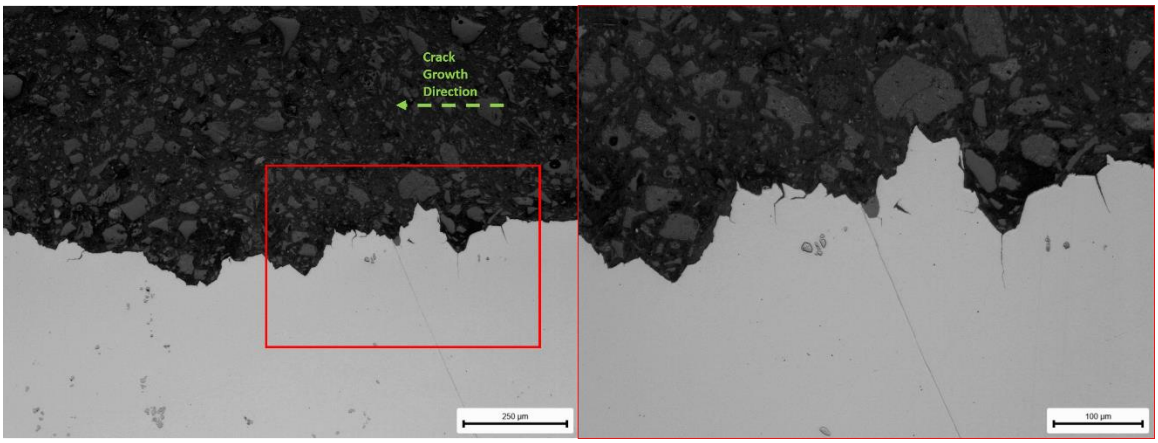

Figure 110: (Left) Un-etched intergranular region of section II showing several small intrusions and dispersed carbides in the bulk material. (Right) Magnified region showing intergranular intrusions and an oxidized carbide in the crack path.

Section III shows many of the same features. The intergranular region has several short intrusions. The same regions of crack growth can be seen in this section as section II. In Figure 111 a grain can be seen that has become completely encompassed by one of these intrusions (at least on the sectioning plane). Figure 112 shows the same section etched confirming the intergranular nature of the fracture and showing the intrusions following grain boundaries. These intrusions often follow grain boundaries that are decorated with the white δ precipitates seen in SEM in Figure 113. However, this is not always true. This concept is explored in greater detail in the discussion around the unbroken sections in this experiment.

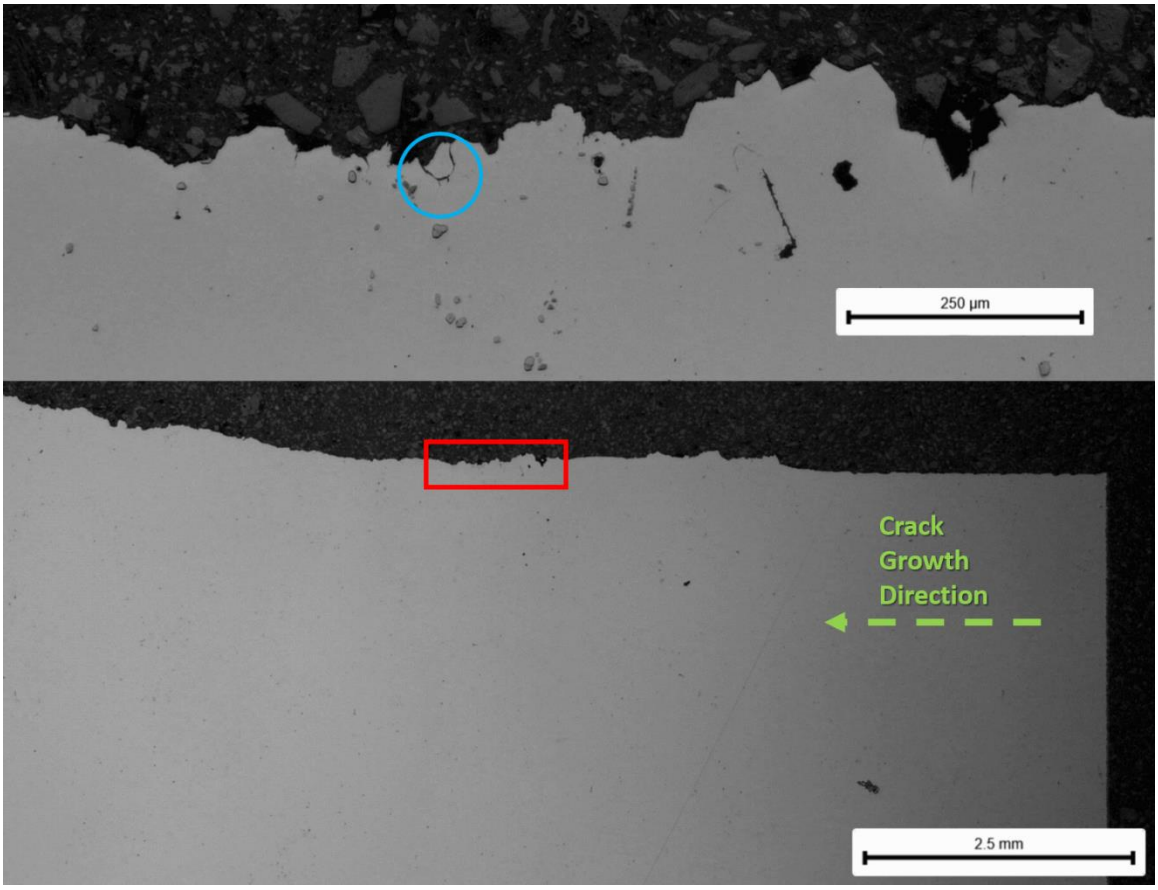

Figure 111: Section III of the broken section of the interrupted K-hold experiment showing the intergranular region in red (bottom) and a fully encompassed grain in this region in blue (top)

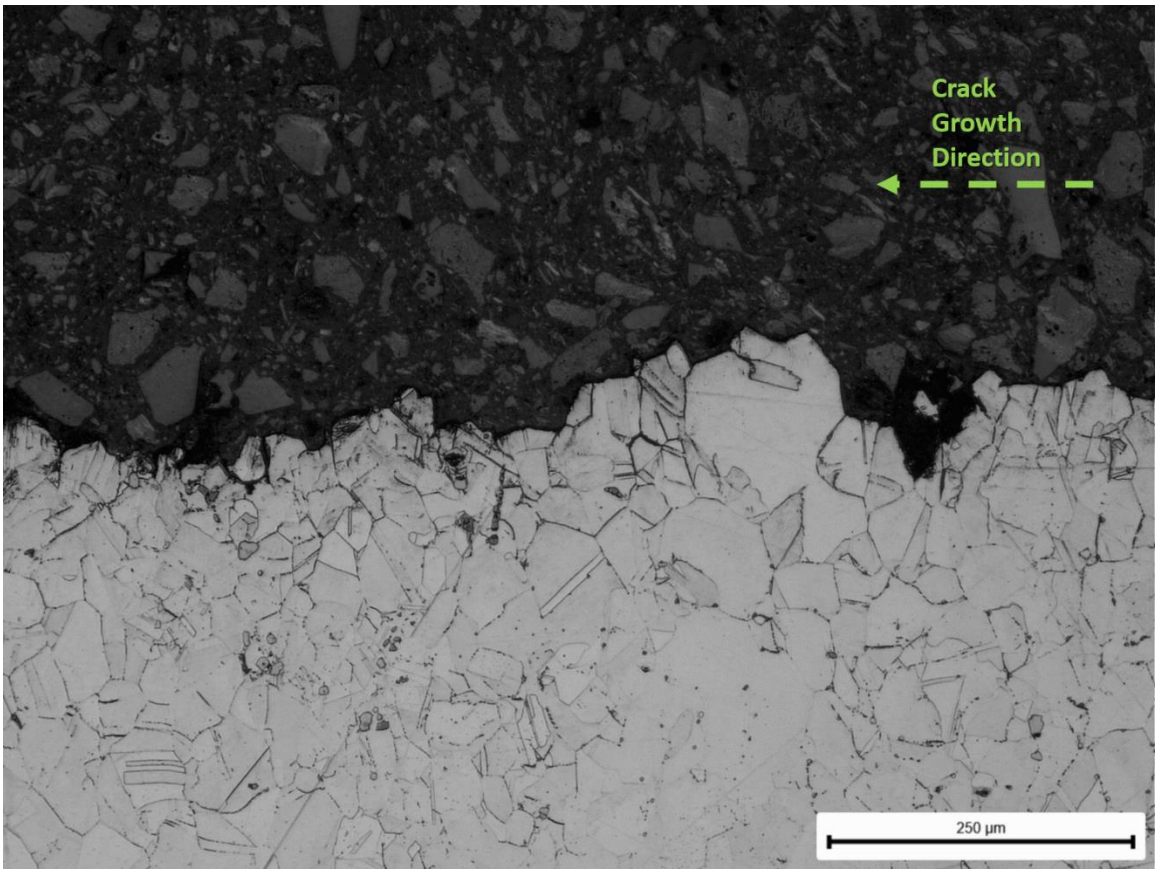

Figure 112: Etched micrograph of Section III of the interrupted K-hold specimen profile mount

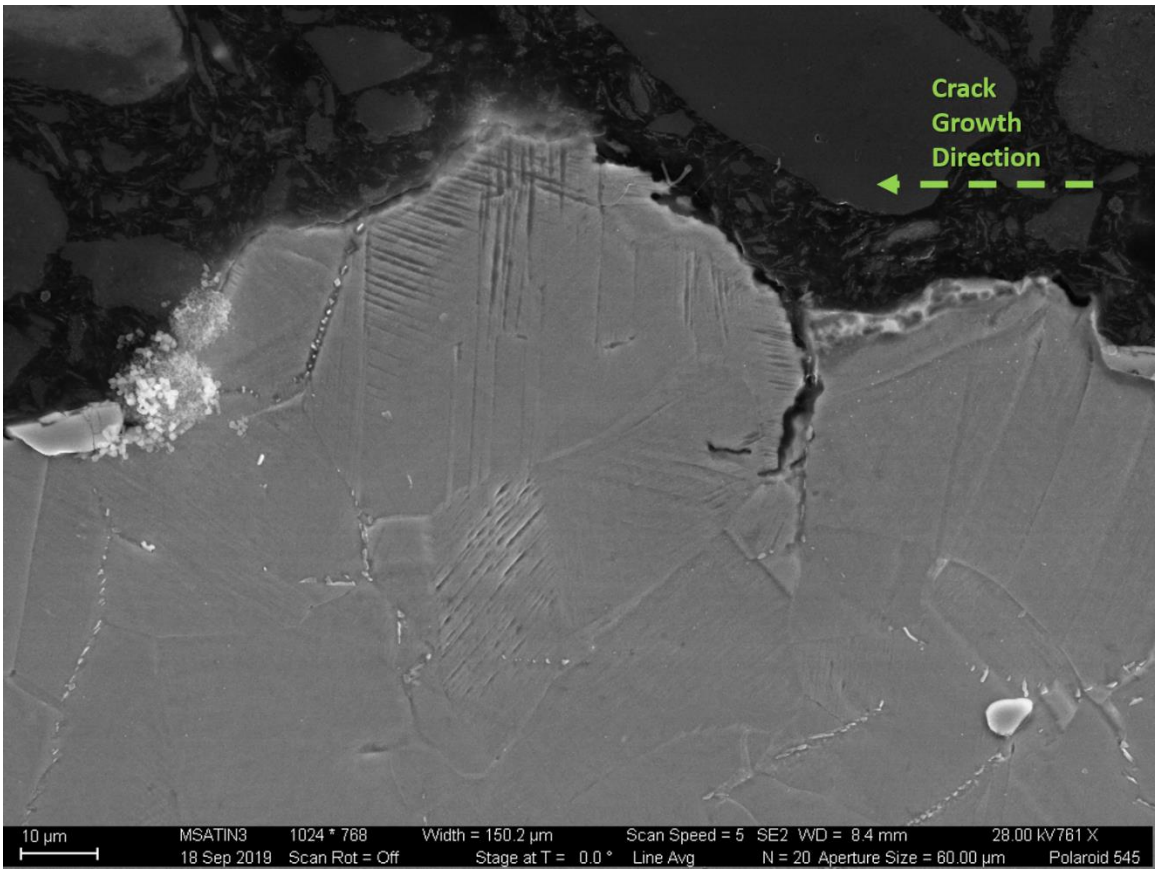

Figure 113: SEM micrograph of Section III of the interrupted K-hold experiment profile showing that intrusions are often associated with the white δ precipitates

Another feature revealed in these mounts through etching is a distinctive cross-hatch pattern on some of the grains. These patterns seem to form mostly in the same direction in small patches and change orientation in different grains. Because of this orientation preference, it is theorized that these are a result of damage forming on slip planes in the crystals form plastic deformation associated with the crack's process zone. Some of these patterns can be seen in Figure 113, but these patterns become more apparent in regions with more cyclic damage. Figure 114 shows an area further down the crack front where more of these patterns can be seen in a higher density.

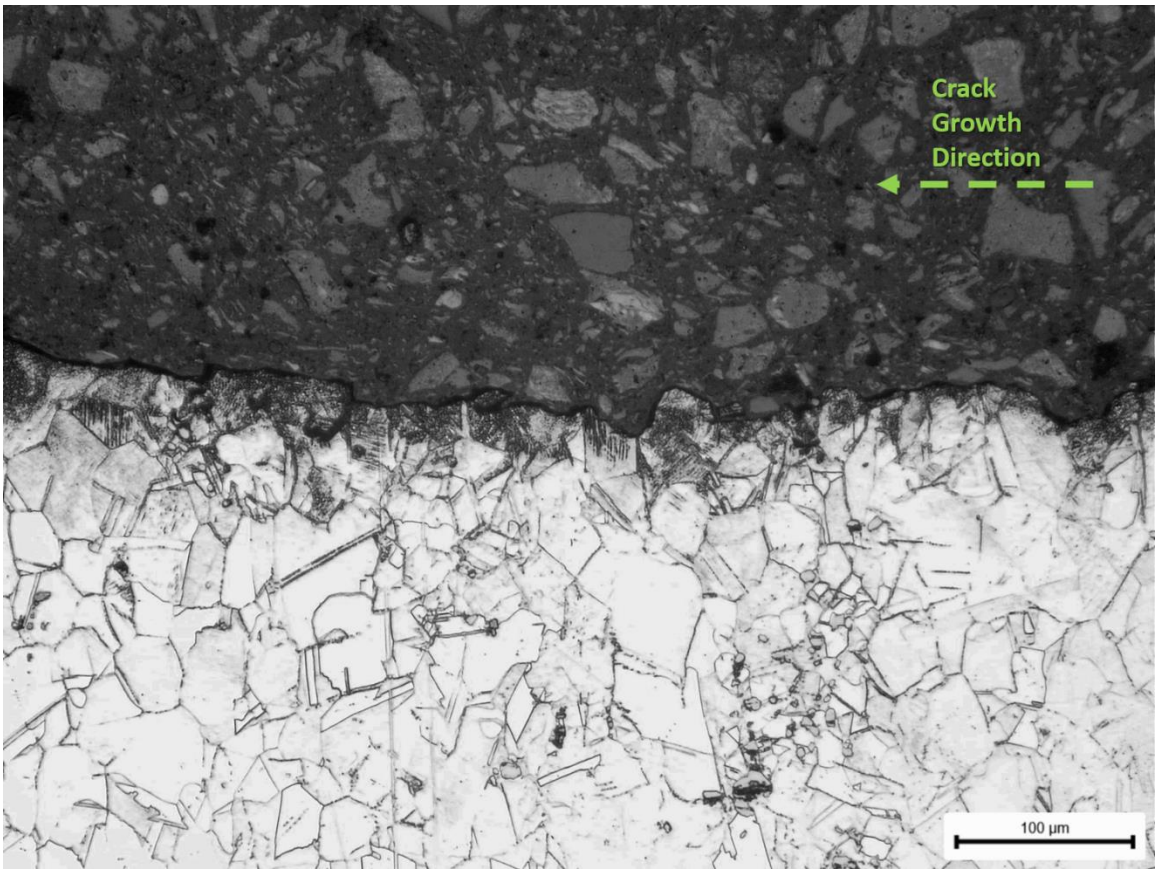

Figure 114: Optical micrograph of Section III of the interrupted K-hold experiment showing additional slip plane damage accumulation in the post K-hold cycling area of the crack profile

2.4.2.4. Unbroken Sections

The unbroken half of the experiment was diamond cut into two blocks which were mounted separately. These mounts provided views in the *c* (surface) and *a* (depth) directions respectively. The sectioning diagram is shown in Figure 115 with diamond cut shown in red and sections at approximately 10, 260, 510, and 1010 µm shown by sections I, II, III, and IV respectively.

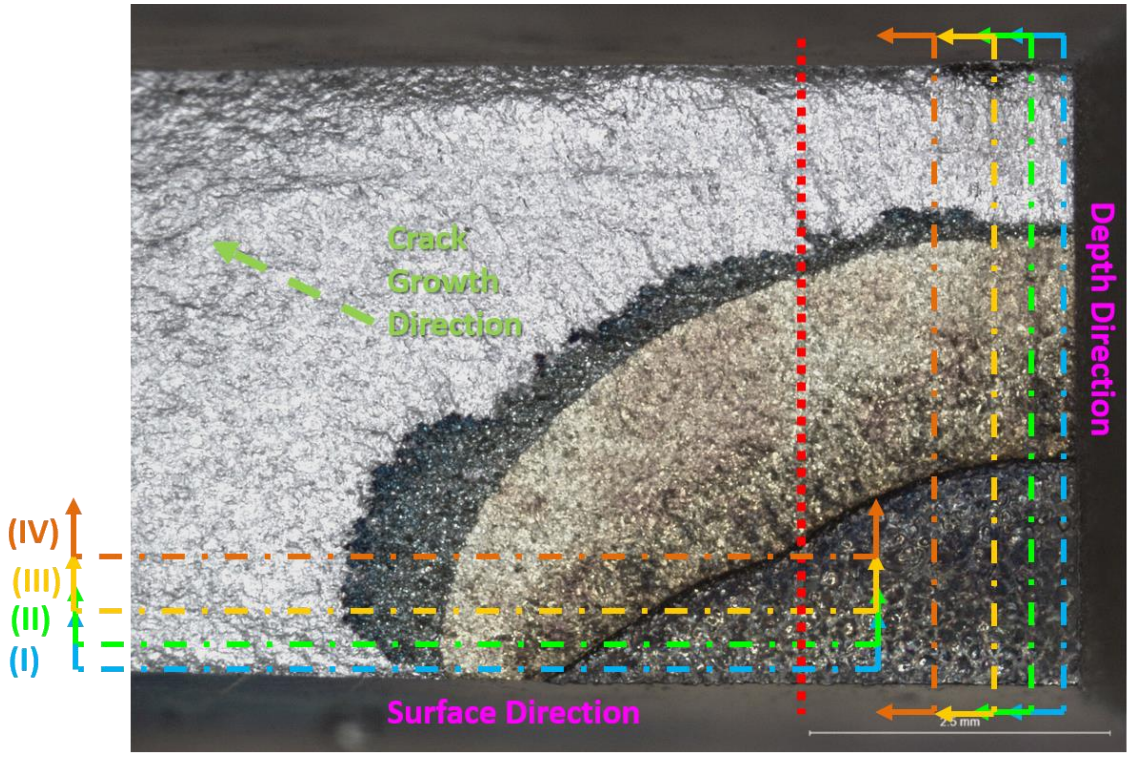

Figure 115: Sectioning diagram of the unbroken half of the interrupted K-hold (718-KH-007) experiment superimposed on the mirror image broken half's fracture surface. The two blocks of material were separated along the dashed red line. Sections were taken at approximately 10 (I), 260 (II), 510 (III), and 1010 (IV) μm respectively.

The depth direction Section I can be seen below in Figure 116. The same regions of crack growth seen in Figure 109 are present in the unbroken half of the specimen. From right to left they are, the EDM notch, the tortuous short crack region, the planar long crack region, and the intergranular region. The intergranular region in this direction mostly shows damaged grain boundaries that mostly lie at 45º angles from the crack growth direction. Where the damage is continuous, the slant sections are connected along grain boundaries that provide the shortest possible paths between the slants. In many places this damage is discontinuous on the image plane. These discontinuities later crack under subsequent cycling and form the transgranular ligaments seen in Figure 105.

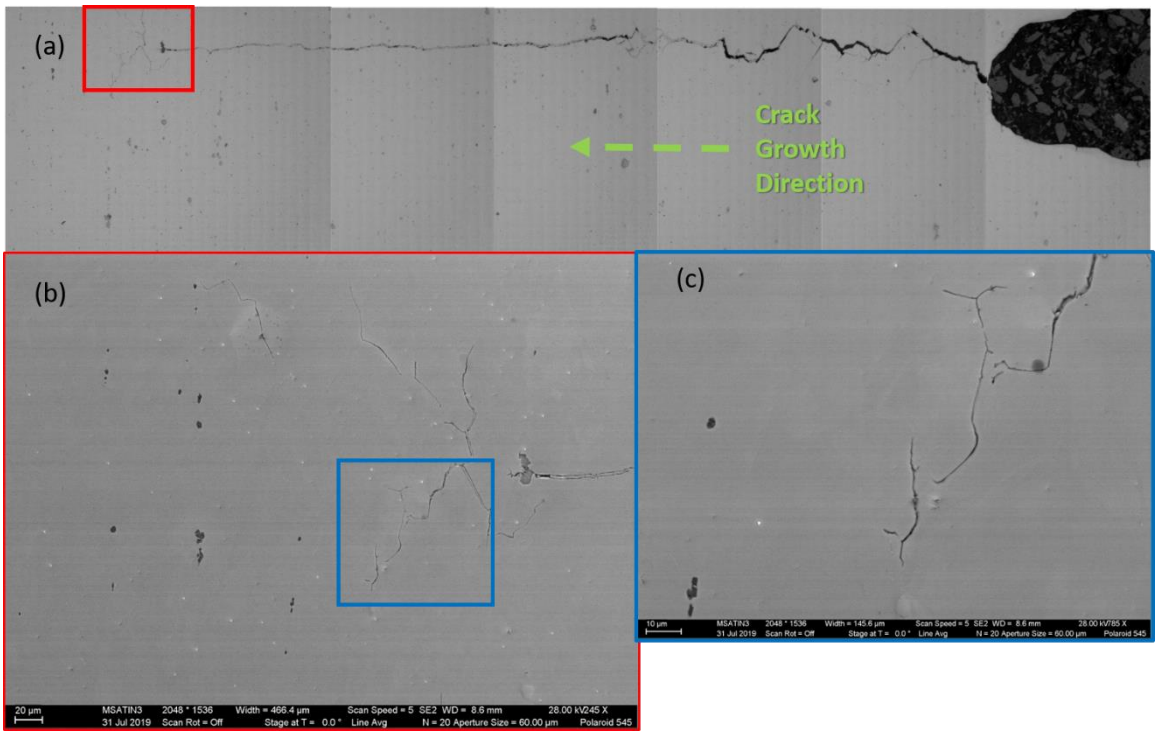

Figure 116: Optical and SEM micrographs of Section I of the a-direction in the unbroken interrupted K-hold experiment. (a) shows the entire crack length from the end of the EDM notch. (b) shows the intergranular portion at the end of the crack. (c) shows the discontinuous nature of the intergranular damage

The full extent of the intergranular region and its discontinuities can be seen in the etched image in Figure 117. The intergranular region is broken into at least four sections with smaller discontinuities contained within. All the damage seems to be limited to grain boundaries.

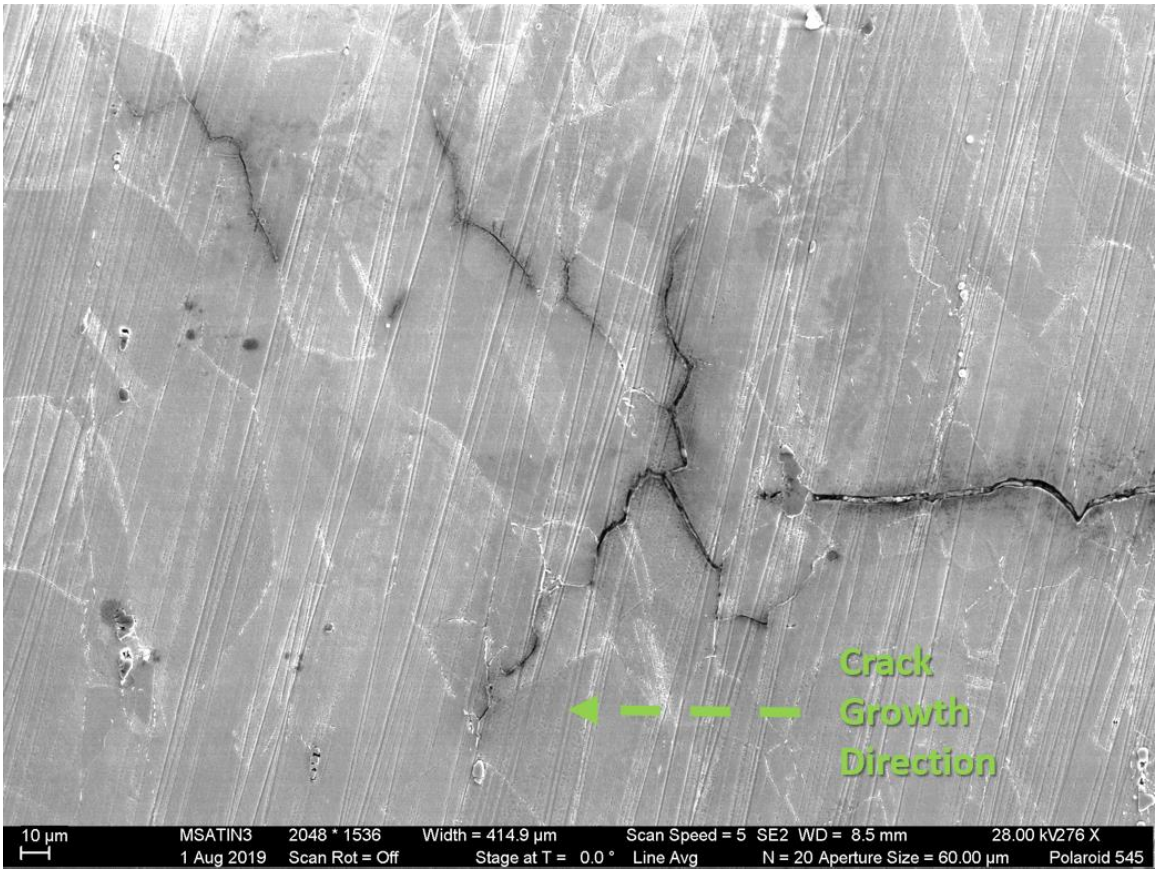

Figure 117: SEM micrograph of Section I in the a-direction in the interrupted K-hold test

The *c*-direction shows a more continuous and seemingly flat intergranular region. However, upon closer inspection it becomes apparent that the majority of damage still occurs at 45º angles that are connected by small segments so that the overall direction is in the crack growth direction. Figure 119 shows a magnified view of the intergranular region. Although the damage is more continuous, there is at least one major discontinuity. Additionally, there are areas where the damage flairs out at 45º angles to distances of 60 µm or more from the main crack plane.

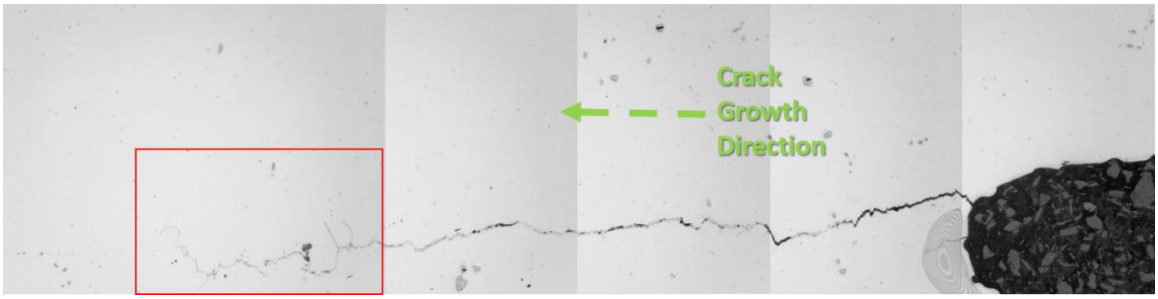

Figure 118: Optical micrograph of Section I in the c-direction in the interrupted K-hold test

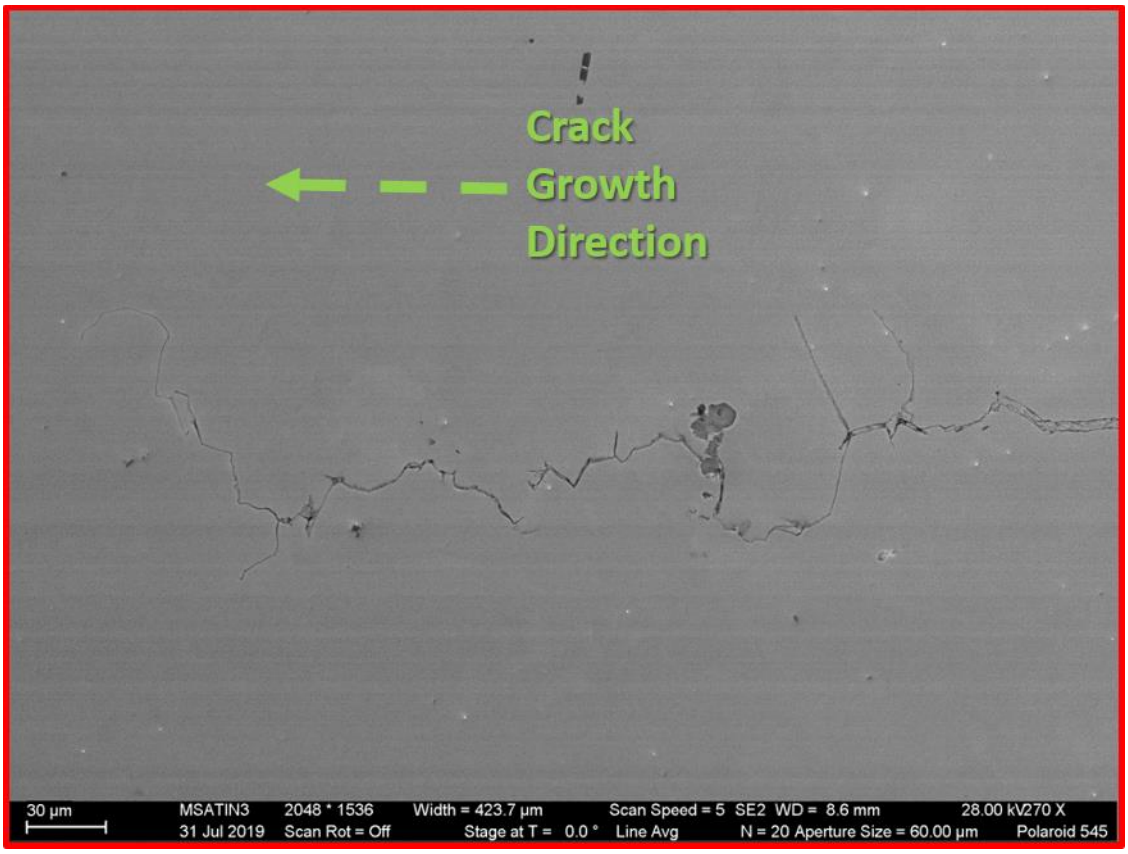

Figure 119: SEM micrograph of the intergranular region of Section I in the c-direction of the interrupted K-hold experiment

Unlike the profile mount, these unbroken mounts are difficult to etch. Because the piece is unbroken, etchant can get wicked into the crack and becomes very difficult to remove. This has the effect of overetching the crack area, and the effect tends to become worse over time. This effect can be seen in Figure 120. Sometimes large white compounds

will appear on the surface around the crack. These compounds and the crack itself can be identified in EDS due to their chlorine content which is not a native component of Inconel 718. Because of this, chlorine content can be used to positively identify cracked areas in the material after etching.

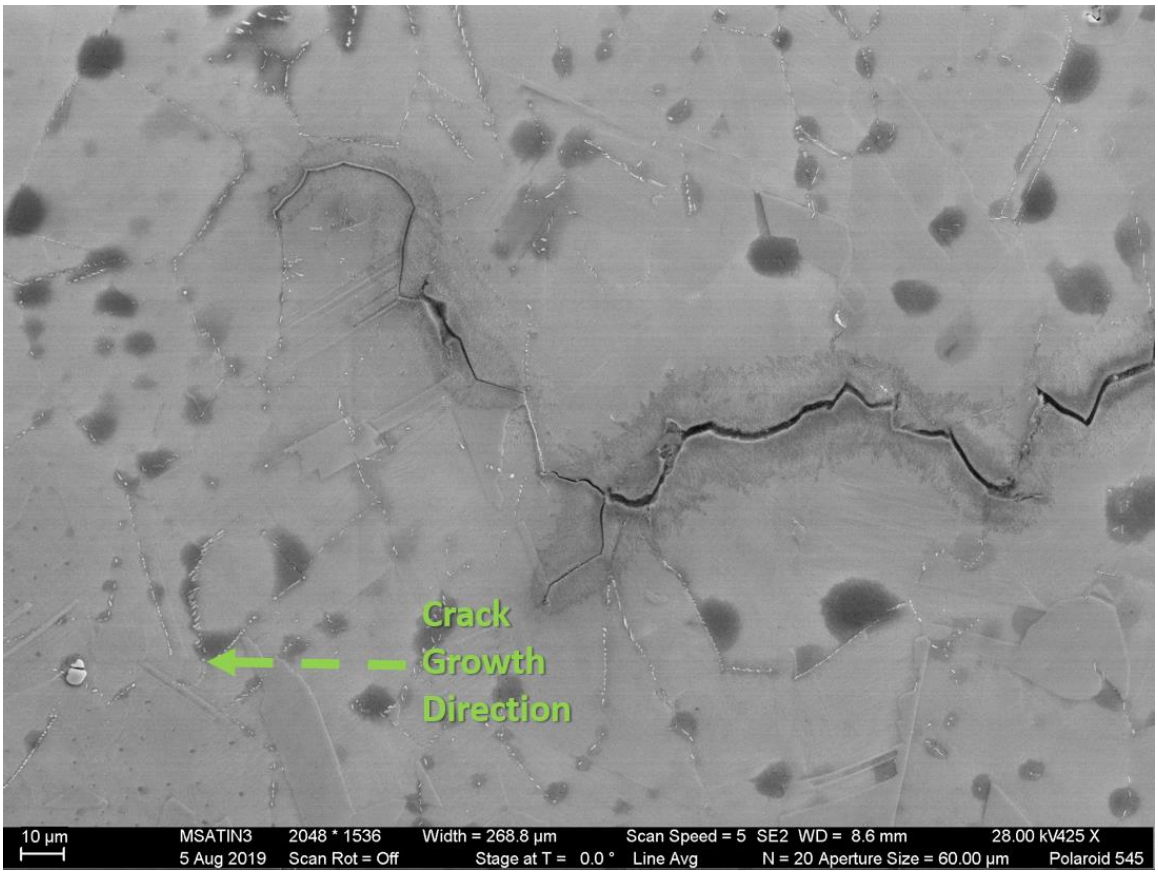

Figure 120: Overetched region of the c-direction in Section I showing a branching damage pattern

EDS can also be used to show the extent of oxygen penetration. Figure 121 shows an EDS map of a gap in the damage (at least on the pictured sectioning plane). Note that the diagonal parallel lines seen traversing the micrograph from the top left to the bottom right are polishing marks and are not part of the microstructure. This map shows that the crack can be identified by both the absence of Ni, but also the presence of oxygen (and

chlorine). This oxygen mapping shows that as expected, there is a significantly larger concentration of oxygen on the damaged grain boundaries. However, it does not show significant oxygen diffusion into the material itself. If oxygen did indeed penetrate into the host material preceding damage, it would be expected that an oxygen path bridging the gap would form. While the oxygen map shows very slightly more area then the absence of nickel, it does not show a significant gradient around the grain boundaries. It should be noted that light elements like oxygen are often not well characterized with EDS.

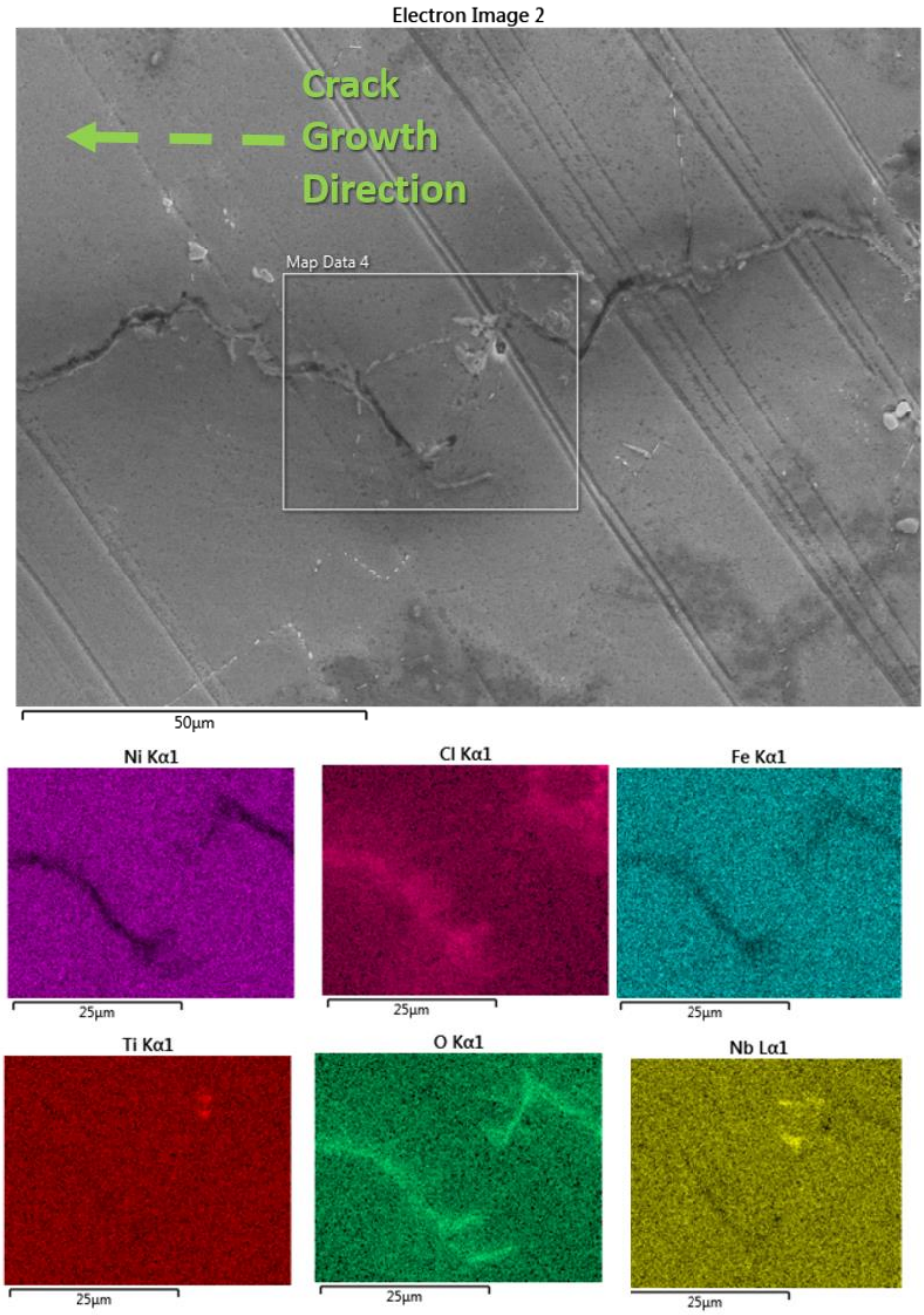

Figure 121: EDS mapping of a gap in the c-direction Section I intergranular region

The 260 µm deep section (Section II) shows development in the extent of damage in the *a*-direction. The two regions of damage seen in Figure 117 are larger but still discontinuous. Figure 122 shows that damage is still primarily comprised of 45º slant grain

boundaries with the exception of a vertical area of damage perpendicular to the crack plane. This may correspond to some of the steep cliff faces or deep secondary cracks seen in Figure 106.

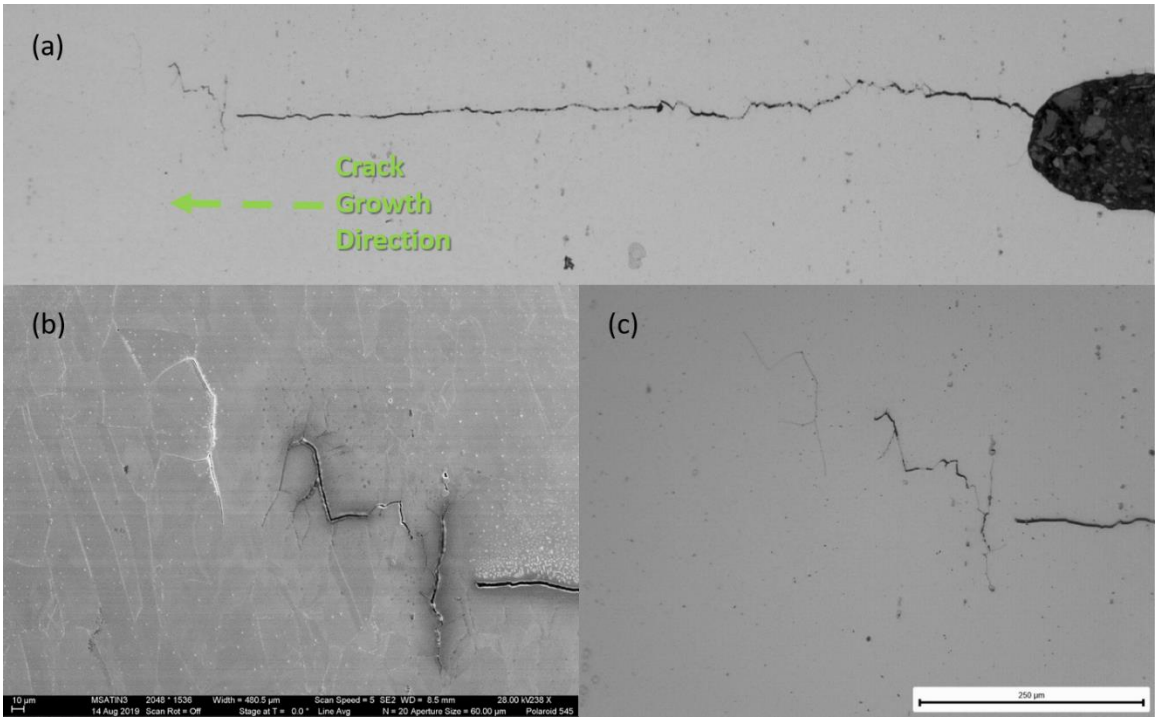

Figure 122: Optical and SEM micrographs of Section II in the a-direction of the interrupted K-hold experiment. (a) Optical micrograph of the entire unbroken fatigue crack showing small intergranular ribbon. (b) SEM micrograph of the etched intergranular region. (c) Optical micrograph of the unetched intergranular region

In this section, most crack branches seem to favor following grain boundaries that are rich with the white δ precipitates. An example of this can be seen in Figure 123 where grain boundaries just beyond the spread of the damaged region can be seen decorated with white δ precipitates.

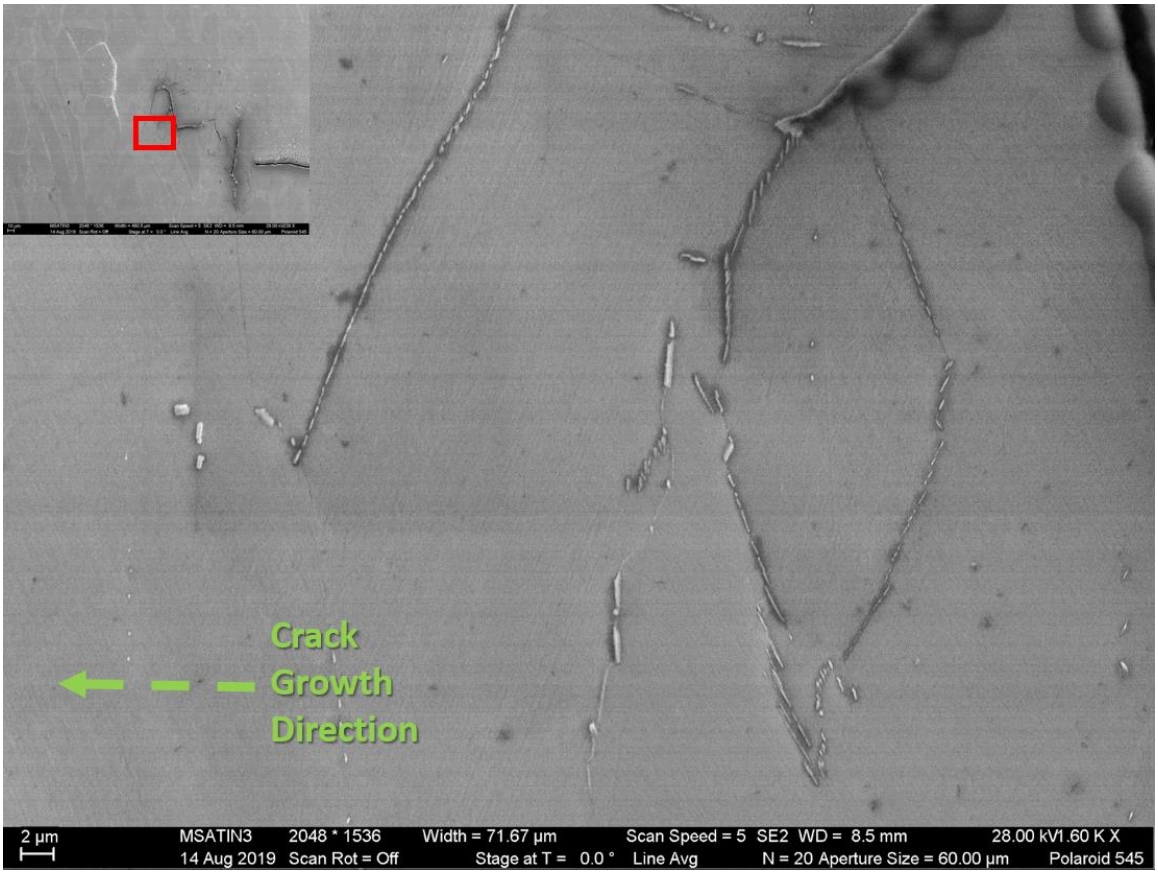

Figure 123: Magnified view of grain boundaries near the damaged area showing white δ precipitates

The *c*-direction of Section II has entered the edge of the main, large intergranular region. In this region the damage has progressed, linking many slanted grain boundaries into a chain extending for the better part of a millimeter. The damage has completely encompassed several grains on this plane but is still discontinuous in some areas especially close to the left side of the region.

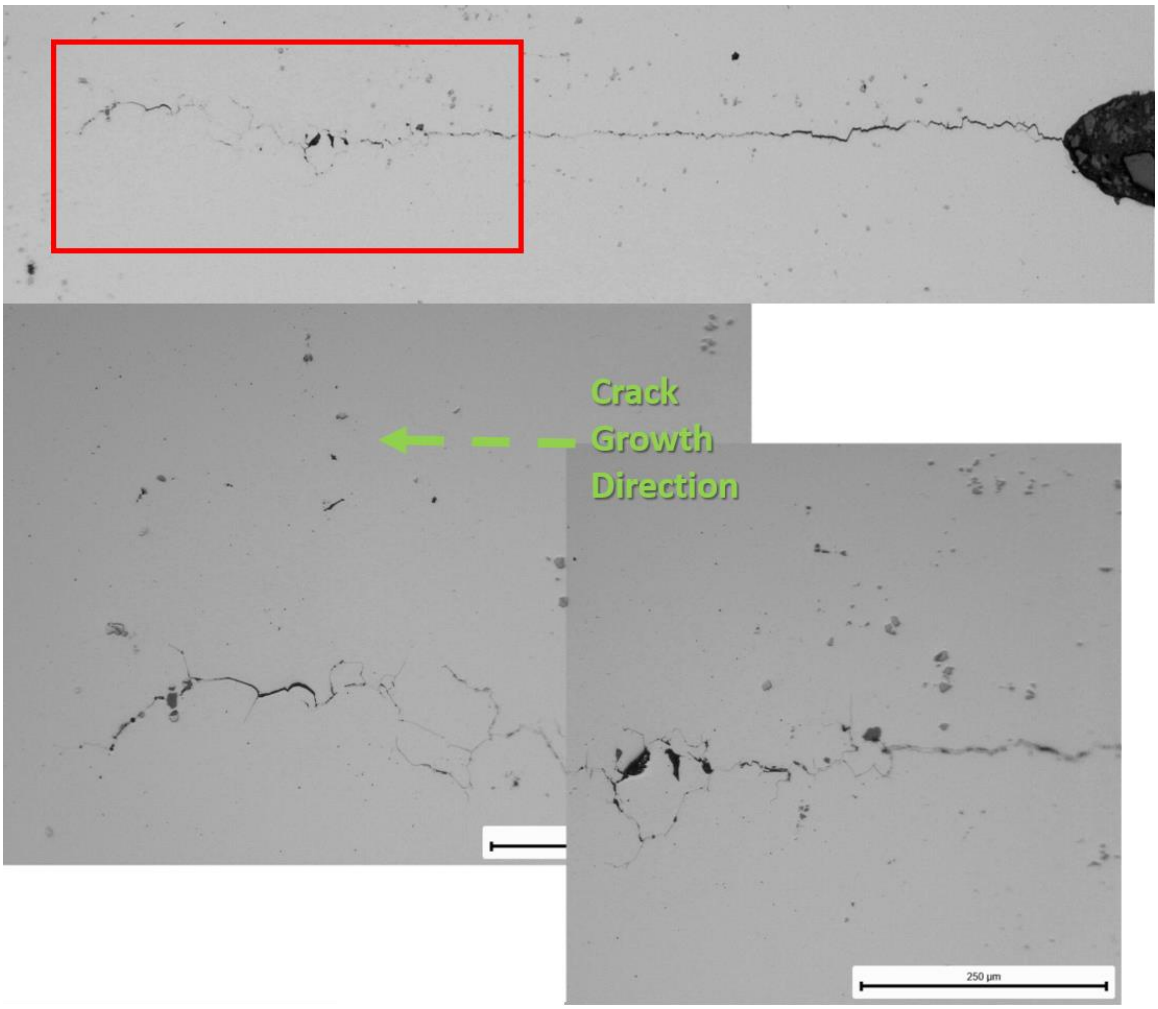

Figure 124: Optical micrograph of Section II c-direction showing the complete crack and damage (top) and a magnified view of the intergranular region (bottom)

EDS has been used to identify the darkened particles on the crack front that are visible to some extent in all sections including the profile sections. These particles have similar shapes and sizes to the carbides in the material around them, and like those carbides they are rich in Nb, Mo, and Ti and lack Ni, Cr, and Fe (Figure 125). One thing that can be seen from the EDS map is that the darkened carbide is rich in oxygen while the "normal" carbides around it do not show this enrichment. This color change induced by the oxidation of the carbides is another way to measure the depth of oxygen penetration into the material. In Figure 125, several carbides lie on or near a compromised grain boundary. However,

the oxygen from this damage has not darkened all of them fully showing that oxygen penetration is still very localized to the grain boundary itself. Careful examination of other micrographs shows that carbides can be very close to these boundaries without darkening, but nearly all carbides on the boundaries themselves are dark.

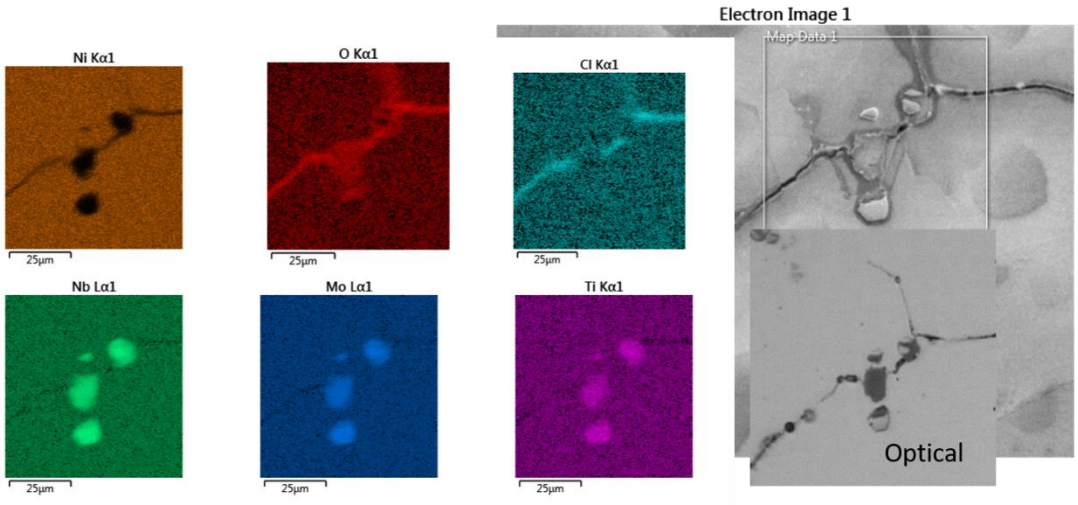

Figure 125: EDS map of oxidized carbides on the damage front in the c-direction of Section II

It should be noted that while there seems to be a preference for the damage to follow grain boundaries with the small white δ precipitates, they don't seem to be necessary. Figure 126 shows some examples of these branches. It is also possible that part of the grain boundaries consumed were previously rich in precipitates that are no longer visible due to the intergranular damage.

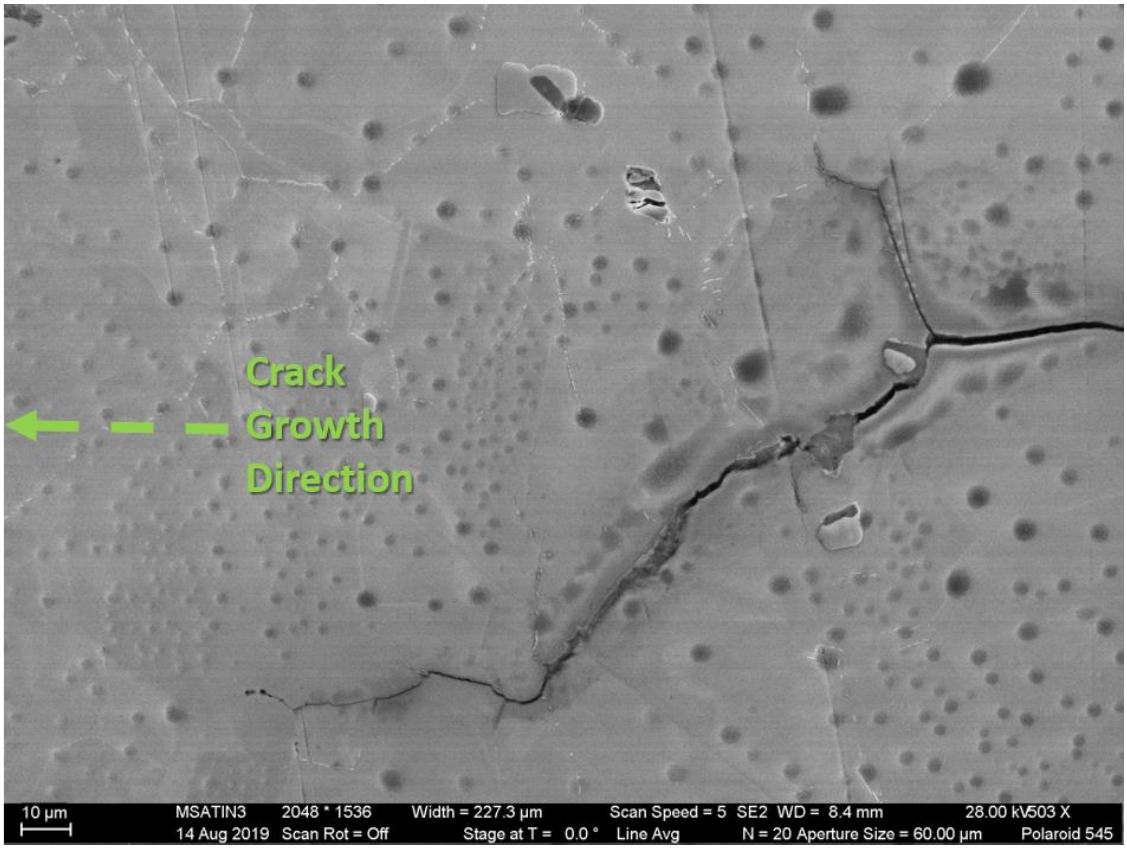

Figure 126: Etched SEM micrograph showing damage branches in the c-direction Section II crack

Section III shows many of the same features as the preceding sections. The damage in Figure 127 (showing the *a*-direction) is still mostly at 45º angles and shows a considerable amount of discontinuity. An interesting phenomenon appears when this area is etched. Figure 128 shows two areas circled in red where the damage seems to have crossed a grain at the exact angle of the twin boundaries within that grain. Although the damage is discontinuous in the viewing plane, it must connect at a different level. If it didn't there would be no path for oxygen to attack the boundaries, since it appears that diffusion through the crystals themselves is very limited. It's possible that the section of the three dimensional grain boundary that was damaged followed the edge of a twin

boundary as a preferred pathway. It could be hypothesized that this damage could spread more easily in heavily twinned grain structures.

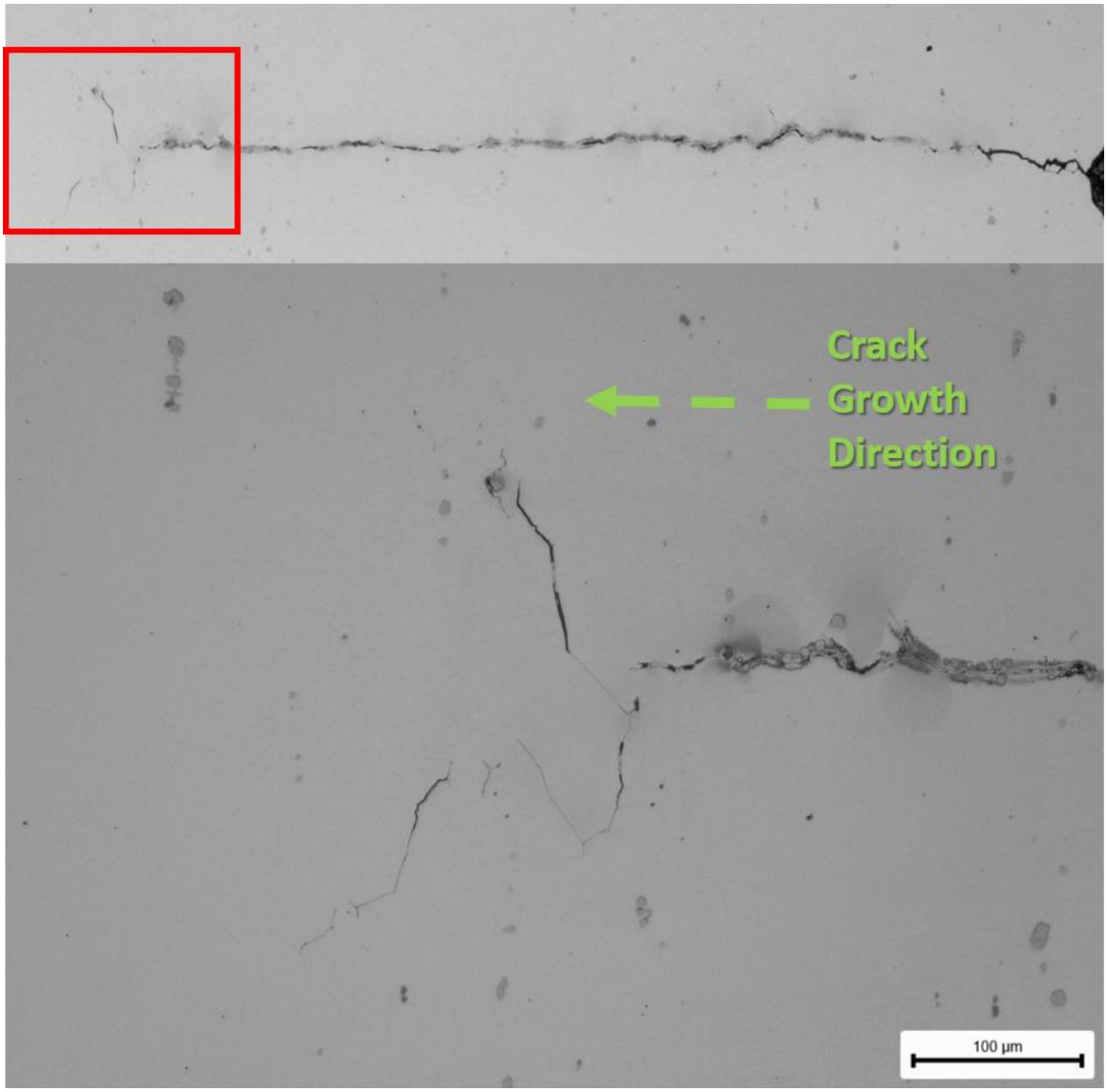

Figure 127: Optical micrograph of unetched section III in the a-direction

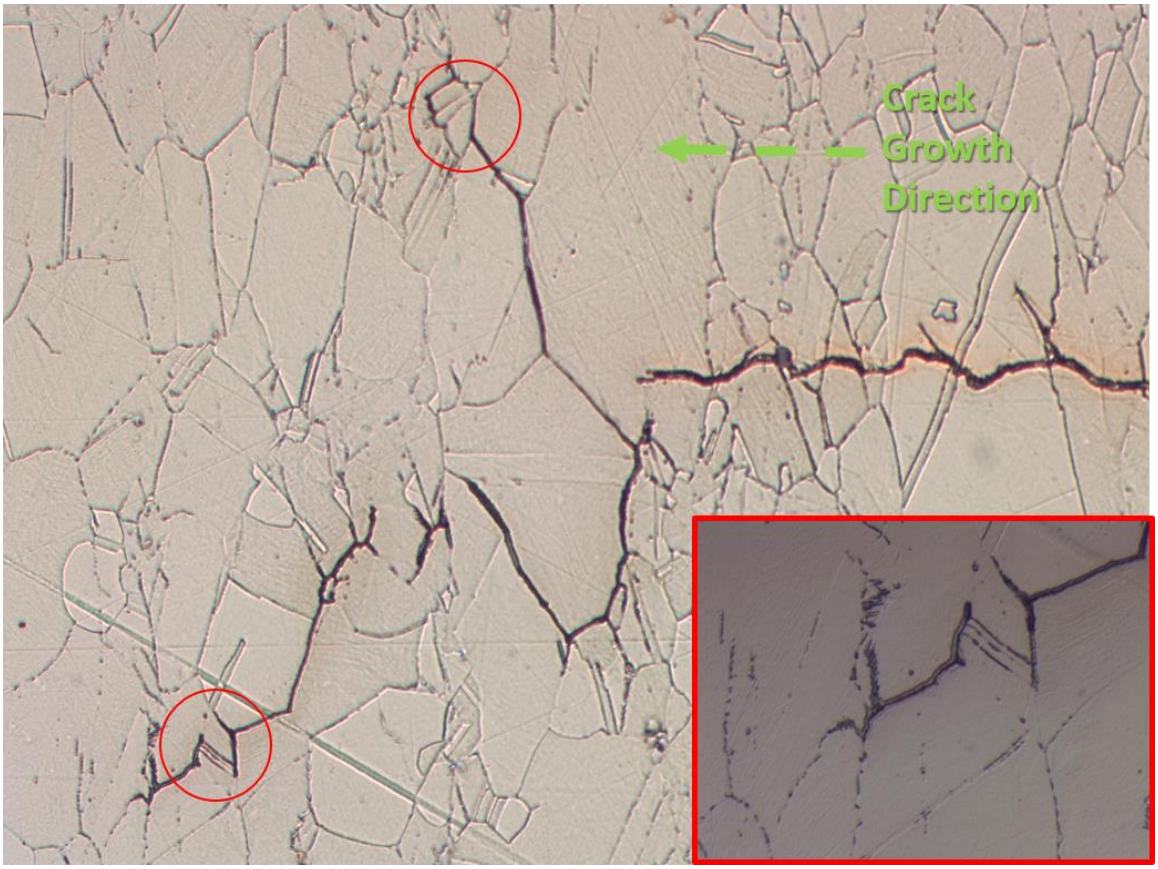

Figure 128: Optical micrographs of the etched intergranular regions of the a-direction in Section III showing two regions in red where damage appears to have crossed grains at the angle of twin boundaries

The Section III micrographs in the *c*-direction show the longest intergranular region yet. This regions extends over 1.2 mm which is very similar to the maximum extent seen in the mirror image fracture surface in Figure 102. The very end of this region shown in Figure 129 is very discontinuous in nature, far more than any of the previous *c*-direction micrographs.

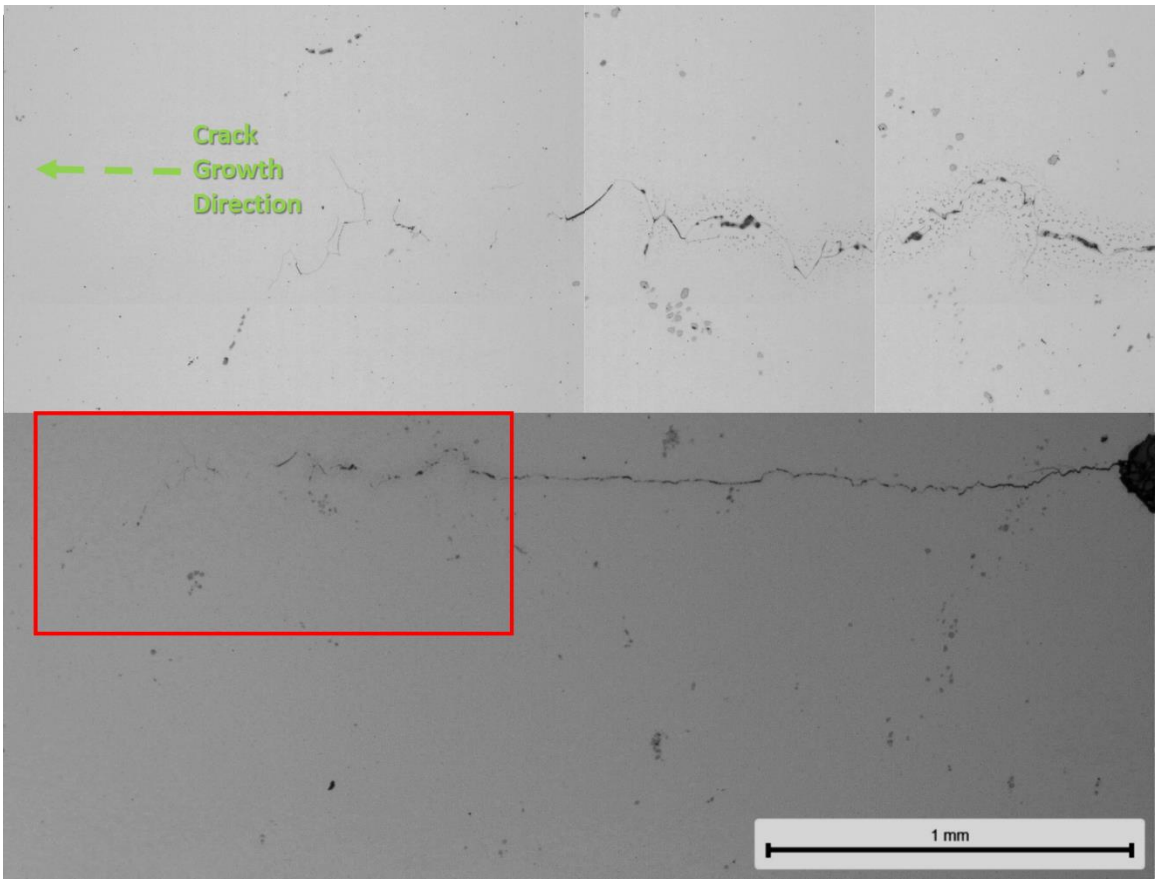

Figure 129: Optical micrograph of Section III in the c-direction showing the overall crack length (bottom) and a magnified view of the intergranular region (top)

Section IV in the *a*-direction finally shows a link between the main crack body and the vertical section that has appeared in the previous sections. Figure 130 shows a much more continuous crack then what's been seen in this direction previously. This could make sense since (on the mirror image fracture surface) this section was taken from a more developed region of the K-hold zone.

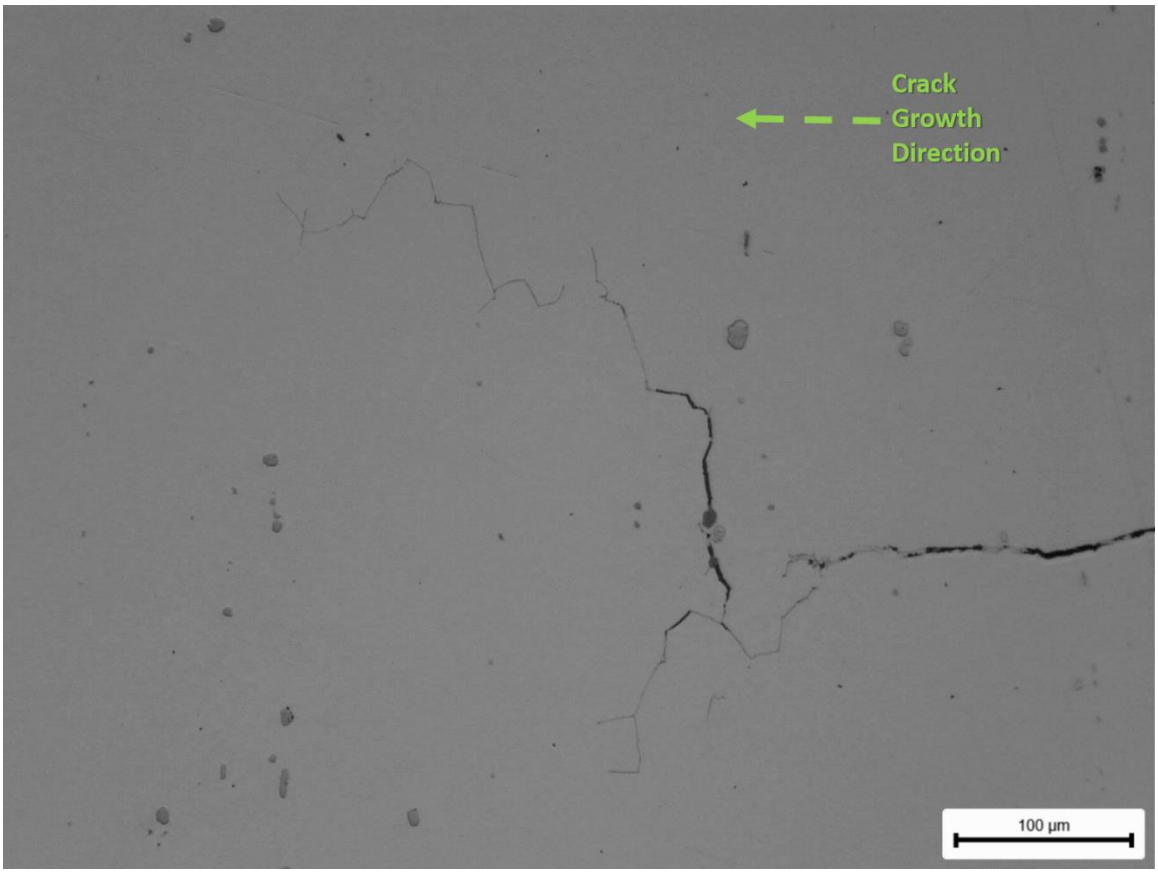

Figure 130: Optical micrograph of the intergranular region of Section IV in the a-direction

Section IV in the *c*-direction shows a less organized, more disconnected intergranular region that actually has a second branch splintering off to the bottom of the main damage region. This region is shown in the red oval in Figure 131 and is much less developed then the main damage path above it.

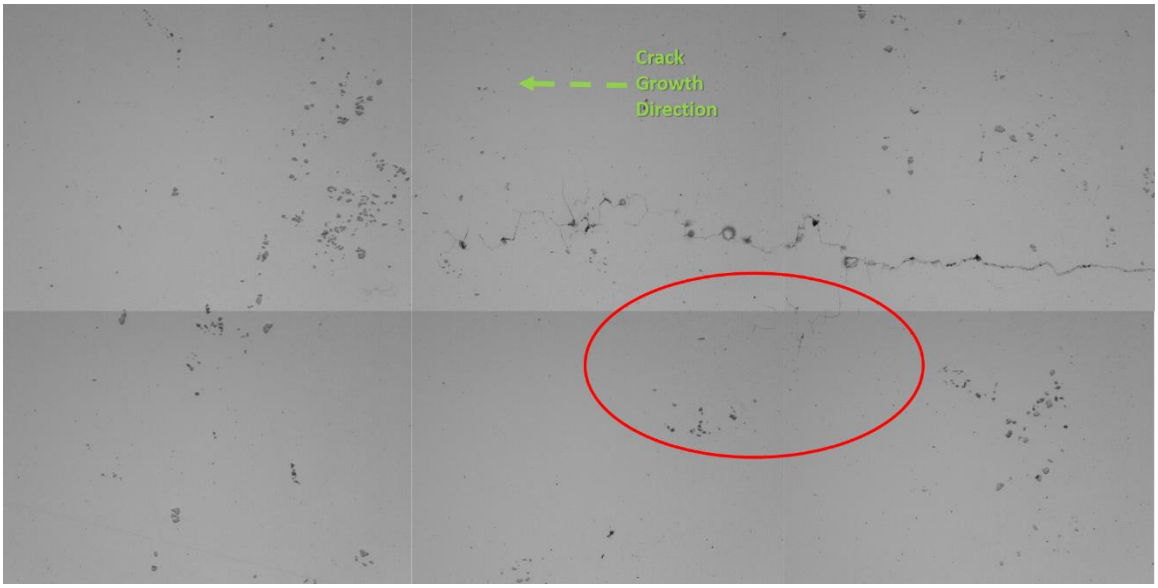

Figure 131: Optical micrograph of the c-direction in Section IV showing a branching damage direction in red

Microhardness testing was performed on the *c*-direction Section IV mount in order represent the "worst case scenario" for material damage. Measurements were taken using a Mitutoyo HM-200 Hardness Testing Machine using 0.5 kg Vickers indentations. First, measurements were taken on a metallographic mount of the CGIN718 material that had been prepared from an untested specimen and as such had not been exposed to high temperatures. The measurements averaged a Vickers hardness value of 488 HV.

A microhardness traverse was performed starting near the center of the intergranular region of the crack and moving away from the crack plane. The closest indention was 60 μm from the crack plane, and the spacing was gradually increased as the indentions moved away from the region of interest (Figure 132).

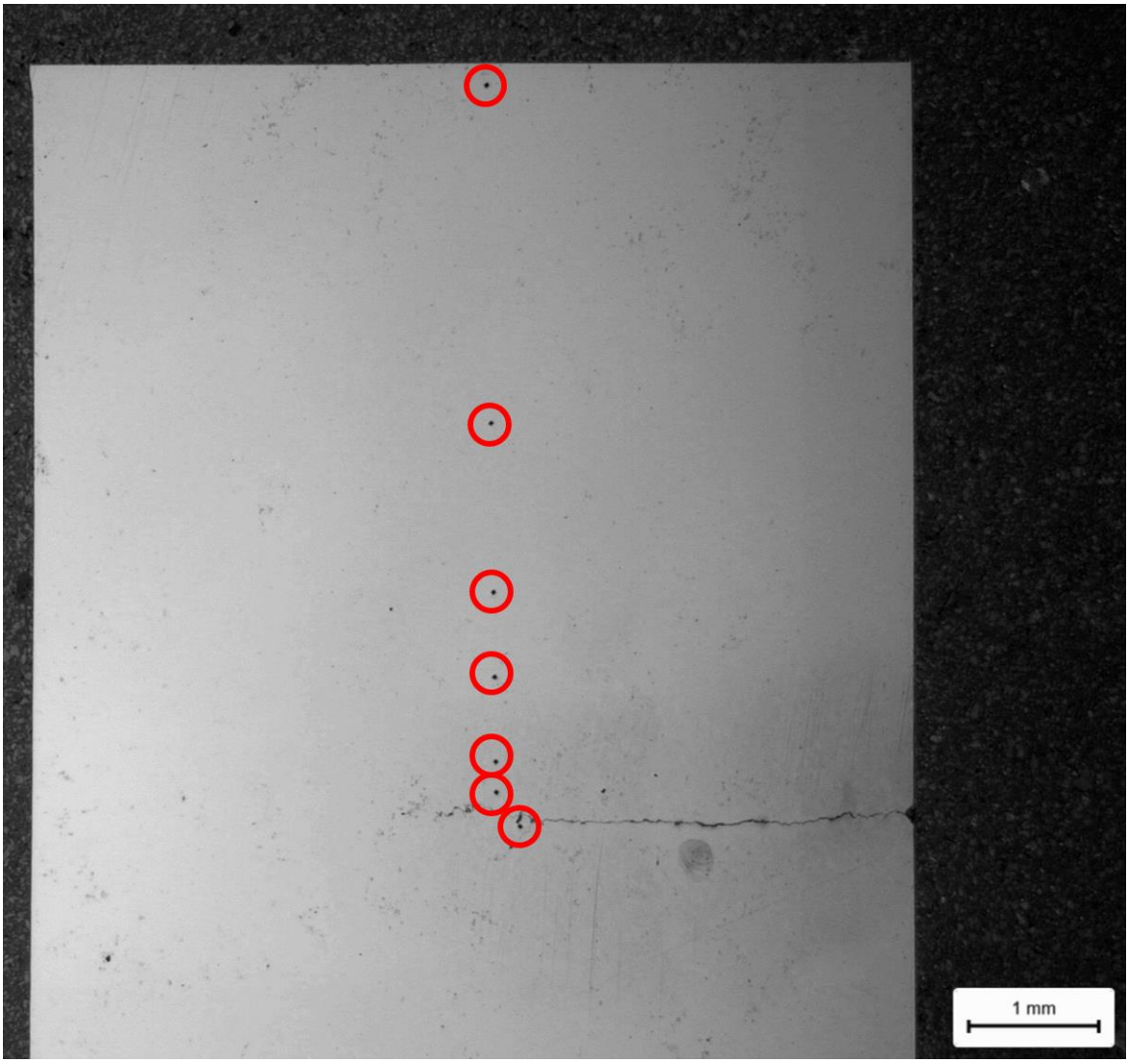

Figure 132: Microhardness Traverse Locations in the c-direction of Section IV

Each hardness indentation was measured and the Vickers hardness values were calculated. Figure 133 shows very little variation in hardness as a function of position. The average hardness value for the traverse was 473 HV which is very similar to the hardness seen in the base CGIN718 mount.

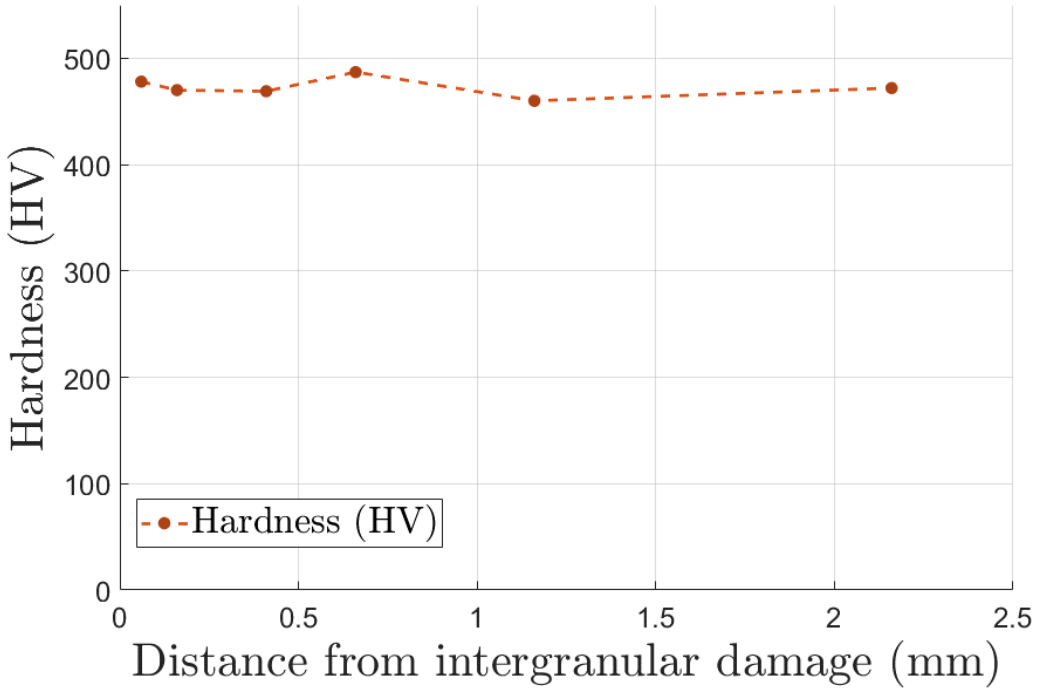

Figure 133: Microhardness values as a function of distance from the crack plane

An additional indentation was made between two branches of the intergranular damage to try to represent an extreme value and can be seen in Figure 134 below. This indentation measured 490 HV which again is very similar to the hardness values seen in the traverse and the base material.

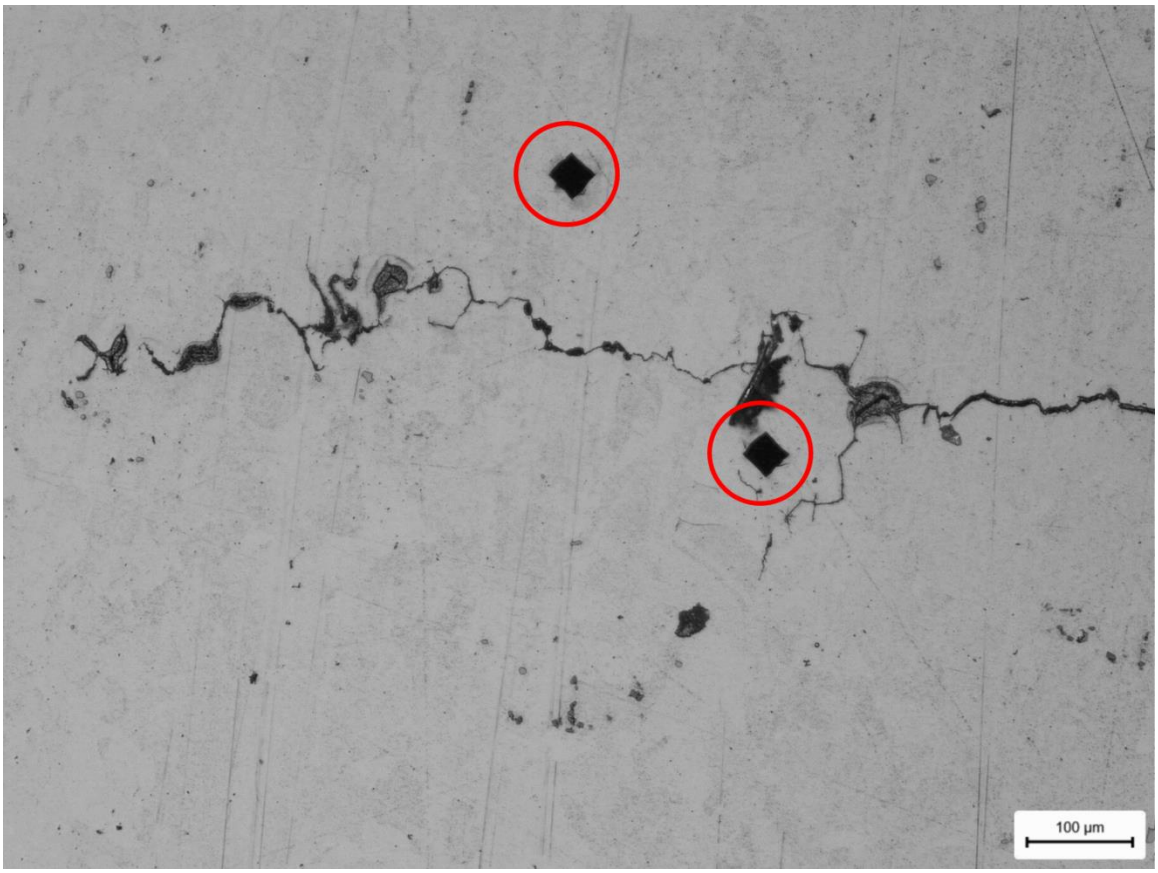

Figure 134: Microhardness indentation locations in the intergranular region of the c-direction Section IV

No large change in hardness was seen in any of the hardness testing performed. This matches observations that there is no apparent change in the microstructure of the material after testing. These observations show that there is no larger scale damage occurring away from the affected grain boundaries in the intergranular region and that the "process zone" for this damage affect is very localized.

It is evident from these unbroken sections that there is wide area of somewhat discontinuous damage that is a mixture of time-dependent crack growth and "TAZ" grain boundary weakening. However, when the profile sections are examined, there are very few secondary cracks and they are all very short. This means through the process of

subsequent cycling and fracture, much of this information is lost. One logical explanation is that in more developed damage regions, entire grains are ringed by broken boundaries. Once the crack progresses through that region and those grains are exposed to a free surface they simply fall out making it appear that the damage region is much thinner in the height direction of the plate.

These micrographs have shown compelling evidence that damage is constrained to grain boundaries and that this damage is not due to oxygen diffusion through the crystal structure itself. When looking at those tests that had intergranular growth and did not break through the back face of the material such as Figure 95 and Figure 102 it is evident that material constraint is an important factor in the extent of this damage. It is likely that in areas that are under a large amount of constraint, grain boundaries can be dilated by the high hydrostatic stress opening pathways for more oxygen penetration. This coupled with plasticity along directions of maximum shear cause boundaries at 45º angles to become compromised opening the boundary for further oxidation.

This experiment also sought to detect any obvious changes in material microstructure due to the oxidation damage. No obvious damage beyond the grain boundaries and the carbides directly on those boundaries was seen. This does not rule out the preferential oxidation of Nb from γ'' precipitates, as they were not visible using the etching techniques in this experiment. However, no obvious change in Nb levels were seen using EDS mapping.

It also seems that there is definite time-dependent crack growth which has been noted in past literature. Although not proven with certainty, it is likely that the lack time-dependent growth seen by Radzicki was due to this damage not accumulating on slant

growth shear lips. Upon examination of Radzicki's research, it is evident that shear lips played an important role in the FGIN718 material he worked with (Figure 135). He showed that at room temperature slant growth started almost immediately and was the preferred growth mode. Because of this any K-hold experiments performed on the FGIN718 material in the thin SENT specimen configuration would likely have had shear lips blocking the view of time dependent crack growth.

(a) Room temperature isothermal crack growth at 8 Hz failure surface showing chevron like shapes

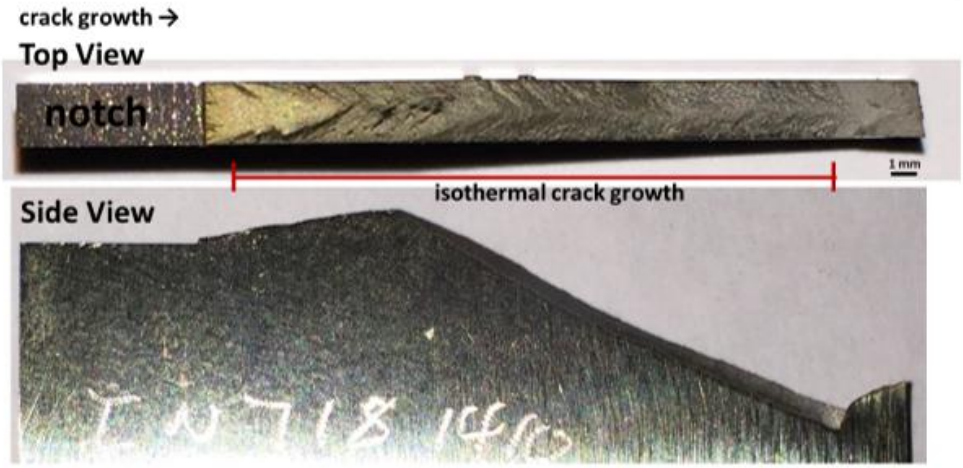

(b) 427°C isothermal crack growth at 10 Hz failure surface showing chevron like shapes

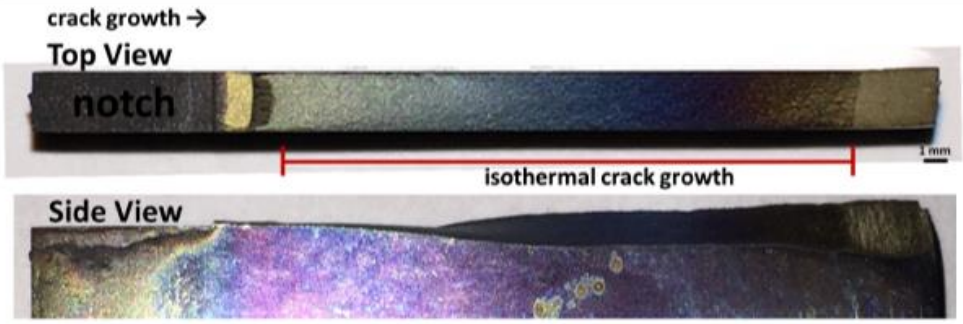

(c) 650°C isothermal crack growth at 10 Hz failure surface showing no chevron shapes

Figure 135: Isothermal fracture surfaces from Radzicki [1] *showing dominant shear lip formation at room temperature*

It is not clear why the TAZ identified by Radzicki had a distinctive pattern of flat transgranular ridges that aren't seen in the present observations. It stands to reason that

this morphology could be a special case that may occur with the FGIN718 material in thin sections.

2.4.3. Isothermal High Temperature Fatigue Results

2.4.3.1. Objectives

Isothermal testing at 650 ºC on the CGIN718 material was used to satisfy two different objectives. The first objective was the need to find a marking technique that worked at high temperatures. It had been observed in earlier testing that R=0.7 marker bands that were inscribed on the surface at room temperature and subsequently exposed to high temperatures were no longer visible. Because in-situ measurements for surface flaws are limited to observing the surface, a marking technique would be necessary if shape information and calculation of K values were to be performed on the future TMF testing.

As stated above in section 2.3.4, the two candidates for marking were switching to an R=0.7 waveform at high temperature, and switching to an R=0.1 f=2 Hz frequency to create a mixed trans/intergranular region on the fracture surface that could be observed post-fracture.

The other objective of the experiment was to evaluate if the TAZ Acceleration Factor (TAF) was active in one direction, neither direction, or both directions. The initial hypothesis based on Radzicki's observations was that TAF might act in the *a*-direction (depth direction) and not the *c*-direction (surface direction). This was based on his observations that the TAZ did not seem to grow in plane stress regions and that the characteristic K-hold shape was elliptical in nature with no growth seen at the surfaces

(Figure 44). However observations from the K-hold experiments in this project showed that time dependent growth does occur and it is not always absent from the surface.

2.4.3.2. Initial Predictions

Changes were made to the MPYZ-TMF code to accommodate surface flaws in the TAZ development model. Because the *c* direction is always at a free surface a value very close to the plane stress condition of α (α=1.2) is assumed to always be true. In addition, the calculation of α in the *a* direction was changed so that the comparisons shown in section 2.3.1 for determining stress state were made with the remaining uncracked ligament length *t-a* instead of the full thickness *t*.

The MPYZ-TMF code was additionally modified so that the TAF could be switched on and off in different directions to see what affect it might have on the simulation. Figure 136 shows the possible shape evolution paths starting at the end of the second room temperature section in the experiment and assuming the 0.1 Hz base waveform was used to failure. The figure shows that if the TAF is active in only one direction it will cause a very obvious change in the shape evolution that can be measured. If instead the experiment shows a shape evolution closer to the center two lines (stable shape) then it won't be possible to decide if TAF is active in both directions or neither direction but it would be obvious it wasn't active in only one direction. It should be noted that all simulations for the high temperature portion of this experiment use Radzicki's Forman fits shown in Figure 39.

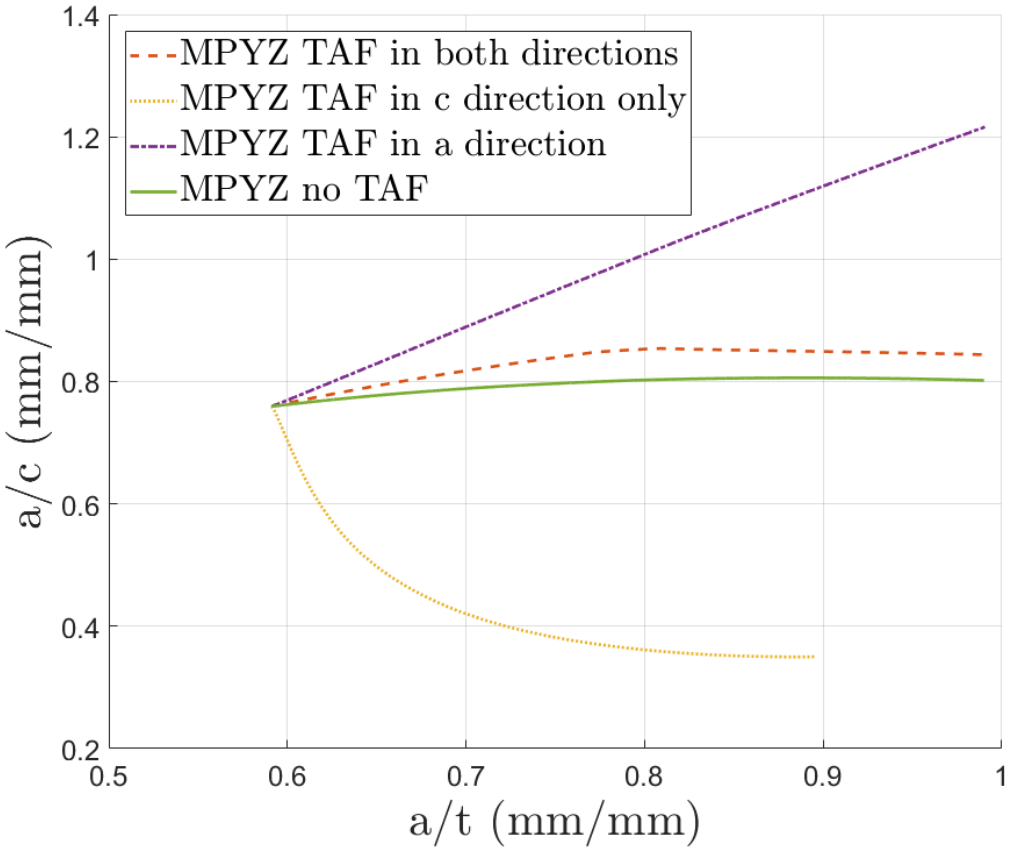

Figure 136: Shape evolution simulations using the high temperature isothermal fatigue experiment conditions sowing different shape paths depending on the application of TAF

2.4.3.3. In-Situ Observations

Abbreviations have been assigned to the loading steps in the isothermal fatigue test to make the bands easier to identify with "S" bands referring to the "slow" 0.1 Hz bands and "F" bands referring to the faster marker band candidates. The table of loading steps with the appropriate abbreviations has been reproduced below:

Table 28: Fatigue steps for the isothermal high temperature fatigue test with abbreviations

Step Label	Abbreviation	Max Load (kN)	Temperature (ºC)	R	Frequency (Hz)	Cycles
Initiation	I	44	RT	0.1	15	300000
Precracking	P	60	RT	0.1	1	10000
Slow 1	S1	60	650	0.1	0.1	8297
Fast 1	F1	60	650	0.1	2	40000
Back to Room Temp	RT	60	RT	0.1	2	65028
Slow 2	S2	60	650	0.1	0.1	1561
Fast 2	F2	60	650	0.7	5	17136
Slow 3	S3	60	650	0.1	0.1	1178
Fast 3	F3	60	650	0.1	2	2225
Slow 4	S4	60	650	0.1	0.1	972
Fast 4	F4	60	650	0.7	5	6006
Slow 5	S5	60	650	0.1	0.1	417
Final	F	60	RT	0.1	2	17422

In-situ observations of fatigue crack growth at 650 ºC looks like a combination of what is expected from a room temperature type fatigue crack and the high temperature K-hold damage. Figure 137 shows a well-defined dark crack surrounded by a darkened damage region. Because of thermal etching effects in the polished region of the surface at high temperatures it is sometimes possible to see grain boundaries and to see that the crack is indeed mostly following them.

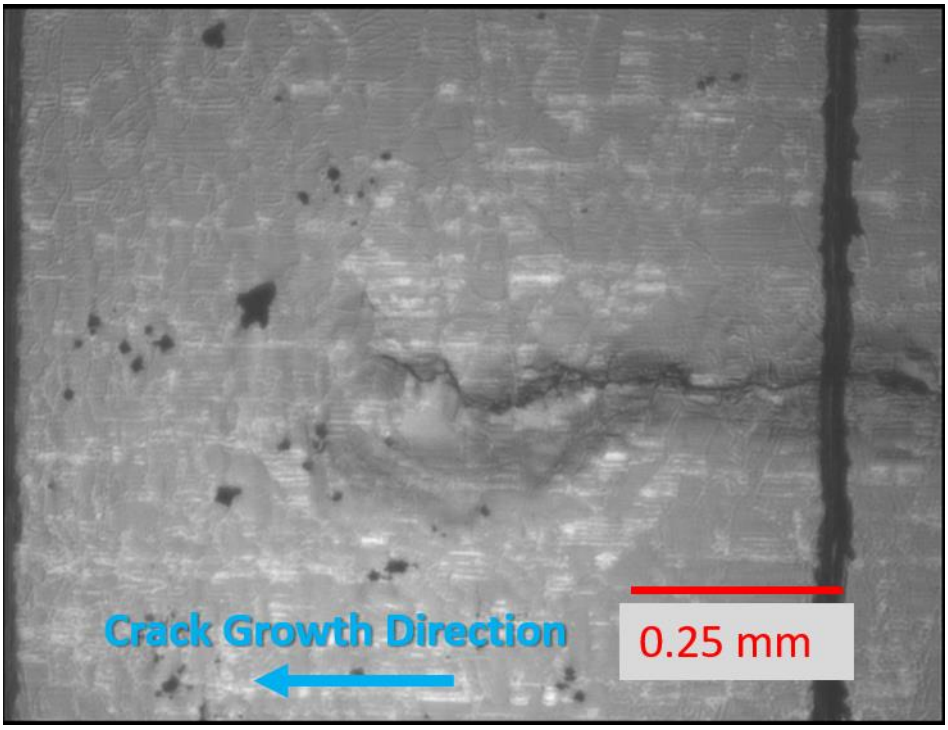

Figure 137: In-situ observation during the S3 band in the high temperature isothermal fatigue experiment

2.4.3.4. Fracture Surface Observations

The optical fracture surface reveals that both banding techniques were successful in creating readable data. The bands created for this experiment were made relatively thick since it was not known how readable they would be. In the optical image (Figure 138) the 0.1 Hz (S) bands have a much rougher appearance, and the final band (S5) (see Table 28) is ringed with a similar looking blue pattern to what is seen in the K-hold tests. Some bowing in at the surface can be seen especially in the blue fringe, however it does not seem to be a factor in the majority of the bands.

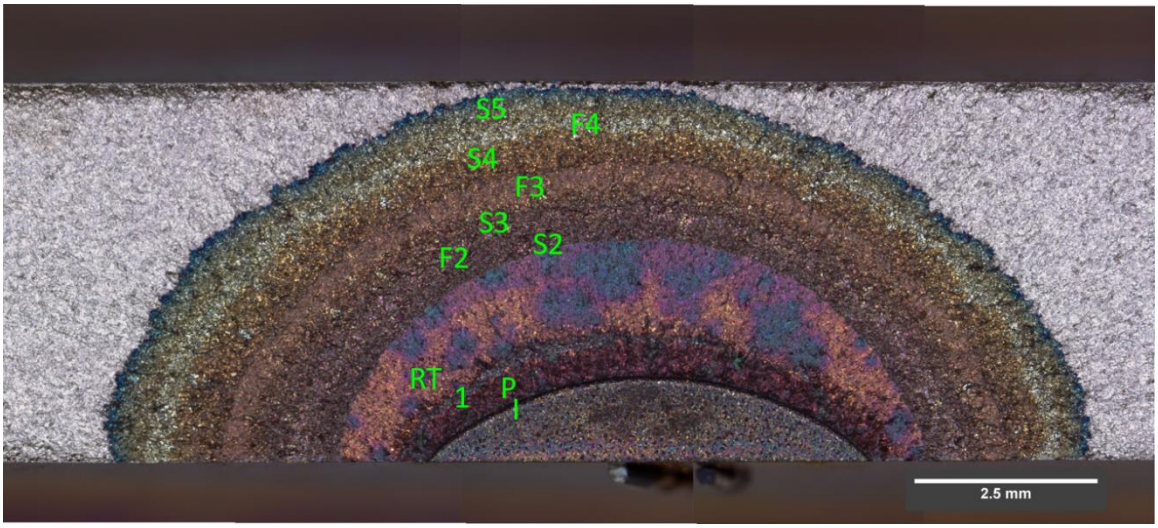

Figure 138: Optical fractograph of the high temperature isothermal test with bands labeled

SEM examination shows a somewhat chaotic mixture of intergranular and partially transgranular regions (Figure 139). Surprisingly the bands are actually easier to resolve with optical microscopy then SEM. Unlike the very clear demarcation seen in pictures like Figure 70, these regions are more difficult to resolve. Figure 140 shows a magnified view of the center region. It is clear that the 0.1 Hz "S" bands are primarily intergranular in nature, but they do not show the absolute-clean "rock candy" structure seen in Figure 70 on the first K-hold test. The R = 0.7, f = 5 Hz band F2 is only visible as pockets of darker, smoother material. The R = 0.1 f = 2 Hz band F3 is more visible showing a darker smoother profile which is why it was chosen as the marking method for the TMF test.

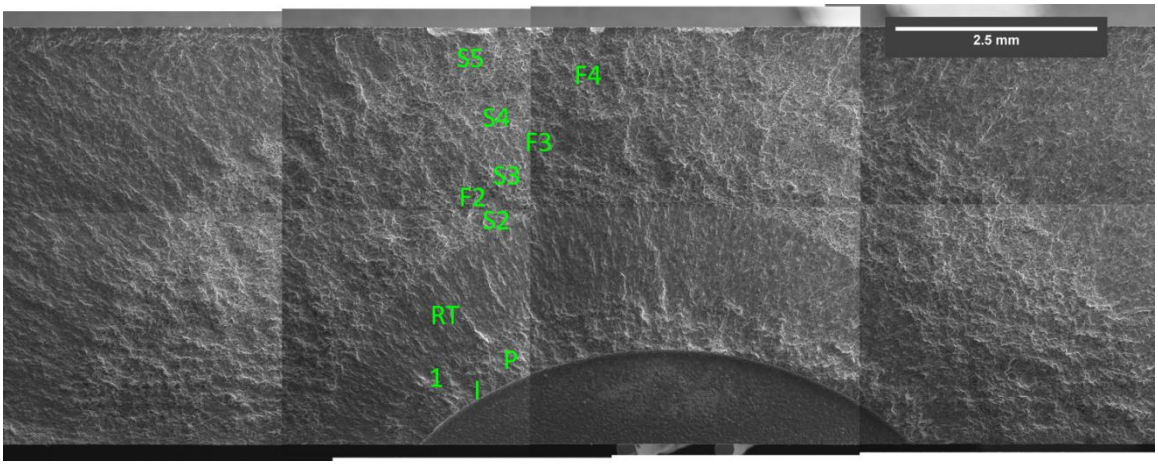

Figure 139: SEM fractograph montage of the high temperature isothermal test with bands labeled

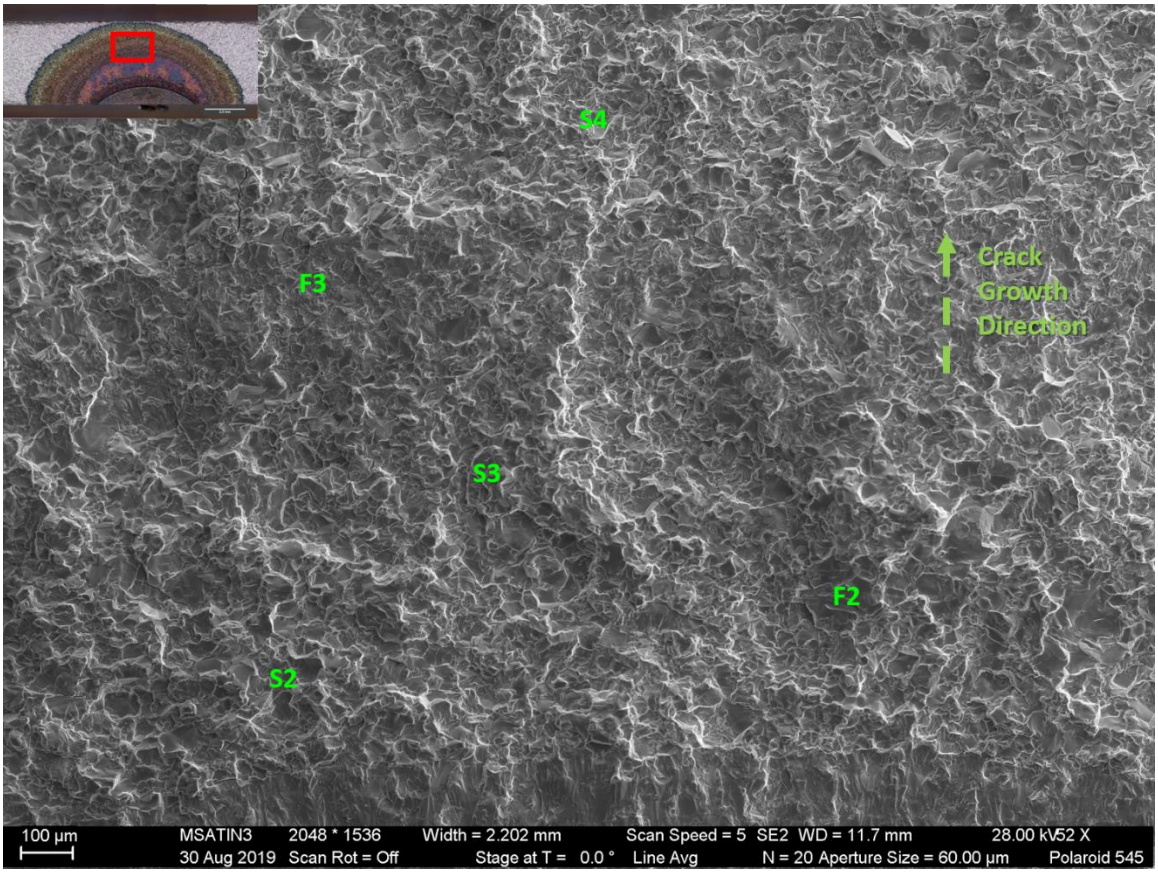

Figure 140: SEM fractograph showing a magnified view of the a-direction showing intergranular and mixed inter/transgranular behaviors

When looking a high magnification view in the surface direction, similar features are seen. The "S" bands show the typical intergranular pattern but with more white rimmed ridges ringing the grains indicating more damage from fatigue being added compared to the pure time-dependent crack growth seen at the beginning of K-hold regions. The F4 band shows a darker smoother pattern that is more planer but where grain boundaries can still be partially resolved. This mixed inter/transgranular growth that is likely due more to the f = 5 Hz frequency of the band then the R = 0.7 lowered amplitude effect which would bring striation spacing closer together.

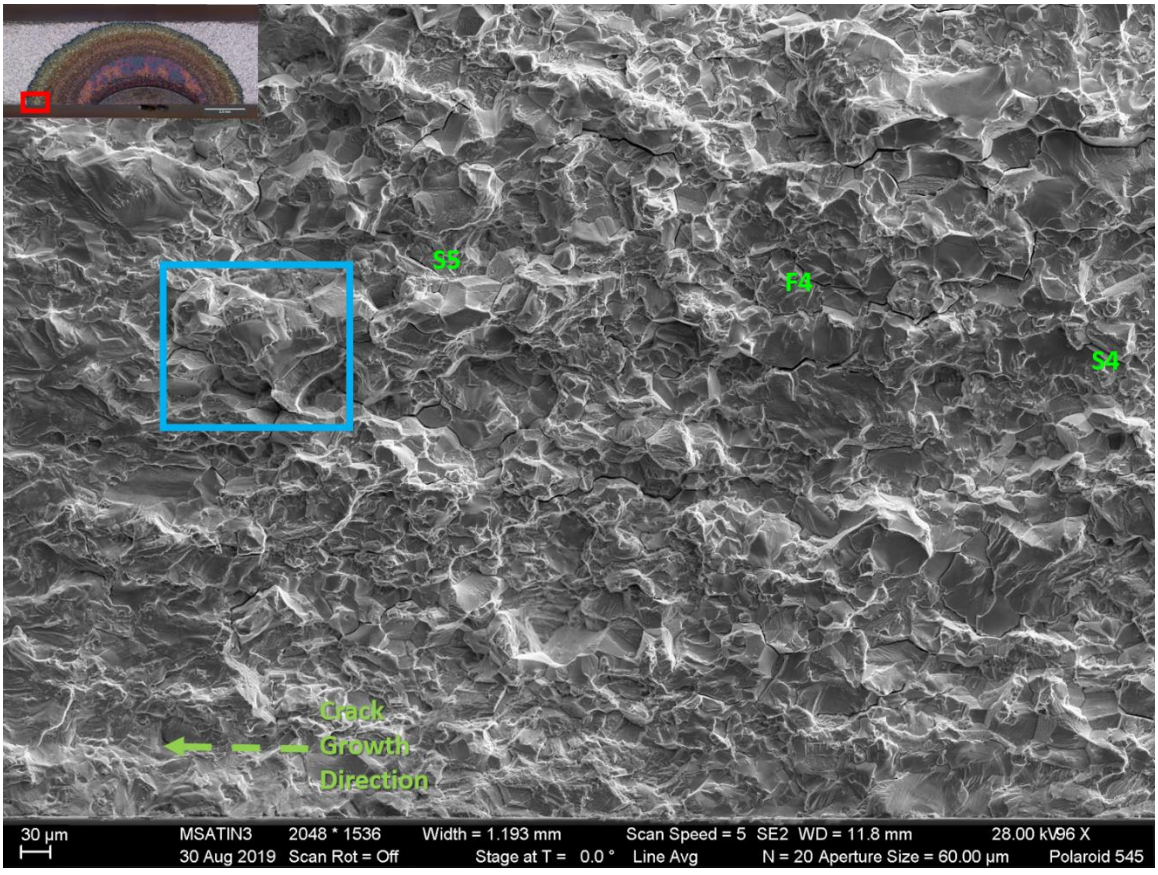

Figure 141: SEM fractograph showing the outer bands of high temperature crack growth in the c-direction with the field of view for Figure 142 highlighted in blue

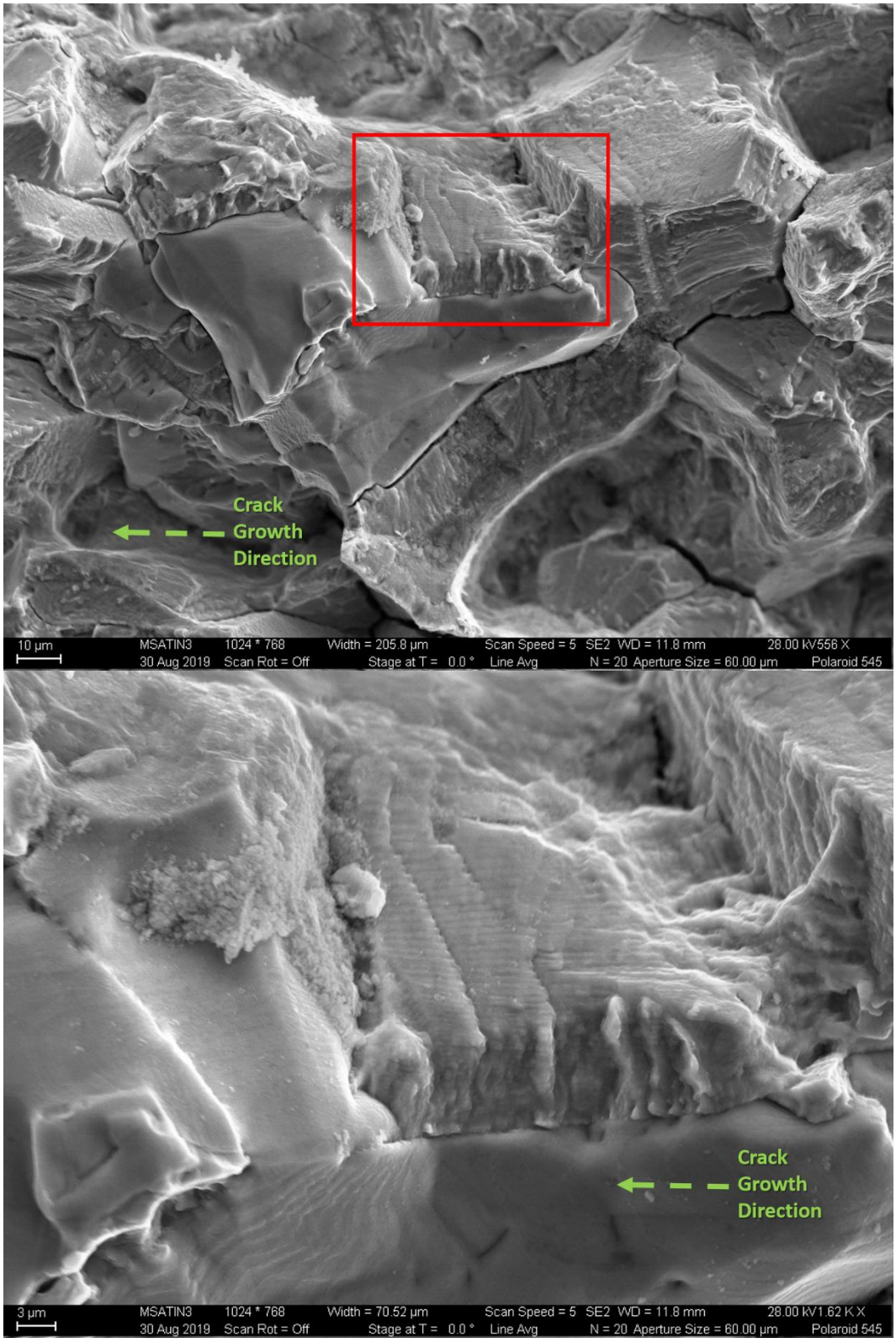

Figure 142: SEM fractograph showing a grain in the S5 band with fatigue striations

In Figure 142 (see above), a grain in the S5 band is magnified. The fracture is still very much intergranular with grain boundaries exposed on the surface. Some of these faces are smooth showing the time-dependent structure while others have well defined fatigue striations showing the cyclic mechanical damage. This further suggests a somewhat chaotic crack progression where grain boundaries are damaged in a time-dependent fashion ahead of the main crack plane and other boundaries are broken cyclically by fatigue under the increased local stress in order to advance the crack and "catch up".

Measurements were taken with the optical fractograph in Figure 138 in order to get shape and life information:

Table 29: Measurements and calculated K-values for bands in the high temperature isothermal fatigue test

Step Label	Abbreviation	Ending *a* (mm)	Ending Average *c* (mm)	*a/t*	*a/c*	Ending K_a Max	Ending K_c Max
Slow 1	S1	1.79	3.39	0.35	0.53	21.77	16.46
Room Temperature	RT	3.04	4.01	0.59	0.76	25.63	24.87
Slow 2	S2	3.39	4.37	0.66	0.78	27.24	27.37
Fast 2	F2	3.51	4.67	0.68	0.75	28.58	28.51
Slow 3	S3	3.80	5.05	0.74	0.75	30.27	30.90
Fast 3	F3	4.12	5.39	0.80	0.76	31.77	33.51
Slow 4	S4	4.53	5.99	0.88	0.76	34.42	37.40
Fast 4	F4	4.87	6.30	0.94	0.77	35.67	40.33
Slow 5	S5	5.11	6.75	0.99	0.76	37.58	43.07

2.4.3.5. Shape and Life Measurments

The shape evolution results are shown in Figure 143 below. The data points gathered from the marker bands in the experiment show that applied the TAF in only one direction is not realistic. While the shape matches the prediction for no TAF, it isn't

possible to rule out TAF in both directions. The simulations do not account for the marker bands, and as such shape resolution is probably not good enough to choose which of the middle lines follows the data.

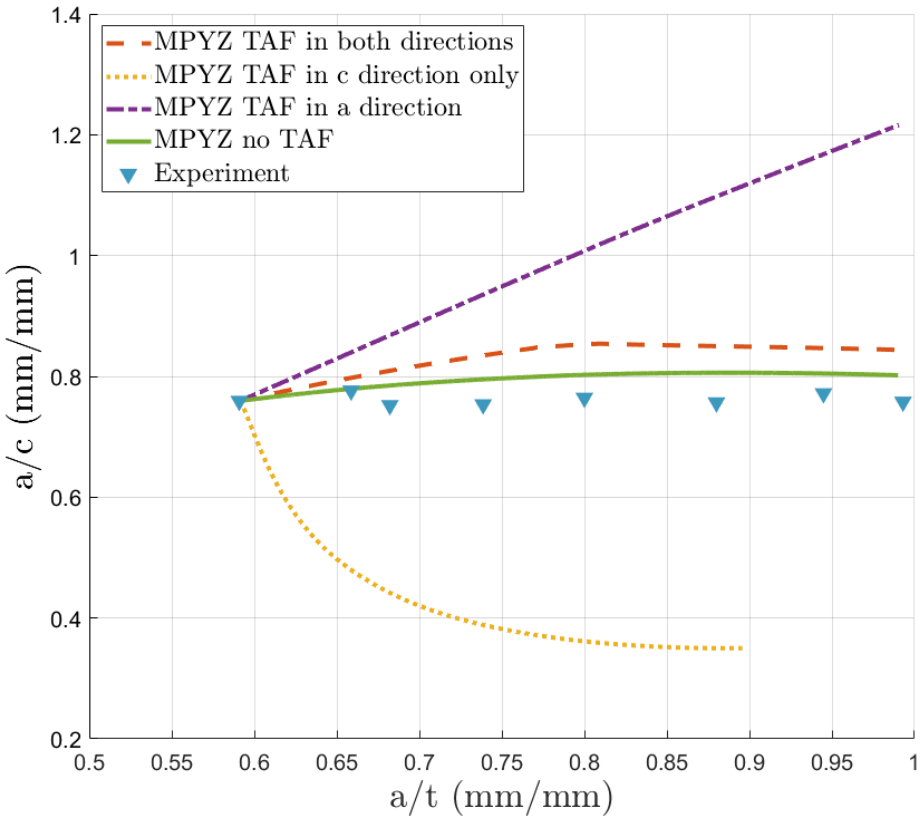

Figure 143: Shape evolution of the high temperature isothermal experiment with marker band data

Figure 144 shows the number of cycles per R=0.1 f=0.1 Hz "S" band (with the exception of S1) in the experiment and in simulations with and without TAF. The simulated lifetimes were generated by putting the flaw geometry measured at the end of each of the preceding marker bands into MPYZ-TMF and then counting the number of cycles until the crack in the *a*-direction (depth direction) reached the *a* length of the beginning of the end of the "S" band from the experiment. This means that each simulation

assumes that there is no TAZ to start with, or that all previous TAZ has been consumed by the preceding marker band.

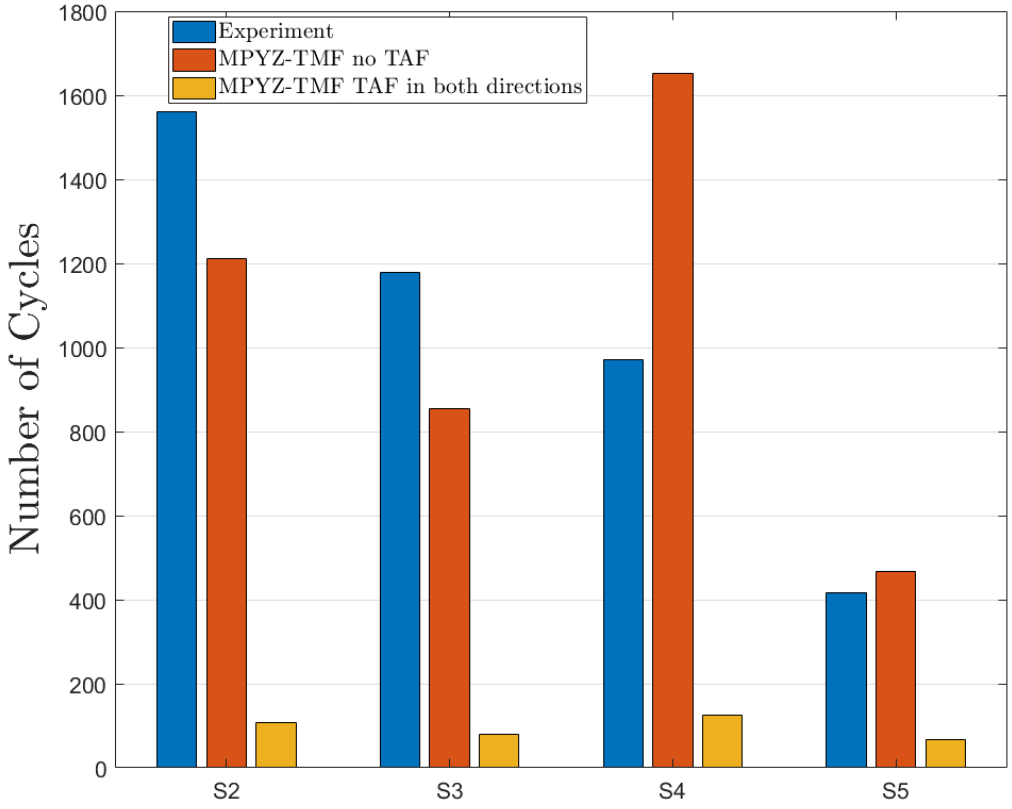

Figure 144: Number of cycles per band for each R=0.1 f=0.1 Hz band in the high temperature isothermal experiment

It is evident from the plot above, that when the TAF is allowed in MPYZ-TMF the simulations are very conservative. The TAF parameters fit by Radzicki for the FGIN718 material are too aggressive and accelerate the crack growth to a greater extent then what is seen in the experiment. When no TAF is applied the expected behavior occurs in the higher K, S4 and S5 bands, where the experiment cracks at a faster rate than when the TAF is not applied. For the lower K (S2 and S3) bands the opposite is seen. It's possible that this

may be due to deviations from the Forman curve at the lower K values. However, it's more likely that this is the TAZ effect increasing in the higher K bands due to more TAZ being generated. There is also a lot scatter inherent in fatigue crack growth scenarios which may partially explain the discrepancy.

Crack growth rate was calculated for each band in the surface direction using the in-situ measurements made with the Questar traveling microscope. The ΔK values were calculated using the dimensions at the end of each band. Figure 145 shows these values along with Radzicki's Forman fit for the FGIN718 material at 650 ºC and 10 Hz (adjusted to R = 0.1). As expected (with the exception of the initial point from S1) the f = 0.1 Hz data lies above the Forman fit showing an acceleration from the time dependent growth. The S1 point likely lies in threshold (Region I) growth region and is significantly below what is predicted by the Forman curve. Also as expected, the f = 2 Hz crack growth rate is lower on a per cycle basis then that seen for f = 0.1 Hz. However, this value lies below the 10 Hz Forman fit, and may be showing a difference in the growth rate of the CGIN718 material from Radzicki's FGIN718 material.

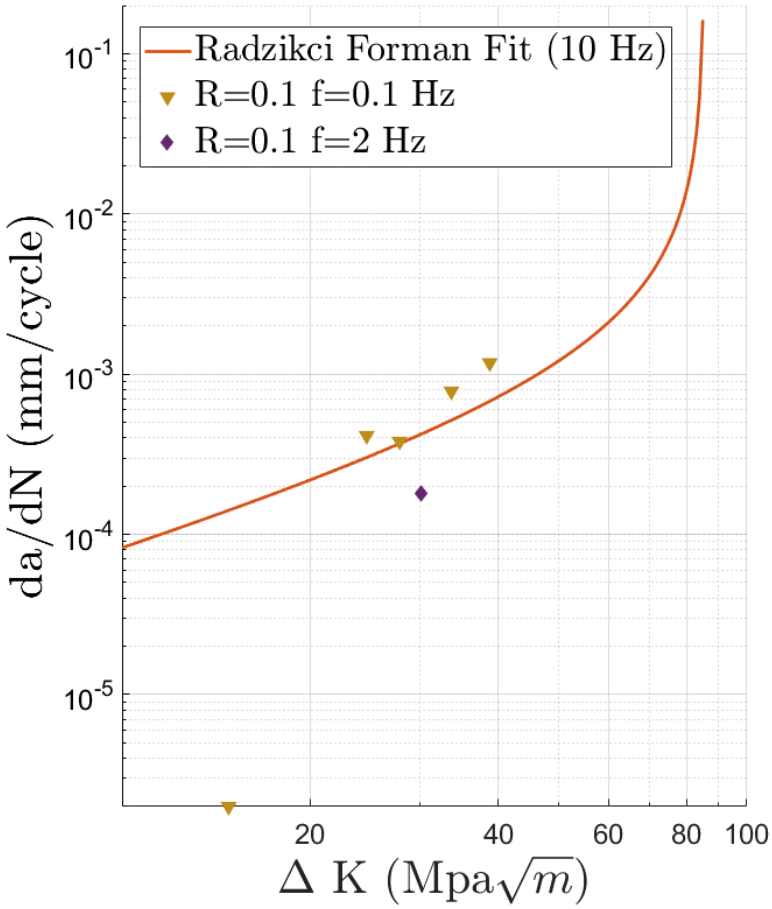

Figure 145: Fatigue crack growth rate at 650 ºC in Radzicki's Forman fit, and experimental data from the high temperature isothermal fatigue test

A review of Radzicki's work shows that he attempted to use his TAZ model in FGIN718 to predict slower frequency fatigue crack growth rates in Inconel 718. He notes that there are complications in these types of comparisons since the fatigue crack growth law for a given frequency would need to be free of TAZ effects so that the effect isn't compounded with environmental factors already present in the growth law. Figure 146 shows data gathered by Radzicki at 10 Hz and 0.1 Hz (R = 0.05) at 650 ºC. The prediction at 10 Hz is shown using the Forman Equation fit to the data and is assumed to be the baseline with no TAZ effect. The dotted blue line shows that when the TAZ effect is

compounded upon this fit, conservative predictions result. When the TAZ effect is used to try to predict the 0.1 Hz fatigue crack growth rate from the 10 Hz data, a closer but still conservative curve is predicted.

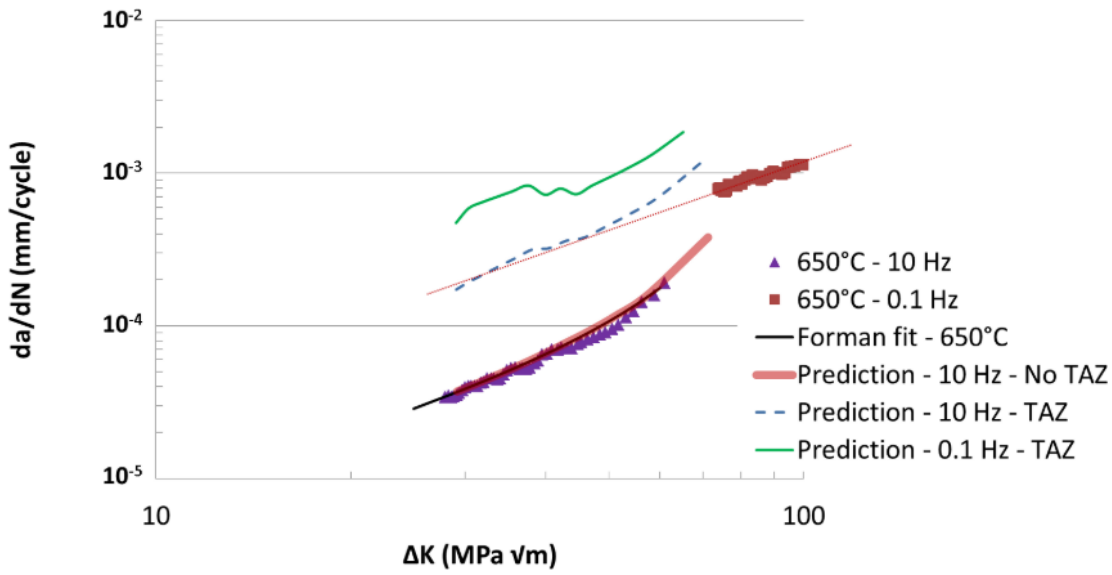

Figure 146: Radzicki's predictions for isothermal slow frequency crack growth using the TAZ acceleration effect in FGIN718 [1]

It is possible that in the future fatigue crack growth data based on tests run in vacuum can be used as a baseline. The effects due to the environment could then be completely removed from consideration, and adjustments using the TAZ model could be used to predict fatigue crack growth rates at different frequencies. Another complication that would need to be overcome is the fact that the TAZ model is history dependent and so a single crack growth rate cannot be found for a give ΔK. Instead a fatigue crack growth rate can be found for a given point in a simulation for a certain ΔK.

2.4.4. TMF Test Results and Discussion

A thermomechanical fatigue test was devised to test the effect of the TAZ on semi-elliptical surface flaws. Using the successful marker banding procedure from the isothermal test, the TMF spectrum was run until sufficient crack growth was observed in the Questar microscope and was interrupted by R=0.1 f=2 Hz loading to mark the fracture surface for measurement.

2.4.4.1. In-Situ Observations

As discussed in the experimental methods section above, a TMF spectrum was derived from Radzicki's fighter spectrum (Figure 48) that was somewhat simplified and designed to ensure that the test completed in a timely manner. The spectrum (Figure 65) is more like out-of-phase TMF then in-phase TMF because the highest load (80 kN) occurs at the lowest temperature (400 ºC). The spectrum also has a 70 kN peak at 650 ºC with a 20 second hold in which the majority of the TAZ is developed. TMF and marker bands will be referred to using the following abbreviations:

Table 30: TMF test load sequence with abbreviations

Step Label	Abbreviation	Max Load (kN)	Temperature (ºC)	R	Frequency (Hz)	Cycles
Initiation	I	44	RT	0.1	15	300000
Pre-Cracking	P	44	RT	0.1	15	285000
TMF-1	T1	80	TMF	TMF	TMF	791
Marker-1	M1	60	650	0.1	2	3245
TMF-2	T2	80	TMF	TMF	TMF	648
Marker-2	M2	60	650	0.1	2	2078
TMF-3	T3	80	TMF	TMF	TMF	661
Marker-3	M3	60	650	0.1	2	2000
TMF-4	T4	80	TMF	TMF	TMF	167
Final	F	60	RT	0.1	2	22507

In-situ observations show an observable difference between the surface appearance of the TMF bands and the marker bands. Figure 147 shows the TMF band T3 underlined in orange and the marker band M3 underlined in purple. The T3 band shows a wide black crack surrounded by dark grey material damage. The marker band presents much like a room temperature crack with a very thin crack front flanked by much less damage.

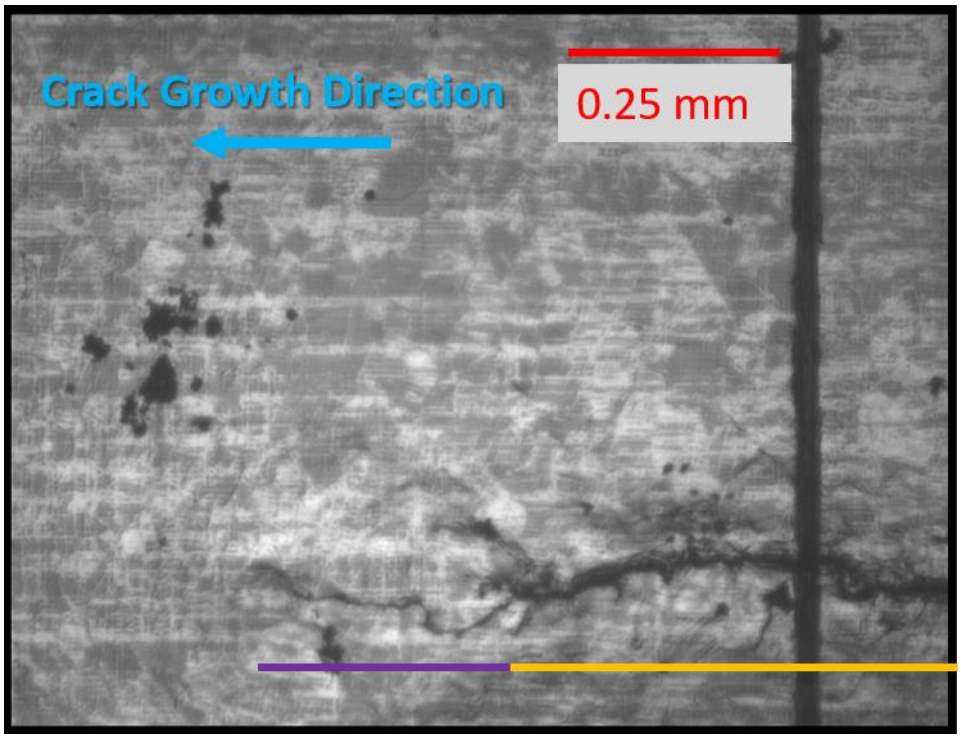

Figure 147: In-situ micrograph of the T3 band (underlined in orange) and the M3 band (underlined in purple) in the TMF test

It was also noted that a bifurcated pattern appears on the specimen surface immediately during the first 80 kN application when a marker has just ended and a new TMF band has started. Figure 148 shows this pattern forming at the beginning of band T3 after 7 cycles and 67 cycles. The bifurcation pattern can be seen on the left, which is then bisected by further crack growth seen on the right. This length of this bifurcation is approximately a quarter of the plane stress plastic zone size in the TMF band and is

showing a sudden expansion in plastic damage upon the first overload after the lower stress marker cycle.

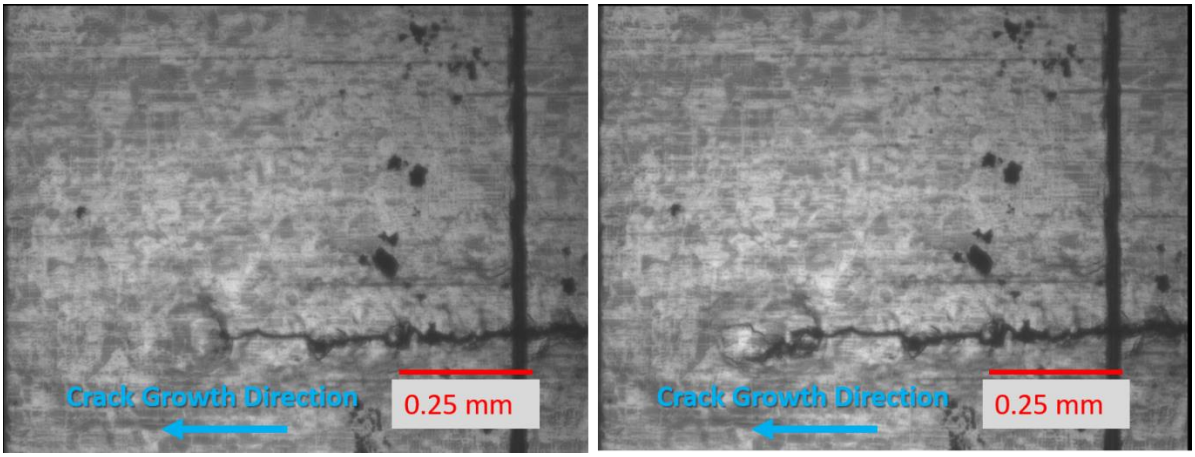

Figure 148: The start of band T3 showing a bifurcated pattern at the end of the crack (Left) After 900 seconds / 7 cycles (Right) After 8400 seconds / 67 cycles

2.4.4.2. Fracture Surface Observations

Inspection of the fracture surface shows that the marker banding was successful in showing the crack location and shape in the applied locations (Figure 149). For the most part ducking in at the surface is limited. Its effects are mostly only seen at the blue fringe at the edge of T4 especially on the right side.

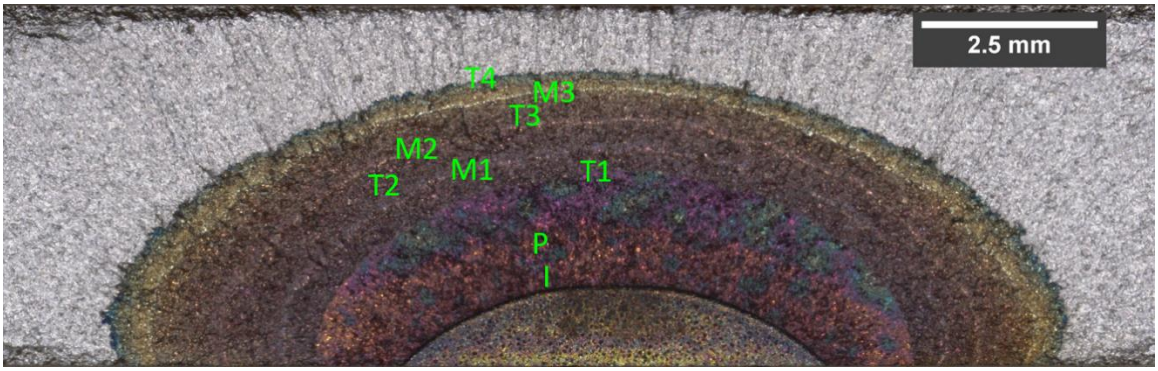

Figure 149: Optical fractograph of the TMF test's fracture surface showing TMF bands separated by thin marker bands

SEM fractography shows the TMF region as a mixed inter/trans granular region. This region can still be clearly distinguished from room temperature fully transgranular crack growth. A clear transition line is seen in Figure 150 with the room temperature growth in the bottom-right changing to the partially intergranular TMF in the top-left.

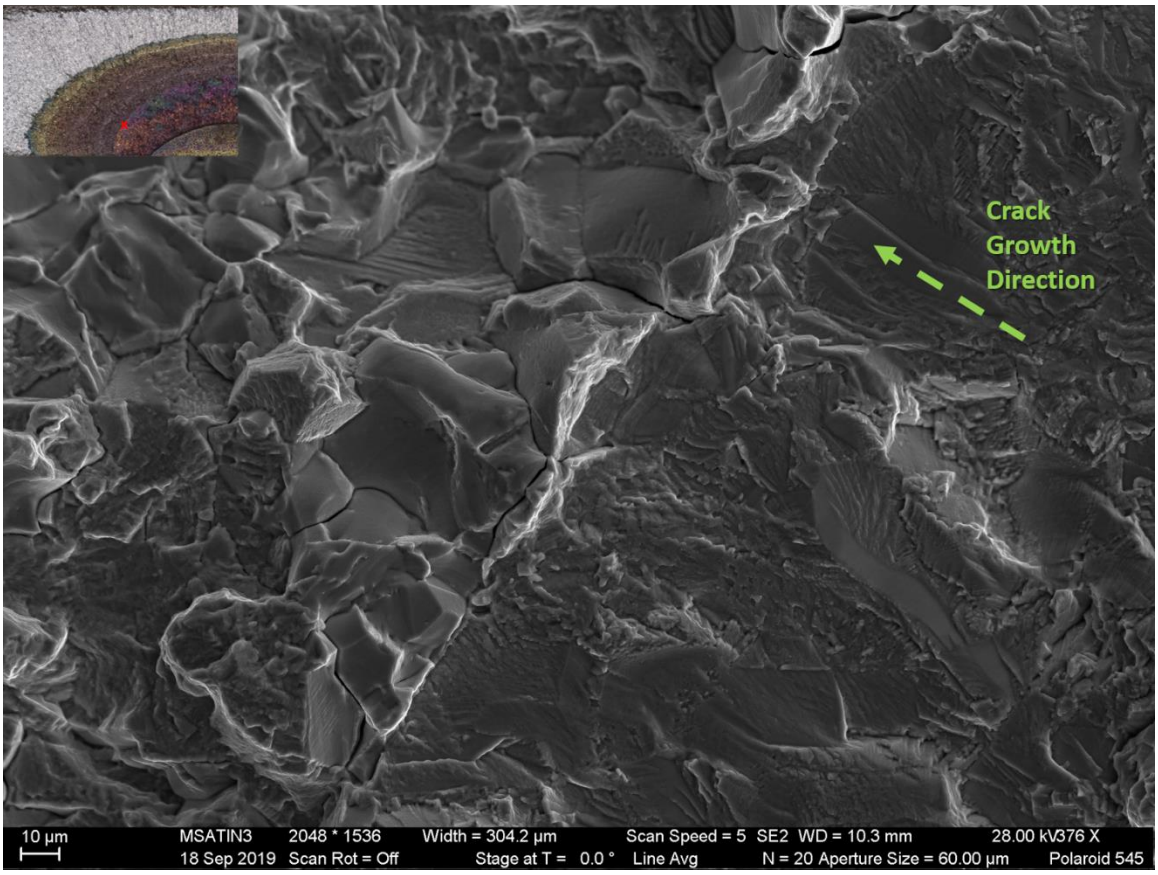

Figure 150: SEM fractograph showing the transition from room temperature crack growth to TMF crack growth

Figure 151 shows the *a*-direction SEM fractograph. The TMF damage is a mixed inter/trans granular region crossed by thin marker bands. Figure 152 shows a magnified view of the TMF bands T2 and T3 with marker M2 in between (highlighted in red). The marker band can be seen due to the change in contrast, however the actual topography of the surface hardly differs. The region appears to have the same mixed character as the

TMF regions around it including white transgranular ligaments crossing the boundary without interruption. This indicates that the TAZ extended into the material through the region where the marker band was grown. The marker band in the *a*-direction is also thinner than a single grain diameter in the material making it more likely that intergranular damage features had crossed the region before marking.

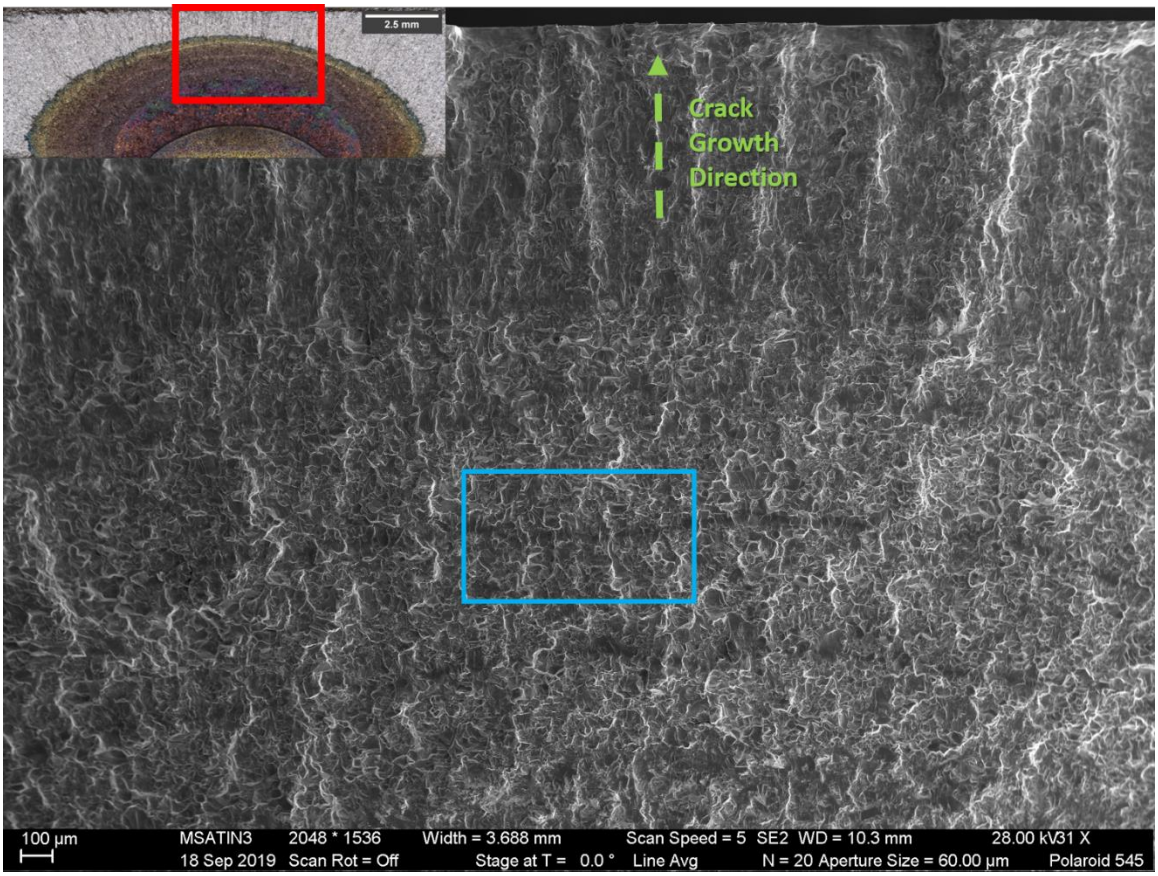

Figure 151: SEM fractograph of the central a-direction region of the TMF test showing mixed intergranular TMF bands interrupted by smaller marker bands. The magnified region in Figure 152 is highlighted in blue

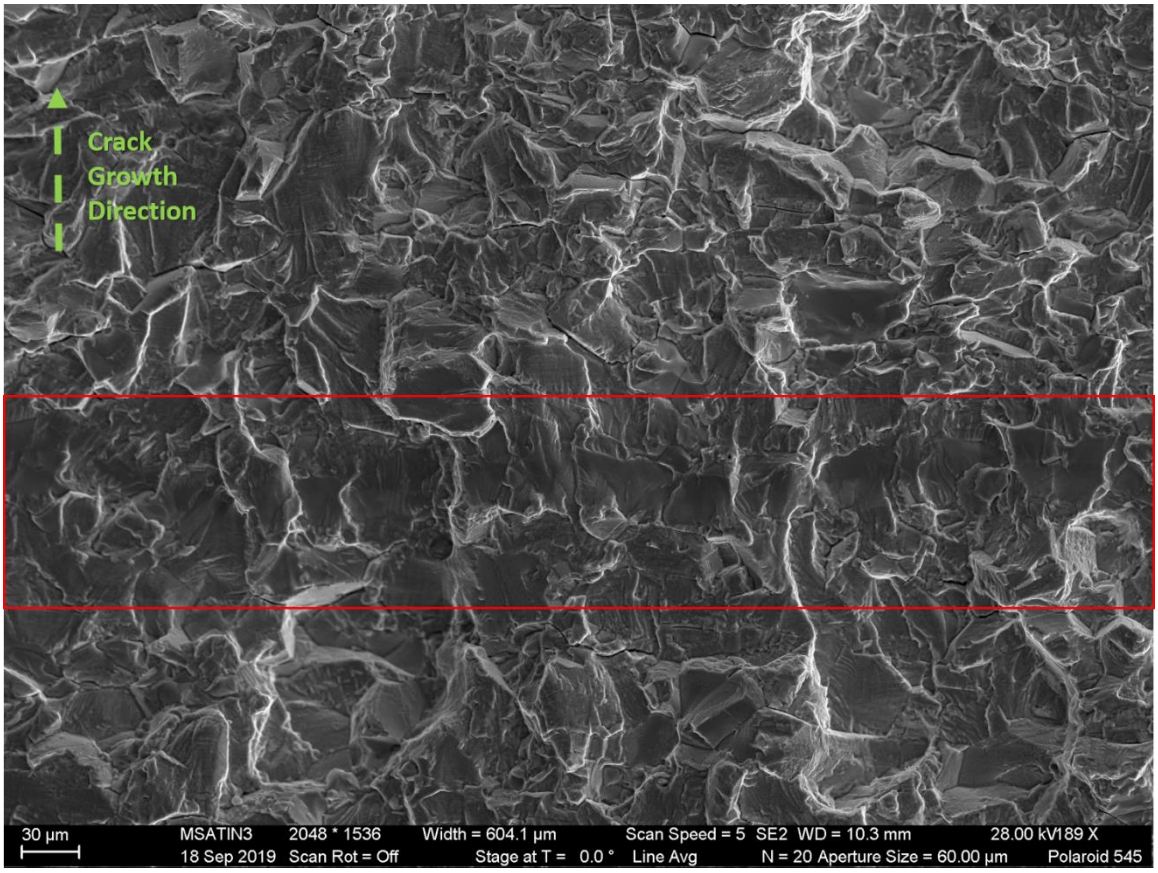

Figure 152: SEM fractograph of marker M2 (highlighted in red) in the TMF test

Markers in the *c*-direction right on the free surface tended to be slightly wider. In Figure 153 marker M3 can be seen highlighted in blue. This band does show a slight change in topography. It appears to have a slightly more transgranular character which may be due to either the higher applied stress intensity, or less TAZ effect due to the lack of constraint in the region as expected.

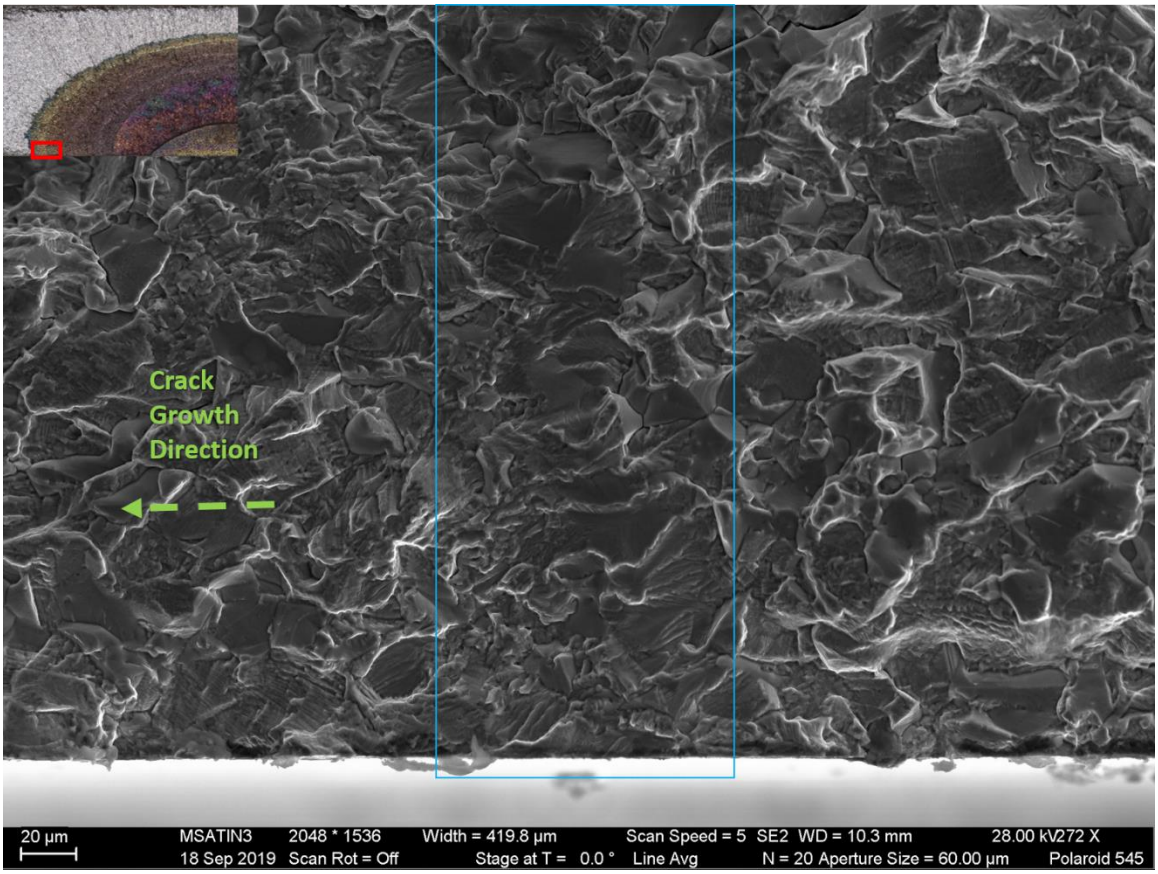

Figure 153: SEM fractograph of the TMF test showing M3 in the c-direction highlighted in blue

2.4.4.3. Shape and Life Measurements

Measurements were made using the optical fractograph, and the following K values were calculated:

Table 31: Measurements and calculated K values for bands in the TMF test

Step Label	Abbreviation	Ending *a* (mm)	Ending Average *c* (mm)	*a/t*	*a/c*	Ending K_a Max	Ending K_c Max
Pre-cracking	P	2.81	4.30	0.54	0.65	35.54	31.46
TMF 1	T1	3.05	4.75	0.59	0.64	38.13	34.02
Marker 1	M1	3.11	4.83	0.60	0.64	38.63	34.66
TMF 2	T2	3.48	5.38	0.68	0.65	42.06	38.86
Marker 2	M2	3.55	5.51	0.69	0.64	40.90	39.13
TMF 3	T3	3.96	6.34	0.77	0.63	47.98	45.20
Marker 3	M3	4.03	6.43	0.78	0.63	48.59	46.03
TMF 4	T4	4.24	6.84	0.82	0.62	51.25	49.11

This allowed for the shape evolution to be compared to MPYZ-TMF simulations using the four different combinations of TAF shown in Figure 154 below.

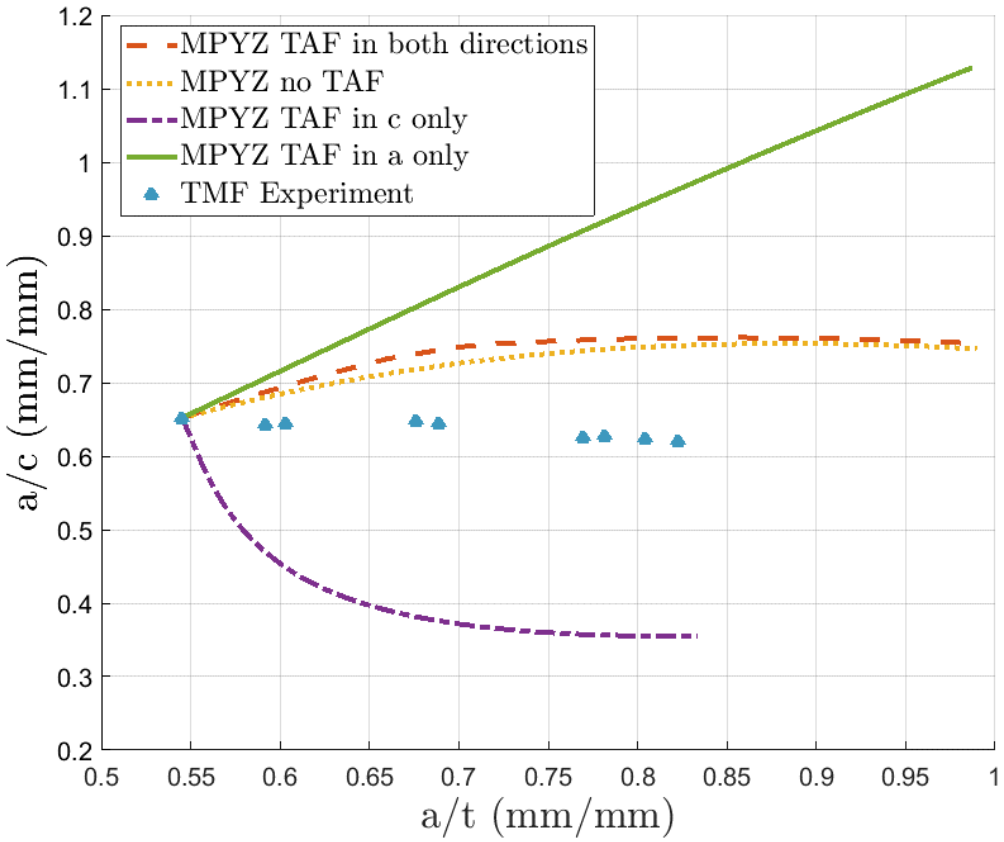

Figure 154: Shape evolution plot of the TMF test and simulated MPYZ-TMF outputs for different TAF conditions

Again, the shape evolution shows that having the TAF operate in only one direction is not realistic. In fact the aspect ratio decreased slightly overtime with more relative growth in the surface direction then what was predicted. This is the opposite of what was hypothesized based on Radzicki's plane stress/plane strain prediction. However, in light of the evidence from the K-hold tests it may be that the surface direction growth is enhanced by the maximum TAZ area that occurs just inside the surfaces in the *c*-direction.

The same life analysis was conducted as the high temperature isothermal test. Each TMF band was simulated in MPYZ-TMF using both the no TAF and TAF in both

directions assumptions. The number of cycles to reach the experimental depth (*a*-direction) for the end of the band were counted and compared.

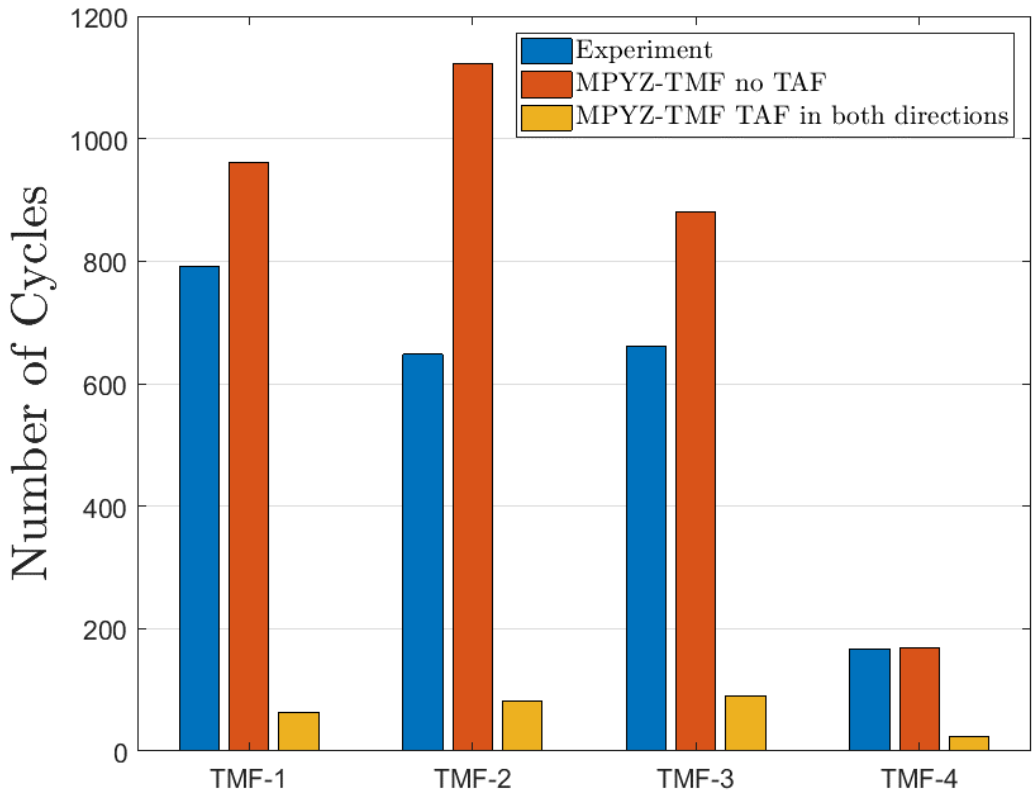

Figure 155: Comparison of number of TMF cycles in the TMF experiment and MPYZ-TMF simulations

Figure 155 shows that again the TAF in both directions simulations were too fast by an order of magnitude. However, unlike the isothermal test this shows a more consistent trend where the experiment grows faster than the predictions without the TAF. The exception is the fourth band (TMF-4) where the experiment was just short of the prediction with no TAF. This shows that the small number of cycles in that band did not have enough time to develop a sufficient amount of TAZ to show a deviation from the acceleration effect.

2.5.MPYZ-TMF Grain Size Dependent Model

Evidence from the two high temperature fatigue tests suggest that the TAZ acceleration effect calibrated to Radzicki's results is overdriven. One of the reasons for this could be that it was fit to the FGIN718 material. Since the TAZ mechanism is completely reliant on grain boundaries it makes sense that a drastic change in grain size would result in a different effect.

A change to the model has been implemented to utilize the mean grain diameter as one of the material parameters to be considered. The form of the TAZ size equation (20) has been changed to a new form:

$$TAZsize = \frac{C}{d} t^{n_1} K_{hold}^{n_2} e^{n_3 \frac{-Q}{RT}} \qquad (32)$$

Where *d* is the mean grain diameter in μm. This changes the value of C which is now equal to 1.164 $\mu m^{-1}(sec)^{-n1}(MPa\sqrt{m})^{-n2}$. The form of the TAF equation (31) has been changed to:

$$TAF = 1 + \frac{D}{d}\left(\frac{TAZsize_{current}}{r_p}\right)^p \qquad (33)$$

Where again *d* is the mean grain diameter in μm. The new value of D is 24.

The increase in mean grain diameter (*d*) decreases both TAZ development and the acceleration factor due to TAZ. This phenomenon can be rationalized by considering how the material weakening may proceed in FGIN718 vs CGIN718. During the weakening phase, the most susceptible grain boundaries (those at 45º angles) are oxidized. In the

FGIN718 there are approximately 230 times more grains that may have susceptible boundaries in the same area.

By the same logic, once mechanical cycling resumes the long, uncracked grain boundaries in the CGIN718 represent additional area that must be mechanically broken before the crack plane can advance. Because of this the TAZ effect is less severe in the larger grained material, and the crack acceleration is less overwhelming.

Another possible explanation could rely upon the fact that larger grains involve a larger deflection of the crack path from the mean crack plane in order to continue following grain boundaries. This requires additional energy and would therefore slow the crack growth when compared to the FGIN718 scenario.

Note that this effect is specifically associated with the material damage or TAZ ahead of the crack tip and not the time-dependent growth seen with very long hold times. In a TMF scenario the time-dependent growth is occurring in concurrence with the mechanical cycling and can be thought of as contributing to the TAZ effect. In order to model the pure time-dependent growth at long hold times, another model may need to be developed.

Figure 156 shows the number of cycles per "S" band (see Table 28) in the high temperature isothermal test. As expected, the predictions for bands S2 and S3 are worse than the no TAF assumption since the experiment outlived the no TAF model. Again, this is likely due to the Forman curve being a poor approximation at lower K-values. For the bands S4 and S5 the grain size adjusted model is well matched to the experimental data

showing a slightly conservative prediction. The yellow columns show the original predictions corresponding to the new model with the FGIN718 material's grain size.

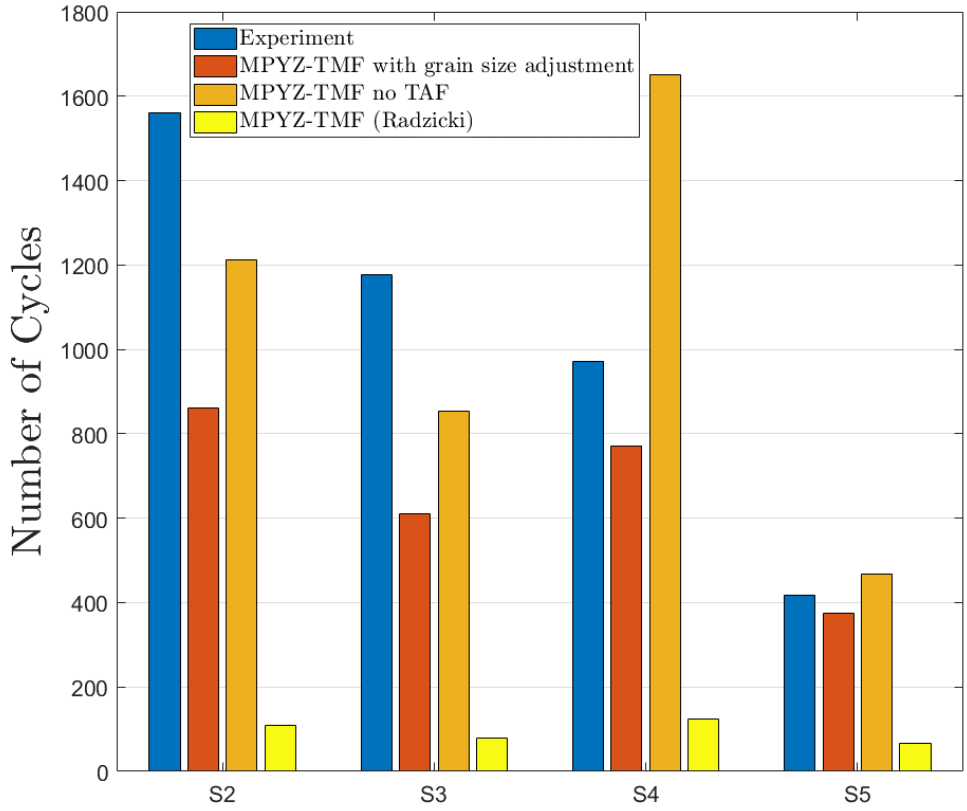

Figure 156: "S" band life analysis including the grain size adjusted MPYZ-TMF model in the high temperature isothermal fatigue test

The TMF test shows even more encouraging results. Figure 157 shows the life analysis of the individual TMF bands (see Table 30) where the new grain size adjusted predictions are very well matched to the experiment. Again, the largest deviation occurs at the lowest K band (TMF-1) due to deviations from the Forman curve. The other predictions are well within 10% of the actual values seen.

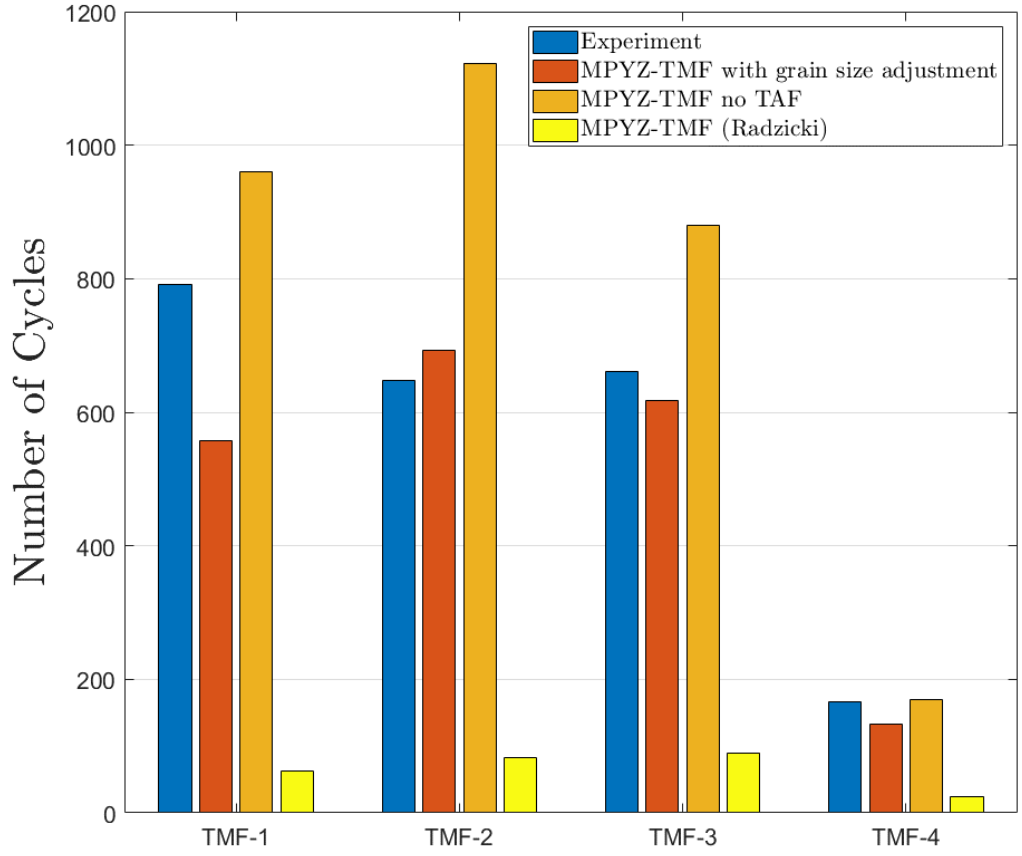

Figure 157: TMF band life analysis including the grain size adjusted MPYZ-TMF model in the TMF test

This model does not do much to change the shape evolution. The shape curve seen in Figure 158 shows almost no change due to the grain size model. This isn't surprising since there is very little difference when the TAF is applied or is absent. These shapes are still considered close to what is seen in the experiment. It may be possible in the future with additional data, changes to the model could be introduced to allow for more accurate shape tracking.

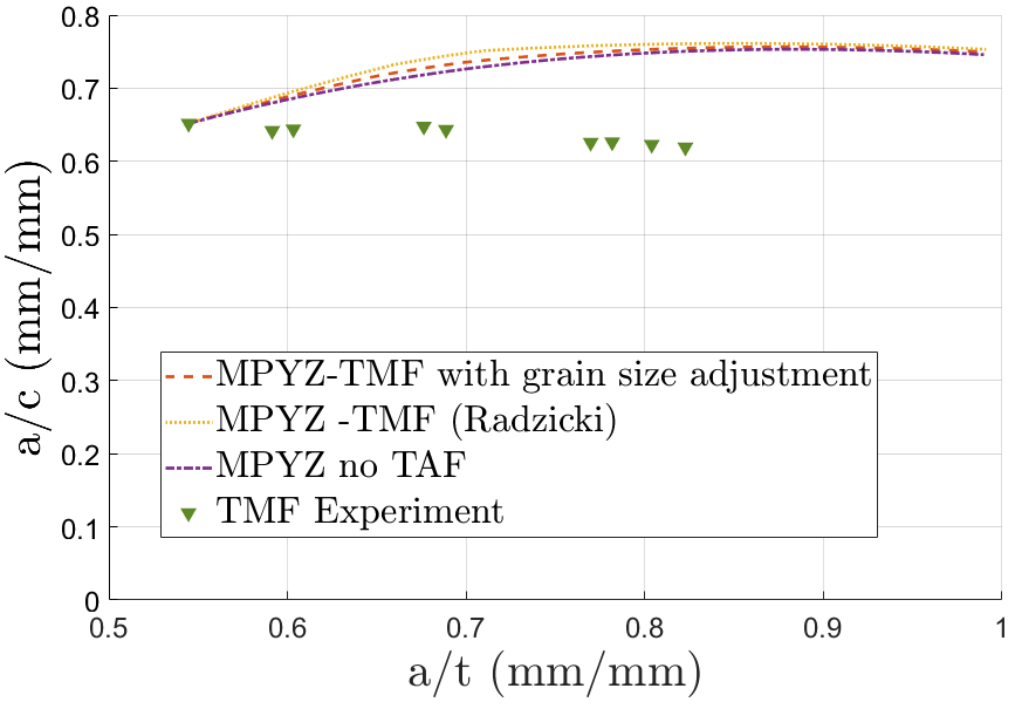

Figure 158: Shape evolution of the TMF test including the MPYZ-TMF model with grain size adjustment

CHAPTER III

CONCLUSIONS, SIGNIFICANCE OF RESEARCH, AND RECOMMENDATIONS FOR FUTURE WORK

3.1. Conclusions

This project had two primary objectives, to find a method for accurately modeling the transition of the surface flaws to through cracks, and to understand how surface flaws are effected by thermomechanical fatigue in Inconel 718. A combination of experimentation, data collection, analysis, and computer modeling was used to derive new methods of predicting fatigue crack growth phenomenon for these scenarios. These methods enhance the predictive capabilities for surface flaws and can be used in the future to better track surface flaws in real components.

3.1.1. Surface Flaw Transitions

A model was developed capable of producing accurate shape and life predictions through the transition of three different types of surface flaws. This model incorporated a careful treatment of the boundary conditions for asymmetric cracks by creating a new system of stress intensity solutions for clamped SENT specimens. The system was derived by running a large number of 3D finite element simulations and fitting solutions that worked for both very large and very small height to width (h/w) ratios.

A method for applying these solutions to quarter-elliptical corner cracks before and during transition was developed. This method defines an "equivalent SENT" crack length that is run through both the remote uniform tension and clamped solution. The equivalent

SENT crack length for a crack before breakthrough is defined by the horizontal coordinate of the centroid of the quarter-ellipse. For cracks after breakthrough, the equivalent SENT crack length is found by calculating the average horizontal coordinate along the crack front bounded by the front and back faces of the plate geometry. From the ratio of clamped to unclamped stress intensity, a penalty to the stress intensity felt due to the clamping can be applied to the corner crack.

A new method for growing surface flaws after breakthrough was developed as a modification to Johnson's Simple Geometric Transition (SGT) model. The SGT(λ) method continues growing surface flaws past breakthrough by using the projected vertical axis intercept *a'* to calculate the aspect ratio of the transitioning surface flaw. The λ parameter is added as a modifier to describe how much the back face crack growth is augmented for each surface flaw geometry. The proposed λ parameters are: 1.4, 1.55, and 1.15 for the semi-elliptical surface flaw, quarter-elliptical corner cracks, and symmetric quarter-elliptical corner cracks at a center through hole respectively. The SGT(λ) method allows for a much more realistic model of how these transitions occur when compared to the traditional instant type methods. This is an advantage in any application where accurate crack shape is required in this transition region.

3.1.2. Thermomechanical fatigue of surface flaws in Inconel 718 at high temperature

A series of high temperature K-hold tests were conducted on CGIN718 material at 650 ºC for 3600 seconds to better define how the TAZ effect might work in semi-elliptical surface flaws. These tests showed that at high temperature an intergranular time-dependent zone

can develop at stress intensities above 25 MPa√m. Unlike what was observed by Radzicki, time dependent growth was seen in the material in both the semi-elliptical and SENT crack geometries. This time-dependent behavior was also observed in a FGIN718 semi-elliptical sample at approximately 31 MPa√m of stress intensity. It was found that this time-dependent behavior could appear very differently on the surface depending on the formation of slant growth (shear lips). It has been proposed that the formation of these shear lips may have blocked the view of Radzicki from observing this time dependent growth in his specimens.

An unbroken specimen exposed to K-hold conditions was sectioned and evaluated to try to characterize the type of damage that had occurred. It was found that the time-dependent damage consisted of cracking with a damaged or temperature affected zone (TAZ) presenting as a discontinuous region of broken grain boundaries. It is thought that the TAF effect observed by Radzicki is a breaking of grain boundaries ahead of the main crack plane. Once cycling resumes, any unbroken links on the crack plane quickly fracture and crack growth is accelerated.

It was found that the extent of damage from the TAZ effect is indeed dependent on the stress state of the material at the crack tip. On a semi-elliptical surface flaw the region of maximum growth of this TAZ is just below the surfaces in the *c* direction. A minimum in TAZ formation appears not only in the unconstrained region at the free surface but also in the depth direction where the shrinking remaining ligament creates less material constraint.

High temperature fatigue tests were performed on the CGIN718 material isothermally and under a TMF spectrum. It was shown that using Radzicki's model the

TAZ effect is overly aggressive for these scenarios. A new grain size dependent model has been proposed to more accurately predict crack growth under TMF in the CGIN718 material. It appears that the TAZ acceleration effect can be mitigated by using a larger grain size.

3.2. Significance of Research

A more accurate description of surface flaws in now available for both their behavior during transition, and how they are effected under TMF in Inconel 718. The behavior of surface flaws during transition can be vital in any application where this region becomes important. If there are any material inhomogeneities in the transition region, an instant transition method will ignore these features. If a flaw is found in the field that is undergoing transition, the SGT(λ) method can be used to predict it's shape and life progression.

Optimum marker banding techniques have been developed for studying surface flaws in both room temperature and high temperature conditions. These bands are essential for tracking how these cracks grow and evolve. Not only can these techniques be used in future scientific endeavors, but the high resolution images of the fracture surfaces in this work can be made available for further analysis. It is possible that more refined models can be made in the future using the data generated for this work.

For high temperature TMF type loading in Inconel 718 this research can be vital to predicting crack lives for vital applications such as jet engines. In these parts, the damage tolerant approach to life management is used to ensure the safety of passengers and crew while also providing an economic benefit by setting safe inspection intervals. Having the most accurate possible methods for tracking and predicting material damage is vital to

optimizing this method. In addition, knowing how and why TAZ develops in Inconel 718 can lead to more intelligent applications of the material in situations where this acceleration effect can be important.

This research shows that a larger grain size can have beneficial effects in applications where the acceleration due to TAZ becomes important. In addition, because the TAZ effect is more severe for materials under a more constrained state of stress, it may be possible for components to be designed in such a way that plane stress conditions become dominant. An example of this is taking a single thick sheet of material, and instead using a stack of thin sheets to keep potential crack growth in a less constrained state.

This research has advanced the basic understanding of thermomechanical fatigue in nickel superalloys. The insights and knowledge gained from this work can be put to use not only in the analysis of current materials, but in the design of future materials optimized for damage tolerance.

3.3.Recommendations for Future Work

No process in the course of scientific discovery can ever truly be complete. Because of this there are several things that would benefit this type of research that could not be done either because of time constraints, material availability, financial resources, or lying outside the scope of this work. Here are a few possible ideas:

- Semi-elliptical surface flaws at a center through hole were not tested in this research, but the SGT(λ) method could easily be extended to this geometry with further testing. In addition, non-symmetric flaws at a center hole may also be added in the future.

- Due to lack of material availability this project was primarily conducted on CGIN718 material. There seem to be many differences in behavior between this and FGIN718 such as the susceptibility to forming shear lips, and how much they are effected by the TAZ acceleration effect. A careful study to really quantify the differences in fatigue crack growth rate, mechanical properties, corrosion properties, and fracture mechanisms could improve understanding of the mechanisms active in this work.
- K controlled tests are not possible in the current experimental apparatus due to interference in EPD readings from the induction heating system. However, K controlled testing could be very useful in teasing apart the different effects that go into fatigue crack growth at high temperatures in Inconel 718. Using a K controlled test, it may be possible to see what effects on the fatigue crack growth rate are due to frequency, or the formation of shear lips. In addition, as cracks grow longer, it may be possible to study how the crack tip stress state effects the fatigue crack growth rate independent of K.
- Marker bands were essential to tracking the shape and location of the surface flaws during high temperature testing. However, this had the effect of consuming some TAZ ahead of the crack tip by growing through it. In the future the grain size dependent TMF model can be tested using pure, uninterrupted TMF experiments to see if the model still holds for larger build ups of TAZ.
- Although the shape evolution pathway modeled in this work for the TMF test was close, additional accuracy could be gained through further testing. Testing

additional aspect ratios and larger numbers of tests could be used to refine the model to ensure that the crack shape is preserved throughout the simulation.

- The transition region of these surface flaws could not be studied at high temperatures in this work due to shortcomings in the available equipment. However, future work could seek to test the combined models using the MPYZ-TMF code to see how surface flaws transition under TMF.
- Another future contribution could use plasticity enabled FEA simulation to look at the state of stress in the *a* direction of these cracks as they near the back face of the material. This could be used to explain why the TAZ seems to be less developed in that direction. The same technique could be used to analyze what situations lead to shear lip development in the *c* direction and why the bifurcation pattern is sometimes seen on the surface during K-holds, and why massive time-dependent growth is sometimes seen instead.
- Spherical nano-indentation could be used to get mechanical properties around the unbroken cracks in both the transgranular and intergranular portions to explore changes. This could be used to observe cyclically hardening or softening behavior or to study amounts of previous deformation.

REFERENCES

[1] A. T. Radzicki, “Characterization and Modeling of the Thermomechanical Fatigue Crack Growth Behavior of Inconel 718,” Georgia Institute of Technology, 2016.

[2] I. S. Raju and J. C. Newman, “Improved Stress-Intensity Factors for Semi-Elliptical Surface Cracks in Finite-Thickness Plates,” 1977.

[3] J. C. Newman and I. S. Raju, “An empirical stress-intensity factor equation for the surface crack,” *Eng. Fract. Mech.*, vol. 15, no. 1–2, pp. 185–192, 1981.

[4] J. C. Newman and I. S. Raju, “Stress-Intensity Factor Equations for Cracks in Three-Dimensional Finite Bodies Subjected to Tension and Bending Loads,” in *Computational Methods in Mechanics of Fracture*, S. N. Atluri, Ed. Elsevier Science Publishers B.V., 1986, pp. 311–334.

[5] J. . Harter, “AFGROW users guide and technical manual.” Air Force Research Laboratory, 1999.

[6] W. S. Johnson, “Prediction of Constant Amplitude Fatigue Crack Propagation in Surface Flaws,” *ASTM STP*, vol. 687, pp. 143–155, 1979.

[7] J. B. Chang, “Assessment of the Sensitivity of Crack Growth Rate Constants to Predictive Accuracy of Part-Through Crack Fatigue Life Predictions,” *ASTM STP*, vol. 687, pp. 156–167, 1979.

[8] A. F. J. Grandt, J. A. Harter, and B. J. Heath, “Transition of Part- Through Cracks at Holes into Through-the-Thickness Flaw,” *ASTM STP*, vol. 833, pp. 7–23, 1984.

[9] L. . Hall, R. C. Shah, and E. W. L., “Fracture and Fatigue Crack Growth Behavior of Surface Flaws and Flaws Originating at Fastener Holes,” 1974.

[10] J. R. Snow, “A Stress Intensity Factor Calibration for Corner Flaws at an Open Hole,” Air Force Institute of Technology, 1975.

[11] R. F. Hall and B. E. Powell, “The growth of corner cracks by fatigue,” *Int. J. Fatigue*, vol. 19, no. 5, pp. 429–435, 1997.

[12] C. Manu, “Three-Dimensional Finite Element Analysis of Cyclic Fatigue Crack Growth of Multiple Surface Flaws,” Cornell University, 1980.

[13] S. A. Fawaz and J. C. Newman, “Experimental Verification of Stress Intensity Factor Solutions for Corner Cracks At a Hole Subject To General Loading,” in *ICAF 2003 - Fatigue of Aeronautical Structures as an Engineering Challenge*, 2003.

[14] Y. Dong, X. He, and Y. Li, “Marker load-aided bidirectional fatigue crack growth rate measurement via a semi-elliptical surface crack,” *Int. J. Fatigue*, vol. 111, no. February, pp. 208–219, 2018.

[15] W. S. Johnson, “Multi-Parameter Yield Zone Model for Predicting Spectrum Crack Growth,” *ASTM STP*, vol. 748, pp. 85–102, 1981.

[16] V. M. Barker, W. S. Johnson, B. S. Adair, S. D. Antolovich, and A. Staroselsky, “Load and temperature interaction modeling of fatigue crack growth in a Ni-base superalloy,” *Int. J. Fatigue*, vol. 52, pp. 95–105, 2013.

[17] V. M. Barker, “Thermo-Mechanical Fatigue Crack Growth Modeling of a Nickel-Based Superalloy,” Georgia Institute of Technology, 2011.

[18] “Metallic materials properties development and standardization (MMPDS) : MMPDS-11, July 2016.” Federal Aviation Administration ;, [Washington, D.C.], 2016.

[19] R. C. Rice and S. of A. E. F. D. and E. Committee, *SAE fatigue design handbook*, 3rd ed.. Warrendale, Pa.: Warrendale, Pa. : Society of Automotive Engineers, 1997.

[20] J. C. Newman and Y. Yamada, “Compression precracking methods to generate near-threshold fatigue-crack-growth-rate data,” *Int. J. Fatigue*, vol. 32, no. 6, pp. 879–885, 2010.

[21] “FRANC3D Reference Manual,” no. Version 7.2. Fracture Analysis Consultants, Inc., 2018.

[22] B. S. Adair, W. S. Johnson, S. D. Antolovich, and A. Staroselsky, “Identification of fatigue crack growth mechanisms in IN100 superalloy as a function of temperature and frequency,” *Fatigue Fract. Eng. Mater. Struct.*, vol. 36, no. 3, pp. 217–227, 2013.

[23] C. Chang and M. E. Mear, “A boundary element method for two dimensional linear elastic fracture analysis,” *Int. J. Fract.*, vol. 74, no. 3, pp. 219–251, 1996.

[24] J. F. Radavich, “The Physical Metallurgy of Cast and Wrought Alloy 718,” *Superalloys 718 Metall. Appl.*, pp. 229–240, 2004.

[25] E. Akca and A. Gürsel, “A Review on Superalloys and IN718 Nickel-Based INCONEL Superalloy,” *Period. Eng. Nat. Sci.*, vol. 3, no. 1, 2015.

[26] R. C. Reed, *The Superalloys Fundamental and Applications*, First. New York: Cambridge University Press, 2006.

[27] M. Sundararaman, P. Mukhopadhyay, and S. Banerjee, “Carbide Precipitation in Nickel Base Superalloys 718 and 625 and Their Effect on Mechanical Properties,” *Superalloys 718, 625, 706 Var. Deriv.*, pp. 367–378, 1997.

[28] “AMS2774E Heat Treatment Wrought Nickel Alloy and Cobalt Alloy Parts.” SAE International, 2016.

[29] V. Acharya, S. Ramesh, and G. V. S. Murthy, “‘Characterization of Intermetallic Precipitates in Ni-Base Alloys by Non-destructive Techniques,’” *Superalloys*, pp. 247–273, 2015.

[30] T. H. Sanders, R. E. Frishmuth, and G. T. Embley, “Temperature Dependent

Deformation Mechanisms of Alloy 718 in Low Cycle Fatigue.," *Metall. Trans. A, Phys. Metall. Mater. Sci.*, vol. 12 A, no. 6, pp. 1003–1010, 1981.

[31] B. Peraggic and J. F. Uginet, "Fatigue and Creep Properties in Relation with Alloy 718 Microstructure," in *LORIA E A. Third International Symposium on Superalloys*, 1994, vol. 718, pp. 625–706.

[32] D. D. Krueger, S. D. Antolovich, and R. H. Van Stone, "Effects of Grain Size and Precipitate Size on the Fatigue Crack Growth Behavior of Alloy 718 at 427 Degrees Celcius," *Metall. Trans. A, Phys. Metall. Mater. Sci.*, vol. 18 A, no. 8, pp. 1431–1449, 1987.

[33] S. Floreen and R. H. Kane, "Effects of environment on high-temperature fatigue crack growth in a superalloy," *Metall. Trans. A*, vol. 10, no. 11, pp. 1745–1751, 1979.

[34] J. P. Pedron and A. Pineau, "The Effect of Microstructure and Environment on the Crack Growth Behaviour of Inconel 718 Alloy at 650 °C under Fatigue, Creep and Combined Loading," *Mater. Sci. Eng.*, vol. 56, no. 2, pp. 143–156, 1982.

[35] H. Ghonem and D. Zheng, "Depth of intergranular oxygen diffusion during environment-dependent fatigue crack growth in alloy 718," *Mater. Sci. Eng. A*, vol. 150, no. 2, pp. 151–160, 1992.

[36] M. Khobaib, N. E. Ashbaugh, G. A. Hartman, T. Weerasooriya, D. C. Maxwell, and R. C. Goodman, "Research on Mechanical Properties for Engine Life Prediction," no. January, 1988.

[37] H. Andersson, C. Persson, and T. Hansson, "Crack growth in IN718 at high temperature," *Int. J. Fatigue*, vol. 23, no. 9, pp. 817–827, 2001.

[38] R. Molins, G. Hochstetter, J. C. Chassaigne, and E. Andrieu, "Oxidation effects on the fatigue crack growth behaviour of alloy 718 at high temperature," *Acta Mater.*, vol. 45, no. 2, pp. 663–674, 1997.

[39] C. F. Miller, G. W. Simmons, and R. P. Wei, "Mechanism for oxygen enhanced crack growth in inconel 718," *Scr. Mater.*, vol. 44, no. 10, pp. 2405–2410, 2001.

[40] S. F. Chen and R. P. Wei, "Environmentally assisted crack growth in a Ni-18Cr-18Fe ternary alloy at elevated temperatures," *Mater. Sci. Eng. A*, vol. 256, no. 1–2, pp. 197–207, 1998.

[41] S. D. Antolovich and A. Saxena, "Thermomechanical fatigue: mechanisms and practical life analysis," in *ASM Handbook Volume 11*, Materials Park, OH: ASM International, 2002, pp. 738–748.

[42] T. Nicholas, M. L. Heil, and G. K. Haritos, "Predicting crack growth under thermo-mechanical cycling," *Int. J. Fract.*, vol. 41, no. 3, pp. 157–176, 1989.

[43] S. Gorgannejad, "On the Development of Data-driven Models to Reveal Links between Microstructure and Thermomechanical Fatigue," Georgia Institute of Technology, 2018.

[44] D. Gustafsson *et al.*, “Fatigue crack growth behaviour of Inconel 718 - The concept of a damaged zone caused by high temperature hold times,” *Procedia Eng.*, vol. 10, no. 10, pp. 2821–2826, 2011.

[45] E. Lundström, “Modelling of Fatigue Crack Growth in Inconel 718 under Hold Time Conditions,” 2014.

[46] K. M. Chang, “Time-dependent mechanisms of fatigue crack propagation in high-strength superalloys,” 1989.

[47] B. C. Collins, “Modified Pwa 1483 Nickel-Based Superalloy for Industrial Gas Turbine Applications,” 2007.

[48] ASTM, “Standard Test Methods for Determining Average Grain Size,” in *ASTM E112-13*, West Conshohocken PA: ASTM International, 2013.

[49] Society of Automotive Engineers, “Aerospace Material Specification 5663M.” 2009.

[50] J. Schuve, “Shear Lips on Fatigue Fractures in,” *Eng. Fract. Mech.*, vol. 14, no. 4, pp. 789–800, 1981.

[51] M. Loo-Morrey and P. A. S. Reed, “Anomalous crack shape development (tear drop cracking) in turbine disc material Udimet 720,” *Mater. Sci. Technol.*, vol. 16, no. 2, pp. 133–146, 2000.